HYBRID SIMULATION OF RETROFITTED RC BRIDGE WITH Fe-BASED SHAPE MEMORY ALLOY

A Thesis Submitted

in Partial Fulfullment of the Requirements

for the Degree of

DOCTOR OF PHILOSOPHY

by

Monjusha Sarmah

Under the Supervsion of

Prof. Sajal Kanti Deb & **Prof. Anjan Dutta**

Department of Civil Engineering
Indian Institute of Technology Guwahati

August, 2022

Dedicated to Ma and Deta

Declaration

I hereby declare that work presented in this thesis entitled "**Hybrid simulation of retrofitted RC bridge with Fe-based shape memory alloy**", submitted in partial fulfilment of the requirement for the award of the degree of Doctor of Philosophy in Civil Engineering, with specialization in Structural Engineering, is an authentic record of my own research work carried out in the Department of Civil Engineering, Indian Institute of Technology Guwahati under the supervision of Dr. Sajal K. Deb and Dr. Anjan Dutta, Professor, Department of Civil Engineering, IIT Guwahati.

The matter embodied in this thesis work has not been submitted by me for the award of any other degree, diploma associate-fellowship, fellowship or its equivalent to any University or Institute.

Date: 17.01.2023

Place: IIT Guwahati

(Monjusha Sarmah)

Certificate

It is certified that the work contained in the thesis entitled "**Hybrid simulation of retrofitted RC bridge with Fe-based shape memory alloy**", by Monjusha Sarmah, a student in the Department of Civil Engineering, Indian Institute of Technology Guwahati, India, for the award of the degree of Doctor of Philosophy, has been carried out under my supervision and, that this work has not been submitted elsewhere for the degree.

17-01-2023

Dr. Sajal Kanti Deb
Professor
Department of Civil Engineering
Indian Institute of Technology Guwahati
Guwahati-781039, India

Anjan Dutta 17.01.23

Dr. Anjan Dutta
Professor
Department of Civil Engineering
Indian Institute of Technology Guwahati
Guwahati-781039, India

Acknowledgement

As I write the concluding portions of this thesis, I am constantly reminded of all those who have helped me at every stage during this six-year long journey. I would, therefore, want to take this opportunity to thank the people and organisations who have made this study possible.

First and foremost, I would like to extend my sincere gratitude to my supervisors, Prof. Sajal K. Deb and Prof. Anjan Dutta, for their continuous guidance and encouragement throughout my time at IITG. Their exceptional abilities in tackling engineering problems, meticulous approach, perfectionism in academic research, and ability to see the bright side even in difficult situations have benefited me during my past six years and will continue to do so, in the years ahead. I am grateful for their contributions of time, ideas and valuable advice to make my Ph.D. experience very enriching and productive. I could not have asked for better Ph.D. supervisors.

Besides my supervisors, I would like to thank the rest of my doctoral committee members: Prof. Arunasis Chakraborty, Dr. Sandip Das and Dr. Atanu Banerjee for reviewing my work and providing their insightful feedback during my research. My humble thanks to Prof. Aminul Islam Laskar for his timely motivation and valuable interactions.

I deeply acknowledge the Scientific Officer, Dr. Arun Ch. Borsaikia, Technical Staff, Mr. Pranab Hazarika and Mr. Sourabh Kr. Mudoi and Support Staff, Suresh Boro, Bipul Bania and Pankaj Khakhlary of Structural Engineering Laboratory, for their invaluable assistance in smooth execution of my experiments. I am especially grateful to the Technical Superintendent of the laboratory, Mr. Biswajit Debnath, for his dedication towards proving technical supervision during the experiments. I am also grateful to the Asst. Workshop Superintendent, Mr. Nandan Kanan Das and Technical Staff, Mr. Manoj Baishya, Mr. Mrinal Sarma, Mr. Joykrishna Saikia, Mr. Dulumoni Das, Mr. Gautam Gogoi and Mr. Gwmchar Baro, for their assistance in cutting, bending and drilling of Fe-SMA strips.

I am thankful to the Managing Director of re-Fer AG, Dr. Julien Michels, for supplying us the Fe-SMA material for this study. I am very grateful to the team at Madona & Co., especially Mr. Paresh Kalita, for their valuable assistance in rehabilitation of the damaged specimens and fixing Fe-SMA strips on it. This endeavour would have been much more difficult without their help. I would also like to acknowledge the Sr. Area Sales Manager of Asian Paints, Mr. Sayan Ghosh and Sales Representative, Mrs. Smita Deka for providing us with poly-urea and arranging for its application at no cost to us.

I would like to express my gratitude to Prof. Deb and Prof. Dutta's research team, who I have had the pleasure of working with. I am very grateful to my colleague-turned-close friends, Dr. Pallab Jyoti Das and Ms. Tori Basar, who have offered tremendous help in many different ways and have supported me throughout my stay at IITG. I would also like to thank my colleagues: Dr. Pranjal Tamuly, Dr. Kamal Jyoti Nath, Ms. Prinza Priya Loying, Ms. Arpita Ghosh and Mr. Subhadip Naskar for their constructive discussions. I also wish to thank Mr. Vivekananda Halder for help and support during material testing at Central Instrumentation Facility, IIT Guwahati.

My humble thanks to the better halves of my supervisors, Mrs. Tumpa Deb and Mrs. Mousumi Dutta, for the care and affection they have shown me. I am also grateful to my friends, Ms. Himakshi Misra and Mrs. Sunanda Chettry, who made my hostel life much more enjoyable. I cannot thank my best friend, Mr. Mohit Kamboj, enough for keeping me grounded and patiently helping me get things in perspective.

Last but certainly not the least, I want to express my deep gratitude to my parents, Dr. Prabhat Ch. Sarmah and Jayashree Devi, and my siblings, Bidisha Sarmah and Hiranmoy Sarmah, who have been with me at every step of this journey. Their unwavering love, support, encouragement, and patience keep me going every day. I am forever indebted to them.

—— *Monjusha*

Abstract

Seismic retrofitting of RC bridge piers aims at improving its seismic performance by increasing its strength and ductility. Most common retrofitting techniques achieve this objective by addition of lateral confinement to concrete sections. Concrete confinement techniques can be divided into two main types - passive and active, based on the mechanism adopted to apply the confining pressure. Several studies have shown that active confinement outperforms passive confinement in terms of enhancing the strength and ultimate strain of concrete. This is because, prior application of confining pressure delays the initiation of damage in concrete. However, conventional active confinement techniques pose numerous constraints in-situ due to its need for specialized equipment and an excessive amount of time, money and labour, hence limiting its practical implementation. As a result, traditional passive confinement techniques have gained greater acceptance in the construction sector.

To address the above-mentioned challenges, a group of smart materials known as Shape Memory Alloys (SMAs) has lately gained interest among researchers for its ability to exert active confining pressure on concrete members without mechanical prestressing. SMAs can recover its original shape after undergoing large inelastic deformations through phase transformation brought about by change in temperature or state of stress. Thermal activation of pre-strained SMA while restrained, leads to the development of a large recovery stress. This recovery stress is utilized to exert active confining pressure externally on RC column. A cost-effective Fe-SMA with the composition Fe-17Mn-5Si-10Cr-4Ni-1(V, C) has shown excellent mechanical properties. Recovery stresses of 300–350 MPa are developed in Fe-SMA strips after heating it to 160°C. However, there are very few experimental and numerical studies pertaining to the uniaxial stress-strain behaviour of Fe-SMA-confined concrete so far, despite huge potential of Fe-SMA-confinement technique in the field of structural retrofitting.

Few studies have been carried out to evaluate the effectiveness of Fe-SMA for strengthening of RC beams. However, use of Fe-SMA for retrofitting of bridge piers have not been explored yet. Additionally, the performance of such structural systems under

seismic loads is an area that requires more research. It is crucial for evaluating the effectiveness of new and advanced materials in terms of enhancing the seismic performance of bridge piers. The use of hybrid simulation technique for investigating the response of RC piers retrofitted with Fe-SMA has not been documented in the literature.

This study focused on utilizing a new scheme of active confinement of concrete using a cost-effective substitute to commonly used expensive NiTi-based SMAs. Characterization of the Fe-SMA strips was done in terms of evaluation of recovery stress after stress relaxation, tensile stress-strain behaviour and cyclic stress-strain behaviour. Phase characterization of Fe-SMA samples was done by XRD and evolution of its microstructure was studied by FESEM.

An experimental study was conducted to evaluate the behaviour of plain concrete cylinders partially confined with Fe-SMA strips under uniaxial compressive loading. Three different grades of concrete and three different active confining pressures were adopted to study its influence on the stress-strain response of Fe-SMA-confined concrete specimens. Thereafter, regression analyses on test data were carried out to propose an empirical stress-strain equation for partially confined Fe-SMA concrete. Next, to understand the total confinement effect of external Fe-SMA and internal longitudinal as well as transverse reinforcement, 3D-FE analyses were carried out using ABAQUS. Furthermore, to achieve a higher degree of accuracy in predicting the values of the intrinsic parameters of the stress-strain relationship of Fe-SMA confined reinforced concrete, regression analyses were carried out utilizing the FE results and an empirical model was proposed.

Five numbers of $1/5^{th}$ scaled damaged pier models of a prototype bridge located in severest seismic zone in India were considered in the present study. These specimens were previously tested by Kotoky et al. (2018) at IIT Guwahati, which resulted in severe damage in the form of crushing of core concrete and yielding as well as rupture of reinforcement at the interface zone of the pier and foundation. A rehabilitation method was designed for the severely damaged pier models by RC jacketing following a systematically adopted step-by-step procedure for shifting the location of plastic hinge away from the pier-foundation interface. The specimens were subjected to lateral cyclic loading to evaluate its performance with respect to that of the original specimen. Calibration of the numerical

model of RC jacketed pier incorporating concrete-rebar interaction and jacket-pier interface shear was done by comparing with experimentally observed responses.

The rehabilitated bridge piers were further retrofitted using three configurations of Fe-SMA strips namely hoop (H), end-anchored (EA) and a combination of the combination of previous two approaches (EAH). In the first retrofitting scheme, Fe-SMA hoops were spaced equally in the plastic hinge zone of the bridge pier. It aims at utilizing the recovery stress of the pre-strained Fe-SMA strips for application of active confinement pressure on the pier. In the EA retrofitting scheme, pre-strained Fe-SMA strips were end-anchored on the surface of the bridge pier. Activation of restrained strips resulted in the development of pre-stress (pre-compression) in the concrete at the plastic hinge zone. It is a simple, fast and efficient retrofitting method of bridge pier, which makes it suitable for easy field implementation. In the EAH retrofitting scheme, a combination of EA and hoop reinforcement was studied for both pre-compression and active confinement.

To investigate the seismic performance of the retrofitted RC bridge piers, hybrid simulation was considered for the detailed study. Hybrid simulation has two modules: numerical module comprising of the numerical model of the prototype bridge and experimental module comprising of the scaled models of the piers. Four input excitations corresponding to different intensity levels were used in the hybrid simulation, followed by quasi-static cyclic tests to determine the ultimate capacity of test specimens. Comparison of effectiveness of the various Fe-SMA retrofitting schemes was made based on the results of the hybrid and cyclic tests.

The comparison of experimental results with those from the numerical model highlighted the need for model calibration to improve the response. Bond-slip effects and slip at the jacket-pier interface was approximately accounted for in the updated model. The parameters of Fe-SMA confined plain as well as reinforced concrete were obtained from the empirical stress-strain model developed earlier. To take into account the prestressing effect of EA Fe-SMA strips, initial stress was assigned to it. The force-displacement hysteretic behaviour of the test specimens obtained from the updated model agreed reasonably well with those obtained from experiments. Additionally, the bridge pier specimens with different Fe-SMA strip configurations were simulated using ABAQUS.

The experimental displacement-time history at the pier top was given as input in the FE model and the resulting base shear-time histories were compared with the experimental results for validation of the 3D FE model.

Test results demonstrated that bridge pier specimens with Fe-SMA in the form of end-anchored reinforcement exhibited enhanced load carrying capacity and marginal improvement in failure displacement, whereas specimens with hoop reinforcement showed improved ductility. Combination of hoops and end-anchored Fe-SMA was successful in improving both the strength as well as ultimate lateral displacement of the control specimen.

Table of contents

List of figures

List of tables

List of symbols

a	acceleration vector
$A_{c,eff}$	effective area of concrete in tension
A_f	austenite finish temperature
A_s	austenite start temperature
A_s	total area of rebars at a section
A_{sp}	area of transverse reinforcement bar
A_{st1}	area of a single leg of stirrup
$\mathbf{C}$	assembled damping matrix
C	cover of concrete
d_b	diameter of rebar
d_c	damage variable in concrete compression
d_c	distance between the extreme tension fibre and centroid of the rebar
d_s	diameter of spiral between bar centres
d_t	damage variable in concrete tension
D	diameter of specimen
e	flow potential
E_D	energy dissipated in a single hysteresis loop
E_0	elastic modulus of concrete
E_{sec}	secant modulus of concrete
E_{S0}	maximum strain energy of equivalent elastic system
E_s^*	modified elastic modulus of rebar model
E_{sp}^*	hardening modulus of the modified rebar model
f	external force vector
f_{b0}	initial biaxial compressive strength
f_{c0}	initial uniaxial compressive strength

f_c	axial stress
f'_{co}	peak stress and corresponding strain of unconfined concrete
f'_{cc}	confined concrete peak stress
f_{cr}	tensile cracking stress of concrete
f_h	SMA recovery stress
f'_l	lateral confining pressure
$f_{l,active}$	active confining pressure
$f_{l,s}$	effective confining pressure of internal steel reinforcement
$f_{l,SMA}$	active confining pressure of Fe-SMA confined concrete
$f_{l,total}$	total confining pressure of Fe-SMA-confined RC columns
f_{res}	residual stress of Fe-SMA confined concrete
f_{ult}	ultimate stress of concrete
f_y	yield stress of streel rebar
f_y^*	effective yield stress of rebars embedded in concrete
f_{yh}	yield strength of transverse reinforcement
G^C	total fracture energy
H_C	height of original pier
H_R	height of repaired region
I_z, I_y	section modulus
k_e	confinement effectiveness coefficient
K	combined confining effect of concrete and steel stirrups
K_{avg}	average secant stiffness of the specimen
K_c	shape factor parameter
K_{co}	confinement effect of concrete
K_{st}	confinement effect of steel
K_{nn}, K_{ss}, K_{tt}	initial stiffness components in the normal and two tangential directions respectively

l	bond strength transmission length
L	length of rebar
ΔL	change in length of rebar
$\mathbf{M}$	assembled mass matrix
M_C	ultimate moment capacity of column
M_f	martensite finish temperature
M_R	ultimate moment capacity of relocated plastic hinge section
M_s	martensite start temperature
N	number of longitudinal bars
p	parameter that controls gradient of ascending slope of stress-strain curve
$P_{\max}, P_{\min}$	maximum and minimum loads at each displacement amplitude
q	parameter that controls gradient of descending slope of stress-strain curve
r	structural restoring force vector
s	centre to centre spacing or pitch of spiral or circular hoop
s'	clear vertical spacing between spiral or hoop bars
S	scaling factor
S_{rm}	average spacing of cracks
S_{st}	spacing of single leg of stirrup
t	time
Δt	change in time
t_n^0, t_s^0, t_t^0	peak value of shear stresses in the normal and two tangential directions respectively
T	temperature
u	displacement vector
$u_{\max}, u_{\min}$	displacements corresponding to maximum and minimum loads at each displacement amplitude
v	velocity vector
X	normalised axial strain
Y	normalised axial stress

μ	Poisson's ratio
σ_0	initial preload
σ_r	initial recovery stress
σ_r^{15m}	reduced recovery stress after 15 minutes
ε_c	axial strain
ε_{co}	strain corresponding to peak stress of unconfined concrete
ε'_{cc}	strain corresponding to peak stress
ε_l	lateral strain of concrete
ε_{ult}	ultimate strain of concrete
$\Delta\varepsilon_0$	strain range of cyclic loading
ε_v^0	initial volumetric strain
ξ	equivalent viscous damping ratio
δ	maximum slip of rebar
δ_n^f	effective displacement at failure
Δ_u	maximum deformation
Δ_y	deformation at yield
2θ	diffraction angle of X-ray
ρ	reinforcement ratio
ρ_{cc}	longitudinal reinforcement ratio
ρ_{eff}	effective reinforcement
ρ_s	internal transverse reinforcement ratio
μ	displacement ductility factor

Chapter 1

Introduction

1.1. General

Bridges are designated as lifeline structures of the transportation infrastructure network. The implementation of capacity design philosophy for seismic design of bridge systems ensures that plastic hinges are located in columns while safeguarding other components against damage (Paulay & Priestley, 1992; Priestley *et al.*, 1996). As a result, bridge systems dissipate the seismic energy transmitted during an earthquake predominantly through inelastic deformation of its bridge piers. For strong earthquakes, plastic hinge formation in piers can result in yielding, buckling and even rupture of longitudinal steel bars, as shown in Fig. 1.1, leading to deterioration in its flexural and shear strength. Replacement of RC bridge columns is time-consuming, laborious, and expensive. Hence, numerous studies have been undertaken by researchers to develop new techniques for retrofitting and rehabilitation of RC bridge piers.

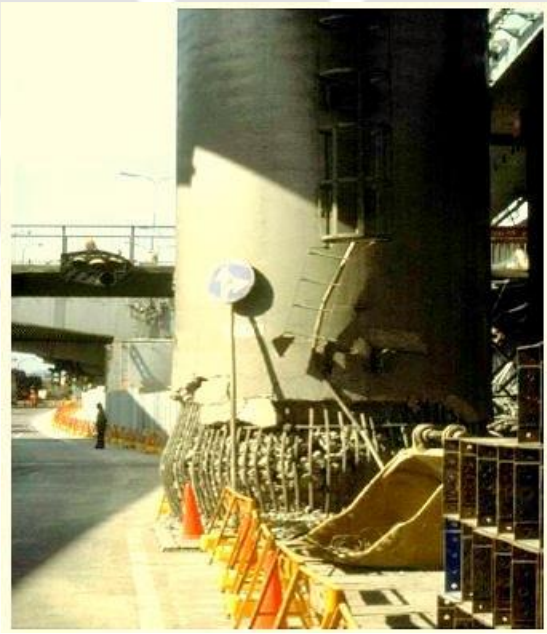

Fig. 1.1. Flexural damage of pier of Hanshin Expressway in 1995 Kobe earthquake (Priestley *et al.*, 1996)

1.2. Repair/Retrofitting techniques using confinement approach

Repair/retrofitting techniques for bridge columns aim at improving the seismic performance of a structure by increasing its strength and ductility. Most common retrofitting techniques achieve this objective by addition of lateral confinement to concrete sections. These concrete confinement techniques can be categorized into two categories: 1) Passive confinement and 2) Active confinement. These are further elaborated in the following subsections:

1.2.1. Comparison of stress-strain behaviour of passively and actively confined concrete

The fundamental difference between passive and active confinement is the instant of mobilization of lateral confining pressure. Fig. 1.2 shows cross-sections of passively and actively confined concrete cylinders. As observed from the figure, lateral confining pressure is applied to the concrete section prior to axial loading in case of active confinement. However, in passive confinement technique, concrete has to dilate for mobilization of the confining pressure. Hence, early application of confinement pressure causes a delay in the onset of damage in actively confined concrete.

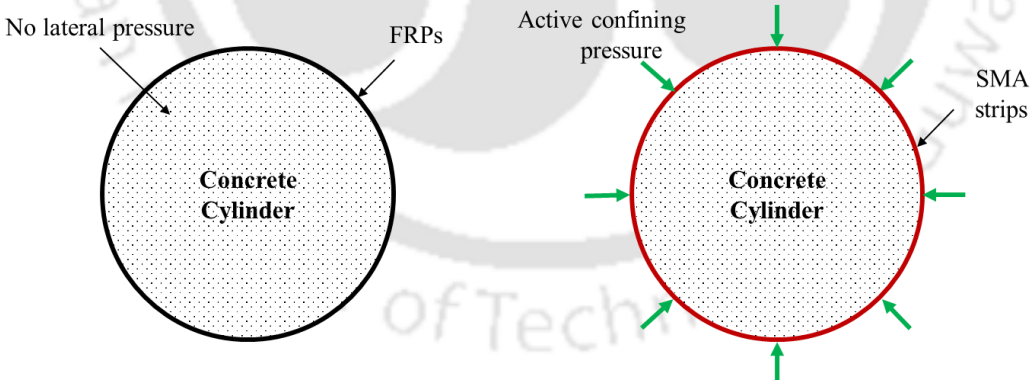

Fig. 1.2. Cross-sections of passively & actively confined concrete before loading

Fig. 1.3 illustrates the typical axial stress versus volumetric strain responses of unconfined, passively confined and actively confined concrete. In the elastic region, the unconfined concrete undergoes volumetric compaction, following which there is rapid expansion leading to failure (Shin & Andrawes, 2010). Similarly, when passively confined concrete is subjected to axial stress, its volume decreases in the elastic region. As the axial

stress increases, passive confining pressure aids in delaying the instant at which the concrete begins to expand volumetrically. However, in the active confinement case, the lateral confining pressure is mobilized on the concrete as a prestress before application of service loading. This leads to the development of an initial volumetric strain ε_v^o, resulting from compaction. Additional axial stress is required in order to counteract the effect of this strain, thus delaying the failure of the concrete as compared to passively confined concrete.

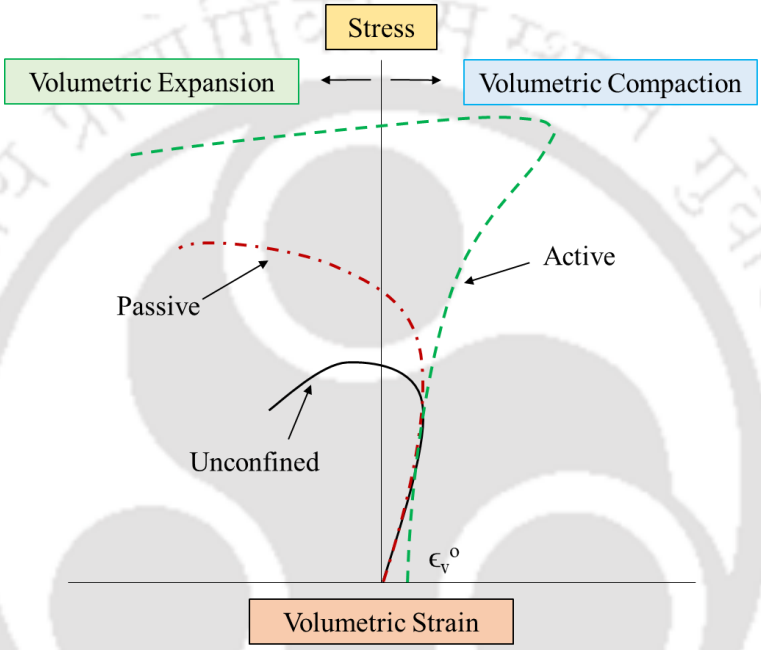

Fig. 1.3. Stress vs. volumetric strain curves of unconfined, passively and actively confined concrete (Shin & Andrawes, 2010)

1.2.2. Passive confinement techniques

Commonly employed passive confinement techniques for bridge columns include the use of concrete jackets (Bett *et al.*, 1988), steel jackets (ChaiI *et al.*, 1991), externally bonded fiber reinforced polymer (FRP) jackets (ElSouri & Harajli, 2011; He *et al.*, 2013; He *et al.*, 2015; Rutledge *et al.*, 2014; Saadatmanesh *et al.*, 1997).

1.2.2.1. RC Jackets

These usually involve enlarging the column cross-section with reinforced concrete, along part of or the entire length of the column, connecting the reinforcement in the jacket to the encased damaged column.

Advantages

1) This method is simple and uses commonly available materials as compared to steel and FRP jacketing.
2) The jacketing enhances both ductility and strength of damaged concrete members.

Disadvantages

1) It is labour intensive
2) Cost of formwork installation is high because roughening, cleaning and adequate integration of the existing concrete is required to ensure strain compatibility in the jacket and column surface to facilitate composite action.
3) It involves drilling of holes to add dowel bars or connectors at fairly close intervals, which may lead to micro-cracking and weakness in the member.

1.2.2.2. Steel Jackets

Repair of RC columns using steel jackets usually involves casting new concrete to restore the cross-section, installing the steel jacket by field welding of steel angles along the length of the jacket, and filling the gap between the jacket and column with epoxy grout.

Advantages

1) Simple and uses commonly available material.
2) It increases the flexural strength, shear strength, ductility, stiffness and serviceability of the element.

Disadvantages

1) Expensive and labour intensive.
2) There is difficulty in transportation, handling and installation of heavy plates.
3) Poor resistance to corrosion

1.2.2.3. Fibre-Reinforced Polymer (FRP) Jackets

FRP is a composite material made of a polymer matrix reinforced with fibres. Carbon, aramid and glass are the most common fibres used. These fibres are held effectively with

the help of resin (which becomes a polymer after curing; e.g. epoxy). Resins provide the mechanism for load transfer between the fibres and are responsible for enhanced strength. It also protects the fibres from environmental effects and buckling.

Advantages

1) High strength and stiffness to weight ratio which makes it one of the most suitable alternatives for seismic retrofit without increasing seismic demand.
2) Ease of production, handling, and installation without any need for heavy machinery.
3) Corrosion resistance and high durability.
4) Flexibility of application due to conformity to any geometrical shape.
5) Minimum modification to aesthetics of structure.
6) Enhancement in both strength and ductility.

Disadvantages:

1) Costly material even though overall cost is low due to small cost of transportation and installation
2) Poor fire resistance
3) Requirement of highly trained professionals for design and construction
4) Sensitivity of composites to geometric imperfections of the column, misalignment of fibres, and the geometric discontinuities within the FRP overlap leading to reduced strain capacity of FRP confinement.
5) FRP behaviour is greatly influenced by the quality of the parent concrete. As a result, if not designed and applied properly, some problems as shrinkage, creep, and debonding may adversely affect its performance.

1.2.3. Active confinement techniques

Active confinement, as compared to passive confinement, effectively slows down the lateral expansion of concrete under compression because the pressure is applied before the concrete dilates; hence increasing the ductility and strength of concrete. These attractive features encouraged many researchers to consider applying active confinement by the following techniques:

1.2.3.1. Triaxial Pressure Vessel/Triaxial Testing Machine

Most of the early studies on active confinement used triaxial testing devices to investigate the behaviour of concrete. The study by (Richart *et al.*, 1928) was one of the first studies on active confinement of concrete, which used fluids in a triaxial pressure vessel to exert a constant lateral confining pressure. After this pioneering study, several researchers conducted experiments on concrete blocks or cylinders under biaxial/triaxial stress using a triaxial testing machine. These studies demonstrated that the strength and the strain at failure of concrete are dramatically improved by increasing the confining pressure.

1.2.3.2. Prestressing Steel Reinforcement/FRP Jackets

Active confinement was applied in the field by researchers using various methodologies. Some researchers adopted lateral prestressed steel strands and special anchorage devices for confinement of RC columns (Saatcioglu & Yalcin, 2003). Others examined the feasibility of applying confining pressures with the help of prestressed FRP belts (Nesheli & Meguro, 2006). A key difference between using triaxial pressure vessel/triaxial testing machine and prestressed steel strands/FRP belts to apply active confining pressure is that the active confining pressures applied through the former remains constant throughout the test, whereas in the latter case, active confining pressure is exerted prior to loading and additional passive confining pressure keeps developing with concrete expansion during loading. Since it incorporates the advantages of both active and passive confinement techniques, it is found to effectively improve the axial and lateral capacity of RC columns.

The behaviour of passively constrained concrete columns, using concrete, steel and fibre-reinforced polymer (FRP) jackets, has been extensively studied and documented in literature. On the contrary, the amount of research on active confinement techniques is very less. Regardless of the methodology adopted, majority of the researchers used prestressed steel strands or FRP belts for application of active confinement on concrete members (Moghaddam *et al.*, 2010; Saatcioglu & Yalcin, 2003). Several studies have shown that active confinement outperforms passive confinement in terms of enhancing the strength and ultimate strain of concrete (Krstulovic-Opara & Thiedeman, 2000; Moghaddam *et al.*, 2010). This is due to the fact that prior application of confining pressure delays the initiation of damage in concrete. However, active confinement techniques pose numerous constraints

in field due to its need for specialized equipment and an excessive amount of time, money and labour, hence limiting its practical implementation. As a result, traditional passive confinement techniques have gained greater acceptance in the construction sector. To address the above-mentioned challenges, a group of smart materials known as Shape Memory Alloys (SMAs) has lately gained interest among researchers for its ability to exert active confining pressure on concrete members without mechanical prestressing.

1.2.3.3. SMA confinement

The concept of employing SMAs to provide active confinement of concrete is based on utilizing the recovery stress generated upon thermal activation of SMAs as illustrated in Fig. 1.4.

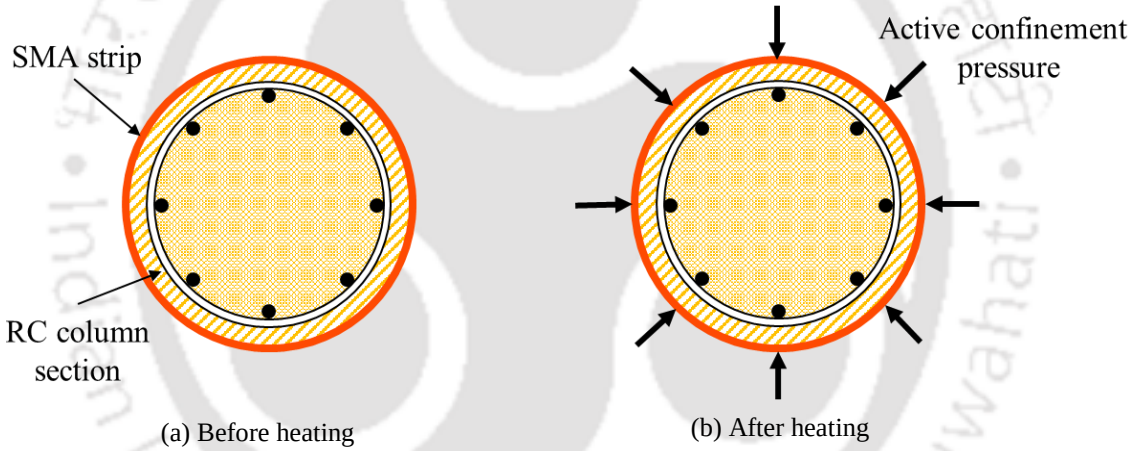

Fig. 1.4. Prestrained Fe-SMA strips used for application of active confining pressure on RC column section (a) before heating (b) after heating

SMAs can regain their original shape even after undergoing excessive deformations up to 8% strain. By virtue of its unique thermo-mechanical property, shape memory effect (SME), prestrained SMAs can regain its original (undeformed) shape when heated above its transformation temperature. If the SMA is restrained before heating, large recovery stresses are developed in it, which in turn aids in prestressing the structural component against which it is fixed. The recovery stress is largely dependent on the SMA composition, manufacturing technique, and level of prestrain prior to shape recovery. Unlike conventional prestressing techniques, this method doesn't require heavy machinery in field. Few studies have been carried out to test the effectiveness of Fe-SMA for strengthening of

RC beams (Michels *et al.*, 2018; Shahverdi, Czaderski, & Motavalli, 2016). However, use of Fe-SMA for retrofitting of bridge piers have not been explored yet.

1.3. Shape Memory Alloys

Shape memory alloys (SMAs) are smart materials that exhibit a unique property of restoring their original shape, after undergoing deformation, through transformations between their phases. There are two phases of SMAs: 1. Austenite phase, which exists at high temperatures and 2. Martensite phase, which exists at low temperatures. Austenite is composed of a face-centred cubic (fcc) structure, while martensite exists in hexagonal close-packed (hcp) structure. The transformation of SMAs from one phase to the other is dependent on four transformation temperatures, which are unique for each type of SMA. The forward transformation from austenite to martensite, also known as martensitic transformation, can be brought about by two ways: (a) changing the alloy's temperature which results in a thermally-induced martensite; (b) by subjecting it to stress which results in the formation of a stress-induced martensite. In the former instance, the forward transformation begins when the alloy in its austenite phase is cooled to M_s (martensite start temperature) and finishes at M_f (martensite finish temperature). The forward phase transformation in SMAs is a martensitic transformation. However, the reverse transformation from martensite to austenite is accomplished only by heating the alloy. It starts at A_s (austenite start temperature) and finishes at A_f (austenite finish temperature). The martensitic transformation is, in general, a diffusion-less solid state transformation in which the atoms move in an organized manner relative to their neighbours. This homogeneous shearing of the parent phase creates a new crystal structure that does not have any compositional change (no diffusion).

Fig. 1.5 shows the variation of martensite fraction of a SMA with temperature. As obseved from the figure, the forward and reverse transformations take place at different temperatures, thus exhibiting thermal hysteresis. The width of thermal hysteresis can be defined as the difference between M_s and A_s and it depends on the type of SMA under consideration.

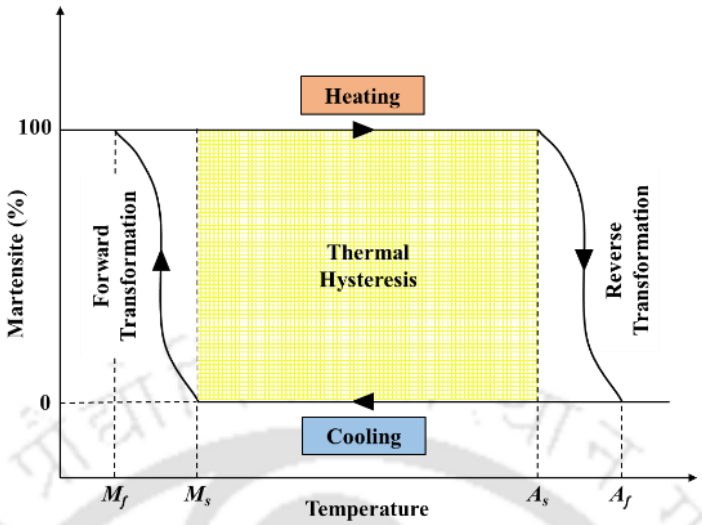

Fig. 1.5. Thermal hysteresis of typical SMAs

Shape recovery of SMAs can be attributed to two unique thermomechanical phenomena namely: Shape Memory Effect (SME) and Superelasticity (SE). Fig. 1.6 shows typical thermomechanical characteristics of SMAs. When the alloy is deformed at temperatures above A_f, stress-induced martensite is formed. However, since martensite is unstable at high temperatures, the alloy transforms back to austenite phase upon load removal with no residual strain. This is known as SE. When the SMA is loaded in its martensite phase (T< M_f), the deformation remains even after removal of the load. If the SMA is heated to a temperature above A_f, the alloy undergoes reverse transformation to austenite phase, thus recovering its original shape. This is known as SME. During the heating process, if the SMA is restrained against movement by fixing it to a parent structure, a recovery stress is generated which acts as the prestressing force on the parent structure. This prestress can be used for active confinement of RC members.

SMAs can be broadly divided into three groups based on its composition: NiTi-based, Cu-based and Fe-based. Economic considerations have played a significant role in the increased interest in Fe SMA systems as base metals, as they are significantly less expensive than NiTi-based SMAs. A cost-effective Fe-SMA with the composition Fe-17Mn-5Si-10Cr-4Ni-1(V, C) has shown excellent mechanical properties. Recovery stresses of 300–350 MPa are developed in Fe-SMA strips after heating it to 160°C. Despite the huge potential of Fe-SMA-confinement technique in the field of structural retrofitting, there are

very few experimental and numerical studies so far pertaining to the uniaxial stress-strain behaviour of Fe-SMA-confined concrete.

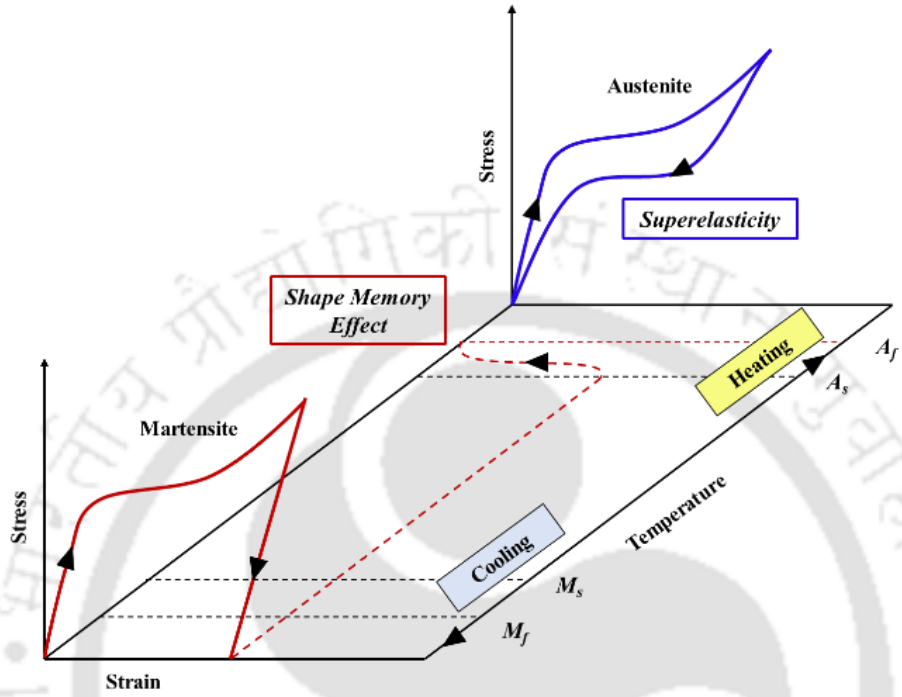

Fig. 1.6. Thermo-mechanical behaviour of typical SMAs

1.4. Hybrid Simulation

A major challenge in dealing with large structural systems is that a few elements may exhibit high nonlinearity, which may be difficult to accurately model numerically. In such cases, if the force-displacement behaviour of those elements can be recorded from a laboratory test while modelling the rest of the structural system numerically, the uncertainties in numerical modelling of the nonlinear elements can be minimized. This particular type of advanced structural simulation methodology comprising both physical and numerical model is facilitated by hybrid simulation which is why it was chosen for experimental investigation in the current study.

Conventional quasi-static tests are useful in predicting the behaviour of structural elements by imposing predefined displacement or force histories. It does not take into consideration the ductility demand of an earthquake ground motion imposes on a structural element. On the other hand, there are limitations of size and weight in shake table test due

to the table capacity. It is at times not easy to reproduce an actual situation due to excessive scaling of the structural system. Such problems can be resolved by hybrid simulation method.

Hybrid simulation technique is executed using a step-by-step numerical solution of the governing equations of motion that uses a hybrid model comprising of both physical and numerical models for evaluating the seismic response of structures. The first successful implemented of hybrid simulation was done by Takahashi *et al.* (1975) who presented an "online test" method as an alternate experimental methodology to shaking table testing. Since then, several modifications to this experimental technique and the corresponding numerical algorithms have been made in an effort to increase its effectiveness, precision, and performance.

In a bridge system, scaled model of the pier is treated as the physical component of the hybrid simulation, while the prototype bridge is simulated numerically. The pier is tested physically because it is a highly nonlinear element of the bridge system and may undergo the most extensive damage under earthquake load. The key components of hybrid simulation are shown in Fig. 1.7.

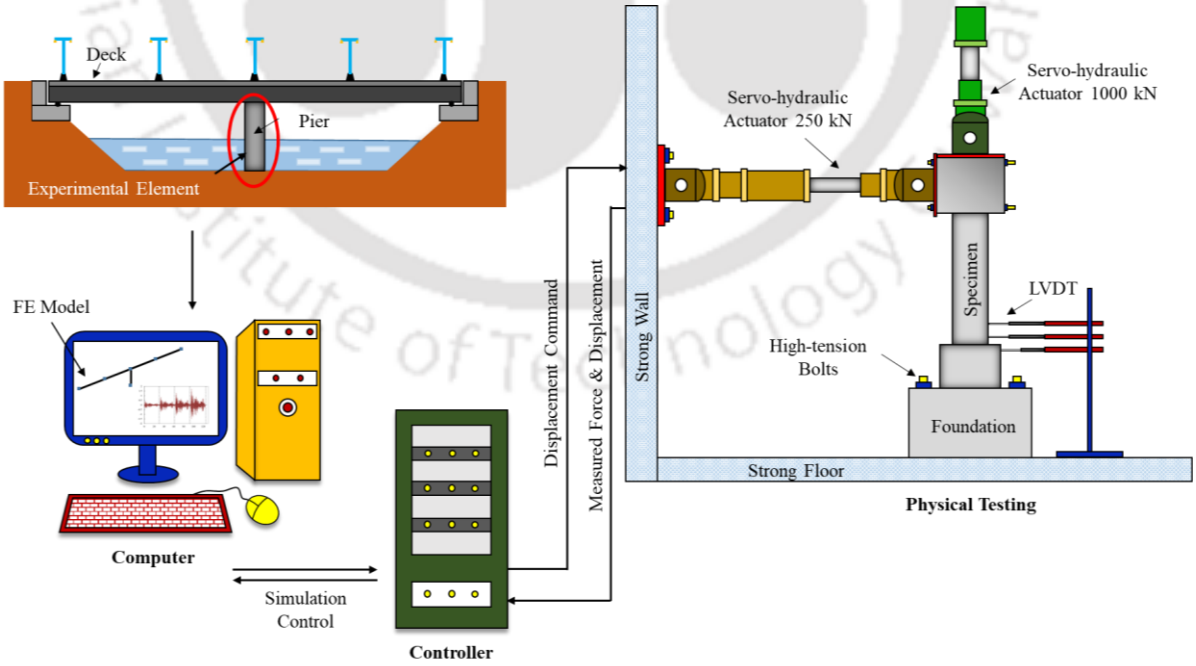

Fig. 1.7. Key components of hybrid simulation

1.5. Objectives of research

In the light of the preceding discussion, the primary objective of this research is to investigate the retrofitting of RC bridge piers using Fe-SMA strips for enhancement of its seismic performance. Scaled damaged pier models of a prototype bridge located in severest seismic zone in India is considered for the detailed study.

The proposed research work in this thesis is undertaken to achieve the following objectives:

- To evaluate behaviour of plain concrete cylinders partially confined with Fe-SMA strips under uniaxial compressive loading
- To propose an empirical stress-strain model for accurate prediction of behaviour of Fe-SMA confined plain concrete
- To develop an empirical model for prediction of uniaxial compressive behaviour of Fe-SMA confined RC specimens
- To rehabilitate severely damaged RC bridge piers using RC jacketing and assess its load-carrying capacity
- To carry out hybrid simulation of rehabilitated bridge piers retrofitted using Fe-SMA strips
- To calibrate numerical model of the bridge using the detailed experimental output from hybrid simulation
- To simulate the rehabilitated RC bridge pier using 3D finite element considering material nonlinearities, bond-slip behaviour of the longitudinal reinforcement bars as well as interaction between the jacket and core concrete
- To compare the numerical results obtained from 3D finite element analysis with experimental results for validation of the numerical model of Fe-SMA confined RC bridge piers

1.6. Scope of research

In the light of the preceding discussion, the primary objective of this research is to investigate the performance of Fe-SMA-retrofitted RC bridge pier in an earthquake scenario using hybrid simulation. It is expected that the use of Fe-SMA strips would

improve seismic performance of the control specimen. The scope of study in the present research comprises of both numerical and experimental investigation. The detailed scope of studies, to achieve mentioned objectives, is outlined as follows:

Experimental study

- To characterize the Fe-SMA strips used in this study in terms of generation of recovery stress, monotonic and cyclic stress-strain behaviour and to evaluate its microstructure and phase transformation behaviour.
- To conduct an experimental study for evaluation of the behaviour of plain concrete cylinders partially confined with Fe-SMA strips under uniaxial compressive loading. Three different grades of concrete and three different active confining pressures were adopted to study its influence on the stress-strain response of Fe-SMA-confined concrete specimens.
- To design a rehabilitation method for retrieving the original capacity of the severely damaged bridge piers using RC jacketing so as to relocate the plastic hinge away from the pier-foundation interface.
- To carry out retrofitting of the rehabilitated bridge piers using three configurations of Fe-SMA strips namely hoop, end-anchored and a combination of previous two approaches.
- To carry out hybrid simulation of bridge structure with retrofitted piers under the action of different intensity levels of earthquake excitation.
- To carry out cyclic tests of the scaled pier specimens for the evaluation of ultimate capacities.

Numerical study

- To carry out regression analyses on test data for proposing an empirical stress-strain equation of partially confined Fe-SMA concrete.
- To carry out 3D-FE analyses for understanding the total confinement effect of external Fe-SMA and internal longitudinal as well as transverse reinforcement using ABAQUS v.2021.
- To carry out regression analyses on the FE results for developing an empirical model for Fe-SMA confined RC specimen.

- To calibrate a 3D-FE model of RC jacketed pier incorporating concrete-rebar interaction and jacket-pier interface shear using ABAQUS v.2021 by comparing with experimentally observed responses
- To calibrate numerical model of the bridge using the experimental output from hybrid simulation.
- To perform 3D finite element analysis of Fe-SMA retrofitted bridge piers utilizing the previously calibrated 3D-FE model using ABAQUS and to compare the obtained results with that from experiments for validation of the numerical model.

1.7. Organisation of thesis

This dissertation mainly focuses on assessing the seismic performance of an RC bridge with pier rehabilitated using Fe-SMA strips by hybrid simulation. Following the general introduction along with the objective and scope of the study given in Chapter 1, Chapter 2 discusses the literature review of previous studies on all the important topics related to this research. These topics include various types of confinement techniques for repair/retrofitting of RC columns/piers with special focus on SMA confinement, thermo-mechanical properties and pilot experiences on the application of Fe-SMAs, experimental evaluation of seismic performance of structural components, hybrid simulation and model calibration.

Chapter 3 presents the description of materials used for rehabilitation of the damaged bridge pier specimens, details of testing procedures used to evaluate the microstructure, phase transformation and thermo-mechanical characteristics of the Fe-SMA strips used in this study.

Chapter 4 presents the details of the experimental study which was conducted to evaluate the behaviour of plain concrete cylinders partially confined with Fe-SMA strips under uniaxial compressive loading. The development of an empirical stress-strain model for partially confined Fe-SMA concrete is also provided. Further, details of the numerical study undertaken to develop an empirical model of Fe-SMA confined RC specimens is presented. To understand the total confinement effect of external Fe-SMA and internal

longitudinal as well as transverse reinforcement, 3D-FE analyses were carried out in ABAQUS.

Chapter 5 provides the details of the rehabilitation method that was designed for retrieving the original capacity of the severely damaged bridge piers. The experimental results obtained from the test program are presented. Calibration details of numerical model of RC jacketed pier is also presented.

Chapter 6 presents the details of the retrofitting schemes of the rehabilitated RC piers using Fe-SMA strips. Methodology of the experimental investigation carried out and experimental results obtained from the test program are also reported. Performance evaluation of the various retrofitting schemes is done with respect to that of the control specimen by comparing the results of hybrid simulation and cyclic tests.

Chapter 7 presents the details of the calibration of the numerical model of the bridge using the experimental output from hybrid simulation. Additionally, the bridge pier specimens with different Fe-SMA strip configurations were simulated in ABAQUS and the results obtained from FE analyses were compared with the experimental results for validation of the 3D FE model.

Chapter 8 concludes with a summary of the results and a set of conclusions that addresses the significance of the findings in this study. Finally, scope of future work is identified.

Chapter 2

Literature review

2.1. General

New developments in the domain of SMAs along with its application in structural elements, for improvement in its strength and ductility, are reported in numerous research papers, proceedings of international conferences/symposia and state-of-the-art reports presented by professional societies. This chapter is a review of some of these documents relevant to the present study. A comprehensive review of techniques for rehabilitation of damaged RC bridge columns is presented. Further, well-established procedures for conducting laboratory testing to evaluate the seismic response of structural component or system are discussed. A brief review of existing stress-strain models of confined concrete and different seismic testing methods is also reported.

2.2. Confinement techniques

Concrete confinement methods can be divided into two types: passive and active. In case of passive confinement, the confining pressure develops gradually after dilation of the concrete during loading. However, in case of active confinement, the lateral confining pressure is applied to the concrete prior to its dilation. The addition of lateral confinement to concrete has been proven to significantly increase the strength and ductility of the concrete. Some of the past research works that have proven the efficacy of repairing damaged concrete using external confinement is discussed here.

2.2.1. Passive confinement techniques

Few studies which discusses the commonly implemented passive confining techniques are presented in the following sub-sections:

1.2.1.1. RC Jacketing

RC jackets have been used to enhance the performance of vulnerable columns for several decades. In traditional RC jacketing, the original column cross-section is enlarged over a

portion or its entire length using reinforced concrete. This new section is integrated to the original section using dowel bars. This retrofitting technique improves the strength and ductility of the columns. Adequate roughening, cleaning and dowelling of the existing damaged concrete section has to be carried out to ensure composite deformation between the jacket and the column surface. It increases the size of the structural element, thereby changing its dynamic properties, which is likely to impose a higher seismic demand on the structure.

Bett *et al.* (1988) investigated the repair of 2/3rd-scaled square RC column using RC jacketing. The column was subjected to a constant axial load and lateral cyclic loading. Test results demonstrated that the column repaired with concrete jacketing displayed higher stiffness and strength as compared to the original column.

Vandoros and Dritsos (2008) used RC jackets with welded stirrup ends, which resulted in the enhancement of the strength and ductility of the RC columns as well as prevention of bucking of longitudinal reinforcement. It was however reported that the jacket got separated from the original column due to a lack of surface treatment at the interface.

Cho *et al.* (2012) used high-performance fibre-reinforced cementitious composite (HPFRCC) in RC jacket for strengthening the plastic hinge region of the column. Results indicated that strengthening with HPFRCC mortar not only reduces bending and shear induced cracks, but also improves the overall force–displacement, energy dissipation and stiffness.

More recently, Rodrigues *et al.* (2018) repaired severely damaged RC columns by replacing the damaged concrete in the plastic hinge region with high-strength micro-concrete and welding of ruptured longitudinal bars. The subsequent testing of the repaired columns under bi-directional lateral loading with constant axial compression showed that the repair technique fully restored the strength and ductility of the columns. However, the stiffness was still observed to be lower than that of the original specimen.

1.2.1.2. Steel Jacketing

Repair of RC columns using steel jackets usually involves restoring the original cross-section, installing the steel jacket by field welding of parts along the length of the jacket, and filling the gap between the jacket and column with cement based grout. The jacket can be considered equivalent to continuous hoop reinforcement, providing passive confinement.

ChaiI *et al.* (1991) proposed a retrofit technique, where the plastic hinge region of a $2/5^{th}$-scaled circular sub-standard RC bridge column was encased in a bonded steel jacket. The column was previously tested under cyclic lateral loading, which resulted in bond failure of the spliced reinforcement in the plastic hinge region. Tests of the retrofitted column showed enhancement in its the strength and ductility as compared to the original column.

Fukuyama *et al.* (2000) carried out strengthening of a 1/2-scaled square RC column by steel jacketing. The column was tested under lateral cyclic loading with a constant axial load of 30%, which resulted in buckling of longitudinal bars and crushing of core concrete. The strengthening process involved addition of new longitudinal reinforcing bars, enlarging the column cross-section by placing steel plates along its perimeter and grouting using flowable concrete in the gap between the steel plates and crushed concrete, which was left untreated. Test results exhibited higher shear strength, stiffness and ductility of the repaired column as compared to the original column.

ElSouri and Harajli (2011) carried out a study on strengthening of RC columns with lap splices in using steel ties and/or FRP wraps for confinement. Three full scale rectangular columns with different longitudinal reinforcement ratios were subjected to cyclic lateral load without axial load. The thickness of confining material was evaluated by the method proposed by Darwin *et al.* (2005). The results indicated that the rehabilitated columns exhibited enhanced lateral load capacity and energy dissipation capacity as compared to the original columns.

1.2.1.3. Fibre-reinforced polymer (FRP) jackets

In recent decades, use of FRP in repairing and strengthening RC members have become increasingly popular. It is a composite material made of a polymer matrix reinforced with fibres. Carbon, aramid and glass are the most common fibres used. These fibres are connected effectively with the help of resin (which becomes a polymer after curing; for example, epoxy). Resins provide the mechanism for load transfer between the fibres and are responsible for composite strength. The resin matrix also protects the fibres from environmental effects and buckling. Fibres may be oriented in different directions to achieve different objectives.

Priestly *et al.* (1993) conducted a study on the repair of a 2/5th-scaled sub-standard circular RC bridge column without lap splices using a glass FRP (GFRP) jacket and epoxy injection. The column was earlier tested to failure under reversed cyclic loading and constant axial load index, defined as the compressive axial force due to gravity loads divided by the product of the cross-section area of the column and the specified concrete compressive strength, of 18%. The damage included open diagonal cracks and spalled concrete. The repair procedure included removing the loose concrete, patching with cement mortar, injecting epoxy in all cracks, and applying a full height GFRP jacket. The test results indicated that the initial stiffness of the column was fully restored by the repair, and the repaired column reached higher displacement ductility than that of the original column.

Vosooghi *et al.* (2008) reported repairing of two high shear, standard RC bridge columns using CFRP jackets. The 1/3rd-scale circular RC bridge columns with spiral reinforcement were tested to near failure on a shake table. The damage included spalling of cover concrete, buckling of longitudinal bars, yielding of spiral reinforcement and damage of core concrete. For both the columns, the damaged concrete was replaced by a rapid setting non-shrink mortar, and the cracks were sealed using epoxy. Jacketing of the repaired piers were carried out with different layers of CFRP, and different mortars with various methods of application. Test results indicated that the repair design method fully restored the lateral load and drift capacity of the columns, although the service stiffness, which is the ratio between elastic stiffness of the repaired column and the original column,

was not fully restored. It was also observed that the yielded spiral reinforcement also contributed for restoration of the shear capacity of the piers.

Yang and Wang (2018) evaluated the seismic performance of shear controlled columns strengthened with CFRP straps and full CFRP sheet. It was observed that irrespective of the pre-damage condition of the columns, the CFRP wrapping enhanced the shear capacity and ductility of the deficient columns. However, the improvement in behaviour reduced with the increasing axial load ratio. CFRP retrofitting also led to gradual post-peak strength degradation and a reduction in the pinching effect in hysteretic behaviour. The authors concluded that at the same volumetric ratio, retrofitting with CFRP straps is a superior strategy compared to the wrapping of columns with full CFRP sheets.

2.2.2. Active confinement

As compared to passive confinement, active confinement effectively reduces the lateral expansion of concrete under compression, because the confining pressure is applied before dilation of concrete, thus enhancing the strength and ductility of concrete. Because of its numerous potential benefits, active confinement has inspired a significant number of researchers to examine its use in the field.

2.2.2.1. Prestressing Steel Reinforcement/FRP Jackets

Saatcioglu and Yalcin (2003) carried out a series of tests on full-scale concrete columns that were retrofitted by hoops made of prestressing strands. For circular columns, twisted ring anchors were used for placing the hoop strands on the concrete surface, while steel spreader frames and raiser discs were used for square columns for uniform distribution of the confining pressure. It was concluded that the retrofitting scheme was effective in improving the shear capacity and ductility of concrete columns.

Miyagi *et al.* (2004) proposed an emergency retrofit strategy for earthquake induced damaged columns using steel plates and prestressing bars. Four blocks were positioned on the four corners of the square column. Prestressing bars of 5.4 mm diameter were used for connecting the corner blocks and prestress was induced with a torque wrench. Four steel plates were attached to the faces of the concrete column beneath the corner blocks. The prestressing force in the bars helped in keeping the steel plates in place without the need

for additional welding or connections. It was experimentally verified that the emergency retrofit on damaged column was effective not only for the improvement of ductility, but also for improvement of axial and lateral load carrying capacities. Additionally, the prestressing force in the bars contributed in closure of the cracks in the damaged columns.

Nesheli and Meguro (2006) proposed the use pretentioned carbon and aramid FRP belts for retrofitting of damaged concrete columns following an earthquake. Carbon FRP belts were wrapped directly around concrete columns with rounded corners, while aramid FRP belts were wrapped around concrete columns by the use of steel angles. At the instant of pretensioning, the initial cracks of the damaged column were closed. Both the retrofitted columns were tested under cyclic lateral loading in addition to a constant axial compressive force. Results demonstrated that the lateral load carrying capacity of the original columns dropped suddenly, indicating a brittle shear failure. However, the flexural and shear strength of the retrofitted columns was restored.

Choi *et al.* (2010) proposed a new scheme of steel-jacketing for RC columns. Turnbuckles and steel bands were used instead of clamps to introduce the external pressure on the steel jackets for its tight attachment on concrete surfaces after which its ends were welded. Additional lateral strips were welded for protecting the welding line of the steel jacket from fracture. Hence, it does not require grout which is commonly used in traditional jacketing methods. Results indicated that the retrofitting scheme was able to enhance the displacement ductility and energy dissipation of RC columns with lap splice. However, there was no increase in the effective stiffness of the columns because of lack of composite behaviour between the jackets and the concrete.

More recently, Rousakis and Tourtouras (2014) conducted experiments to investigate the effectiveness of high extension capacity polypropylene fibre ropes as a method for externally confining square plain or reinforced concrete columns. The results showed that this technique performed well in improving the stress–strain behaviour with a 40% increase in the ultimate strength. However, after unwrapping of the ropes following completion of experiments, extensive cracking of the concrete core was observed along with the buckling of multiple steel bars.

2.2.2.2. SMA Confinement

SMAs can be added in the form of external or embedded spirals and jackets to increase the confinement of RC columns. In contrast to the passive confinement offered by traditional steel spirals, active confinement using SMAs results in enhanced ductility and energy dissipation capacity.

Krstulovic-Opara and Thiedeman (2000) investigated the use of self-stressing composites made with shape memory fibres, which get activated on heating, to apply active confining pressure to concrete structure. Results of compressive tests carried out on a series of concrete cylinders demonstrated that concrete specimens confined by self-stressing composites improved its strength and ductility by limiting the development of micro-cracks.

Andrawes and Shin (2008) originally introduced the concept of utilizing SMA rings to provide active confinement prior to application of loads, based on analytical simulation. Results demonstrated significant enhancement in the seismic performances of reinforced concrete bridge columns.

Shin and Andrawes (2010) conducted a material-level study on the use of SMA spirals for active confinement of concrete. NiTiNb SMA wires with 6.4% prestrain were wrapped around the concrete cylinder and heated after restraining, leading to the induction of recovery stress. Uniaxial compressive tests were carried out on the SMA confined concrete cylinders and the results were compared with the stress-strain behaviour of concrete cylinders confined by GFRP wraps and SMA-GFRP hybrid confinement. Results demonstrated that the new confinement technique significantly improved concrete strength and ductility. It was also reported that the behaviour of SMA confined concrete was quite different from purely active or purely passive confinement. It worked as a combination of active and passive confinement.

Shin and Andrawes (2011b) investigated the lateral force-displacement behaviour of large-scale RC columns retrofitted using different schemes in its plastic hinge zone as shown in Fig.2.1. The three different schemes were: NiTiNb SMA spirals, GFRP jackets and a combination of SMA-GFRP jacket. The columns were tested under quasi-static

lateral cyclic loading. Test results showed a significant increase in the displacement ductility, energy dissipation, and equivalent viscous damping ratio of the SMA-retrofitted columns as compared to the GFRP-retrofitted columns. Besides, the SMA retrofitted columns experienced much less damage as compared to the control and GFRP retrofitted columns as it delayed the concrete dilation during loading.

Shin and Andrawes (2011a) investigated the feasibility of repairing RC columns with NiTiNb SMA spiral wires. Two 1/3rd-scaled severely damaged RC columns were selected for this purpose. 6% prestrained SMA spirals were first wrapped around the plastic hinge zone of the column and then thermally activated at 100°C. The experimental results revealed that the use of SMA spirals in the repair enhanced the ductility of the column while restoring the lateral strength. In addition to this, there was a 150% increase in the initial stiffness of the columns after these were repaired. It was concluded that only a small quantity of SMA was necessary to considerably enhance the seismic behaviour of the columns.

Choi *et al.* (2012) utilized Ni-Ti SMA and Ni-Ti-Nb SMA wires for retrofitting of RC columns with lap splices. The study first assessed the mechanical behaviour of the two alloys and thereafter investigated the seismic performance of SMA wire jackets on the lap-spliced columns. Thermal activation of the SMA wires were carried out at 200°C. Results indicated superior performance of the retrofitted columns. The SMA jackets were found to increase the ductile behaviour of the lap-spliced columns without significant strength degradation. The drift capacity of the strengthened columns was found to be up to thrice that of the un-strengthened columns. Overall, Ni-Ti SMA and Ni-Ti-Nb SMA wires had comparable effects on increasing the ductility of the columns. However, use of Ni-Ti-Nb SMAs was recommended as it work better in civil engineering structures, since it has a wider thermal hysteresis.

Chen and Andrawes (2017) carried out an experimental investigation with a total of 20 concrete cylinders with varying unconfined strengths, and lateral active confinement levels using NiTiNb SMA wires by varying its spacing. Cyclic compression tests were performed on the cylinders and extensive instrumentation was employed to monitor the axial strain and lateral strain progressions. The experimental results accurately captured the

material behaviour of NiTiNb SMA confined concrete. Empirical equations to predict key characteristics of the stress strain curve of SMA confined concrete, such as peak stress, residual stress, and ultimate strain were also proposed.

Jung *et al.* (2018) assessed the seismic performance of RC columns retrofitted with Ni-Ti-Nb SMA spirals subjected to bidirectional loads. The 6.5% prestrained SMA spirals were activated and a recovery stress of 447 MPa was achieved. It was observed that the retrofitted columns demonstrated better ductility and much lesser residual deformations as compared to the un-retrofitted columns. Crushing of concrete was not observed till a drift ratio of 10.5%. The damaged un-retrofitted column was later repaired with SMA spirals and retested. The repair strategy was successful in restoring the seismic capacity of the damaged column while preventing further damage.

More recently, Zerbe *et al.* (2022) experimentally evaluated the behaviour of fully wrapped Fe-SMA-confined concrete columns subjected to uniaxial compressive loads and an analytical model was proposed to simulate the same. Two internal reinforcement configurations were adopted, columns with transverse reinforcement only and columns with both longitudinal and transverse reinforcement, along with plain concrete columns. Two configurations of SMA wrapping were chosen, one with a single layer and the other with two layers. The results of Fe-SMA confined columns without internal reinforcement were reported to be random. Further, full activation of Fe-SMA strips was not achieved in columns with two layers when a heating cable was used. Thus, the inner layer of Fe-SMA did not attain the target phase transformation temperature which led to an approximation of the initial confining stress adopted in this group of specimens.

2.3. Development of cost-effective SMAs

Shape memory alloys (SMAs) are smart materials that exhibit a unique property of restoring its original shape through transformations between its two crystallographic phases. The first discovery of a material with shape memory was reported by Chang and Read (1951), after a reversible phase transformation in an Au-Cd alloy was observed. Following the discovery of Ni-Ti SMA in 1963, numerous commercial products were developed in 1970s. The main drawback of these alloys for its application in civil

engineering structures is its high cost, due to which its applications are limited to aerospace engineering, military and bioengineering field. However, following the discovery of SME in an Fe-Mn-Si alloy by Sato *et al.* (1982), new iron-based SMAs with improved SME properties have been developed. This improvement is expected to reduce the cost of these materials and make them more competitive for civil engineering applications.

2.3.1. Crystallography and thermal hysteresis of SMA

At the atomic level, there are two phases of SMAs: 1. Austenite phase, which exists at high temperatures and 2. Martensite phase, which exists at low temperatures. The martensite phase has two variants: twinned martensite and detwinned martensite as shown in Fig. 2.1. The transformation of SMAs from one phase to the other is dependent on four transformation temperatures, which are unique for each type of SMA. The forward transformation from austenite to martensite, also known as martensitic transformation, can be brought about by two ways: (a) changing the alloy's temperature which results in a thermally-induced martensite; (b) by subjecting it to stress which results in the formation of a stress-induced martensite.

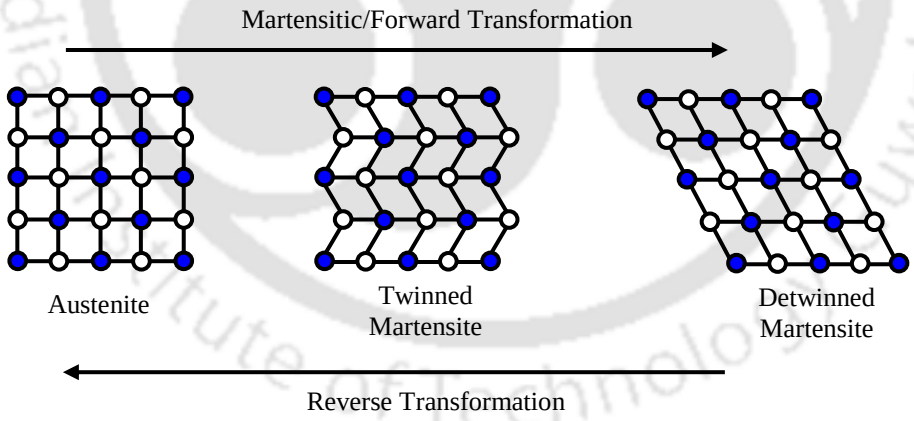

Fig. 2.1. Matrix of the atoms at different phases

In the former instance, the forward transformation begins when the alloy in its austenite phase is cooled to M_s (martensite start temperature) and finishes at M_f (martensite finish temperature). However, the reverse transformation from martensite to austenite is accomplished only by heating the alloy. It starts at A_s (austenite start temperature) and finishes at A_f (austenite finish temperature). The forward and reverse transformations take

place at different temperatures, thus exhibiting thermal hysteresis (Fig. 1.5). The width of thermal hysteresis can be defined as the difference between M_s and A_s and it depends on the type of SMA under consideration. This property must be carefully considered when selecting SMA materials for specific technical applications; for example, a small hysteresis is required for fast actuation applications (such as MEMSs and robotics), while a larger hysteresis is required to retain the predefined shape over a wide temperature range (such as in deployable structures). Large thermal hysteresis is a critical feature for civil engineering applications to maintain phase stability at ambient temperatures.

2.3.2. Thermomechanical phenomena of SMA

Shape recovery of SMAs can be attributed to two unique thermomechanical phenomena namely: SME and SE. When the alloy is mechanically deformed at temperatures above A_f, stress-induced martensite is formed. However, since martensite is unstable at high temperatures, the alloy transforms back to austenite phase upon load removal with no residual strain. This is known as SE. The deformation in SMA in its martensite phase ($T< M_f$), under applied loads remains same even after removal of the load. If the SMA is heated to a temperature above A_f, the alloy undergoes reverse transformation to austenite phase, thus recovering its original shape. This is known as SME. During the heating process, if the SMA is restrained against movement by fixing it to a parent structure, a recovery stress is generated which acts as the prestressing force on the parent structure. This prestress can be used for active confinement of RC members.

2.3.3. SMA groups

SMAs can be broadly divided into three groups based on its composition, namely: NiTi-based alloys, Cu-based alloys and Fe-based alloys. The characteristics and properties of these three categories of SMAs will be reviewed in the following sections.

2.3.3.1. Ni-Ti-based alloys

The Ni-Ti alloy has been the most extensively investigated of all SMA compositions and has become the most important SMA for commercial purposes. The Ni-Ti material is capable of completely recovering strains up to 8 %. These are available in different forms, like wires, bars, tubes, and plates. Hence, Ni-Ti alloys are used as reinforcement in

structural members, in dynamic response control systems, and in structural isolators. However, the manufacturing costs of Ni-Ti-based alloys are very high.

Addition of a third metal X to Ni-Ti to form ternary Ni-Ti-X alloys, can be beneficial for potential use in particular applications. For e.g. addition of Cu to form NiTiCu alloy results in a narrower thermal hysteresis which makes it a better choice for actuator applications (Bassani & Besseghini, 2001). Similarly, addition of Nb to form NiTiNb alloy results in a wider thermal hysteresis making it apt for coupling applications and prestressing applications in civil structures, where the recovery stress should not change much with variations in ambient temperatures (Melton *et al.*, 1986).

2.3.3.2. Copper-based alloys

Cu-based SMAs, while lacking the superior shape memory properties of Ni-Ti alloys, are used for their modest shape memory properties, lower manufacturing costs, and ease of fabrication. Cost-effectiveness is attributed to the ease with which they are manufactured utilising the same methods as that of any standard Cu-based alloys (Dasgupta, 2014). Additionally, because of its low reactivity, it does not require the same stringent furnace conditions as those required for Ni-Ti manufacturing.

Two commonly used Cu-based alloys are: Cu-Zn-Al having the good ductility and Cu-Al-Ni, which is less sensitive to aging effect. However, majority of the Cu-based alloys have limited applicability due to brittleness induced by coarse grain size, restrictions in thermal stability, and mechanical strength, which are directly related to the microstructure of Cu-based SMAs. These alloys also undergo aging, which causes martensitic stabilization leading to a shift in its transformation temperatures. This makes it difficult to obtain stable actuation response required across well-defined temperature ranges for sensing applications.

2.3.3.3. Iron-based alloys

Fe-based SMA have found successful applications in the field of civil engineering because of its remarkable properties such as high stiffness, high strength, and cheap production cost. There are two different groups of Fe-based SMAs (Maruyama & Kubo, 2011). The first category includes alloys such as Fe-Pt, Fe-Pd, and Fe-Ni-Co, which undergo thermoelastic

martensitic transformations similar to Ni-Ti with a narrow thermal hysteresis. Despite significant research, no pseudoelasticity has been reported for Fe-Pt or Fe-Pd alloys at room temperature.

Tanaka *et al.* (2010) developed a Fe-29Ni-18Co-5Al-8Ta- 0.01B (mass %) SMA with a recovery strain of more than 13% at ambient temperature and a high tensile strength of 1200 MPa. Another remarkable Fe-based SMA with composition Fe-36Mn-8Al-8.6Ni was developed by Omori *et al.* (2011), which exhibited good superelastic properties at room temperature with a recovery strain of more than 5%, and a fracture tensile strain of more than 8%. However, further development is required before these two alloys can be produced in large quantities for application in the construction industry. Additionally, the composition of the alloys necessitates that they be cast under special conditions, which would raise the cost of the material.

The second group comprises of alloys such as Fe–Ni–C and Fe–Mn–Si, which have a larger thermal hysteresis yet exhibit SME. A low cost Fe-SMA with composition Fe–17Mn–5Si–10Cr–4Ni–1(V, C) (mass %), exhibiting high tensile strength and good recovery stress properties was developed by Dong *et al.* (2009) at the Swiss Federal Laboratories for Materials Science and Technology (Empa). Recovery stresses of 300–350 MPa were reported after heating the Fe-SMA to 160 °C, thus making it appropriate for applications in concrete structural members. Additionally, as compared to Ni-Ti SMA, manufacturing process is simpler and less expensive.

2.4. Fe-Mn-Si SMAs as elements for structural pre-stressing applications

The thermo-mechanical characteristics of Fe-SMAs used for pre-stressing applications in structural systems are presented in the following subsections:

2.4.1. Phase transformation behaviour and recovery stress generation of Fe–17Mn–5Si–10Cr–4Ni–1(V, C)

In general, the shape memory effect (SME) in Fe-Mn-Si alloys (Fe-SMAs) is a result of a stress-induced phase transformation from a parent γ-austenite (fcc - face-centered cubic) phase to an ε-martensite (hcp - hexagonal close-packed) phase at ambient temperatures and its reverse phase transformation (ε-martensite to γ-austenite) upon heating at high temperatures (Sato *et al.*, 1982). Differential scanning calorimetry (DSC) testing was carried out by Lee *et al.* (2013) to measure the phase transformation temperatures of the Fe-SMA strips. The results are enlisted in Table 2.1.

Table 2.1. Phase transformation temperatures of Fe-SMA (Lee *et al.*, 2013)

M_f	M_s	A_s	A_f
64°C	*60°C*	*103°C*	*163°C*

The schematic phase diagrams of a typical Fe–Mn–Si alloy is shown in Fig. 2.2.

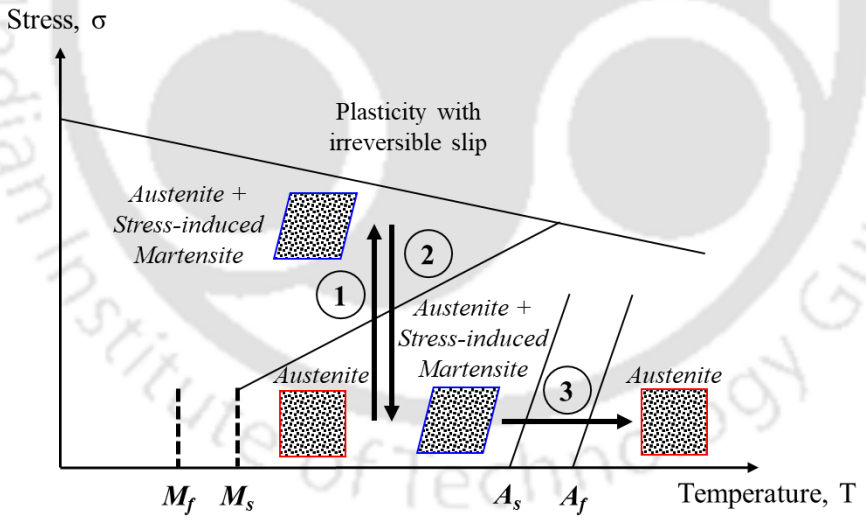

Fig. 2.2. Schematic phase diagrams of Fe–Mn–Si alloy (Cladera *et al.*, 2014)

The initial phase of Fe-SMA can be considered as pure γ-austenite since it undergoes annealing during manufacturing process, which is comparable to the reverse transformation (Fig. 2.2). During the process of prestraining, with increase in the strain, part of the parent γ-austenite gradually transforms into ε-martensite (Path 1; Fig. 2.2). However, complete austenite–martensite transformation is not attained for this stress-

induced path. For an Fe–Mn–Si–Cr alloy, the percentage of stress-induced ε-martensite has been reported to be 30% or less (Otsuka, 1991). During unloading, the stress deviates from the linear elastic behaviour [Path 2; Fig. 2.3(a)] and this deviation is called pseudoelastic strain. Reverse transformation (ε-martensite to γ-austenite) does not take place in the region, where both phases are equally stable (Path 2; Fig. 2.2). Due to the large thermal hysteresis of these Fe-Mn-Si alloys, this region spans over a wide temperature range. The reverse transformation, which is crucial for the generation of recovery stresses, gets activated upon heating the alloy above A_s. A portion of the strain is recovered when the temperature exceeds A_f (not all because of trapped martensite plates retained by various defects) (Path 3; Fig. 2.2) (Cladera *et al.*, 2014).

Fig. 2.3 shows the development of the recovery stress in the phase diagrams during heating and cooling.

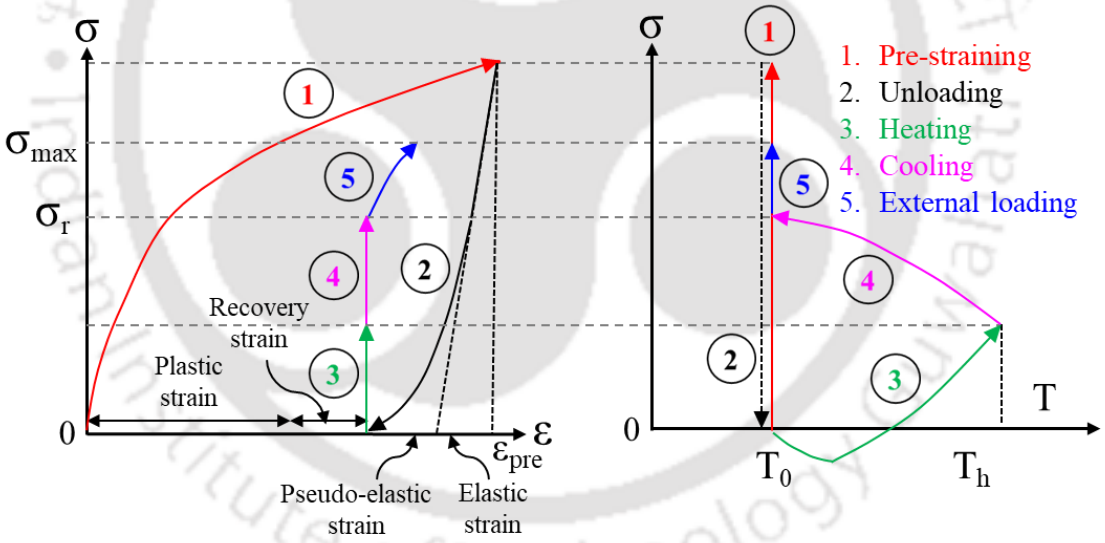

Fig. 2.3. (a) Stress-strain behaviour and (b) stress-temperature behaviours of Fe–17Mn–5Si–10Cr–4Ni–1(V, C) (Ghafoori *et al.*, 2017)

During heating, initially the stress in the Fe-SMA element drops slightly as observed from Path 3 in Fig. 2.3(b). This indicates the dominance of thermal expansion effect (TEE) over shape memory effect (SME). However, once the stress-temperature path crosses the A_s boundary, reverse transformation of martensite to austenite starts. As a result, the SME dominates and suppresses the TEE, leading to the development of tensile stress in

the SMA. However, when the SMA is cooled to room temperature [Path 4 in Fig. 2.3(b)], the effect of the thermal expansion is recovered by the thermal contraction of the member. This results in enhanced tensile stress development in the SMA. Additionally, when the recovery stress surpasses the threshold stress for the martensitic forward transition during the cooling phase, a non-linear behaviour is observed in the stress-temperature diagram. The final recovery stress tends to be lower due to the formation of new martensite and a prominent relaxation at higher stress levels.

2.4.3. Material behaviour of Fe–17Mn–5Si–10Cr–4Ni–1(V, C)

To have a better understanding about the newly developed Fe-SMA, various aspects such as optimum prestrain, recovery stress, tensile behaviour, high-cycle fatigue (HCF), creep and relaxation, corrosion, thermal expansion and high temperature behaviour are discussed in this section.

2.4.3.1. Pre-strain and recovery stress

Shahverdi *et al.* (2018) carried out material characterization of Fe-SMA strips for its application in RC members as externally fixed reinforcements. It was observed that the recovery stress obtained after thermal activation was dependant on the amount of prestraining in the Fe-SMA strip before its activation. Prestrain amount was varied from 0.5-4% and corresponding recovery stresses were recorded after heating the strip to various temperatures in range of 120°C - 195°C to determine the optimum level of Prestrain as well as the optimum temperature for activation. It was found that the increasing trend of recovery stress with increase in the amount of prestrain reached a plateau at 2% prestrain. It was hence concluded that a prestraining level of 2.0% was sufficient for obtaining the maximum possible recovery stress after heating the Fe-SMA strips to 160°C. Additionally, it was found that activation of the strips at higher temperatures leads to the development of higher recovery stresses and this increasing trend reached a maximum at an activation temperature of about 400°C. The recovery stress at this temperature was about 450 MPa.

2.4.3.2. Tensile behaviour

Based on the tensile tests conducted on Fe-SMA strips of thicknesses 0.5 mm and 1.5 mm by Shahverdi *et al.* (2018), it was found that the ultimate tensile strength of the Fe-SMA strips was about 1000 MPa and corresponding strain at failure was more than 40%. The elastic modulus, determined by the best-fit trend line fitted within stress range of 20–200 MPa, was found to be approximately 160 GPa. An offset yield point was established at 0.2% plastic strain since the yield point could not be clearly defined from the stress-strain curve. The corresponding values were around 500 MPa.

2.4.3.3. *High cycle fatigue*

Ghafoori *et al.* (2017) carried out a series of HCF tests using activated Fe-SMA dog-bone samples under strain control and a constant frequency of 10 Hz. Prior to the fatigue testing, the samples were prestrained and then activated using an inductive heating method up to 160°C. Three strain ranges $\Delta\varepsilon_0$, 0.07%, 0.035% and 0.105% were chosen for the HCF tests. Strain ranges of 0.035% and 0.07% were representative of the ranges of service loads encountered in steel and concrete members, whereas the strain range of 0.105%, although larger than the expected service loads range, provided a useful parametric evaluation in the investigation. After 2×10^6 cycles, it was observed that the recovery stress decreased by nearly 20%. Material fracture was however not observed.

Hosseini *et al.* (2018) conducted another study where a series of HCF tests was performed on activated Fe-SMAs under similar strain rates as those of Ghafoori *et al.* (2017). The primary purpose of the study was to investigate the influence of multiple activations on the recovery stress behaviour of Fe-SMA strips under HCF loading. It was found that a second was successful in retrieving a significant part of the relaxed recovery stress. In real-world situations, if the prestress force in Fe-SMA reinforcements gets reduced while in service, due to HCF loading, accidental overloading, or relaxation, the capacity of Fe-SMA to undergo repeated activations is crucial since a reactivation can restore the prestress level.

2.4.3.4. Creep and relaxation

Leinenbach *et al.* (2016) investigated the creep and relaxation behaviour of Fe-SMAs in step-wise stress and strain controlled tensile tests in the temperature range -45°C<T<50°C. Creep of the material was measured at constant stress over a period of time, whereas relaxation loss was measured at constant strain. It was found that a major part of creep and stress relaxation occurred in the first few minutes after activation. A 10% decrease in the initial recovery stress was observed. Moreover, creep and relaxation became more evident upon decreasing the testing temperature. The reason for this increase in creep and relaxation was attributed to stress-induced martensitic transformation during mechanical loading. Martensite phase is thermodynamically more stable at low temperatures, hence leading to an increased creep rate.

2.4.3.5. Corrosion

Lee *et al.* (2016) performed electrochemical characterization tests which demonstrated that the corrosion resistance of Fe-SMA was superior as compared to that of conventional structural steel grade S500. This property was attributed to its chemical composition (it contains about 10% chromium). Additionally, water-induced stress corrosion tests were performed on Fe-SMA strips of 1.5 mm thickness according to the guidelines of the former International Association for Prestressed Concrete (FIP). The results showed that standing duration of the alloy in thiocyanate (NH_4SNC) solution prior to rupture at 50°C were satisfactory, thus indicating superior corrosion resistance of Fe-SMA.

2.4.3.6. Thermal expansion

For both internal and external reinforcing/strengthening applications, thermal compatibility of a reinforcement material with the base material (typically steel or concrete) is critical. This is because a significant mismatch of the thermal expansion between the reinforcement and the base material can induce undesirable stresses in the strengthened member thus rendering the strengthening ineffective. It can also lead to significant thermal-induced fatigue problems as the temperature changes throughout the day. Tests conducted by Hosseini *et al.* (2018) revealed that the behaviour of Fe-SMA in thermal expansion is very similar to that of other austenite steels. The co-efficient of thermal expansion (CTE) of Fe-

SMA was found to be around 14.9 × 10^{-6} K^{-1}, which is very similar to steel (CTE 11-13 × 10^{-6} K^{-1}) and concrete (CTE 12 × 10^{-6} K^{-1}).

2.4.3.7. High temperature and fire behaviour

Ghafoori *et al.* (2019) carried out a study on the behaviour of Fe-SMA strengthened structural members under fire exposure. A series of transient total deformation tests were conducted on prestressed Fe-SMA strips of thicknesses 0.5 mm and 1.5 mm to determine the temperature of creep onset and failure. Three different service load levels 0, 80 and 240 MPa and three heating rates of 5, 15 and 50 °C/min were considered. It was observed that the temperature for onset of creep was greater than 500°C for all the cases considered. Additionally, increase in service load levels led to the decrease in creep-onset and failure temperature. A simple engineering model was developed to predict the temperature at which complete loss of prestress would occurr in a shotcrete-embedded prestressed Fe-SMA member. A complete loss of prestress in the Fe-SMA bars was observed at 320°C after an exposure time of 20 minutes with a 20 mm thick cover concrete. This can be delayed by addition of a thicker shotcrete cover or by application of thermal insulation material.

2.4.4. Applications of Fe-Mn-Si alloys:

The first practical application of Fe-SMA in prestressing dates back to 2001, when a bridge girder in Michigan, USA, experienced fatigue-induced cracking. After a laboratory investigation on the possibility of providing external reinforcement to address shear cracks, the bridge girder was strengthened using external post tensioning with Fe-Mn-Si-Cr SMA rebars by Soroushian *et al.* (2001). After heating the SMA rebars to 300°C, recovery stresses of 255 MPa were induced in it. Field measurements revealed that post-tensioning with SMAs allowed the closure of the shear cracks to a large extent, which helped in restoring the load-carrying capacity of the bridge.

Watanabe *et al.* (2002) used 1 mm diameter prestressed wires of Fe-27Mn-6Si-5Cr-0.05C alloy for reinforcement of an 80 mm long mortar prism specimen. These wires were prestrained to 1%, 2% and 3% at room temperature before being embedded into a plaster mix. The specimens were then heated to a temperature of 250°C in order to induce a

compressive stress in the matrix. Pull-out tests and three-point bending tests were carried out to characterize the mechanical properties of the specimen. Results demonstrated that the increasing the prestrain level in the SMA wires increased the bending strength of the specimen and improved the fracture toughness of the plaster.

Sawaguchi *et al.* (2006) reinforced small size mortar prisms with square Fe-28Mn-6Si-5Cr-1(NbC) bars. The motivation was from the work of Kajiwara *et al.* (2001), who reported that the fine dispersion of NbC carbides could improve the shape memory properties of Fe-Mn-Si based SMAs. Three types of test specimens were used: specimen with implanted SMA square bars (2x2 mm square section), specimen with steel bars of the same size and specimen without any reinforcement. These mortar specimens were initially cured for two days, after which moulds were removed and these specimens were subjected to high-temperature curing in an autoclave in stages. The first stage of curing was done at 87°C for 24 hours for increasing the compressive strength of the mortar mix. The second stage of curing was performed at 177°C for 6 hours and 247°C for 30 min for generation of prestress in the SMA bars. Upon comparing the results of the different specimens, it was found that Fe-SMAs were more effective at increasing the bending stress as compared to the steel-reinforced or unreinforced samples of the mortar prisms. Furthermore, it was stated that additional strengthening could be accomplished by lowering the reverse phase transformation temperature of the SMA, to avoid considerable thermal damage to the mortar matrix during activation.

Czaderski *et al.* (2014) performed a feasibility study of utilizing ribbed Fe-SMA strips of composition Fe–17Mn–5Si–10Cr–4Ni–1(V, C) as near-surface mounted reinforcements. The recovery stress after heating to 160°C and cooling down to room temperature, measured in a tensile testing machine with climate chamber was in the range of 250-300 MPa. The bond behaviour of the ribbed Fe-SMA strips were tested in lap-shear after gluing them in grooves using a cement-based mortar. Results indicated that the strips were adequate for reinforcing applications. Additionally, two concrete bars of lengths 70 cm were centrally reinforced with Fe-SMA strips having cross-sections of 1.50 × 15.97 mm and 1.63 × 14.23 mm. A high current density of 15 A/mm^2 was used for thermal activation so as to minimize the heating time and heat flow into the concrete. The activation

was controlled by a LabView programme. Compressive stresses in the range of 3 MPa observed after activation of the Fe-SMA strips demonstrated its feasibility for applications as reinforcement and prestressing elements.

Shahverdi, Czaderski, and Motavalli (2016) investigated the use of near-surface mounted (NSM) Fe-SMA strips for the flexural strengthening of RC beams. The benefits of NSM strengthening include its capacity to considerably reduce the likelihood of damage resulting from acts of vandalism, corrosion, and fire. Experimental investigation was conducted in four stages: prestraining of the Fe-SMA strips up to 1.5 percent, grouting of the Fe-SMA into grooves, thermal activation of the strips by resistive heating, followed by cooling to room temperature and lastly, the strengthened beams were loaded to failure in a four-point bending test. Recovering stresses of 200 MPa were generated, and the SMA strips inserted in the grooves were bonded well with cement mortar. Results indicated that the cracking load of specimens with activated SMA strips was found to be 80% more than that of specimens with non-activated SMA strips. Additionally, a considerable decrease in the mid-span vertical deflection was also observed for beams with activated SMA strips.

In another study, Shahverdi, Czaderski, Annen, *et al.* (2016) carried out a pilot study for strengthening of RC beams by embedding ribbed Fe-SMA bars in a shotcrete layer and compared it to a similar ribbed steel bar strengthened beam. The Fe-SMA bars were prestrained upto 4% and activated by resistive heating with a current density of 7.6 A/mm^2. The uplift of the beams was measured after thermal activation and was found to be around 1.18 mm. Recovery stresses of around 300 MPa were generated in the ribbed bars upon activation at 160°C. The strengthened bars were then subjected to four-point bending test. Results demonstrated that the beam with ribbed SMA rebars exhibited roughly twice the cracking load resistance as compared to the beam with ribbed steel rebars. The loads resisted by the beams reinforced with two- and four-ribbed SMA rebars were 163% and 265% greater, respectively, as compared to the un-strengthened beam at a mid-span deflection of 0.2 percent. According to the study, the formation of shrinkage cracks in the shotcrete layer is a possible concern linked with this strengthening technique that requires further examination.

Michels *et al.* (2018) carried out flexural strengthening of RC beams by mechanically anchoring Fe-SMA strips to the beam soffit. This was accomplished by using 2% prestrained Fe-SMA strips that were activated by resistive heating at 160°C. The experimental findings revealed that the flexural strength of beams enhanced by the Fe-SMA strip was much higher than that of the control beams and beams strengthened by CFRP strips. Furthermore, the Fe-SMA strip-strengthened beams exhibited increased stiffness, which reduced the vertical deflection in the four-point bending tests.

Rojob and El-Hacha (2017) and El-Hacha and Rojob (2018) carried out similar studies for flexural strengthening of RC beams using Fe-SMA as NSM reinforcement. While the former employed Fe-SMA rebars grooved into the tension side of the beams, the latter used Fe-SMA strips. The rebars and the strips were prestrained to 6% and 3% respectively. Rojob and El-Hacha (2017) reported an increase of more than 30% in the yield, ultimate load-bearing capacity as well as ductility of the RC beams. The study concluded that SMA strengthening is preferable to FRP strengthening since it increases both strength and ductility, as compared to FRP strengthening, which frequently results in a strength-ductility trade-off. El-Hacha and Rojob (2018) reported an increase of 30%-60% in the flexural strength of Fe-SMA strengthened beams as compared to the control specimen. Upon comparison of the NSM Fe-SMA-strengthened beams to NSM CFRP-strengthened beams, it was found that the latter exhibited slightly higher strength but the ductility was significantly lower as compared to the former.

Rojob and El-Hacha (2018) experimentally investigated the behaviour of RC beams strengthened with Fe-SMA bars as NSM reinforcement under fatigue loading. Results indicated that the beam strengthened with NSM Fe-SMA performed much better than the control beam at relatively low levels of fatigue loading. Stabilization of the stiffness degradation of the strengthened beam occurred after two million loading cycles. However, with increase in loading limits, the bond between the Fe-SMA bar and the grouting material continued to deteriorate causing high stress levels at the anchors. This finally lead to the rupture of the Fe-SMA bar after 5.5 million load cycles.

Montoya-Coronado *et al.* (2019) investigated the use of Fe-SMA strips for shear strengthening of deficient RC beams. Prestrained Fe-SMA strips were externally wrapped

around the RC beams and thermally activated at 160°C. The shear strength of the reinforced beams increased significantly (up to more than 80%), resulting in flexural failure as opposed to the shear failure of the un-strengthened beams. The strengthened specimens also exhibited higher ductility, demonstrating the efficacy of the suggested strengthening method.

Similarly, Cladera *et al.* (2020) explored the strengthening RC T-beams by the use of externally anchored U-shaped Fe-SMA strips. The prestrained Fe-SMA strips were thermally activated at 160°C. The experimental results showed that the shear capacity of the strengthened beams increased by 30% as compared to the control beam. The strengthening of the beams using Fe-SMA strips resulted in a delay in the appearance of cracks, as well as a reduction in the crack width. However, the ductility of the specimens was significantly lower than what was expected.

More recently, Czaderski *et al.* (2021) utilized Fe-SMA in a new form of U-shaped (stirrups) ribbed bars with a nominal diameter of 12 mm for shear strengthening of reinforced concrete (RC) structures, in combination with sprayed mortar. These U-shaped stirrups were first installed in holes that had been drilled inside the flange, after which a mortar layer was sprayed on top of the stirrups to embed them. In comparison to non-activated stirrups, activated SMA stirrups reduced beam deflection, the number and width of cracks, and stresses in the internal steel at the serviceability limit state. Furthermore, the shear capacity of the beams was significantly increased. For SMA stirrup reinforcement ratios of 0.31 percent and 0.47 percent, the load-carrying capacity of the reinforced beams increased by 71% and 86% respectively. It was found that the beams with activated Fe-SMA stirrups developed shear cracks at higher applied loads than those with a similar amount of non-activated Fe-SMA stirrups. The study further stated that the proposed strengthening technique was well-suited for onsite applications due to its ease of application.

2.5. Stress-strain models of confined concrete

Despite the amount of experimental studies being conducted in the field of SMA confinement, there hasn't been many numerical studies in this area. SMA confinement is a combination of active confinement applied prior to loading and passive confinement that

develops when concrete dilates during loading. A review of some of the previous confined concrete models are presented in this section.

Richart *et al.* (1928) developed one of the first models for concrete confinement. The following equations were proposed to predict the confined concrete peak stress f'_{cc}, and its corresponding strain ε_{cc} as:

$$f'_{cc} = f'_{co}\left(1+4.1\frac{f'_l}{f'_{co}}\right) \tag{2.1}$$

$$\varepsilon_{cc} = \varepsilon_{co}\left(1+20.5\frac{f'_l}{f'_{co}}\right) \tag{2.2}$$

where, f'_{co} and ε_{co} are peak stress and corresponding strain of the unconfined concrete respectively and f'_l is the lateral confining pressure.

Popovics (1973) proposed the following model to predict the complete stress-strain behaviour of normal weight concrete:

$$f = f_o\frac{\varepsilon}{\varepsilon_o}\frac{n}{n-1+(\varepsilon/\varepsilon_o)^n} \tag{2.3}$$

where,

f and ε are the stress and strain at any point of the curve respectively;

f_o and ε_o are the peak stress and corresponding strain respectively;

$E_o = (f_o/\varepsilon_o)n/(n-1)$ and $E_{\text{sec}} = (f_o/\varepsilon_o)$;

$n = 0.4\times10^{-3}f_o + 1.0$, for normal weight concrete.

Mander *et al.* (1988) proposed a model to predict the stress-strain relationship of concrete confined by transverse reinforcement. The effect of different types of confinement namely spiral or circular hoops; or rectangular hoops with or without supplementary cross ties was considered by defining an effective lateral confining stress, that was dependent on the configuration of the transverse and longitudinal reinforcement. The stress-strain model

was based on the equation proposed by Popovics (1973). For a slow strain rate and monotonic loading, the axial compressive stress in concrete f_c', was given as:

$$\frac{f_c}{f_{cc}'} = \frac{\varepsilon_c / \varepsilon_{cc} \times n}{n - 1 + (\varepsilon_c / \varepsilon_{cc})^n} \tag{2.4}$$

where, $n = \frac{E_o}{(E_o - f_{cc}' / \varepsilon_{cc})}$; $\varepsilon_{cc} = \varepsilon_{co}\left[1 + 5\left(\frac{f_{cc}'}{f_{co}'} - 1\right)\right]$; f_{co}' and ε_{co} are the unconfined concrete compressive strength and its corresponding axial strain; f_{cc}' and ε_{cc} are the confined concrete peak stress and its corresponding axial strain; E_c is the elastic modulus of concrete.

A five parameter multiaxial failure criterion was used to calculate the confined concrete strength f_{cc}', assuming that lateral confining pressures from spirals/hoops in the two principal directions were equivalent, as:

$$f_{cc}' = f_{co}'\left(-1.254 + 2.254\sqrt{1 + \frac{7.94 f_l'}{f_{co}'}} - 2\frac{f_l'}{f_{co}'}\right) \tag{2.5}$$

where, f_l' is the effective confining pressure. For a circular cross-section, it is calculated as:

$$f_l' = k_e \frac{2 f_{yh} A_{sp}}{s d_s} \tag{2.6}$$

where, f_{yh} = yield strength of the transverse reinforcement; A_{sp} = area of transverse reinforcement bar; s = centre to centre spacing or pitch of spiral or circular hoop; d_s = diameter of spiral between bar centres and k_e is the confinement effectiveness coefficient, which is the area of the confined core divided by the total area of concrete core and is given by:

$$k_e = \frac{\left(1 - \frac{s'}{2d_s}\right)^2}{1 - \rho_{cc}} \text{ for circular hoops} \tag{2.7}$$

$$k_e = \frac{1-\frac{s'}{2d_s}}{1-\rho_{cc}} \text{ for circular spirals} \tag{2.8}$$

where, s' = clear vertical spacing between spiral or hoop bars; and ρ_{cc} = ratio of area of longitudinal reinforcement to area of core of section.

Tsai (1988) recommended a generalized form of the Popovics (1973)'s equation, which can control both the initial slope and the descending branch of the stress-strain curve as:

$$Y = \frac{mX}{1+\left(m-\frac{n}{n-1}\right)X+\frac{X^n}{n-1}} \tag{2.9}$$

where, Y is the normalized axial stress; X is the normalized axial strain; parameters m and n controls the steepness rates of the ascending and descending branches of the stress-strain curve respectively. When $m = n/(n-1)$, the Tsai (1988)'s equation is reduced to Popovics (1973)'s equation; $m = E_o / E_{\text{sec}}$, in which E_o is the elastic modulus of concrete and E_{sec} is defined as per Popovics (1973)'s equation.

Teng *et al.* (2007) derived an equation based on careful interpretation of experimental results to determine the relation between axial strain and lateral strain of concrete under lateral confinement, which is applicable to unconfined, actively confined as well as passively confined FRP concrete as:

$$\frac{\varepsilon_c}{\varepsilon_{co}} \Big/ \left(1+8\frac{\sigma_l}{f'_{co}}\right) = 0.85\left\{\left[1+0.75\left(\frac{-\varepsilon_l}{\varepsilon_{co}}\right)\right]^{0.7} - \exp\left[-7\left(\frac{-\varepsilon_l}{\varepsilon_{co}}\right)\right]\right\} \tag{2.10}$$

where, σ_l is a constant value for active confinement but for FRP-confined concrete, it is the current confining pressure which increases with the hoop strain; ε_l is the lateral strain; f'_{co} and ε_{co} are the peak stress and corresponding strain of unconfined concrete.

Ilki *et al.* (2008) proposed a design-oriented model for FRP confined reinforced concrete in circular columns. The compressive strength f'_{cc} and the corresponding axial

strain ε_{cc} are composed of individual contributions from the FRP jacket and the transverse steel reinforcement (TSR) respectively:

$$\left[\frac{f'_{cc}-f'_{co}}{f'_{co}}\right]_{TOTAL}=\left[\frac{f'_{cc}}{f'_{co}}-1\right]_{FRP}+\left[\frac{f'_{cc}}{f'_{co}}-1\right]_{TSR} \tag{2.11}$$

$$\left[\frac{\varepsilon'_{cc}-\varepsilon_{co}}{\varepsilon_{co}}\right]_{TOTAL}=\left[\frac{\varepsilon'_{cc}}{\varepsilon_{co}}-1\right]_{FRP}+\left[\frac{\varepsilon'_{cc}}{\varepsilon_{co}}-1\right]_{TSR} \tag{2.12}$$

The enhancements in peak stress and corresponding strain due to the FRP jacket and the transverse reinforcement were calculated using different expressions.

Chen and Andrawes (2017) developed an empirical stress-strain model for NiTiNb-SMA-confined concrete based on an experimental investigation carried out on concrete cylinders confined with NiTiNb-SMA wires, having different concrete strengths, confining pressures, and loading protocols. The following equations were proposed:

$$f'_{cc}=f'_{co}\left(1+6.41\frac{f_{l,active}}{f'_{co}}\right) \tag{2.13}$$

$$\varepsilon'_{cc}=\varepsilon_{co}\left(1+19.1\frac{f_{l,active}}{f'_{co}}\right) \tag{2.14}$$

$$f_{res}=9.22\,f_{l,active}+9.73 \tag{2.15}$$

$$f_{ult}=10.43\,f_{l,active}+6.25 \tag{2.16}$$

$$\varepsilon_{ult}=0.176\left(\frac{f_{res}}{f'_{cc}}\right)^{4.229}+0.057 \tag{2.17}$$

where, f'_{cc}, ε'_{cc}, f_{res}, f_{ult} and ε_{ult} are the peak stress, strain corresponding to peak stress, residual stress, ultimate stress and ultimate strain respectively. A two-stage empirical equation was developed to predict the stress-strain relationship of NiTiNb-SMA-confined concrete. The first stage was based on Tsai's (1988) equation and the second stage was defined such that the relationship between the axial strain and the axial stress was linear until failure once the axial stress reached residual stress, f_{res}.

Zerbe *et al.* (2022) proposed an analytical model for predicting the axial compressive behaviour of fully wrapped Fe-SMA confined columns. The model considered simultaneous confinement mechanism of external and internal transverse reinforcement. The following expressions were proposed:

$$f_{cc}^{*} = f_{co}' + \kappa_{sma} f_{co}'^{0.91} \left(\frac{f_{lsma}}{f_{co}'} \right)^{a} + \kappa_{s} f_{co}'^{0.91} \left(\frac{f_{ls}}{f_{co}'} \right)^{a} \tag{2.18}$$

$$\varepsilon_{cc}^{*} = \varepsilon_{co} + \gamma_{sma} \left(\frac{f_{lsma}}{f_{co}'} \right)^{1.15} + \gamma_{s} \left(\frac{f_{ls}}{f_{co}'} \right)^{1.15} \tag{2.19}$$

$$f_{c,res} = 1.6 f_{cc}^{*} \left(\frac{(f_{lsma} + f_{ls})^{0.24}}{f_{co}'^{0.32}} \right) \leq f_{cc}^{*} - 0.15 f_{co}' \tag{2.20}$$

$$\varepsilon_{c,i} = 2.8 \varepsilon_{cc}^{*} \left(\frac{f_{c,res}}{f_{cc}^{*}} \right) f_{co}'^{-0.12} + 10 \varepsilon_{cc}^{*} \left(1 - \frac{f_{c,res}}{f_{cc}^{*}} \right) f_{co}'^{-0.47} \tag{2.21}$$

$$\varepsilon_{cf} = \varepsilon_{co} + 0.04 \varepsilon_{l}^{0.7} \left[1 + \alpha_{sma} \left(\frac{f_{lsma,rup}}{f_{co}'} \right)^{0.8} + \alpha_{s} \left(\frac{f_{ly}}{f_{co}'} \right)^{0.8} \right] \tag{2.22}$$

where, f_{cc}^{*}, ε_{cc}^{*} , $f_{c,res}$, $\varepsilon_{c,i}$ and ε_{cf} are the peak stress, strain corresponding to peak stress, residual stress, strain at inflection point and ultimate strain respectively; κ_{sma}, γ_{sma} and α_{sma} are coefficients to represent the effectiveness of SMA confinement; κ_{s} , γ_{s} and α_{s} are coefficients to represent the effectiveness of steel confinement. Calibration of these confinement effectiveness coefficients, were determined using a multiple linear regression analysis of experimental data collected for circular RC columns with FRP confinement. The expressions for stress-strain curve adopted were based on the unified stress-strain model for FRP and actively confined normal-strength and high-strength concrete proposed by Lim and Ozbakkaloglu (2015).

2.6. Repair of RC Bridge Columns with Fractured Longitudinal Bars

Fracture of longitudinal bar at high drift levels is a common occurrence in RC columns that are dominant in flexure. In such RC columns, the objective of restoring its strength is

comparatively simpler as compared to restoring its ductility. There have been fewer studies on the repair of RC columns with fractured longitudinal bars as compared to those without. Investigated methods include the use of couplers to join the fractured bars together, anchoring new longitudinal bars and enlarging the cross-sections, and providing external confinement to the restored concrete section.

Cheng *et al.* (2003) proposed a method for repairing RC columns with fractured longitudinal bars by the use of dog-bone shaped steel bars and a FRP jacket. Two-full size hollow circular columns were tested to failure in lateral cyclic loading, which led to the fracture of outer layer of longitudinal bars, buckling of inner layer bars, and crushing of core concrete in one of the columns. Another column exhibited a flexural-shear failure mode with fractured outer layer bars and diagonal shear cracks at the mid-height of the column. These outer layer fractured and buckled longitudinal bars were replaced by dog-bone shaped bars and FRP wrap was used for enhancement of the deformation capacity of columns. The repair technique was successful in changing the mode of failure from flexural-shear to flexure-dominant failure mode. However, the strength of the repaired columns was lower than that of the original columns as the buckled inner layer longitudinal reinforcing bars were left as it was. Although there was improvement in the displacement capacity of the repaired columns, its ductility was lower than that of the original columns.

He *et al.* (2013) proposed a rapid repair method for a 1/2-scale square RC bridge column with buckled and fractured longitudinal bars using externally bonded CFRP without treating the damaged reinforcement. The column was subjected to cyclic loading and a constant axial load of 7%, which resulted in the buckling and fracturing of rebars in the plastic hinge region at the base of the column, and crushed core concrete. The process of repairing involved removal of loose concrete, application of quick-setting non-shrink mortar, and fixation of unidirectional CFRP sheets in both the longitudinal and transverse directions of the column. A novel anchorage system was developed to anchor the longitudinal CFRP to the column footing. Results indicated that the repair technique was unsuccessful in restoring the strength of the columns owing to the limitations in anchoring the longitudinal CFRP and developing the design force required at the critical section.

Rutledge *et al.* (2014) proposed the repair of a severely damaged column with fractured longitudinal rebars by plastic hinge relocation technique using carbon fiber anchors along with externally bonded CFRP anchored to the footing. The columns were tested under lateral cyclic loading and an axial load of 6% which resulted in damage in the form of buckled and fractured bars along with crushed concrete. Test results demonstrated that the repaired column exhibited increased strength and displacement capacity as compared to the original column, and the initial stiffness was also restored. However, this repair technique was not recommended for columns with multiple fractured bars as it was not possible to install enough anchors to guarantee failure at the relocated hinge.

Parks *et al.* (2016) developed a repair technique for severely damaged precast reinforced concrete (RC) bridge columns with grouted splice sleeve (GSS) connections that utilized a carbon fiber-reinforced polymer (CFRP) shell and epoxy anchored headed bars to relocate the column plastic hinge. Four original specimens were built using an accelerated bridge construction (ABC) technique with two different GSS systems and were tested to failure using cyclic quasi-static loads. One GSS system was used to connect an RC bridge pier cap to a column and the second GSS system was used to connect an RC footing to a column. Failure of the four original specimens occurred at drift ratios between 5.6 and 8.0% with longitudinal bar fracture or pullout from the GSS connections. The repair method successfully relocated the plastic hinge to the original column section on the top end of the CFRP shell and was capable of restoring its original load and displacement capacity.

More recently, Krish *et al.* (2021) investigated the repair of six extensively damaged columns by plastic hinge relocation technique. The repair strategy comprised of a grouted annular ring made of conventional materials i.e. steel rebars, steel sleeves and concrete. A corrugated steel sleeve was also installed between the original column and the repair bars and backfilled with a flowable grout mix. The repaired columns were tested under lateral cyclic loading. Results demonstrated that the repaired columns developed and sustained higher levels of force for a longer duration throughout the test. Furthermore, the repair technique was successful in restoring the displacement capacity of the highly damaged columns.

2.7. Experimental evaluation of seismic performance of structural components

Traditionally, seismic assessment of structural systems has been performed using either experimental or numerical approaches. It's challenging to numerically predict the dynamic responses of structures to catastrophic occurrences like earthquakes with absolute precision, especially at extreme deformations, because the structures undergo severe material nonlinearity. Hence, experiments are vital for understanding the seismic performance of structures during earthquake events. There are three well-established structural laboratory testing methods: quasi-static testing, shake table testing and hybrid simulation.

In the quasi-static testing procedure, a predefined load or displacement history is applied on the test specimen by actuators to evaluate the initiation and progression of nonlinearity. This has served as the basis for design recommendations in codal provisions. Although performing such tests are generally simple and economical, however, it is difficult in drawing conclusions about the inertial and damping effects of the test specimen under seismic excitation. Shake table testing makes use of a rigid table on which the structure being tested is fixed and is dynamically excited. Conceptually, it can provide a realistic simulation of the response due to real-earthquakes, but has significant drawbacks. Large-scale testing necessitates the use of expensive, high-capacity actuation devices, resulting in the widespread usage of highly simplified small-scale models. Preventative steps also need to be implemented so that expensive testing equipment is shielded from the impact of specimens during collapse. Furthermore, interactions between the table and the mounted specimen, particularly when the latter responds nonlinearly, might make it challenging to carry out the testing accurately. Hence, the hybrid simulation technique evolved to eliminate the shortcomings of both quasi-static testing and shake table testing.

2.7.1. Hybrid simulation and its applications

Hybrid simulation is the most advanced seismic testing in the recent times. In this testing approach, simulation of structural responses under seismic loading is based on a step-by-step numerical integration of governing equations of motion that takes into account both

the numerical and physical components of a structural system. In contrast to purely numerical simulation, the hybrid simulation technique combines physical testing of the most vulnerable element of a structure with numerical simulation of the remaining structure, which is expected to remain elastic during seismic excitation. It gives a detailed representation of the damage sustained by large structures like buildings and bridges during seismic events without needing to physical test of the entire structure.

There are two basic variants of hybrid simulation i.e. pseudo-dynamic (PsD) hybrid simulation and real-time (RT) hybrid simulation. In the PsD test, the mass and the viscous damping of the entire structure are treated numerically because the experimental resisting force does not include any inertial or viscous damping force contribution due to slow execution of the test. In contrast, RT tests are executed more rapidly leading to the generation of inertial and viscous damping forces in the physically tested portion of the structure.

Hakuno *et al.* (1969) first proposed the concept of the PsD test by testing a single-degree-of-freedom system using an analogue computer in combination with an electromagnetic actuator to solve the equation of motion of the system. A digital computer was recommended for improved accuracy of solution of the system's equation of motion.

The PsD test method was successfully implemented by Takahashi *et al.* (1975). This technique was found to be important for creation of more accurate analytical models for capturing the degradation of stiffness and strength under seismic loads. In order to analyse the nonlinear response of a structure during an earthquake, the PsD approach used a physical test specimen in place of a numerical model to model the stiffness nonlinearity. The stiffness of the test specimen was provided as input into the computer model from the physical experiment of the structure. The predicted deformations were calculated by a piecewise linear method and sent back to the actuator. This allowed the actuator to determine the target displacement to be applied to the test specimen for the next time step. This procedure was repeated until the end of the test.

Yamazaki *et al.* (1989) carried out comparative study on the pseudo-dynamic and shake table testing techniques and indicated issues regarding loading-rate effects and experimental errors. Takanashi and Nakashima (1987) and Mahin *et al.* (1989) presented

descriptions of the early development of pseudo-dynamic testing in Japan and U.S., respectively. They also pointed out the necessity for improved control of hydraulic actuators. Takanashi and Nakashima (1987) and Mahin *et al.* (1989) provided summaries of the early development of the PsD testing in Japan and U.S., respectively. Necessity for improved control of hydraulic actuators was also pointed out to reduce the inevitable experimental errors. Thewalt and Mahin (1987) developed the first implicit unconditionally stable integration method for hybrid simulations that was based on the alpha method by Hilber *et al.* (1977) and utilized analog feedback signals of the measured resisting forces instead of numerical equilibrium iterations.

Nakashima *et al.* (1988) proposed a specialized operator-splitting (OS) method based on implicit-explicit predictor-corrector schemes of Hughes *et al.* (1979). Emphasis on the need for an efficient and unconditionally stable numerical algorithm was made for integration of the equations of motion of large multi-degrees-of-freedom hybrid models. Nakashima (1990) subsequently investigated the stability and accuracy properties of the OS method. Schellenberg and Mahin (2006) demonstrated the inclusion of geometric nonlinearities in the numerical module of hybrid simulation on a simple one-story one-bay portal frame with two ductile columns.

Schellenberg (2008) introduced a framework for communication, simulation and control by virtue of which numerical partitioning tests could be done easily. In this concept of hybrid simulation, portions of large structures were tested in different laboratories while the remainder of the structure was simulated numerically. In this study, the Open-source Framework for Experimental Setup and Control (*OpenFresco*) was used in combination with the object-oriented finite element software framework *OpenSees* (Open System for Earthquake Engineering Simulation) and the graphical user interface OpenSees Navigator. This enabled an unlimited number of users to connect multiple laboratories, throughout the world, to define specialized experimental setups. Advanced integration operators could be implemented and high performance control methodologies could be utilized, in a highly modular and scalable fashion.

Significant research has been conducted on the PsD testing technique, which has contributed to its development and improvement over the years. Early studies on PsD

testing focused more on the accuracy, stability, and dependability of the testing technique as compared to its actual application as a method for testing of structures under dynamic loads. Some of the important studies on dynamic testing of bridges using PsD tests are discussed in this section.

Obata and Goto (2002) performed one of the earliest multi-directional pseudo dynamic test to investigate the effect of multi-directional loading on the ultimate behaviour of a steel bridge pier.

Pinto *et al.* (2004) performed PsD tests of a six pier model of an existing bridge using the sub structuring technique. Two 1/2.5th-scaled piers were constructed and tested in the laboratory while the abutments, four remaining piers and bridge deck were modelled numerically. The scaled weight of the deck was applied as vertical loading. Asynchronous input excitations were generated for the specific site of the bridge as per the method developed by Pegon and Pinto (2000). Three intensity ground motions with increasing intensities were applied to test the seismic vulnerability of the bridge which was constructed prior to the development of modern seismic codes. Experimental results confirmed the poor performance of the bridge supported by inconsistent damage distribution, limited deformation capacity and undesirable failure location.

Carrion *et al.* (2009) presented an approach for real-time hybrid simulation (RTHS) in which compensation for actuator dynamics was implemented using a model-based feed forward compensator. Experimental results showed good agreement with the predicted numerical responses, demonstrating the effectiveness of hybrid simulation method for performance assessment of structural control system.

Dang and Aoki (2013) performed three-dimensional PsD tests of a quarter-scale stiffened square cross-section steel bridge pier subjected to vertical and bi-directional horizontal loading. Comparison of the results showed that the maximum load in bi-directional loading was the same as the average of unidirectional loading in the NS and EW directions. Additionally, a modified seismic design was proposed considering these bidirectional loading effects.

Terzic and Stojadinovic (2014) adopted hybrid simulation technique for investigating the response of a typical California highway overpass bridge under the earthquake excitation followed by truck load. The prototype bridge used in this study was a five-span single-column-bent reinforced concrete overpass. The bridge was modelled in OpenSees and was integrated with the physical column specimen using the OpenFresco framework. Two hybrid simulation tests were performed on the same bridge for two scaled recorded ground motions. Ground motion intensities was chosen corresponding to two different damage states in the physical model of the column: moderate and high corresponding to different levels of maximum column displacement ductility demands. After the earthquake, the ability of the bridge to further carry traffic loads was evaluated by applying heavy vehicle loads on the hybrid model at locations which were critical for the pier being physically tested in the laboratory. Results obtained from the tests showed that the typical modern overpass bridges in California had the capacity to carry heavy truck loads after a major earthquake.

Abbiati *et al.* (2015) carried out PsD tests of an existing 1950s reinforced concrete bridge that was to be retrofitted using isolation devices. Numerical simulations were initially carried out to analyse the existing and retrofitted structure for design of the PsD tests. Out of the twelve bridge piers, two were tested physically in the laboratory, whereas the remaining piers and the deck were modelled numerically. The physical specimens comprised of $1/2.5^{th}$-scaled models of the bridge piers. Hence, using the hybrid simulation technique, the finite element model of the bridge was calibrated using the experimental data obtained from the experiments for further use in design of retrofitting.

Kotoky *et al.* (2018) carried out an experimental investigation for evaluating the seismic performance of hybrid fiber-reinforced concrete (HyFRC) bridge pier along with additional detailing features at the pier–foundation interface. HyFRC was obtained by mixing appropriate volume fractions of steel and polypropylene fibres with concrete. At the pier-foundation interface, three different detailing techniques were examined: normal reinforcement detailing, additional dowels and corrugated sheet duct. Hybrid simulation was conducted with input excitations scaled to different intensity levels so that the specimens experienced different levels of damage. It was found that the piers with dowel

reinforcement at the pier-foundation interface showed enhanced seismic performance parameters as compared to the other two types.

Guo *et al.* (2021) carried out RTHS of high-speed train-track-bridge interactions (TTBIs) using the moving load convolution integral method (MLCIM). The physical model of a train was tested on a shake table, while the track-bridge structure was modelled numerically. The MLCIM was adopted for calculation of the real-time responses of the track-bridge structure. Results demonstrated that the RTHS method was capable in accurate representation of the dynamics of TTBI.

2.8. Concluding Remarks

In the light of the preceding review, it can be concluded that active confinement techniques outperform traditional passive confinement techniques like RC Jacketing, steel jacketing and FRP jacketing, in terms of enhancing the strength and ultimate strain of concrete. However, active confinement techniques pose numerous in-situ constraints due to its need for specialized equipment and an excessive amount of time, money and labour, hence limiting its practical implementation. To address the above-mentioned challenges, a group of smart materials known as Shape Memory Alloys (SMAs) has lately gained interest among researchers for its ability to exert active confining pressure on concrete members without mechanical prestressing.

A cost-effective Fe-SMA with the composition Fe-17Mn-5Si-10Cr-4Ni-1(V, C) has shown excellent mechanical properties. Despite the huge potential of Fe-SMA-confinement technique in the field of structural retrofitting, there are still very few experimental and numerical studies pertaining to the uniaxial stress-strain behaviour of Fe-SMA-confined concrete. SMA confinement is a combination of active confinement applied prior to loading and passive confinement that develops when concrete dilates during loading. A review of some of the previous confined concrete models was presented in this chapter with the objective of developing a new empirical stress-strain material model to represent the behaviour of Fe-SMA confined concrete.

Few studies have been carried out to test the effectiveness of Fe-SMA for strengthening of RC beams. However, use of Fe-SMA for retrofitting of bridge piers have not been explored yet. Additionally, the performance of such structural systems under seismic loads is an area that requires more research. It is crucial for evaluating the effectiveness of new and advanced materials for enhancing the seismic performance of structural elements.

Hybrid simulation technique combines physical testing of the most vulnerable element of a structure with numerical simulation of the remaining structure, which is expected to remain elastic during seismic excitation. It gives a detailed representation of the damage sustained by large structures like buildings and bridges during seismic events without needing to physical test of the entire structure, thus eliminating some of the shortcomings of both quasi-static testing and shake table testing. The use of hybrid simulation technique for investigating the response of RC piers retrofitted with Fe-SMA has not been documented in the literature. Hence, it is adopted in the present study.

Chapter 3

Characterization of constituent materials

3.1. General

This chapter presents the characterization of materials used for casting of concrete cylinders and that for rehabilitation of the damaged bridge pier specimens. Further, details of testing procedures used to evaluate the microstructure and phase transformation characteristics of the Fe-SMA strips used in this study are also presented. Results of thermo-mechanical tests carried out to study the recovery stress generation and stress-strain behaviour of the Fe-SMA strips are also reported in this chapter.

3.2. Concrete

The constituent materials of the concrete mix were tested as per relevant Indian Standard (IS) codal provisions and the results are presented in Tables 3.1-3.4. Portland pozzolana cement (PPC) was used and largest size of coarse aggregates used was 10 mm. A superplasticizer, Sikament-2004NS with a specific gravity of 1.2 was used for imparting high workability.

Three grades of concrete with target cube strengths of 25 MPa, 30 MPa and 35 MPa were adopted for the three design mixes used in this study. The compressive strength of each design mix was determined using cube specimens with dimensions of 150 x 150 x 150 mm. The results are presented in Table 3.5. Cylinder specimens with dimensions 150 x 300 mm were used to calculate the cylinder compressive strength for each of the design mixes. The results are presented in Table 3.6.

Table 3.1. Results of tests on cement

S. No.	Name of test	Relevant IS code	Test result
1	Standard consistency	IS: 4031(4):1988	50 %
2	Initial setting time	IS: 4031(5):1988	1 hr. 45 min.
3	Final setting time	IS: 4031(5):1988	6 hr. 15 min.
4	Specific gravity	IS: 4031(11):1988	2.91

Table 3.2. Compressive strength of cement cube

No. of days	Compressive strength (MPa)	
	According to IS 1489 (Part 2):1991	Test Results
3	16	16.8
7	22	22.6
28	33	34.5

Table 3.3. Result of sieve analysis of sand

S. No.	IS Sieve designation	Wt. retained (gm)	% Wt. retained (gm)	Cumulative % wt. retained	Cumulative % wt. passing	As Per IS 383-2016 Table no. 9 for Zone III
1	4.75 mm	0	0	0	100	90-100
2	2.36 mm	0	0	0	100	85-100
3	1.18 mm	134	13.4	13.4	86.6	75-100
4	600 µm	228	22.8	36.2	63.8	60-79
5	300 µm	476	47.6	83.8	16.2	12-40
6	150 µm	138	13.8	97.6	2.4	0-10
8	Pan	24	2.4	100	0	-

Specific gravity as per IS: 2386(III)-1963 = 2.58

Table 3.4. Result of sieve analysis of coarse aggregates

S. No.	IS Sieve designation	Wt. retained (gm)	% Wt. retained (gm)	Cumulative % wt. retained	Cumulative % wt. passing	As Per IS 383-2016 Table No. 7 for Zone III
1	10 mm	0	0	0	100	90-100
2	4.75 mm	1906	95.3	95.3	4.7	85-100
3	3.36 mm	94	4.7	100	0	75-100
Specific gravity as per IS: 2386 (III)-1963 = 2.66						
Fineness Modulus as per IS: 2386 (I)-1963 = 5.95						

Table 3.5. Details of concrete mixes

S. No.	Target (MPa)	Mix ratio	Water-cement ratio	Superplasticizer by weight of cement (%)	Average compressive strength (MPa)
1	25	1:2.24:2.09	0.525	-	26.52
2	30	1:2.25:2.14	0.5	0.48	31.6
3	35	1:1.91:1.93	0.425	0.71	36.67

Table 3.6. Cube and cylinder compressive strengths of design mixes

S. No.	Average cube compressive strength (MPa)	Average cylinder compressive strength (MPa)
1	26.52	21.7
2	31.6	26.3
3	36.67	30.3

3.3. Materials used in repairing of damaged specimens

Different materials were utilized for repairing the damaged bridge pier specimens by RC jacketing. Description of the materials utilised as well as their properties obtained from the product data sheet supplied by the manufacturer are presented in the following subsections.

3.3.1. Moisture insensitive epoxy resin injection [Sikadur-53 (UF)]

Sikadur-53 (UF) is a solvent-free injectable resin grout designed for sealing crack widths upto 5 mm under dry/damp/submerged conditions by high-pressure injection. It is an all-liquid system consisting of a base (colourless) and a hardener (reddish brown) mixed in the ratio of 2:1 (by weight). The properties of the epoxy resin obtained from the product data sheet supplied by the manufacturer are presented in Table 3.7.

Table 3.7. Properties of epoxy resin

Pot life	Density	Compressive strength (As per ASTM C 579)	Tensile strength (As per ISO 527)
~ 15 minutes (at +30°C)	~ 1.1 kg/l (at +27°C)	1 day ≥ 40 MPa 7 days ≥ 45 MPa 14 days ≥ 50 MPa	14 days ≥ 40 MPa

3.3.2. Micro-concrete (SikaRep Microconcrete-4)

Micro-concrete is a pourable, non-shrink, repair concrete which comprises of cement, graded aggregates and other chemicals which impart controlled expansion characteristics in the plastic state, while reducing water demand. SikaRep Microcrete-4 was supplied as a ready to use blend of dry powders, which required only addition of clean water in-situ to produce a free-flowing non-shrink mix. Recommended water: powder ratio by the manufacturer was 0.14 to 0.16 by weight (dependent on the desired flow). The low water requirement ensured high early strength and long-term durability. For repairs requiring a considerable quantity of materials, this mix was modified by the addition of 10 mm down (or as per requirement) clean, graded, saturated surface dry aggregates in proportion of 2:1 (SikaRep Microcrete-4: Coarse Aggregate) by weight at site. The properties of the normal micro-concrete obtained from the product data sheet supplied by the manufacturer are presented in Table 3.8.

Table 3.8. Properties of micro-concrete

Bulk Density (As per ASTM C1107)	Compressive strength (As per ASTM C 109, 70 mm cube)	Tensile strength (As per ASTM C 293-79)
1.2 kg/l	1 day ≥ 25 MPa 7 days ≥ 45 MPa 28 days ≥ 65 MPa	7 days ≥ 7 MPa 28 days ≥ 8 MPa

3.3.3. High performance injection mortar (FIS V 360 S)

The Fischer styrene-free, quick-curing high-performance mortar FIS V is a 2-component injection mortar based on vinyl ester hybrid. Resin and hardener are stored in two separate chambers and are not mixed and activated until extrusion through the static mixer. It is used for anchoring post-installed reinforcing bars (rebars) in existing structures made of normal weight concrete. The gelling and curing time of injection mortar FIS V is presented in Table 3.9.

Table 3.9. Gelling and curing time of Injection mortar FIS V

Cartridge temp. (mortar)	Gelling time	Temp. at anchoring base	Curing time
+ 10°C — + 20°C	5 min.	+ 10°C — + 20°C	60 min.
+ 20°C — + 30°C	4 min.	+ 20°C — + 30°C	45 min.
+ 30°C — + 40°C	2 min.	+ 30°C — + 40°C	35 min.

3.3.4. Acrylic modifier (Mastercrete M 81)

Mastercrete M-81 is a single component 100% acrylic polymer admixture specially developed to improve the properties of cementitious compositions. When it is used in combinations with ordinary Portland cement, it enhances the mechanical properties such as bonding (adhesion) with various building materials, flexural, compression and impact strength. Mixing ratio applicable for different applications is presented in Table 3.10.

Table 3.10. Mixing ratio of Master Crete with Cement

Application	Mixing Ratio
Bonding coat	Cement: Master Crete M-81-2:1 parts by weight
Repair mortar of RCC members	15-20% by weight on cement quantity

3.3.5. Quick setting and rapid hardening admixture for plain cement concrete and mortar (CICO NO.3)

CICO No.3 is a high versatile free flowing colourless concrete additive in liquid form used as quick setting cum rapid hardening admixture for concrete. It is useful for sealing nozzles after injectable resin grout (for sealing cracks) is pumped under pressure. For this, CICO solution was added to cement in the ratio 1:3 (CICO No.3: Cement), and mixed thoroughly and quickly so as to avoid stiffening during mixing. The initial setting time varied from 2 to 3 minutes and the final setting time varies from 4 to 6 minutes.

3.3.6. Epoxy bonding agent for concrete (Masterbond EP)

Masterbond EP is a two-component epoxy resin-bonding agent for concrete. Part 1 (Base) is mixed with Part 2 (Hardener) in the ratio 65:35. It gives strong bonding in between old and new concrete. The properties of the epoxy-bonding agent obtained from the product data sheet supplied by the manufacturer are presented in Table 3.11.

Table 3.11. Properties of epoxy bonding agent for concrete

Pot life	Full hardness time	Full cure time	Overlay time
~ 1.5-2 hrs. (at +30°C)	~ 48 hrs. (at +30°C)	~ 6 days (at +30°C)	5-6 hrs.

3.4. Characterization of Fe-SMA strips

Prestrained Fe-SMA strips (2%) used in the current study were procured from re-fer AG, Switzerland, and its manufacturing procedure is described in Dong *et al.* (2009). These were cut from Fe-SMA sheets of length 9 m, width 120 mm and thickness 1.5 mm. Details of experimental investigation carried out for determining its thermo-mechanical properties, phase transformation behaviour and microstructure are presented in the following sub-sections.

3.4.1. Thermo-mechanical properties

3.4.1.1. Test specimen

To characterize the thermo-mechanical properties of the Fe-SMA strips after thermal activation, three rectangular strips of dimension 400 mm × 30 mm × 1.5 mm were cut from the Fe-SMA sheets. The central portions of the rectangular strips were cut using a CNC wire cut EDM machine (Make: Berlin Machine Corporation; Model No.: FDK 7735). The dimensions of the resulting dog-bone specimens, S1, S2 and S3, are shown in Fig. 3.1. The subsize specimens of 6 mm width and 25 mm gauge length were prepared to conform to ASTM E8/E8M (2016). The final widths of the test specimens were measured using a digital Vernier calliper with an accuracy of 0.01 mm. An additional grip length of 150 mm was provided at the top and bottom to insert the test specimen into the electric furnace and to ensure the safety of the load-cell as well as cross-head grips during thermal activation of the Fe-SMA strips.

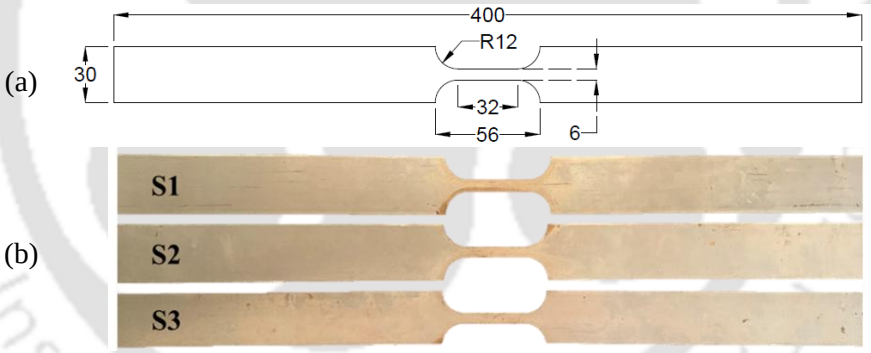

Fig. 3.1. Dog-bone specimens used for tensile test (a) geometry (dimensions in mm) (b) actual image

3.4.1.2. Test set-up

All the dog-bone specimens were tested in a 250kN servo hydraulic universal testing machine (UTM) (Make: BISS, India). It was integrated with an electric furnace which was capable of generating high temperatures upto 1400°C. Fig. 3.2 shows the overall test set-up. The electric furnace had two heating elements. The air temperature inside the heating chamber was measured using two internal thermocouples that were fitted in the furnace lining. The top and bottom parts of the furnace were sealed with glass wool to facilitate high thermal insulation during heating.

3.4.1.3. Activation of Fe-SMA strips

Before heating, an initial preload of σ_0 = 50 MPa was applied to the test specimens. In the initial stage of the heating process, the stress in the Fe-SMA element underwent a slight drop due to the effect of thermal expansion. The test specimens were heated up to a target temperature of 160°C at a rate of 10°C/min by the heating elements inside the electric furnace, while maintaining a constant strain. This led to the activation of shape recovery and generation of recovery stress in the test specimen. An average temperature of 169 °C was recorded by the two thermocouples, which was held constant for 10 min, and then the electric furnace was switched off to facilitate air cooling of the test specimens to the room temperature of 23°C. The recovery stress generated throughout the test was calculated based on the force recorded by the load cell of the UTM.

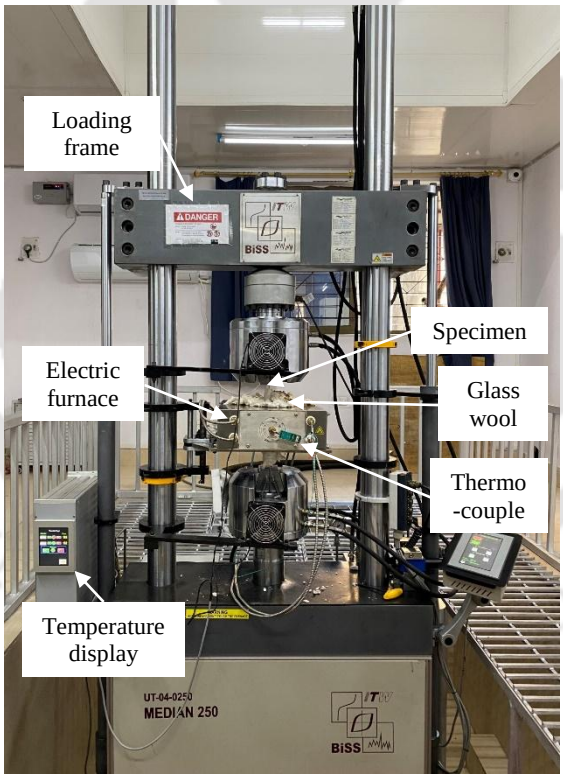

Fig. 3.2. Servo-hydraulic universal testing machine with electric furnace

3.4.1.4. Recovery stress characteristics

Fig. 3.3 shows the resulting recovery stress versus temperature variation for the test specimen. Initial recovery stress, σ_r in the range of 361-367 MPa was generated in the three

coupon specimens, which was in good agreement with the values reported by Shahverdi *et al.* (2018). Reduced recovery stress, σ_r^{15m} in the range of 352-356 MPa was obtained after holding the specimen in the same position at room temperature for a duration of 15 minutes, as reported in Ghafoori *et al.* (2017). The 15-minute waiting period was chosen in accordance with a previous study, which demonstrated that a significant portion of the stress relaxation in this kind of alloy happened within the first few minutes after activation.

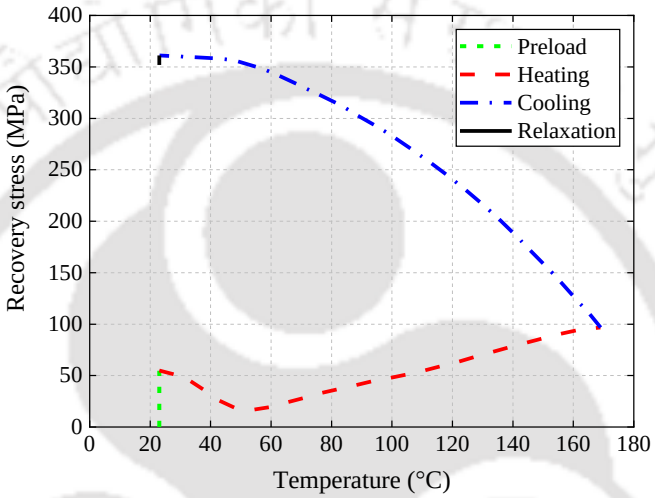

Fig. 3.3. Recovery stress vs. temperature variation of Fe-SMA

3.4.1.5. Tensile characteristics

To examine the stress-strain behaviour of the activated test specimens, tensile tests were performed at a strain rate of 0.15% s^{-1}. Strain measurements upto 10% were acquired using a clip-on extensometer. For strains greater than 10%, the crosshead displacement rate was adjusted to match the strain rate of 0.15% s^{-1} in the gauge length of the specimen. The loading continued till the specimen ruptured. The resulting stress-strain curve for specimen S1 is shown in Fig. 3.4.

The tensile test results of the Fe-SMA strips after activation showed that the tangent modulus of elasticity is in the range of 74-78 GPa. Ultimate tensile strength and strain at rupture of the specimens was found to be in the range of 937-942 MPa and 33-37% respectively.

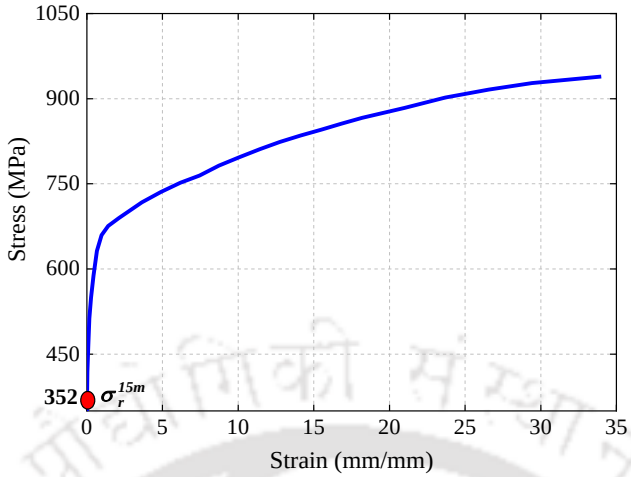

Fig. 3.4. Stress-strain behaviour of Fe-SMA coupon specimen after activation

3.4.1.6. Cyclic loading characteristics

Three coupon specimens, S4, S5 and S6 were thermally activated, after which these were subjected to 10 cycles of loading-unloading at a strain range of $\Delta\varepsilon_0$ = 0.2%. The main aim of this test was to understand the stress-strain behaviour of Fe-SMA strips under cyclic loading conditions when they were used as prestressing elements in a bridge pier. This 0.2% strain range was chosen based on the maximum strain recorded by the strain gauges fixed on the Fe-SMA strips during hybrid simulation. A loading frequency of 0.025 Hz was chosen for consistency with the loading protocol during cyclic tests of the RC bridge piers. After 10 cycles of loads, the specimens were subjected to increasing tensile loads at a displacement rate of 1 mm/min until its failure.

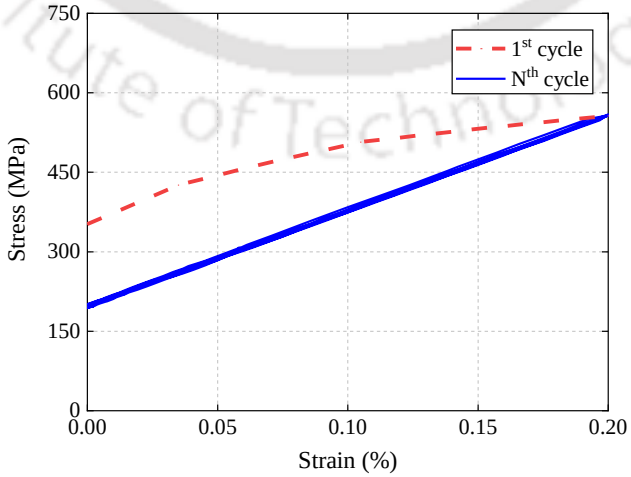

Fig. 3.5. Cyclic stress-strain behaviour of Fe-SMA coupon specimen after activation

The stress-strain behaviour of test specimen during cyclic loading is presented in Fig. 3.5. In the first load cycle, it was observed that the Fe-SMA exhibited nonlinear behaviour. For the S4 specimen, recovery stress increased from 352 MPa to 559 MPa at the end of the first loading segment. At the end of the first unloading segment, the recovery stress decreased from 352 MPa to 195 MPa. A similar reduction in recovery stresses was also observed for specimens S5 and S6. This loss in recovery stress may be attributed to the forward phase transformation from austenite to martensite. However, for subsequent cycles an almost linear behaviour was observed with an apparent Young's modulus of 175 GPa which is very close to the Young's modulus of the parent material (Ghafoori *et al.*, 2017). This observation is in accordance with the results of similar tests carried out by Ghafoori *et al.* (2017) for various strain ranges, loading frequencies, and load cycles.

Fig. 3.6. shows the stress-strain behaviour during tensile loading of the test specimen S4 at the end of the cyclic test upto failure. It was observed that the stress-strain curve followed a similar pattern as compared to that of Fe-SMA with 2% pre-strain (Fig. 3.4). The ultimate tensile strength of specimen and corresponding elongation of the specimens at failure were 935 and 32% respectively. These values were comparable to those obtained from the tensile tests of the Fe-SMA material without activation.

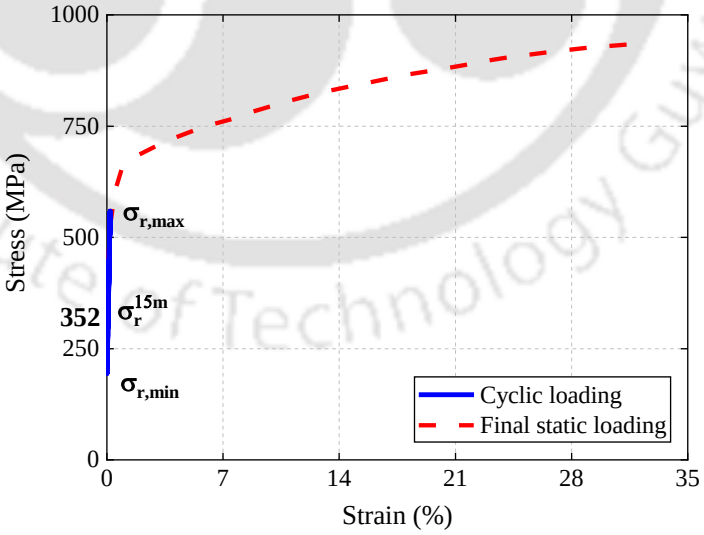

Fig. 3.6. Tensile stress-strain behaviour of Fe-SMA coupon specimen after cyclic tests.

3.4.2. Phase characterization of Fe-SMA

The X-ray diffraction (XRD) technique was utilized in this study to evaluate the phases present in the 2% prestrained Fe-SMA samples as well as the changes that occurred after its thermal activation. The diffraction patterns were acquired using a 9kW powder X-ray diffraction system (Model: SmartLab; Make: Rigaku Technologies, Japan) with Cu Kα radiation corresponding to a wavelength of 1.54 Å, at 45kV and 200mA, over a two-theta range from 35° to 95°. PDXL software was used to determine the position of the peaks, which were identified using the International Centre for Diffraction Data powder diffraction database.

The XRD phase analysis of the Fe-SMA sample with a pre-strain of 2% is shown in Fig 3.7. It was observed that the highest diffraction peaks at 2θ = 43.5° and 2θ = 50.7°corresponded to γ-austenite phase with reflection planes (111) and (200) respectively. Lower intensity peaks which corresponded to the reflections of (220) and (222) planes were located at 2θ = 74.7° and 2θ = 90.7° respectively. Additionally, only one small peak located at 2θ = 46.8° assigned to the (10.1) plane, confirmed the presence of ε-martensite phase. With reference to microstructural characterization of Fe-SMA carried out by previous researchers (Koster *et al.*, 2015; Leinenbach *et al.*, 2016), ε-martensite peaks were also detected at 2θ = 41°, 2θ = 62° and 2θ = 93°. Since these peaks are usually quite thin, these were missed in the current XRD analysis (Ghafoori *et al.*, 2017).

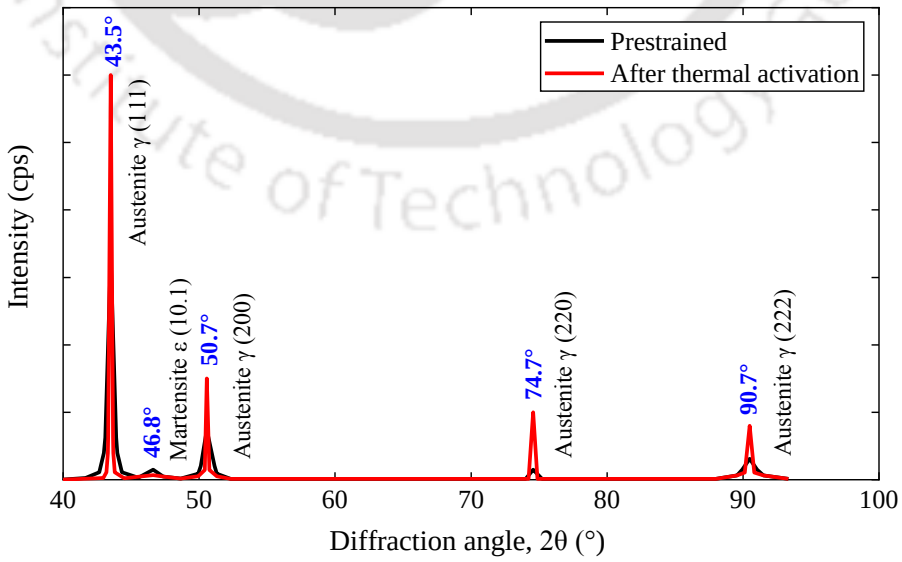

Fig. 3.7. Comparison of XRD spectrum of pre-strained and activated Fe-SMA sample

If a pre-strained SMA is heated to a temperature above A_f, the alloy undergoes reverse transformation to austenite phase (ε-martensite to γ-austenite), thus recovering its original shape. This phenomenon known as shape memory effect (SME). The reversibility in a prestrained Fe-SMA specimen was observed by heating the specimen to a temperature of 160° for 10 minutes. XRD analysis was carried out on this activated specimen and the resulting diffraction patterns are shown in Fig 3.7. The intensity of the ε-martensite peak corresponding to the (10.1) peak showed a clear drop in intensity, as predicted. The intensity of all the austenite peaks also increased significantly. In addition, the austenite peaks showed a considerable decrease in peak width. Consequently, the rise in peak intensity observed in all γ-austenite grain types following thermal activation confirmed the reverse transformation of ε-martensite to γ-austenite.

3.4.3. Microstructure of Fe-SMA

Field-emission scanning electron microscopy (FESEM) was used for observing the changes in the microstructure of the Fe-SMA samples before and after thermal activation. The Fe-SMA samples were mechanically grounded using progressively finer grades of SiC papers (Make: Buehler) upto a grade of 1200. To achieve a mirror-like finish, the samples were then polished with a monocrystalline diamond paste (MetaDi II Paste, Make: Buehler, USA) of grain size 1μm. The surface of the samples was cleaned using ethanol, rinsed with distilled water and dried. Finally, the samples were etched with a Kalling 2 etching solution for revealing microstructural details. Its formula, as listed in ASTM E407 is 2 g $CuCl_2$, 40 mL HCl and 40–80 mL ethanol (95 %) or methanol (95 %). A field emission scanning electron microscope (FESEM) with element EDS Detector (Model: Sigma 300, Make: Zeiss) was used for studying the microstructure of the samples. The electron beam voltage was set to 5 kV and the images were obtained at a magnification of 2 kX. Fig 3.8 shows the SEM image of the prestrained Fe-SMA sample.

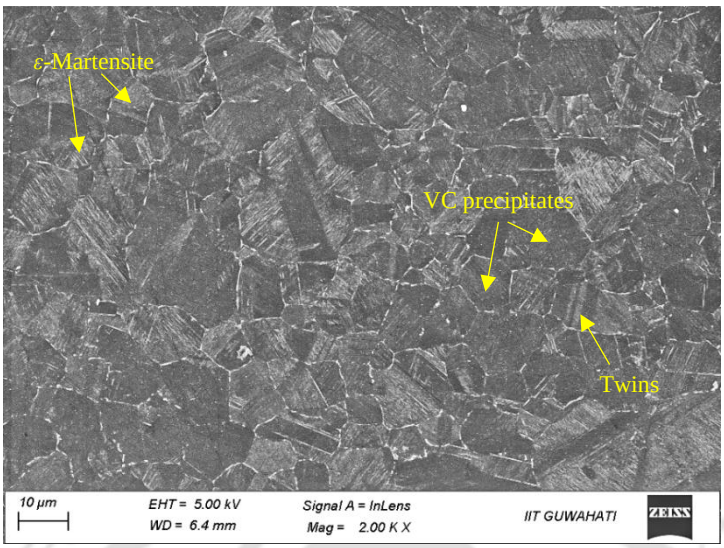

Fig. 3.8. SEM micrograph showing Fe-SMA sample in pre-strained state

It was observed that the γ-austenite grains were randomly oriented and VC particles were finely dispersed. Stress-induced ε-martensite plates, appearing as light parallel lines inside the austenite grains was clearly distinguished. Deformation twins were also observed in the γ-austenite grains. The microstructure of the Fe-SMA sample after being heated to a temperature of 160° is shown in Fig. 3.9. The observed microstructure showed the disappearance of martensite plates to a large extent which was indicative of the reverse transformation of ε-martensite to γ-austenite.

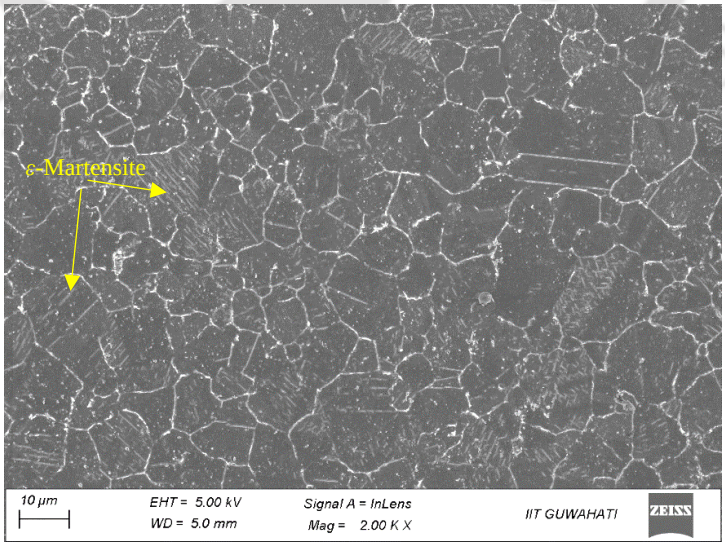

Fig. 3.9. SEM micrograph showing Fe-SMA sample after thermal activation

3.4.4. Factography analysis of Fe-SMA

The large elongation value, observed when the specimen failed in the tensile tests described in the earlier sections (Secs. 3.4.1.5-6), confirmed that the nature of fracture of the Fe-SMA used in the present study was ductile in nature. The ductile failure of coupon specimen during tensile test was exhibited by nucleation, growth and coalescence of voids near to its centre. Fig 3.10 shows morphology of the fracture zone using FESEM. At a high magnification, a huge number of dimples of unequal sizes were observed on the fracture surface, which was indicative of a ductile failure.

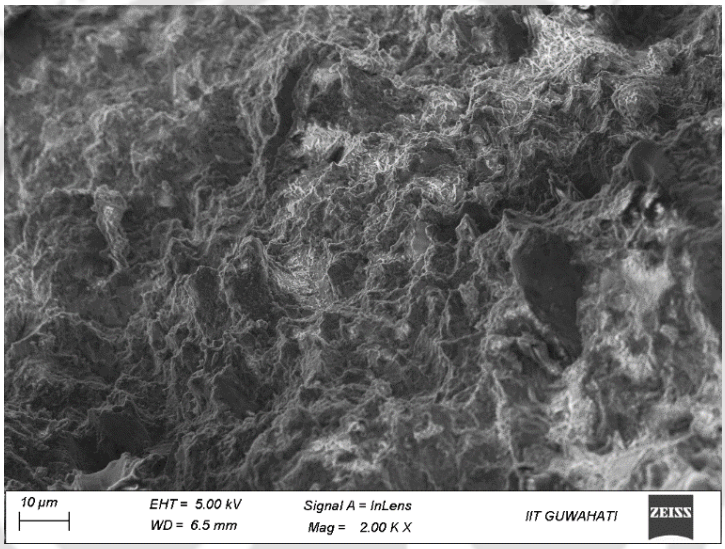

Fig. 3.10. SEM micrograph showing Fe-SMA sample taken from the fracture zone of tensile test coupon specimen after failure

3.5. Concluding Remarks

In this chapter, details of materials used for rehabilitation of damaged bridge pier specimens are reported. Material-level tests were carried out for determining the thermo-mechanical properties of the Fe-SMA used in the present study. Evaluation of recovery stress after stress relaxation, tensile stress-strain behaviour, cyclic stress-strain behaviour was done. Reduced recovery stress after stress relaxation was obtained in the range of 352-356 MPa. The ultimate tensile strength and strain at rupture was found to be in the range of 937- 942 MPa and 33-37% respectively. During the first load cycle of cyclic test, Fe-SMA exhibited nonlinear behaviour. However, for subsequent cycles an almost linear behaviour was

observed with an apparent Young's modulus of 175 GPa. Phase characterization of Fe-SMA samples was done by XRD and evolution of its microstructure was studied by FESEM. Comparison of test data of Fe-SMA samples before and after its thermal activation confirmed the reverse transformation of ε-martensite to γ-austenite upon heating.

Chapter 4

Axial stress-strain model for concrete actively confined with Fe-SMA strips

4.1. General

This chapter presents a new scheme for active confinement of concrete using cost-effective Fe-shape memory alloy (Fe-SMA) strips as an alternative to the expensive NiTi-based SMAs. The axial stress-strain behaviour of concrete partially wrapped by Fe-SMA strips was experimentally investigated. An empirical stress-strain model was proposed for accurate prediction of behaviour of Fe-SMA confined plain concrete. The predicted model for Fe-SMA confined concrete and Mander's model for steel rebar confined concrete were combined to propose a model for predicting the behaviour of Fe-SMA confined RC specimen. Additionally, 3D FE analyses of concrete specimens with varying concrete strength, internal steel reinforcement and external Fe-SMA confinements were carried out and an empirical model was proposed for improved prediction of uniaxial compressive behaviour of Fe-SMA confined RC specimens.

4.2. Experimental investigation

Details of the experimental investigation carried out to evaluate the stress-strain relationship of concrete, partially wrapped by Fe-SMA strips, under monotonic compressive loading are presented in the following subsections.

4.2.1. Cylinder specimens and test matrix

In this study, a total of 12 concrete cylinders, each measuring 150 mm in diameter and 300 mm in height, were prepared and tested under monotonic compressive loading. Table 4.1 shows the details of all the tested specimens which includes unconfined concrete compressive strength, Fe-SMA strip spacing and active confining pressure. Three different concrete mixes, A1, A2 and A3 were used in this study. Test specimens with Fe-SMA

confinement pressures S1, S2 and S3 corresponding to strips spacings 92 mm, 69 mm and 55 mm are shown in Fig. 4.1(a-c).

Active confining pressures $f_{l,active}$, corresponding to different strip spacings were calculated based on effective confining pressure. According to Mander *et al.* (1988) , the effective confining pressure f_l' for a circular section, is given by:

$$f_l' = \frac{2k_e A_{sp} f_h}{sD} \tag{4.1}$$

where, k_e is the confinement effectiveness ratio, f_h is the SMA recovery stress (Chen & Andrawes, 2017), A_{sp} and s are the cross-sectional area and centre-to-centre distance of Fe-SMA strips respectively and D is the diameter of the specimen.

Table 4.1. Specifications of test specimens

Specimen ID	Concrete compressive strength (MPa)	Fe-SMA strip spacing (mm)	Active confining pressure (MPa)
A1-S0	21.7	-	-
A1-S1		92	1.09
A1-S2		69	1.76
A1-S3		55	2.44
A2-S0	26.3	-	-
A2-S1		92	1.09
A2-S2		69	1.76
A2-S3		55	2.44
A3-S0	30.3	-	-
A3-S1		92	1.09
A3-S2		69	1.76
A3-S3		55	2.44

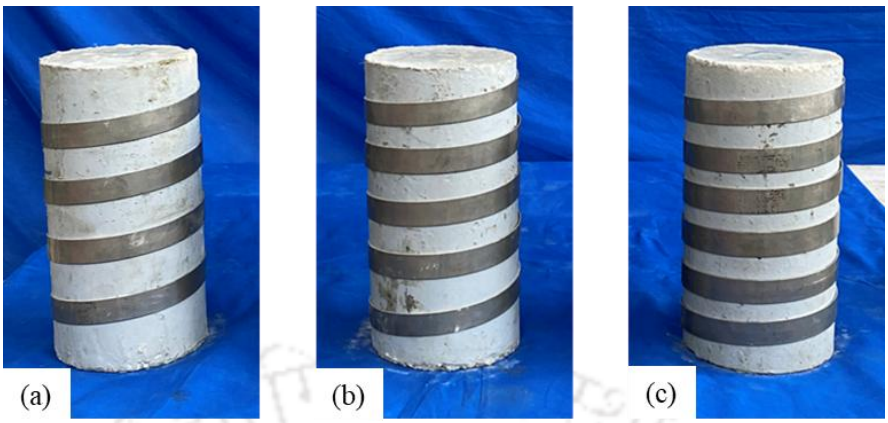

Fig. 4.1. Sample of test specimens (a) A1-S1 (b) A1-S2 (c) A1-S3

4.2.2. Preparation of test specimens

Twelve numbers of 150 × 300 mm concrete cylinders were cast and cured for 28 days before fixing Fe-SMA strips on it. Fe-SMA strips of width 24 mm were cut into required lengths in a hydraulic shearing machine. The thermal activation of the restrained Fe-SMA strips was carried out using a step-down transformer as shown in Fig. 4.2.

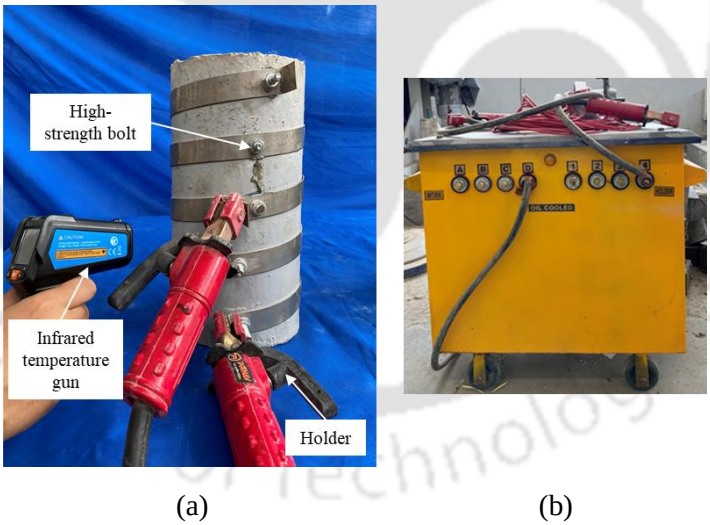

Fig. 4.2. Preparation of test specimen (a) thermal activation procedure (b) step-down transformer

A current density of 6 A/mm^2 was chosen for activation of the Fe-SMA strips. A high current density is preffered so as to reduce the exposure of concrete to a high temperature for longer duration. Additionally, to protect the surface of the concrete during thermal activation of Fe-SMA strips, a heat-resistant protective coating was applied. Since there is a high current requirement in the laboratory for resistive heating, the width of the

strips used in this study was limited to 24 mm. High strength bolts of 8 mm diameter, FBN II 8/10 (Make: Fisher) were used for anchorage of the strips into the concrete. Fe-SMA strips were fixed at their locations. In order to carry out resistive heating, two ends of the Fe-SMA strips were held tightly by the two holders of the step-down transformer and power was turned on. The temperature was continuously checked by an infrared temperature gun. Resistive heating of the strips took less than a minute for attaining a temperature of 160°C. Power supply was cut once the required temperature was achieved. Shortening of the strips was even visible to the naked eye.

4.2.3. Test set-up and Instrumentation

The test specimens were subjected to uniaxial compressive load monotonically using a 1,000-kN capacity servo-hydraulic MTS actuator as shown in Fig. 4.3(a). A schematic diagram indicating all the components of the test set-up is shown in Fig. 4.3(b).

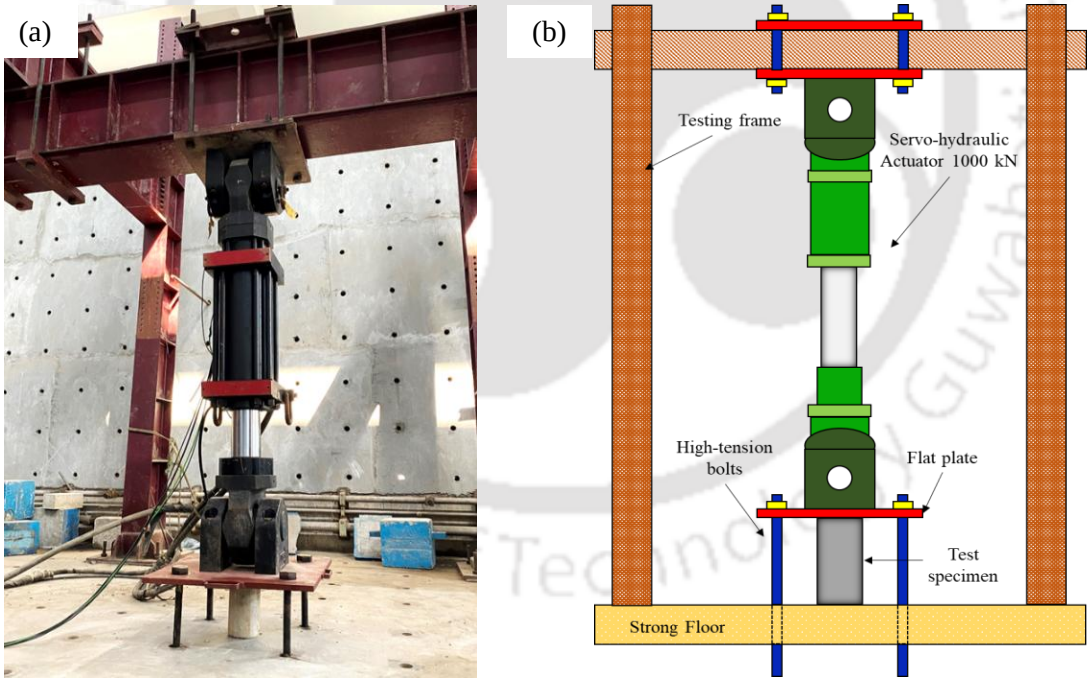

Fig. 4.3. Experimental set-up for testing of cylindrical specimens (a) actual test set-up (b) schematic diagram

A flat plate of thickness 30 mm was bolted to the actuator head. Another set of four high strength bolts were fixed at the four corners of the plate to constrain the movement of actuator head in the vertical direction. Displacement controlled loading was applied to the

test specimens at a strain rate of 0.1%/min (Chen & Andrawes, 2017). Four strain gauges having a gauge length of 3 mm were fixed on the surface of the Fe-SMA strips, around the cylinder's mid-height to record its hoop strains. The four strain gauges were 90 degrees apart from each other as shown in Fig. 4.4. The strain recorded in these were a measure of the lateral deformation of the concrete test concrete specimens during loading due to strain compatibility between the Fe-SMA strips and concrete. The axial loads and axial displacements were recorded by the built-in load cell and tempo-sonic displacement sensor of the MTS actuator.

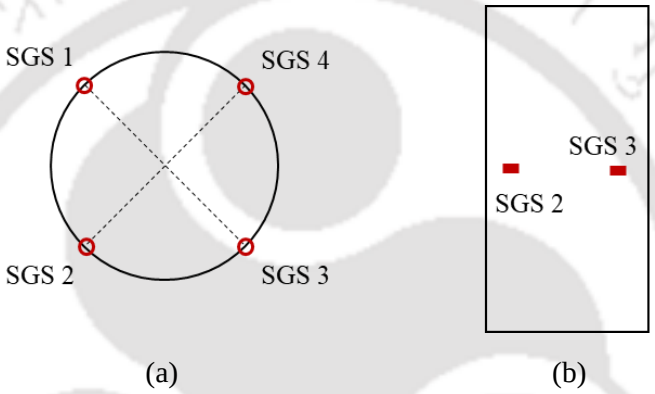

Fig. 4.4. Layout of strain gauges in (a) plan and (b) elevation

4.3. Results and discussion

This section summarises the results obtained from the experimental study of the test specimens. Failure modes of the test specimens, axial stress-axial strain and axial stress-lateral strain behaviour of Fe-SMA confined concrete were investigated in this study. Further, contribution of active confining pressure to the total confining pressure acting on each test specimen was determined.

4.3.1. Failure modes of test specimens

The modes of failure of specimens A1-S0, A1-S1, A1-S2 and A1-S3 are compared in Fig. 4.5. The plain concrete cylinders failed in a brittle manner, with wide diagonal cracks extending down the cylinder height [Fig. 4.5(a)]. Most of the specimens confined with Fe-SMA strips failed in a ductile manner. S1-series specimens with large strip spacing however experienced lateral deformation in the early stages of loading due to less lateral

confinement offered by the strips. Shear failure eventually occurred in the S1-sereies specimens, as may be observed from Fig. 4.5(b). The overall damage of S2 and S3 specimen types were however minimal till the rupture of Fe-SMA strips. More localised crushing was observed at top and bottom regions of these specimens. Since the Fe-SMA strips provided strong resistance to lateral deformation of concrete, these specimens could withstand higher loads. The failure of these specimens were preceded by rupture of Fe-SMA strips at its mid-height as maybe observed in Figs. 4.5 (c) and (d). However, as may be observed from Fig. 4.5(e), the diagonal cracks leading to failure of specimen types A1-S2 and A1-S3 were observed after snapping of the Fe-SMA strips, which is primarily due to reduction in confinement of concrete specimens.

Fig. 4.5. Different failure modes of specimens (a) A1-S0 (b) A1-S1 (c) A1-S2 (d) A1-S3 (e) A1-S2/S3

4.3.2. Stress-strain behaviour of Fe-SMA confined concrete

An idealized diagram of the experimental stress-strain behaviour of SMA confined concrete and its key features in axial compression are depicted in Fig. 4.6 (Chen & Andrawes, 2017). During the initial loading stage concrete exhibits elastic behaviour upto 45% of its peak axial stress. The Young's modulus E_0, is represented by secant modulus at this stress-limit, beyond which nonlinearity arises in the concrete. The ascending branch of the stress-strain curve peaks at f'_{cc} with corresponding strain ε'_{cc}, is followed by a descending branch. The slope of the descending branch drastically decreases at first, after which it stabilizes. Residual stress (f_{res}) is defined at the transition point at which the stress-strain curve begins to flatten, and the variance in slope is minimal. From experimental data, it is observed that

transition point for all the test specimens lies in the range of 2.3% to 2.7% axial strain. Hence, the transition point in this study is approximately defined at 2.5% axial strain. The failure of the test specimen is defined by ultimate stress (f_{ult}) and corresponding ultimate strain (ε_{ult}). Cylinder test results of all twelve specimens are presented in Table 4.2.

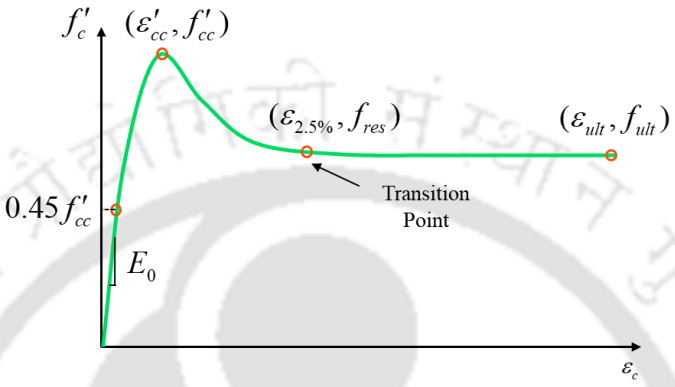

Fig. 4.6. Typical axial stress-strain behaviour of Fe-SMA confined concrete (Chen & Andrawes, 2017)

Table 4.2. Summary of cylinder test results

Specimen ID	$f_{l,active}$ (MPa)	f'_{cc} (MPa)	ε'_{cc}	f_{res} (MPa)	f_{ult} (MPa)	ε_{ult}	Transition Point	
							Lateral strain	Passive confinement (MPa)
A1-S0	0	21.7	0.0016	-	-	-	-	-
A1-S1	1.09	27.1	0.0032	15.9	14.7	0.0706	0.0298	1.09
A1-S2	1.76	30.3	0.004	19.7	18.9	0.0796	0.0225	1.71
A1-S3	2.44	36.6	0.0048	23.7	22.6	0.081	0.0167	2.29
A2-S0	0	26.3	0.0017	-	-	-	-	-
A2-S1	1.09	33.2	0.0031	15.1	14.3	0.0573	0.0306	1.1
A2-S2	1.76	36.6	0.0037	19.2	19.9	0.0635	0.0267	1.74
A2-S3	2.44	40.4	0.0045	23.2	22.9	0.068	0.0186	2.34
A3-S0	0	30.3	0.0018	-	-	-	-	-
A3-S1	1.09	39.5	0.0029	15.6	15.3	0.0555	0.0325	1.12
A3-S2	1.76	43.6	0.0035	18.7	18.1	0.0569	0.0296	1.75
A3-S3	2.44	48.3	0.0046	24.4	23.9	0.0608	0.0241	2.39

Sample axial stress-strain curves of Fe-SMA confined concrete cylinders of Type A1 with different confinement pressures are shown in Fig. 4.7. As the confinement level of concrete is increased from S1 to S3, it is observed that the peak stresses increased by 24.8%, 39.4% and 68.5% respectively as compared to that of the unconfined concrete specimens A1-S0. The ultimate axial stresses of A1-S1, A2-S2 and A3-S3 were 14.7 MPa, 18.83 MPa and 22.6 MPa respectively and the corresponding strains at failure were 0.0706 mm/mm, 0.0795 mm/mm and 0.0809 mm/mm respectively. It can be observed that there is substantial improvement in the peak stress, ultimate stress as well as ductility due to Fe-SMA confinement.

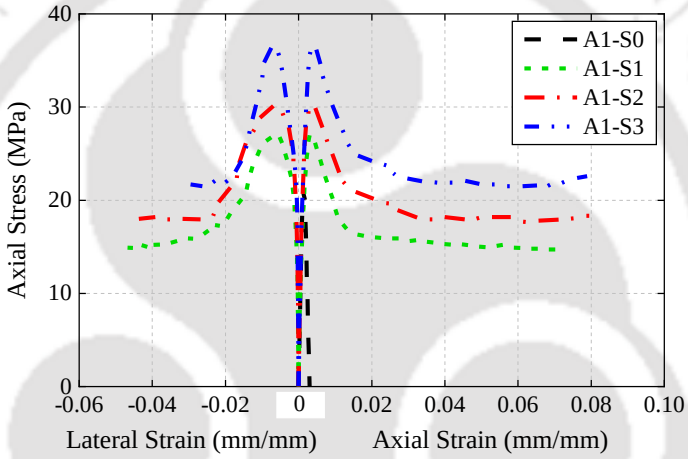

Fig. 4.7. Comparison of stress–axial strain and axial stress-lateral strain relations of unconfined and confined concrete with strength of 21.7 MPa (Type A1) and different SMA confinement levels.

Comparison of axial stress-strain curves of test specimens of different concrete grades with the same active confinement pressures are shown in Fig. 4.8. The peak stresses of A1-S1, A2-S1 and A3-S1 were 27.1 MPa, 33.2 MPa and 39.4 MPa respectively. For confinement level S1, as the grade of concrete increased from A1 to A3, the peak stresses increased by 24.8%, 26.3% and 29.9% respectively as compared to that of A1-S0. However, it may also be noted that all the three specimens, regardless of the concrete grade, displayed similar values of residual stresses at the transition point and maintained the same until failure. Similar trend was observed for specimens with SMA confinement level S2 and S3. This observation is in agreement with the experimental results obtained by Chen and Andrawes (2017) for NiTiNb-SMA spirals confined concrete. Hence, it may be

concluded that the residual stress of Fe-SMA confined concrete is dependant only on the active confining pressure acting on it.

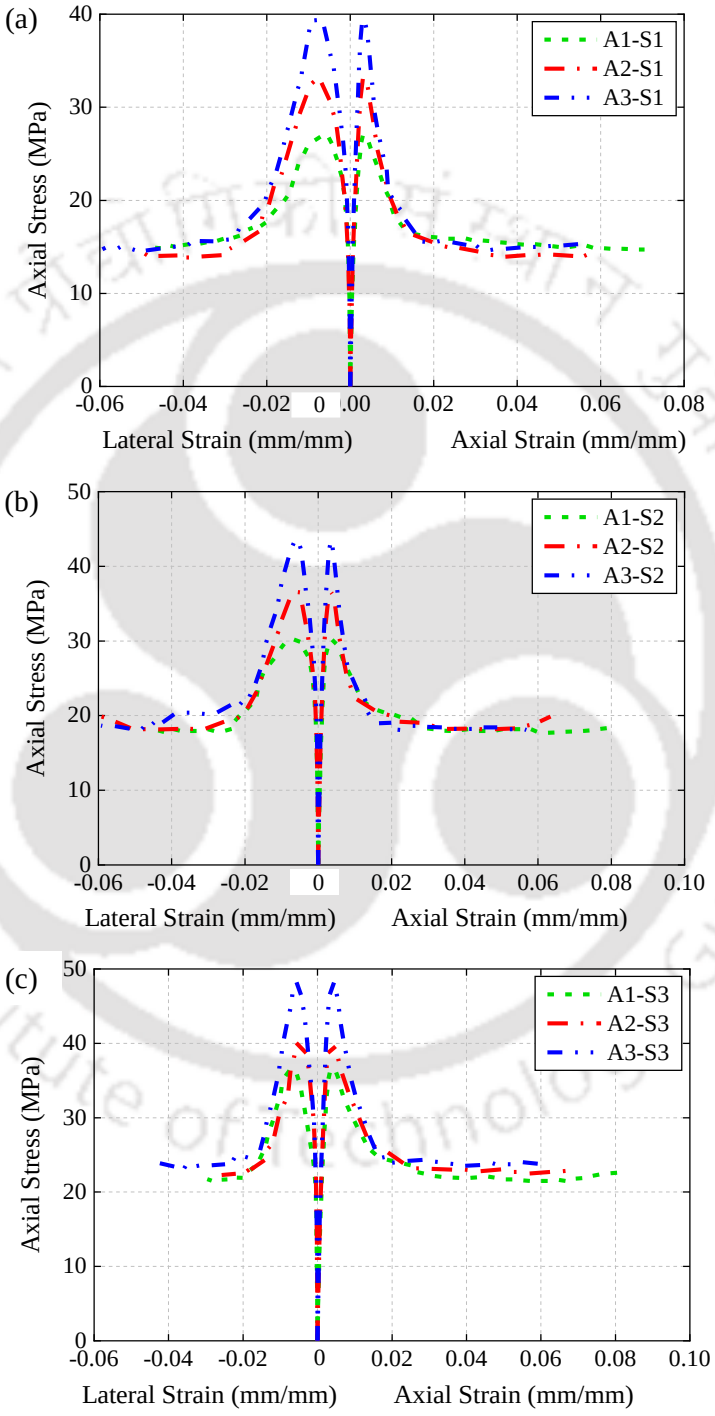

Fig. 4.8. Comparison of stress–axial strain and axial stress-lateral strain relations of Fe-SMA confined concrete for various concrete strengths with the same level of active confining pressure of (a) 1.09 MPa (b) 1.76 MPa and (c) 2.44 MPa

4.3.3. Comparison of average active, passive and total confining pressure at transition point

The lateral strains of all the Fe-SMA confined specimens were found at the transition point, which corresponds to 2.5% axial strain. Corresponding axial stresses in the Fe-SMA strips, obtained from Fig. 3.4, were then substituted in Eq. (4.1) for evaluation of average passive confining pressures for each specimen. The confinement effect of Fe-SMA–confined concrete is a combination of actively and passively confined concrete. Hence, determining the contribution of active confining pressure to the total confining pressure acting on each test specimen is crucial. Total confining pressure is given as the sum total of the average active and passive confining pressures. The ratio of active to total confining pressure is plotted against active confinement pressure values for each specimen in Fig. 4.9.

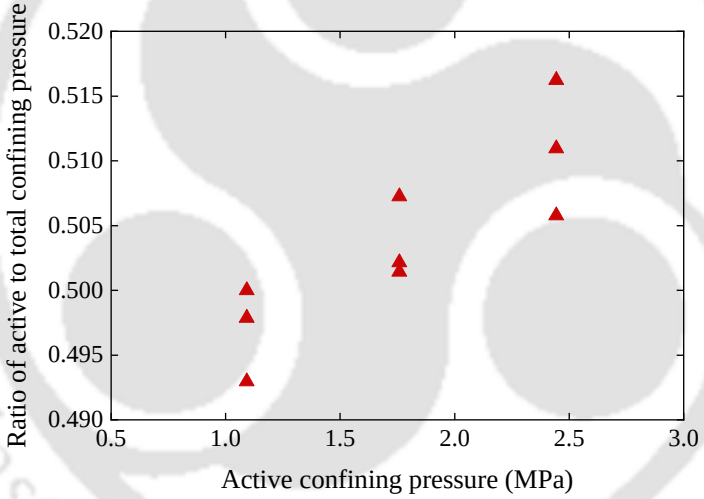

Fig. 4.9. Comparison of ratio of active to total confining pressure for Fe-SMA confined concrete specimens

From the figure, it may be observed that the contribution of active confining pressure to the total confining pressure of all the Fe-SMA confined specimens ranges from 0.49 to 0.52. Additionally, this ratio marginally increases with an increase in the active confinement values. This is in contrary to the ratios reported for NiTiNb-SMA confined concrete specimens wherein the values ranges from 0.67 to 0.81 (Chen & Andrawes, 2017). As discussed earlier, active confining pressure is a function of the recovery stress generated in the SMAs during thermal activation. High recovery stresses of around 600 MPa are developed in the NiTiNb-SMA wires during activation, which led to a higher contribution

of active confining pressure to the total confining pressure acting on concrete specimens as compared to that of Fe-SMA strips with recovery stresses of around 350 MPa.

4.3.4. Relationship between axial and lateral strain

Confinement of concrete improves its strength and ductility by effectively delaying lateral dilation. For unconfined concrete, the Poisson's ratio is typically used to represent the axial-lateral strain relation. Its value varies from 0.15 to 0.2 till concrete attains around 70% of its peak stress, after which it rises drastically till failure (Mirmiran & Shahawy, 1997). Poisson's ratio may be classified as secant and tangent variants owing to the nonlinearity of the stress-strain curves of concrete. Elwi and Murray (1979) demonstrated that the values of both the variants are in the similar range. In the case of confined concrete, the same axial–lateral strain relationship is represented by a dilation ratio (Chen & Andrawes, 2017). This study utilizes a dilation ratio based on the secant poison's ratio to evaluate the dilation characteristics of Fe-SMA confined concrete.

Fig. 4.10 illustrates the relationship between the measured secant dilation ratio and the normalised axial strain, which is defined as the ratio of axial strain and axial strain at peak stress of unconfined concrete. The active confinement ratio, $f_{l,active} / f'_{co}$, is shown in the legend for each test specimen.

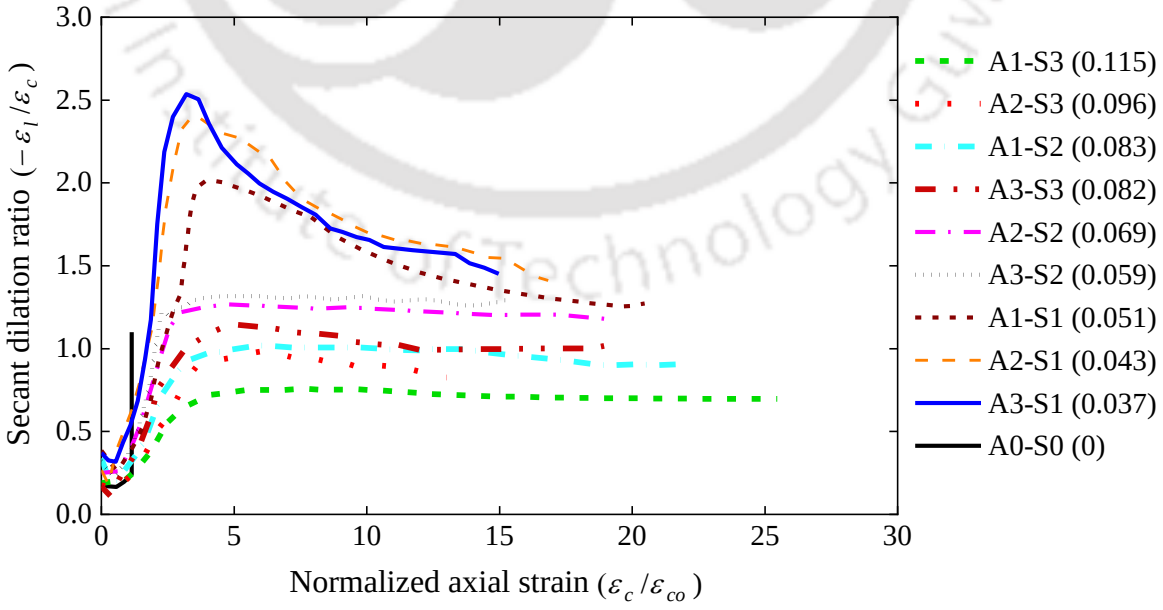

Fig. 4.10. Dilation ratio of Fe-SMA–confined concrete vs. normalized axial strain

It can be observed that the confined as well as unconfined concrete test specimens displayed a similar dilation ratio at the initial stages of loading. With an increase in the loading intensity, the dilation ratio increases to a maximum value, after which it decreases and reaches a stable value. At this stage, the concrete is solely dependent on the Fe-SMA strips to hold it in place. In the case of specimens with lower active confinement ratios, the slope of the ascending branch of the curve was steeper, indicating accelerated dilatation. Furthermore, there was a substantial decrease in the peak dilation ratio from 2.54 (Specimen A3-S1) to 0.76 (Specimen A1-S3) as the corresponding active confinement ratio was increased from 0.037 to 0.115 respectively. The peak dilation ratio of specimens with lower active confinement ratios decreased to an asymptotic value at a faster rate which indicated that the Fe-SMA strips were ineffective in controlling the dilation. However, the decrease in dilation ratio was more gradual in case of specimens with higher confinement ratios, and also exhibited an increase in normalised axial strain.

4.4. Empirical model to predict stress–strain behaviour of Fe-SMA-confined concrete

Developing an appropriate constitutive model for Fe-SMA-confined concrete depends on the accuracy with which the intrinsic features of the stress-strain curve such as peak stress, ultimate stress and corresponding strains and residual stress are predicted. Figs. 4.11(a,b) shows the variation of the normalized peak axial stress, f'_{cc}/f'_{co} and normalized peak axial strain, $\varepsilon'_{cc}/\varepsilon_{co}$ with the active confinement ratio, $f_{l,active}/f'_{co}$, which is a measure of the level of confinement in the concrete cylinders. To predict the peak axial stress and corresponding axial strain of Fe-SMA confined concrete, linear regression analyses were carried out and the following empirical equations are proposed with *R*-square values of 0.80 and 0.96 respectively:

$$f'_{cc} = f'_{co}\left(1+6.11\frac{f_{l,active}}{f'_{co}}\right) \tag{4.2}$$

$$\varepsilon'_{cc} = \varepsilon_{co}\left(1+17.6\frac{f_{l,active}}{f'_{co}}\right) \tag{4.3}$$

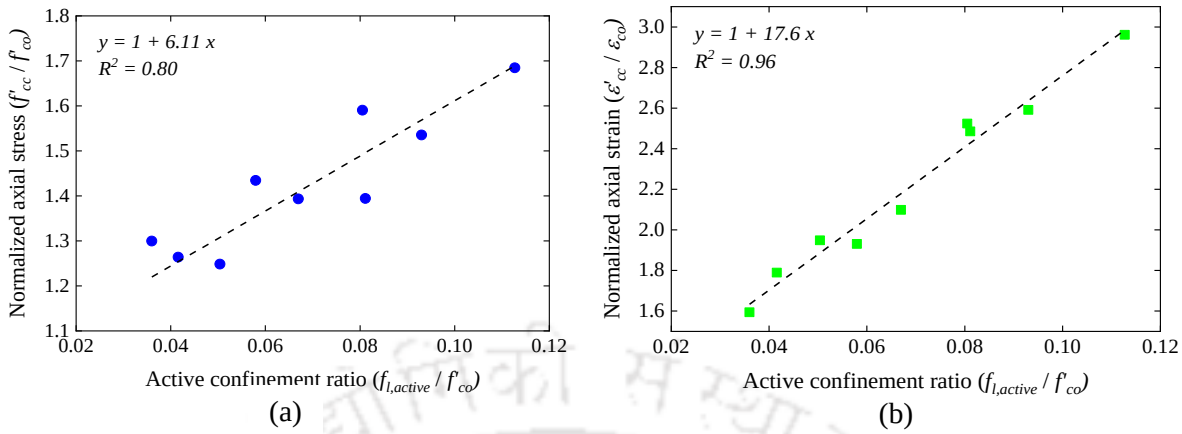

Fig. 4.11. Proposed model for (a) peak axial stress (b) strain corresponding to peak axial stress

It has been shown earlier (Fig. 4.8) that the residual and ultimate stresses of the test specimens depend only on the active confining pressure acting on it. Hence, the variation f_{res} and f_{ult} of test specimens with respect to the active confining pressure is plotted in Fig. 4.12 (a,b). From the experimental results, it can be observed that both f_{res} and f_{ult} increases linearly with an increase in the active confining pressure of the test specimens. Using linear regression analyses, the following equations are proposed for Fe-SMA confined concrete with *R*-square values of 0.98 and 0.97 respectively:

$$f_{res} = 6.07\, f_{l,active} + 8.76 \tag{4.4}$$

$$f_{ult} = 6.17\, f_{l,active} + 8.05 \tag{4.5}$$

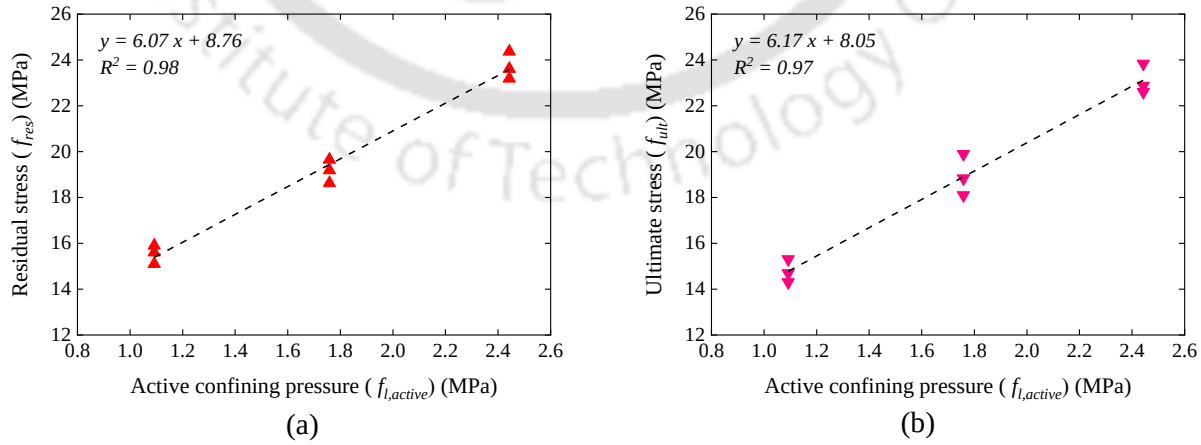

Fig. 4.12. Proposed model for (a) residual stress (b) ultimate stress

Active confinement using SMAs has the ability to significantly increase the ultimate strain of concrete. A previous study by Chen and Andrawes (2017) on NiTiNb-confined concrete has shown that ultimate strain is a function of strength degradation of SMA-confined concrete, which is defined as the difference between its peak strength and residual strength. Hence, after a thorough evaluation of the experimental results the variation of the ultimate strain with respect to the ratio of residual stress and peak axial stress, is plotted in Fig. 4.13. Regression analysis was carried out and the following equation was proposed for Fe-SMA confined concrete with an *R*-square value of 0.96:

$$\varepsilon_{ult} = 0.0294e^{1.51\left(\frac{f_{res}}{f'_{cc}}\right)} \tag{4.6}$$

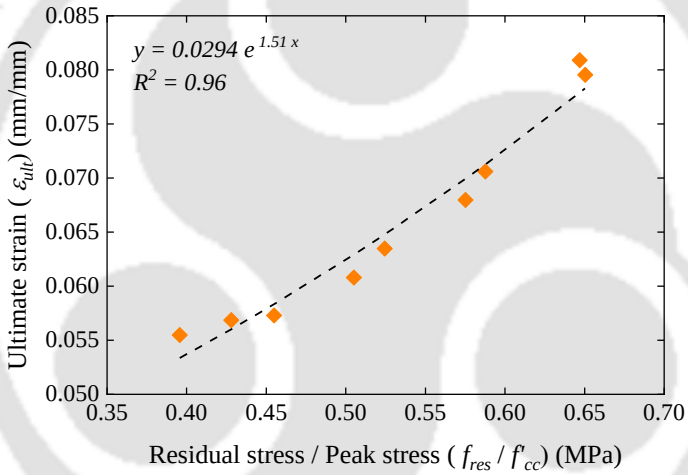

Fig. 4.13. Proposed model for ultimate strain

The stress-strain relation of Fe-SMA confined concrete under compression, as observed earlier, comprises of an ascending portion, a descending portion and a stress plateau portion. Previous researchers (Chen & Andrawes, 2017) have found that Tsai's (1988) empirical equation was capable of accurately capturing the ascending as well as descending portions of the stress-strain curves of confined concrete. In order to capture the ascending or descending behaviour of the stress-strain curve, there are two parameters in this model, which can be refined to improve its accuracy. Hence, in this study, an empirical stress-strain model based on Tsai's (1988) equation (Eq. 4.7) is used, to characterize the ascending and descending portions of the stress-strain relationship through curve fitting, as:

$$Y = \frac{pX}{1 + \left(p - \frac{q}{q-1} \right) X + \frac{X^q}{q-1}} \tag{4.7}$$

where, Y = normalised axial stress, f_c/f'_{cc}; X = normalised axial strain, $\varepsilon_c/\varepsilon'_{cc}$; parameter $p = \partial Y/\partial X = E_0 / E_{sec}$, controls the gradient of the ascending slope; $E_0 = 5000\sqrt{f'_{co}}$ (MPa); $E_{sec} = f'_{cc}/\varepsilon'_{cc}$; parameter q, which is a function of concrete strength, controls the gradient of the descending slope of the stress-strain relation and is obtained from experimental data through regression analysis with an R-square value of 0.85 as:

$$q = 0.0578 f'_{c0} + 0.5577 \tag{4.8}$$

From the stress-plateau portion of the experimental stress-strain curve, it can be observed that the stress and strain exhibit an almost linear variation until failure. Thus, this portion can be defined in such a way that after the transition point is reached, axial stress and axial strain varies linearly until the ultimate strain is reached. Fig. 4.14 (a-i) compares the stress-strain relationship obtained from the experimental results with those from the empirical model proposed in this study.

It can be observed that the empirical model is able to closely capture peak stress and corresponding strain, residual stress, ultimate stress and corresponding strain. stress and corresponding strain, residual stress, ultimate stress and corresponding strain. From the perspective of practical implementation, active confinement of columns using Fe-SMA involves its fixation on concrete columns with internal steel reinforcement both in the longitudinal as well as lateral direction. Hence, development of an empirical stress-strain model which is capable of capturing the combined effect of internal steel and external Fe-SMA confinement is of utmost importance.

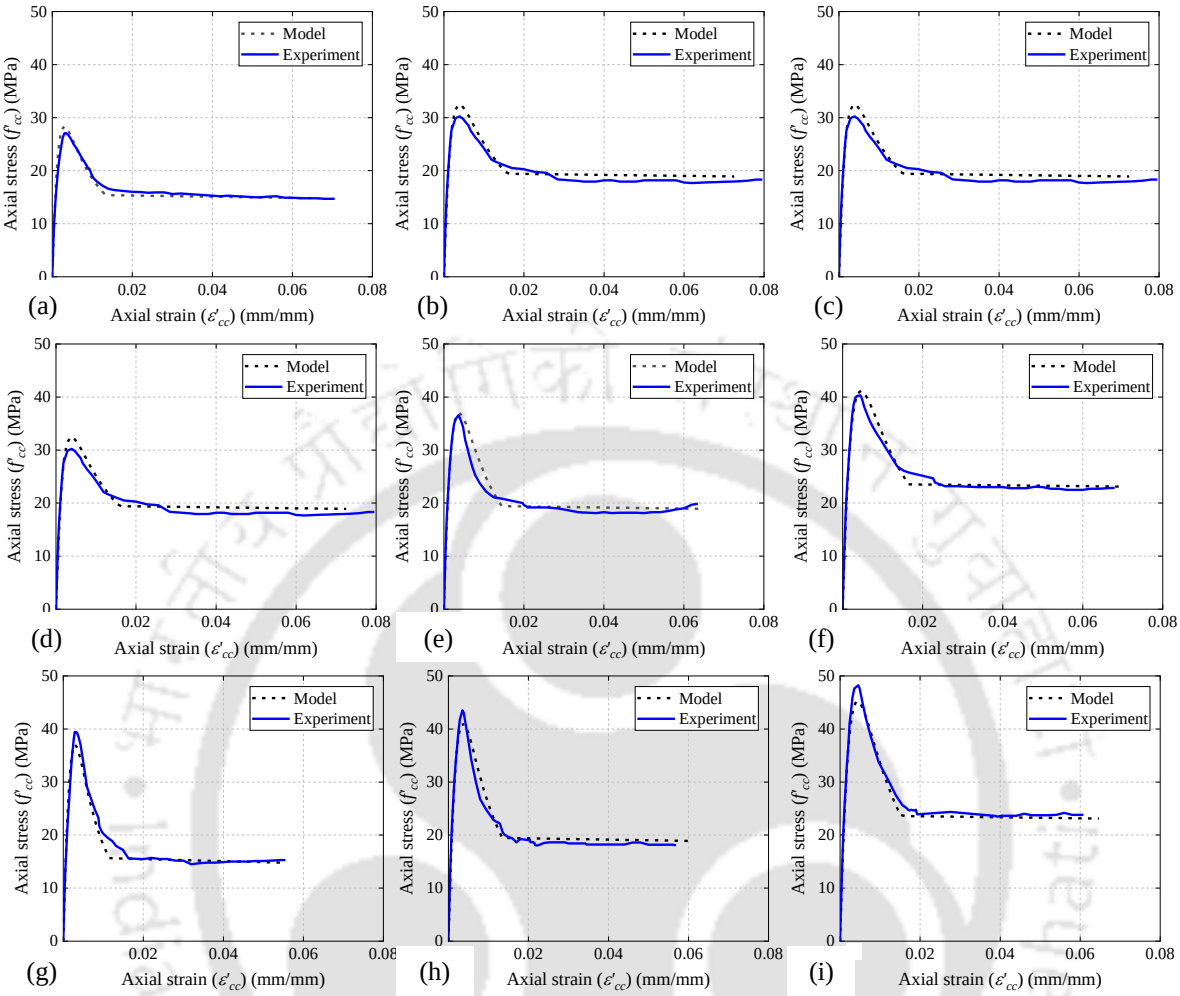

Fig. 4.14. Comparison of axial stress–strain relation of Fe-SMA confined cylinders from experimental results and proposed empirical model: (a) A1-S1; (b) A1-S2; (c) A1-S3; (d) A2-S1; (e) A2-S2; (f) A2-S3; (g) A3-S1; (h) A3-S2; (i) A3-S3

4.5. Numerical approach

For the development of a stress-strain model that can take into account the combined behaviour of internal steel and exterior Fe-SMA confinement when test measurements are unknown, finite element analyses (FEA) proves to be one of the most cost-effective tools. Nonlinear finite element models, on the other hand, are inherently complicated owing to the use of different theories proposed by different researchers for modelling of materials, selecting elements and solution techniques. Hence, a three-step procedure was adopted in order to minimize the uncertainties that may arise while developing the stress-strain model:

(1) Parameters of material models of unconfined concrete and internal steel reinforcement were chosen to accurately evaluate the response of reinforced concrete columns.

(2) The validated material model of unconfined concrete was adopted in combination with the material model of Fe-SMA strips, based on experimental investigation, to simulate the axial stress-strain response of plain concrete confined with Fe-SMA strips. Comparison of the numerical results is carried out with experimental results, as presented in Section 5.2, for validation of the FE model.

(3) Subsequently, both the validated FE models were integrated to establish the axial stress-strain relationship for Fe-SMA confined RC specimens under monotonic compressive loading.

This study used a three-dimensional (3D) nonlinear finite-element software ABAQUS/CAE 6.20, for modelling concrete columns with internal longitudinal and transverse reinforcement and external Fe-SMA strip reinforcement.

4.5.1. Material models

Constitutive models of the materials adopted in the finite element analysis of the test specimen are presented in the following sub-sections.

4.5.1.1. Concrete

In the present study, Concrete damaged plasticity (CDP) model available in ABAQUS was utilized to predict the inelastic behaviour of concrete using the concepts of isotropic damage elasticity as well as isotropic tensile and compressive plasticity. The yield surface corresponding to the Mohr-Coulomb criteria on the deviatoric plane was adopted in this study through a shape factor parameter K_c = 0.667. Based on the experimental results reported by (Kupfer *et al.*, 1969), a value of 1.16 was adopted for the stress-ratio parameter in the present study. The dilation angle was considered as 32° and the default value of flow potential (e = 0.1) was selected so that concrete has almost the same dilation angle for a wide range of confining stress. The viscosity parameter was adopted as 0.0001 to avoid convergence issues, while ensuring reliable results. In this model, damage mechanism is

represented by tensile cracking and compressive crushing. Both the cracking and crushing behaviour of concrete were defined using damage variables d_t and d_c, which ranges from 0 to 1 (0 corresponds to undamaged state; 1 corresponds to a complete loss of strength), to model the degradation of strength and stiffness.

To model the behaviour of concrete under compression, the axial stress-strain model of unconfined concrete as proposed by Mander *et al.* (1988) was used. Longitudinal and lateral steel reinforcements were modelled separately. The confinement effect of steel stirrups on the concrete in terms of increase in strength as well as ductility was automatically captured by the 3D FE model. In the elastic range, the stress-strain behaviour of concrete was defined using two parameters, i.e., Young's modulus and Poisson's ratio. Beyond this, the stress-strain behaviour was defined in terms of yield stress (compressive stress) versus inelastic strains. Fig. 4.15(a) shows the compressive behaviour of concrete. To model the tensile behaviour of concrete, a linear elastic stress-strain relationship was considered in the pre-cracking stage. The tensile strength was defined as per IS 456 . Tension stiffening was accounted for in the computational model by defining a softening branch in the tensile stress-strain curve of concrete. Fig. 4.15(b) shows the tensile behaviour of concrete. The damage parameter of concrete under uniaxial compression and tension were defined as per Yu *et al.* (2010).

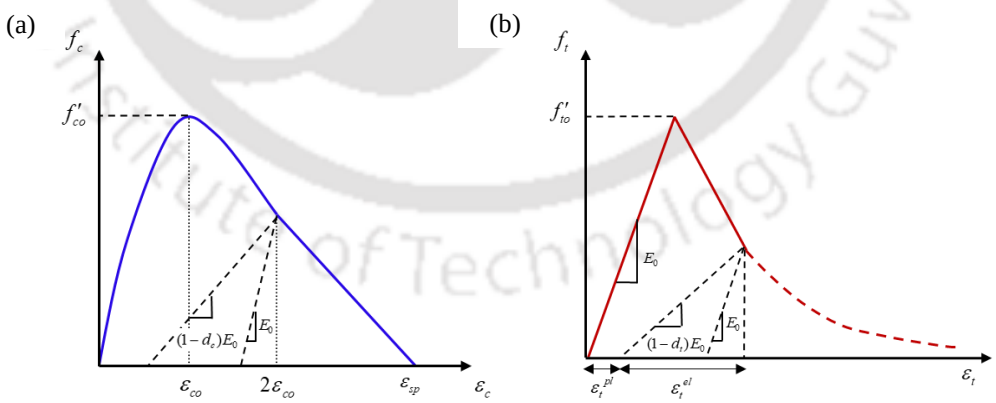

Fig. 4.15. Material models of concrete in (a) compression; (b) tension

4.5.1.2. Steel reinforcements and Fe-SMA strips

For simulating the material behaviour of longitudinal and transverse steel reinforcements, an isotropic hardening plasticity model was adopted. The uniaxial stress-strain relation in

the elastic range is defined using Young's modulus and Poisson's ratio as 200 GPa and 0.3 respectively. The plastic behaviour was defined by yield stress and corresponding plastic strain in a tabular form. A simple bilinear elasto-plastic stress-strain curve was used in this study, as shown in Fig. 4.16.

An isotropic hardening plasticity model was adopted for representing the material behaviour of the Fe-SMA strips. The stress-strain curve of the Fe-SMA coupon specimen after thermal activation (Fig. 3.4) as obtained from the tensile test specified in Section 3 was assigned to the Fe-SMA strips in the FE model. Hence, the stress-strain curve starts at the point of recovery stress at the beginning of loading after which it follows the stress-strain curve as shown in Fig. 3.4.

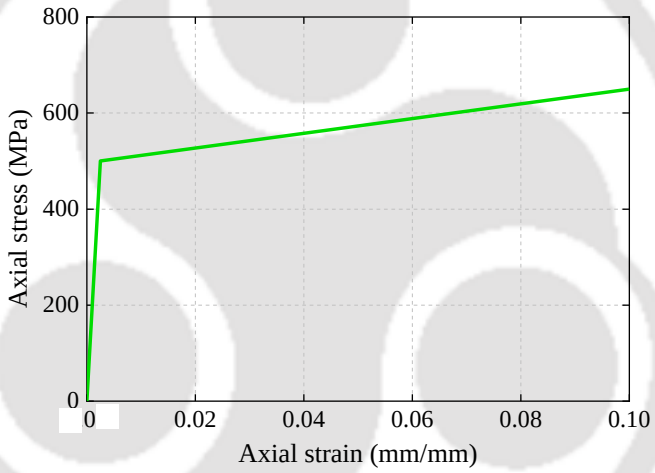

Fig. 4.16. Material model for steel reinforcements

4.5.2. Geometry of specimens and nomenclature

A total of 57 numerical simulations involving circular concrete columns subjected to uniaxial compressive loading were performed using ABAQUS. The diameter and height of the circular concrete columns was taken as 300 mm and 900 mm respectively, an aspect ratio of 3:1. These columns were divided into three groups, as shown in Fig. 4.17, based on the presence of internal steel reinforcement and/or external Fe-SMA strips:

1. Group 1 (AX-RY) – columns with internal longitudinal and transverse steel reinforcements only (3 columns).

2. Group 2 (AX-SZ) – columns with Fe-SMA confinement only (9 columns). Active confinement ratios same as that considered in the experimental study for validation of test results.

3. Group 3 (AX-RY-SZ) – columns with both internal steel and external Fe-SMA reinforcements (45 columns).

Here, X–denotes the three variants (1-3) having unconfined concrete strength, f'_{co}, with values- 21.7 MPa, 26.3 MPa and 30.3 MPa respectively. Y–denotes the five variants (1-5) of internal transverse reinforcement ratio, ρ_s, with values- 1.31%, 1.53%, 1.74%, 2.01% and 2.61% and corresponding to 100 mm, 85 mm, 75 mm, 65 mm and 50 mm respectively. The spacing of transverse reinforcement adopted in this study were in accordance with the provisions of IS-13920:2016. Z–denotes the three variants (1-3) of active confining pressure levels, $f_{l,active}$, with values- 1.09 MPa, 1.76 MPa and 2.44 MPa respectively. The longitudinal reinforcement in all the columns of Group 1 & 3 consisted of 6 nos. of 16 mm dia. bars, which resulted in a longitudinal reinforcement ratio, ρ_{cc}, of 1.7% based on gross area. The lateral reinforcement had a diameter of 10 mm in all the columns and the dimensions of Fe-SMA strips were 24 mm × 1.5 mm.

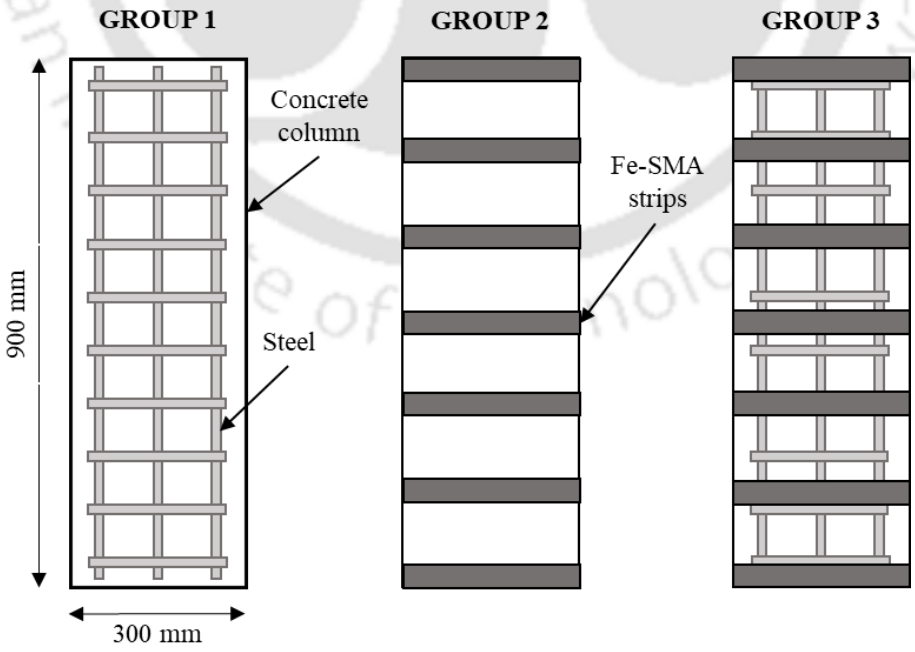

Fig. 4.17. Specimen groups for 3D-FE simulations

4.5.3. Types of elements used in FE analyses and meshing

Three element types, namely, C3D8R, B31 and T3D2 were utilized for development of all the FE models. The concrete was modelled using continuum eight-node linear brick elements with reduced integration and hourglass control (C3D8R). The internal longitudinal and transverse reinforcements were modelled using two-nodded linear truss elements (T3D2). The Fe-SMA strips were modelled using the two-node Timoshenko beam elements (B31) with linear interpolation (Abouali *et al.*, 2019). A set of mesh sensitivity analyses were carried out to arrive at an optimum mesh density for both accuracy as well as computational efficiency. The dimensions of C3D8, T3D2 and B31 elements were 20 mm, 15 mm and 10 mm respectively.

4.5.4. Boundary conditions

The base of the column was fixed using the "encastre" boundary condition as shown in Fig. 4.18. The lateral and longitudinal reinforcement was embedded in the concrete column by applying the "embedded region" constraint. Effect of bond-slip in the steel-concrete interface was approximately accounted for by the tension stiffening effect of concrete after cracking as shown in Fig. 4.15(b) (Liang & Sritharan, 2018). The Fe-SMA strips were tied to the surface of the concrete cylinders using a tie constraint, which allowed complete transfer of load between the two.

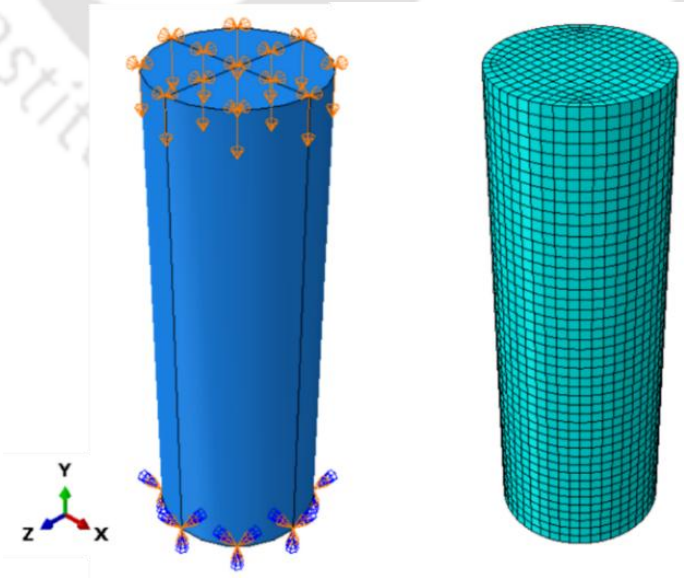

Fig. 4.18. Finite element model of a typical column specimen (a) boundary conditions (b) meshing

4.5.5. Modelling of prestressing effect in Fe-SMA strips

Activation of the Fe-SMA strips was achieved by applying a prestress along its length to simulate the recovery stress generated in it during thermal activation. The Fe-SMA strips were assigned an initial stress equivalent to its recovery stress in the initial step in ABAQUS. After this, another step was defined without any loading to facilitate redistribution of the initial stress for attainment of force equilibrium in the whole model as reported by Abouali *et al.* (2019).

4.5.6. Loading

The columns were subjected to displacement-controlled loads by assigning a uniform compressive displacement at the top surface of the concrete section. An implicit static analysis procedure was utilised for obtaining the nonlinear response. An automatic time-incrementation scheme was selected to improve the rate of convergence of the solution.

4.6. Results and discussion

The following subsections present results of the 57 numerical simulations involving three groups of circular concrete columns subjected to uniaxial compressive loading performed using ABAQUS.

4.6.1. Validation of numerical model of RC column

Three concrete specimens, A1-R3, A2-R3 and A3-R3 with variable unconfined compressive strengths 21.7 MPa, 26.3 MPa and 30.3 MPa respectively and a constant internal transverse reinforcement ratio of 1.74% corresponding to 75 mm stirrup spacing was considered in this study. Fig. 4.19 (a-c) shows the comparison of the axial stress-strain response of three specimens obtained from FE simulation and those derived from the model proposed by Mander *et al.* (1988). The confined concrete stress-strain behaviour obtained from FE matched accurately with that of the Mander's model. Hence, it established that the modelling technique and the material models adopted in the FE simulation accurately captured the confinement effect both in terms of increased strength as well as ductility of concrete.

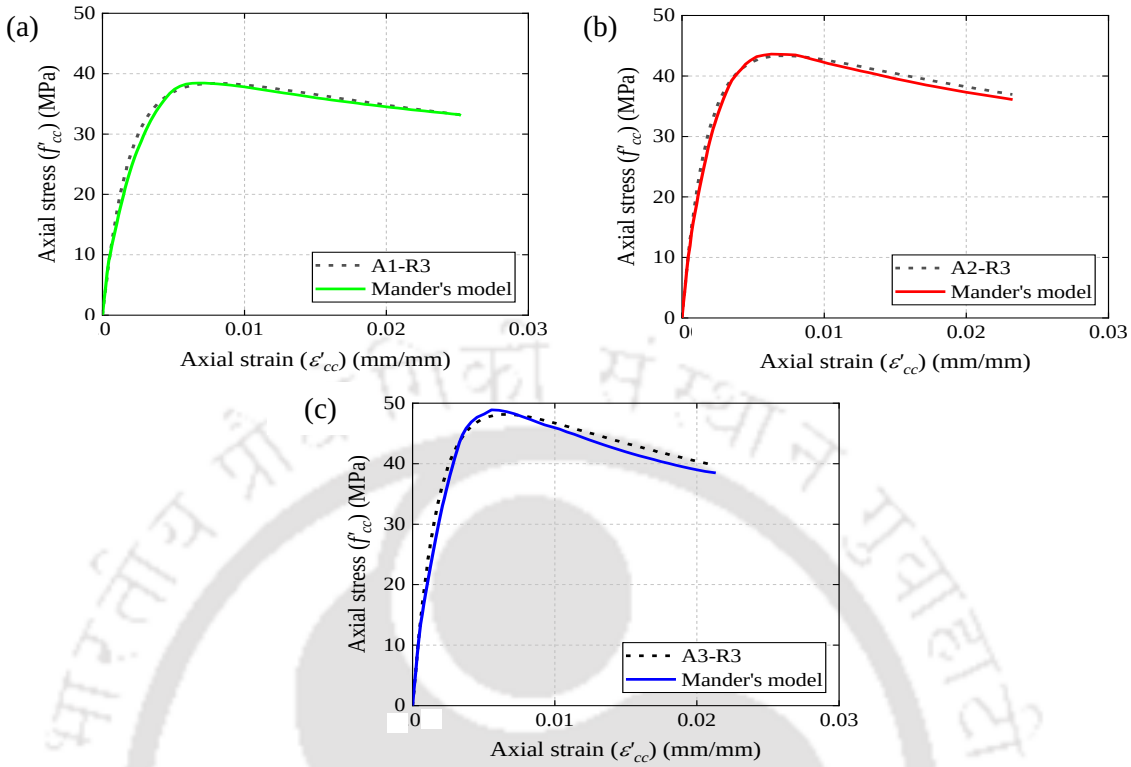

Fig. 4.19. Comparisons of axial stress-strain responses of concrete columns obtained from FE simulations with those from Mander *et al.*'s model (1988): (a) A1-R1; (b) A2-R1; and (c) A3-R1.

4.6.2. Validation of FE-model of plain concrete column confined by Fe-SMA strips

Results obtained from numerical simulation of the Fe-SMA-confined concrete columns subjected to uniaxial compression are compared with those recorded during experiments. Fig. 4.20 shows the comparison of a typical axial stress-strain response of an Fe-SMA-confined concrete column obtained from experiment with that derived from finite element simulation and proposed empirical model. Table 4.3 summarizes the values of the intrinsic features of the stress-strain curves for all the specimens.

Error percentage corresponding to peak stress, strain at peak stress, residual stress and ultimate stress were calculated to examine the accuracy of the FE-model. It can be observed that the maximum error in predicting each of the above parameters was less than 7.3%. Thus, the values obtained from numerical analysis and experiments are in reasonably good agreement. Hence, the FE- model adopted in this study may be considered acceptable

for studying the combined effect of internal steel and external Fe-SMA confinement of concrete under compression.

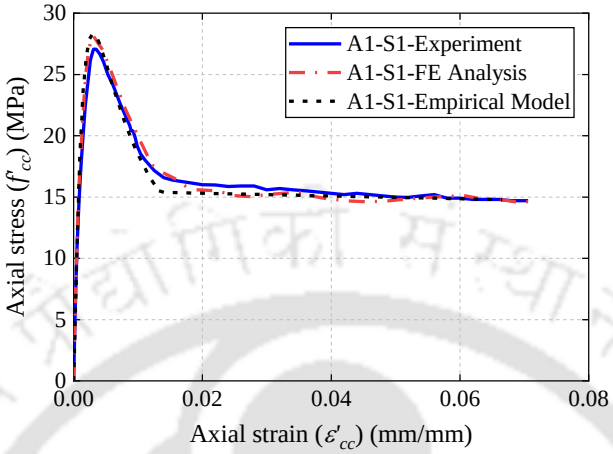

Fig. 4.20. Comparisons of experimental axial stress-strain response of specimen A1-S1 with that obtained from FE simulation and proposed empirical model.

Table 4.3. Comparison of parameters of axial stress-strain responses of concrete columns obtained from FE simulations with those from experiments

Specimen ID	f'_{cc} (MPa)			ε'_{cc} (mm/mm)			f_{res} (MPa)			f_{ult} (MPa)		
	Exp	*FE*	*Error (%)*	*Exp*	*FE*	*Error (%)*	*Exp*	*FE*	*Error (%)*	*Exp*	*FE*	*Error (%)*
A1-S1	27.1	28.2	4.06	0.0032	0.0033	3.13	15.9	15.2	4.4	14.7	14.7	0
A2-S1	33.2	32.3	2.71	0.0031	0.0031	0	15.1	15.4	1.99	14.3	14.9	4.2
A3-S1	39.5	37	6.33	0.0029	0.0031	6.9	15.6	16	2.56	15.3	14.9	2.61
A1-S2	30.3	32.5	7.26	0.004	0.0039	2.5	19.7	19.9	1.02	18.9	18.7	1.06
A2-S2	36.6	37	1.09	0.0037	0.0038	2.7	19.2	19.6	2.08	19.9	19	4.52
A3-S2	43.6	40.9	6.19	0.0035	0.0037	5.71	18.7	20	6.95	18.1	19.2	6.08
A1-S3	36.6	36.9	0.82	0.0048	0.0047	2.08	23.7	24	1.27	22.6	23.6	4.42
A2-S3	40.4	41.3	2.23	0.0045	0.0046	2.22	23.2	24.3	4.74	22.9	23.4	2.18
A3-S3	48.3	45.5	5.8	0.0046	0.0043	6.52	24.4	24.8	1.64	23.9	23.4	2.09

4.6.3. FE results of Fe-SMA-confined reinforced concrete columns

Fig. 4.21 shows a typical axial stress-strain response of an Fe-SMA-confined concrete column obtained from finite element simulation. Table 4 lists the values of the parameters: f'_{cc}, ε'_{cc}, f_{res}, f_{ult} and ε_{ult} of the stress-strain curves of nine specimens with internal steel spacing R1. Similarly, parameters were also obtained for all the other specimens adopted in this study.

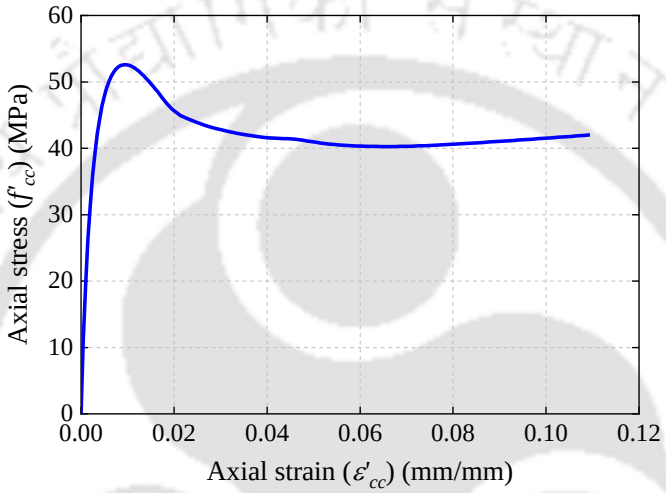

Fig. 4.21. Axial stress-strain response of specimen A1-R1-S1 obtained from FEA

The stress-strain behaviour of Fe-SMA confined RC, similar to Fe-SMA concrete, is observed to contain an ascending portion, a descending portion and a stress plateau portion. However, few specimens exhibited weak hardening, which was also noticed in the experimental stress-strain response of Fe-SMA confined concrete (Fig. 4.8). Similar weak hardening behaviour was also observed for NiTiNb-SMA confined concrete (Chen & Andrawes, 2017). A considerable decrease in the rate of convergence was observed at failure, due to highly non-linear structural response (Abouali *et al.* 2019).

Table 4.4 lists the values of the parameters: peak axial stress, corresponding axial strain, residual stress, ultimate stress and ultimate strain of the stress-strain curves of all the 45 Fe-SMA confined RC specimens adopted in this study.

Table 4.4. Parameters of axial stress-strain responses of Fe-SMA confined RC columns obtained from FE simulations

S. No.	Specimen ID	f'_{co} (MPa)	ε_{co} (mm/mm)	$f_{l,SMA}$ (MPa)	$f_{l,s}$ (MPa)	f'_{cc} (MPa)	ε'_{cc} (mm/mm)	f_{res} (MPa)	f_{ult} (MPa)	ε_{ult} (mm/mm)
1	**A1-R1-S1**	21.7	0.0016	1.09	2.21	44.33	0.008	36.25	36.74	0.106
2	**A2-R1-S1**	26.3	0.0017	1.09	2.21	48.18	0.008	36.39	36.1	0.089
3	**A3-R1-S1**	30.3	0.0018	1.09	2.21	54.21	0.007	36.49	35.85	0.072
4	**A1-R1-S2**	21.7	0.0016	1.76	2.21	48.85	0.01	41.19	41.87	0.114
5	**A2-R1-S2**	26.3	0.0017	1.76	2.21	52.6	0.009	41.7	42.02	0.098
6	**A3-R1-S2**	30.3	0.0018	1.76	2.21	58.82	0.009	41.37	41.51	0.077
7	**A1-R1-S3**	21.7	0.0016	2.44	2.21	54.21	0.011	46.39	47.46	0.118
8	**A2-R1-S3**	26.3	0.0017	2.44	2.21	58.09	0.01	46.64	47.42	0.101
9	**A3-R1-S3**	30.3	0.0018	2.44	2.21	63.88	0.009	46.61	47.15	0.083
10	**A1-R2-S1**	21.7	0.0016	1.09	2.79	46.27	0.009	38.16	39	0.108
11	**A2-R2-S1**	26.3	0.0017	1.09	2.79	49.64	0.008	38.02	38.59	0.091
12	**A3-R2-S1**	30.3	0.0018	1.09	2.79	55.99	0.008	38.16	37.91	0.073
13	**A1-R2-S2**	21.7	0.0016	1.76	2.79	50.99	0.011	43.6	44.33	0.118
14	**A2-R2-S2**	26.3	0.0017	1.76	2.79	54.34	0.01	43.36	43.39	0.1
15	**A3-R2-S2**	30.3	0.0018	1.76	2.79	61.18	0.009	43.5	44.07	0.079
16	**A1-R2-S3**	21.7	0.0016	2.44	2.79	55.74	0.012	48.36	49.64	0.123
17	**A2-R2-S3**	26.3	0.0017	2.44	2.79	59.16	0.011	48.09	49.11	0.104
18	**A3-R2-S3**	30.3	0.0018	2.44	2.79	65.78	0.011	48.71	49.68	0.085

19	**A1-R3-S1**	21.7	0.0016	1.09	3.32	47.92	0.01	39.83	40.63	0.11
20	**A2-R3-S1**	26.3	0.0017	1.09	3.32	51.09	0.009	40.11	40.42	0.096
21	**A3-R3-S1**	30.3	0.0018	1.09	3.32	57.75	0.008	40.03	39.69	0.075
22	**A1-R3-S2**	21.7	0.0016	1.76	3.32	52.77	0.012	45.18	46.07	0.119
23	**A2-R3-S2**	26.3	0.0017	1.76	3.32	55.96	0.011	45.11	46.03	0.102
24	**A3-R3-S2**	30.3	0.0018	1.76	3.32	62.38	0.01	45.36	45.44	0.082
25	**A1-R3-S3**	21.7	0.0016	2.44	3.32	56.99	0.014	50.2	50.93	0.128
26	**A2-R3-S3**	26.3	0.0017	2.44	3.32	60.17	0.013	50.66	51.16	0.114
27	**A3-R3-S3**	30.3	0.0018	2.44	3.32	66.92	0.012	50.87	51.3	0.09
28	**A1-R4-S1**	21.7	0.0016	1.09	4.01	50.92	0.011	42.98	42.87	0.114
29	**A2-R4-S1**	26.3	0.0017	1.09	4.01	54.06	0.01	43.18	42.27	0.1
30	**A3-R4-S1**	30.3	0.0018	1.09	4.01	60.09	0.009	42.54	41.82	0.078
31	**A1-R4-S2**	21.7	0.0016	1.76	4.01	54.68	0.013	47.66	48.29	0.124
32	**A2-R4-S2**	26.3	0.0017	1.76	4.01	57.66	0.012	47.82	47.74	0.109
33	**A3-R4-S2**	30.3	0.0018	1.76	4.01	64.12	0.011	47.77	47.6	0.086
34	**A1-R4-S3**	21.7	0.0016	2.44	4.01	59.09	0.015	52.53	53.24	0.131
35	**A2-R4-S3**	26.3	0.0017	2.44	4.01	62.17	0.014	52.5	53.2	0.114
36	**A3-R4-S3**	30.3	0.0018	2.44	4.01	68.43	0.013	52.94	53.36	0.093
37	**A1-R5-S1**	21.7	0.0016	1.09	5.58	54.82	0.013	47.82	47.74	0.125
38	**A2-R5-S1**	26.3	0.0017	1.09	5.58	57.6	0.012	48.12	47.38	0.111
39	**A3-R5-S1**	30.3	0.0018	1.09	5.58	63.41	0.011	47.73	46.94	0.088
40	**A1-R5-S2**	21.7	0.0016	1.76	5.58	59.45	0.015	52.79	53.18	0.131

41	**A2-R5-S2**	26.3	0.0017	1.76	5.58	62.37	0.014	53.14	52.96	0.117
42	**A3-R5-S2**	30.3	0.0018	1.76	5.58	68.24	0.013	52.46	52.54	0.092
43	**A1-R5-S3**	21.7	0.0016	2.44	5.58	63.58	0.017	57.67	58.31	0.139
44	**A2-R5-S3**	26.3	0.0017	2.44	5.58	66.46	0.016	57.98	58.15	0.125
45	**A3-R5-S3**	30.3	0.0018	2.44	5.58	72.51	0.014	57.85	57.98	0.1

4.7. Empirical stress–strain model of Fe-SMA-confined reinforced concrete (Model-1)

An empirical stress-strain model for RC columns with Fe-SMA confinement subjected to uniaxial compressive loading is presented in this section. The resulting model combines the stress-strain responses obtained from steel confined concrete determined from Mander *et al.*'s model (1988) and Fe-SMA confined concrete model proposed in Section 4.6.1. It has been established by several researchers (Eid & Paultre, 2007; Eid & Paultre, 2008) that the combined confining pressure of FRP-confined concrete may be approximated to the sum of individual contributions from FRP and the internal steel reinforcement. The same concept is extended in this study to arrive at the total confining pressure of Fe-SMA-confined RC columns as:

$$f_{l,total} = f_{l,s} + f_{l,SMA} \tag{4.9}$$

where, $f_{l,s}$ is the effective confining pressure of internal steel reinforcement (Mander *et al.* 1988) as:

$$f_{l,s} = \frac{2k_e A_{sp} f_{yh}}{sD} \tag{4.10}$$

f_{yh} is the yield strength of steel; $f_{l,SMA}$ is the active confining pressure of Fe-SMA confined concrete, previously defined as $f_{l,active}$ [Eq. (4.1)]. This approximation is appropriate only for cases where the cover thickness is reasonably small (c/D ≤ 0.1) (Eid & Paultre, 2007; Eid & Paultre, 2008).

Ilki *et al.* (2008) proposed equations for determining the peak compressive strength f'_{cc} and corresponding axial strain ε_{cc} of FRP confined RC circular columns, which were composed of individual contributions of FRP jacket and the transverse steel reinforcement (TSR). These expressions have been used for calculation of f'_{cc} and ε_{cc} for Fe-SMA confined RC concrete:

$$\left[\frac{f'_{cc} - f'_{co}}{f'_{co}}\right]_{TOTAL} = \left[\frac{f'_{cc}}{f'_{co}} - 1\right]_{SMA} + \left[\frac{f'_{cc}}{f'_{co}} - 1\right]_{S} \tag{4.11}$$

$$\left[\frac{\varepsilon'_{cc}-\varepsilon_{co}}{\varepsilon_{co}}\right]_{TOTAL}=\left[\frac{\varepsilon'_{cc}}{\varepsilon_{co}}-1\right]_{SMA}+\left[\frac{\varepsilon'_{cc}}{\varepsilon_{co}}-1\right]_{S} \quad (4.12)$$

The enhancements of parameters, f'_{cc}, ε'_{cc}, f_{res}, f_{ult} and $\varepsilon_{ult,}$ by the Fe-SMA confinement are calculated using the empirical equations (Eqs. 4.2-4.3) proposed for Fe-SMA-confined concrete. Similar enhancements by the internal steel confinement are calculated from Mander *et al.*'s model (1988). Eqs. (4.4), (4.5) and (4.6) proposed for calculating f_{res}, f_{ult} and ε_{ult} of Fe-SMA confined concrete are extended here for Fe-SMA confined RC column wherein, $f_{l,active}$ term is replaced by f_{total} (Eq. 4.10). The variation of the parameters, f'_{cc}, ε'_{cc}, f_{res}, f_{ult} and ε_{ult} obtained from the empirical model and that obtained from FE analysis is plotted in Fig. 4.22 (a-e) respectively.

The performance of the models of the above mentioned parameters were assessed using the following indicators: average absolute error (AAE), average ratio (AR), standard deviation (SD) and coefficient of variation (COV). The values of these parameters are shown in the legend for each parameter. It can be observed that the maximum AAE in predicting each of the above-mentioned parameters is less than 12.85%. The AR corresponding to all the parameters is in the range of 0.88-0.96. AR value less than 1 indicates that the predicted empirical parameter underestimates the results obtained from FE analyses. Nevertheless, it can be concluded that the empirical model provides satisfactory predictions for the Fe-SMA confined RC columns.

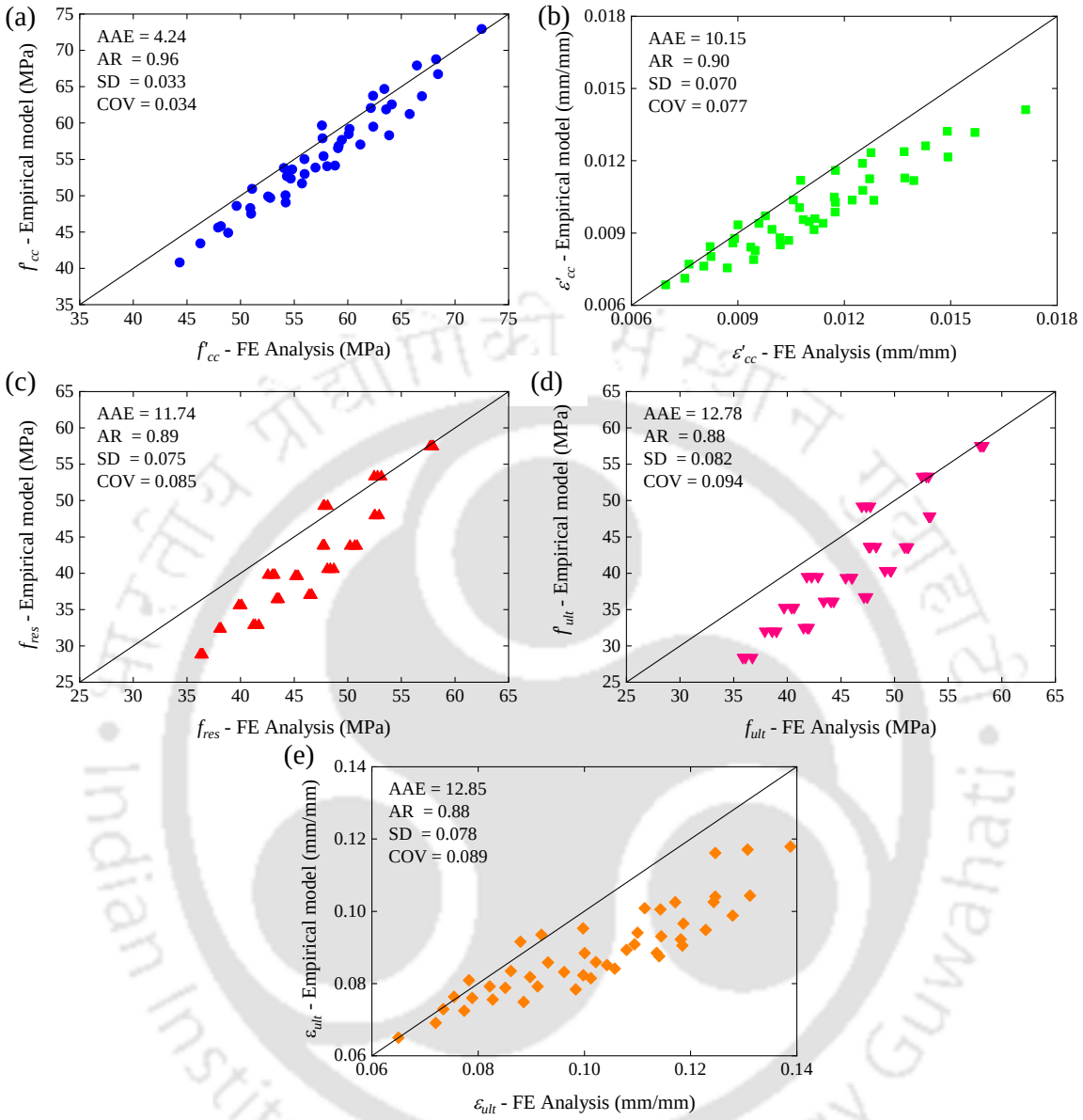

Fig. 4.22. FE Analysis vs. empirical model values for parameters (a) f'_{cc} (b) ε'_{cc} (c) f_{res} (d) f_{ult} and (e) ε_{ult}

4.8. Empirical stress–strain model Fe-SMA-confined RC from results of FE analysis (Model-II):

The empirical model proposed for Fe-SMA confined reinforced concrete by combining the individual responses of steel confined concrete (Mander *et al.* 1988) and Fe-SMA confined concrete (proposed in Section 4.4) provided satisfactory predictions when compared to results obtained from FE simulation. However, to achieve a higher degree of accuracy in

predicting the values of the parameters: peak axial stress, corresponding axial strain, residual stress, ultimate stress and corresponding strain of the stress-strain curves of Fe-SMA confined reinforced concrete, regression analyses were carried out on the FE results of all the 45 specimens adopted in this study.

The following empirical equations are proposed with an *R*-square values of 0.99 as:

$$f'_{cc} = f'_{co}\left(1+9.43\frac{f_{l,SMA}}{f'_{co}}+4.03\frac{f_{l,s}}{f'_{co}}\right) \tag{4.13}$$

$$\varepsilon'_{cc} = \varepsilon_{co}\left(1+39.64\frac{f_{l,SMA}}{f'_{co}}+20.25\frac{f_{l,s}}{f'_{co}}\right) \tag{4.14}$$

$$f_{res} = 7.51 f_{l,SMA} + 3.40 f_{l,s} + 20.69 \tag{4.15}$$

$$f_{ult} = 8.09 f_{l,SMA} + 3.23 f_{l,s} + 20.56 \tag{4.16}$$

$$\varepsilon_{ult} = 0.0105 e^{2.83\left(\frac{f_{res}}{f'_{cc}}\right)} \tag{4.17}$$

The variation of the parameters obtained from the empirical model and that obtained from FE analysis is plotted in Fig. 4.23 (a-e). It can be observed that the maximum AAE in predicting each of the above-mentioned parameters is less than 3.4%. The AR corresponding to all the parameters is 0.99. Additionally, the maximum SD and COV is 0.041 and 0.040 respectively. Hence, it can be concluded that the empirical model provides very accurate predictions of the above-mentioned parameters for the Fe-SMA confined RC columns. Therefore, the empirical model adopted in this study may be considered for studying the combined effect of internal steel and external Fe-SMA confinement of concrete under compression.

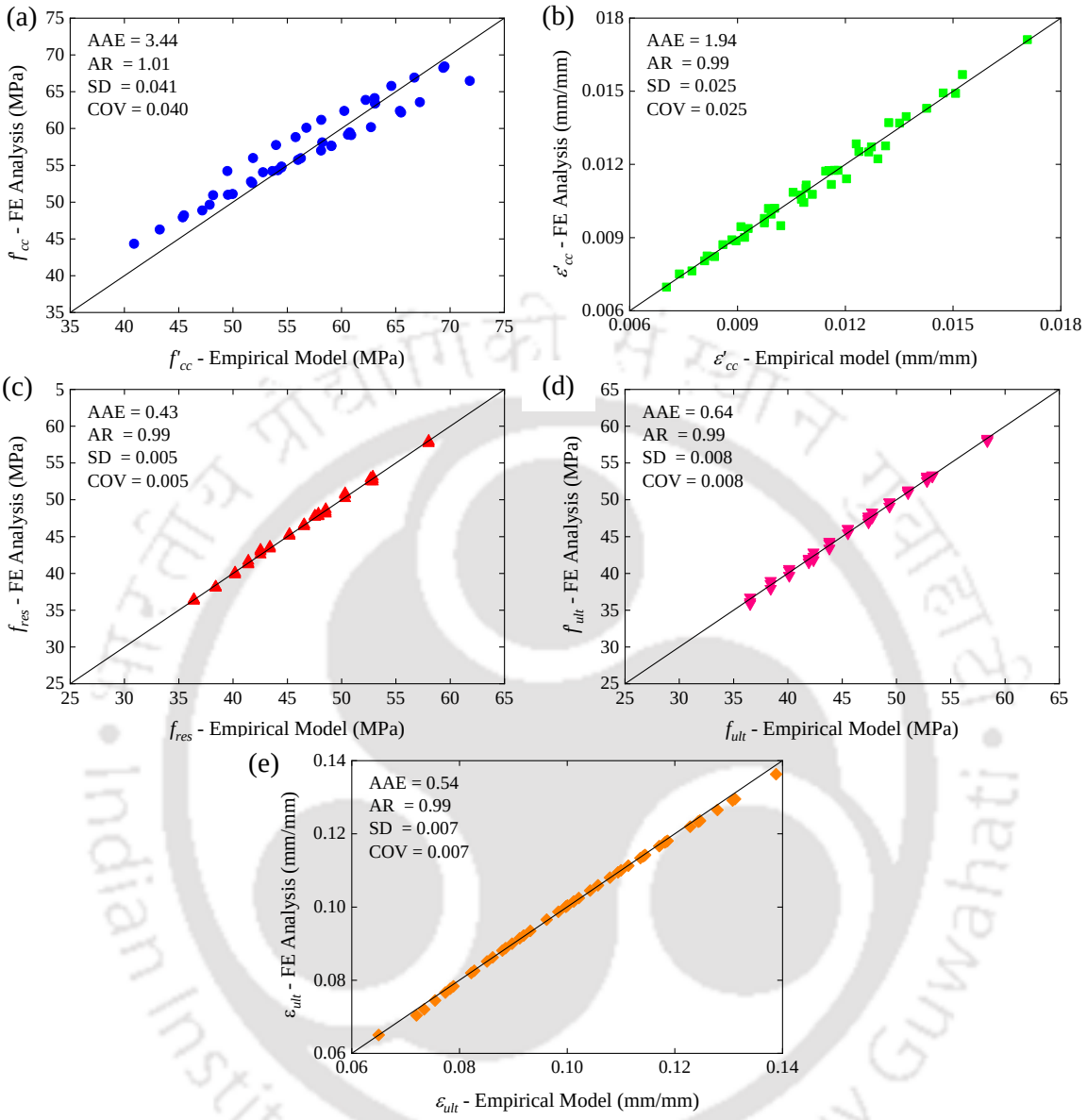

Fig. 4.23. Empirical model vs. FE values for parameters (a) f'_{cc} (b) ε'_{cc} (c) f_{res} (d) f_{ult} and (e) ε_{ult}

The stress-strain model of Fe-SMA confined concrete based on the equation proposed by Tsai (1988) (Eq. 4.7) is extended for Fe-SMA confined reinforced concrete to characterize the ascending and descending portions of the stress-strain relationship through curve fitting. The parameters utilized in this model are evaluated from Eqs. (4.13-4.17). Fig. 4.24 shows the comparison of a typical axial stress-strain response of an Fe-SMA-confined RC column obtained from FE simulation with that derived from the proposed empirical model.

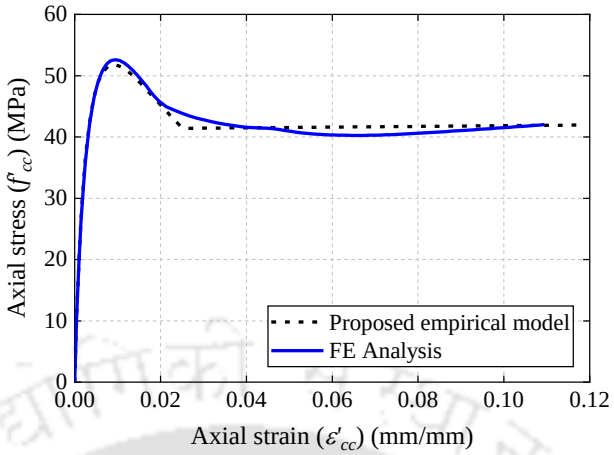

Fig. 4.24. Comparisons of axial stress-strain responses of specimen A1-R1-S1 obtained from FE simulation with proposed empirical stress-strain model.

4.9. Concluding remarks

This study focused on utilizing a new scheme of active confinement of concrete using a cost-effective substitute to commonly used expensive NiTi-based SMAs. The spacing of Fe-SMA strips was varied to arrive at different confining pressures. First, an experimental study was conducted to evaluate the behaviour of plain concrete cylinders partially confined with Fe-SMA strips under uniaxial compressive loading. Three different grades of concrete (21.7 MPa, 26.3 MPa and 30.3 MPa) and three different active confining pressures (1.09 MPa, 1.76 MPa and 2.44 MPa) were adopted to study its influence on the stress-strain response of Fe-SMA-confined concrete specimens. On increasing the active confining pressure from 1.09 MPa to 2.44 MPa, corresponding increase in the peak stress in the range of 24.9%-68.5% was observed as compared to that of the unconfined concrete specimens. Similarly, it can be observed that there is substantial improvement in ultimate stress as well as ductility due to Fe-SMA confinement. Thereafter, regression analyses on test data were carried out to propose an empirical stress-strain equation of partially confined Fe-SMA concrete. Next, to understand the total confinement effect of external Fe-SMA and internal longitudinal as well as transverse reinforcement, 3D-FE analyses were carried out. The results obtained from FE analyses were compared with an empirical stress-strain model for Fe-SMA-confined concrete, obtained by combining the individual stress-strain model of steel confined concrete as well as Fe-SMA confined concrete, and reasonably good agreements were observed. It is observed that the maximum AAE in predicting the

intrinsic parameters of the stress-strain curve was less than 12.85% and the corresponding AR was in the range of 0.88-0.96. Furthermore, to achieve a higher degree of accuracy in predicting the values of the parameters of the stress-strain relationship of Fe-SMA confined reinforced concrete, regression analyses were carried out on the FE results and an empirical model was proposed based on it. The maximum AAE reduced to 3.4% and the corresponding AR for all the parameters increased to 0.99. This improved empirical model (Model-II) for Fe-SMA confined RC specimens can be easily incorporated in any standard FE software for analysis of such Fe-SMA confined RC specimens using a stick model.

Chapter 5

Experimental and numerical investigation on rehabilitation of severely damaged RC bridge piers

5.1. General

This chapter presents rehabilitation details of severely damaged bridge pier models using reinforced concrete jacketing method adopting a plastic hinge relocation technique. The test specimens were tested under cyclic loading. All the important seismic performance parameters of the rehabilitated specimen were evaluated. A 3D finite element model was simulated considering concrete-rebar interaction and jacket-pier interface shear. Calibration of the numerically simulated model was done by comparing with experimentally observed responses.

5.2. Specimen details

The test specimens consisted of 1/5th-scaled damaged pier models of a prototype bridge in Tripura, India, designed as per provisions of IRC-6, which were subsequently rehabilitated using concrete jacketing for further testing in the present study. The prototype bridge has two spans with its ends supported on rollers, and an integral pier as shown in Fig. 5.1. Table 5.1 presents details of the scaled models of the bridge pier and Fig. 2 shows its reinforcement detailing.

These specimens were previously tested by Kotoky *et al.* (2018) in the Structural Engineering Laboratory of Civil Engineering Department of Indian Institute of Technology, Guwahati which resulted in severe damage in the form of crushing of core concrete and yielding as well as rupture of reinforcement at the interface zone of the pier and foundation as may been observed from Fig. 3(a). A typical fractured rebar of the specimen at the end of experimental investigation is showed in Fig. 3(b). Crushing of core concrete is also visible in the figure.

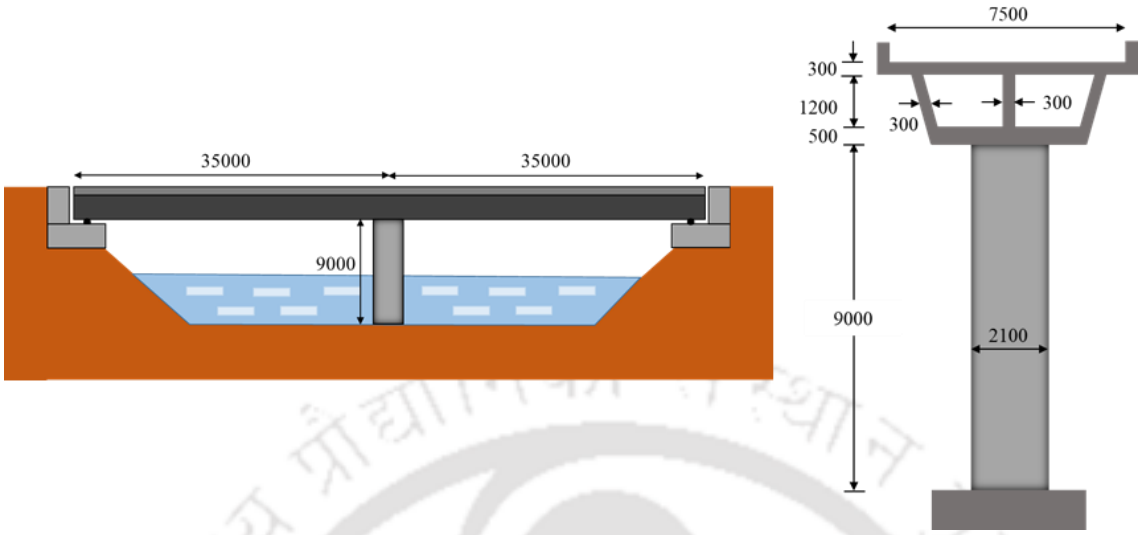

Fig. 5.1. Prototype RC bridge (Kotoky *et al.* 2018)

Table 5.1 Details of scaled bridge pier model (Kotoky *et al.* 2018)

Item	**Prototype**	**Model**	**Remarks**
Longitudinal steel ratio	1.12%	1.12%	Conserved during scaling
Longitudinal steel reinforcement	36 mm Ø – 38 nos.	16 mm Ø – 8 nos.	Conserved during scaling
Transverse reinforcement dia.	8 mm	8 mm	-
Spacing of transverse reinforcement	300 mm	60 mm	1/5 scale
Pier dia.	2100 mm	420 mm	1/5 scale
Pier height	9000 mm	1800 mm	1/5 scale
Cover	40 mm	20 mm	1/2 scale

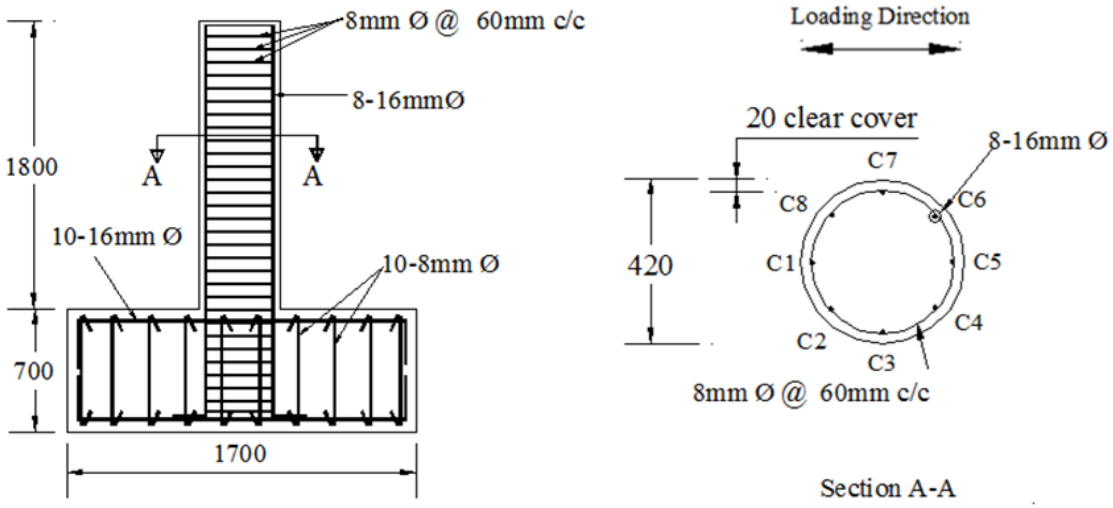

Fig. 5.2. Reinforcement details of scaled model of prototype bridge pier (Kotoky *et al.* 2018)

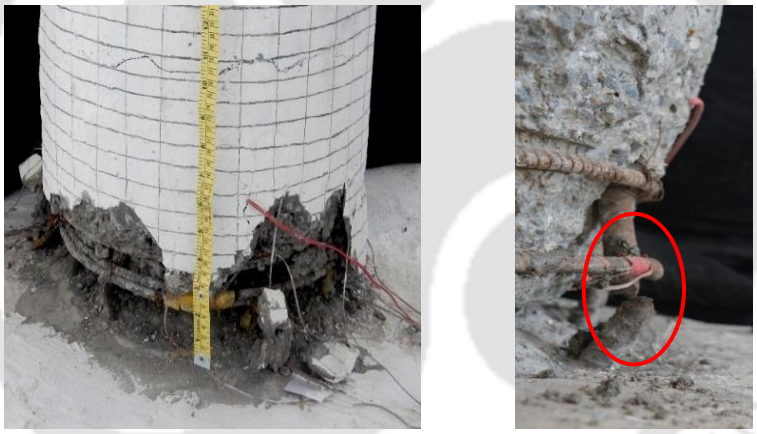

(a) (b)

Fig. 5.3. Damaged specimen showing (a) crushing of core concrete and buckling of longitudinal reinforcement (b) fractured rebar (Kotoky *et al.* 2018)

5.3. Rehabilitation of damaged bridge pier specimens

The objective of seismic rehabilitation in the current study was to repair and recast the original plastic hinge region of the damaged bridge pier specimen by RC jacketing so as to attain the desired load carrying capacity and to relocate the plastic hinge away from the pier-footing interface. This makes it easier to subsequently repair the pier following a seismic event. The idea of relocation of plastic hinges of RC bridge piers away from the footing was first proposed by Hose *et al.* (1997), was later extended by other researchers

for seismic repair of bridge piers (Krish *et al.*, 2021; Parks *et al.*, 2016; Rutledge *et al.*, 2014). This was implemented by increasing the longitudinal and transverse reinforcement ratio of the pier at the damaged original plastic hinge region.

5.3.1. Design philosophy

The philosophy behind designing such a rehabilitation scheme is illustrated in Fig. 5.4. A cantilever column of length H_C, representative of a bridge pier, is considered. When a plastic hinge forms at the base of the pier after localization of damage, its ultimate moment capacity, M_C is reached. The same bending moment M_C should be reached at a desired location for formation of a new plastic hinge since the pier has a uniform cross-section throughout its height. Sectional analysis is carried out using SAP 2000 to find the value of M_C. Assuming that H_C and H_R are the heights of the original pier and repaired region respectively, the increased moment and shear demands at the new plastic hinge location are given as:

$$M_R = \frac{M_C H_C}{H_C - H_R} \tag{5.1}$$

$$V_R = \frac{M_C}{H_C - H_R} \tag{5.2}$$

As can be observed from Eqs. (5.1) and (5.2), the height of repair is directly proportional to the moment and shear demands of the repaired pier. It is therefore essential to keep the repair height at minimum. Rutledge *et al.* (2014) evaluated the required moment capacity at the base of the column by extrapolating the moment capacity of the relocated plastic hinge section and considered an over-strength factor of 5% as:

$$M_R = 1.05 \times \left(\frac{M_C H_C}{H_C - H_R} \right) \tag{5.3}$$

At the same time, the repair should be of sufficient height so as to ensure that the cross-section of the column at the newly located plastic hinge has minimal damage. According to Parks *et al.* (2016), the new plastic hinge should be located above structural cracks of widths equal to or larger than 0.254 mm.

Based on the minimum offset requirement for the jackhammer to drill holes in the footing for anchoring of dowel bars and minimum cover of the RC jacket, the diameter of the bridge pier was increased from 420 mm to 600 mm. The height of the concrete jacket was obtained as 450 mm from Eq. (5.3). It was further ascertained that no structural cracks larger than 0.254 mm were located at the new located plastic hinge. Eight numbers of 16 mm dia. dowel bars, with yield strength of 500 MPa, were installed around the damaged section for increasing the flexural strength. These were epoxy anchored into the footing with a development length of 150 mm. Transverse reinforcement comprising of steel stirrups of dia. 8mm were provided at 60 mm centre-to-centre spacing for enhanced confinement and shear strength. The shear capacity at the relocated plastic hinge location was adequate to ensure that the rehabilitated column would fail in flexure.

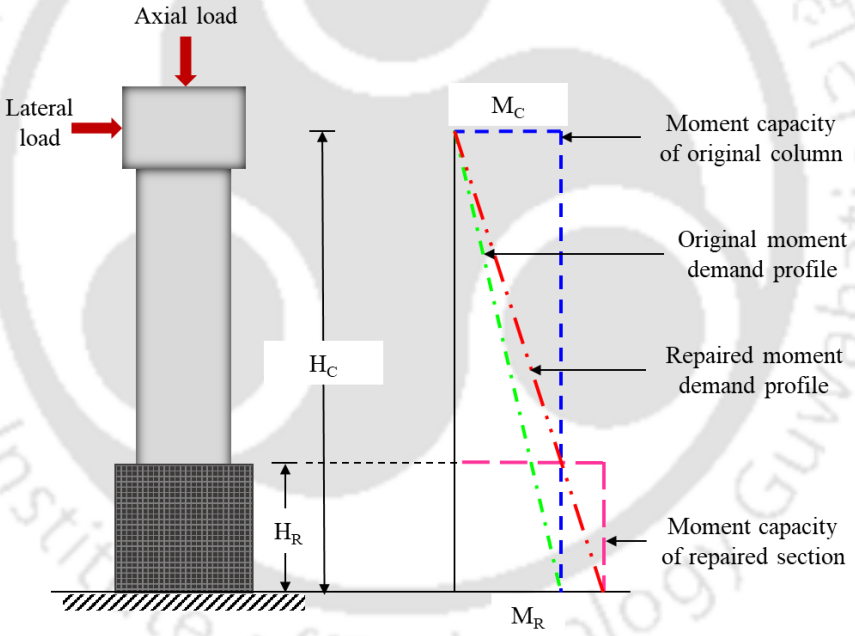

Fig. 5.4. Moment demand vs. moment capacity

5.3.2. Methodology adopted for rehabilitation of damaged test specimen

The rehabilitation strategy, as shown in Fig. 5.5(a-o), was aimed to retrieve back the lost capacity of the damaged bridge pier specimens to its original capacity in terms of strength, stiffness, energy dissipation capacity, ductility etc. The core concrete at the interface zone was first repaired followed by concrete jacketing to ensure that its load carrying capacity was similar to that of the undamaged specimens.

Holes were drilled at regular intervals in the damaged zone of the specimens, as shown in Fig. 5.5(a), up to a height of about 450 mm from the column-footing interface to facilitate the sealing of cracks by epoxy grouting. Loose materials present in this region were first removed manually [Fig. 5.5(b)] and then with a jackhammer. An air blower was used to clean the drilled holes as well as the concrete surface [Fig. 5.5(c)]. Aluminium nozzles were placed into those drilled holes and anchored with a high performance injection mortar (Fisher FISV 360S) [Fig. 5.5(d)]. The specimens were brought back to its original vertical position with the help of a chain-pulley system, as shown in Fig. 5.5(e). The surface was cleaned using water. After it was allowed to dry for a sufficient amount of time, ordinary Portland cement (OPC) and an acrylic modifier, Master Crete M-81 were mixed in the ratio 2:1 homogeneously till no lump or air bubble remained in the mix for preparation of a bond coat. Acrylic modifiers enhance the strength and adhesion of Portland cement mortar mixes. This coating was applied on the surface by a brush [Fig. 5.5(f)]. A polymer modified mortar was prepared using 10% of Master Crete by weight of cement for use as a repair mortar. The polymer mortar was used for patching the damaged zone of the specimen so as to prevent epoxy from oozing out from the cracks when it would be injected under a high pressure [Fig. 5.5(g)].

Parts A and B of an injectable resin grout, Sikadur-53 (UF) were mixed together in the ratio 2:1 (by weight) for at least 3 minutes until the material achieved consistency. It is designed for sealing crack widths upto 5 mm by high pressure injection systems. A hand injection pump, as shown in Fig. 5.5(h), was used to inject the epoxy resin into the nozzles starting from the lowest level and against gravity under a high pressure of 4 kg/cm^3 [Fig. 5.5(i)]. A quick setting and rapid hardening admixture (CICO No.3) was added to cement in the ratio 1:3 and mixed thoroughly and quickly to avoid stiffening during mixing, to form a sealant. It is used for sealing nozzles after the resin grout is pumped under pressure. As soon as injection resin oozed out of the diametrically opposite injection port, the first one was sealed and injection process was continued at the next higher level. When all the nozzles were sealed [Fig. 5.5(j)], the specimens were left undisturbed for a day to facilitate curing of the epoxy resin.

Once the epoxy was cured, the nozzles are cut, as shown in Fig. 5.5(k), and the mortar used for patching was chiselled out from the damaged zone of the specimens. The concrete surface was cleaned thoroughly after removal of loose materials. A suitable bonding agent, Part 1 and Part 2 of Masterbond EP mixed in the ratio 65:35 was brush applied on the clean surface, as shown in Fig. 5(l), for attaining adequate bond between the old and fresh concrete. After putting the formwork in place, restoration of the original cross-section was done by pouring micro-concrete prepared with SikaRep Microcrete and aggregates in the ratio 2:1 and water: powder ratio of 0.15 by weight in the damaged zone of the specimens [Fig. 5.5(m)]. The formwork was removed after a day and curing of concrete was done.

Fig. 5.5. Rehabilitation methodology (a) drilling of holes to facilitate epoxy injection; (b) chiseling of loose damaged concrete; (c) cleaning of drilled holes and concrete surface using air blower; (d) placing of aluminium nozzles into drilled holes; (e) bringing the inclined pier to vertical position using chain-pulley system; (f) application of acrylic modifier over the concrete surface; (g) application of polymer mortar; (h) epoxy injection pump; (i) epoxy grouting; (j) sealing of nozzles; (k) cutting of nozzles after curing of epoxy; (l) application of bonding agent after chiseling of polymer mortar and cleaning of concrete surface ; (m) casting of concrete; (n) application of bonding agent after hacking of concrete surface and installation of reinforcement cage application of bonding agent; (o) casting of concrete jacket.

Since the eight longitudinal rebars at the base of the pier had already buckled or ruptured, additional eight nos. of HYSD dowel bars were installed adjacent to it. These bars were 16 mm dia., 600 mm in length and were anchored into the footing with an anchorage length of 150 mm. High performance injection mortar (Fisher FISV 360S) was applied for proper anchorage of these rebars into the footing. To ensure proper load distribution from

the existing column to the newly constructed jacketed part, shear connectors were provided. For this, holes were drilled and cleaned by blowing air. These were filled with high performance injection mortar after which shear connectors were anchored in the holes. The mortar was then allowed to cure. Two numbers of U-shaped shear connectors 8 mm dia. and 80 mm in length, per dowel bar were provided at distances of 120 mm and 360 mm from the base of the specimen as shown in Fig. 5.5(n). Transverse reinforcement, 8 mm dia. and 60 mm c/c were tied around the new dowel bars. These were also tied with the shear connectors using binding wire. Hacking of the newly cast concrete surface of the original pier was done using a chisel and a hammer so as to ensure proper bond between the original pier and the jacket. The surface was then cleaned using a brush and an air blower. A bonding agent (Masterbond EP) was brush applied on the clean surface for attaining adequate bond between the old and fresh concrete as shown in Fig. 5.5(n). A formwork with internal diameter 600 mm and height 450 mm was put in place. Concrete of grade M30 was prepared in a tilting drum type mixer. Needle vibrator was used to ensure appropriate compaction of the poured concrete placed inside the formwork [Fig. 5.5(o)]. The formwork was removed after 24 hours and water-curing was done for 28 days.

5.4. Experimental investigation

The objective of the experimental programme was to evaluate strength, stiffness, energy dissipation capacity and ductility of the rehabilitated test specimen under cyclic loading. Appropriate loading protocol was adopted to access the seismic performance of the test specimens. Details of the test set-up along with instrumentation and testing procedure are described in the subsequent sections.

5.4.1. Test set-up and instrumentation

The weight of the superstructure on the prototype bridge pier was evaluated using the detailed drawings of the bridge. For the test specimen, scaling factor was decided considering artificial mass simulation, based on the similitude laws proposed by Harris and Sabnis (1999). Accordingly, a servo-hydraulic actuator of 1000 kN capacity (Make: MTS Inc., USA) was used to apply a load of 140 kN to simulate self-weight of the bridge deck, through a loading arrangement as shown in Fig. 5.6.

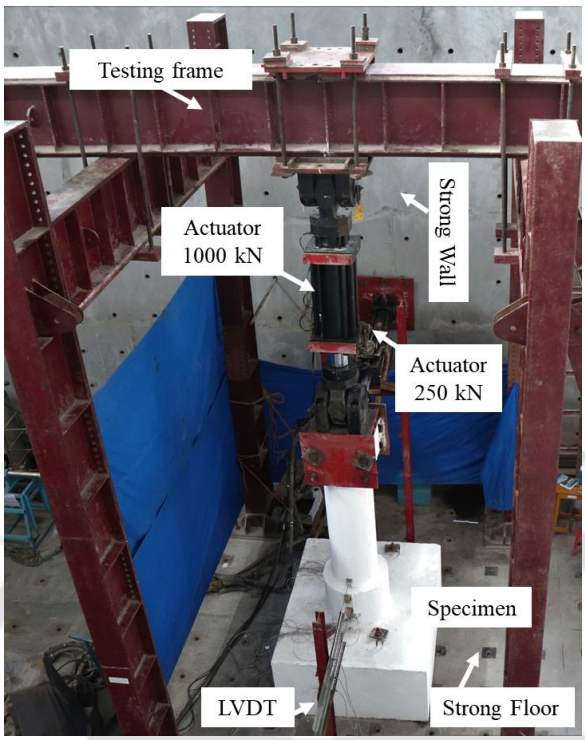

(a)

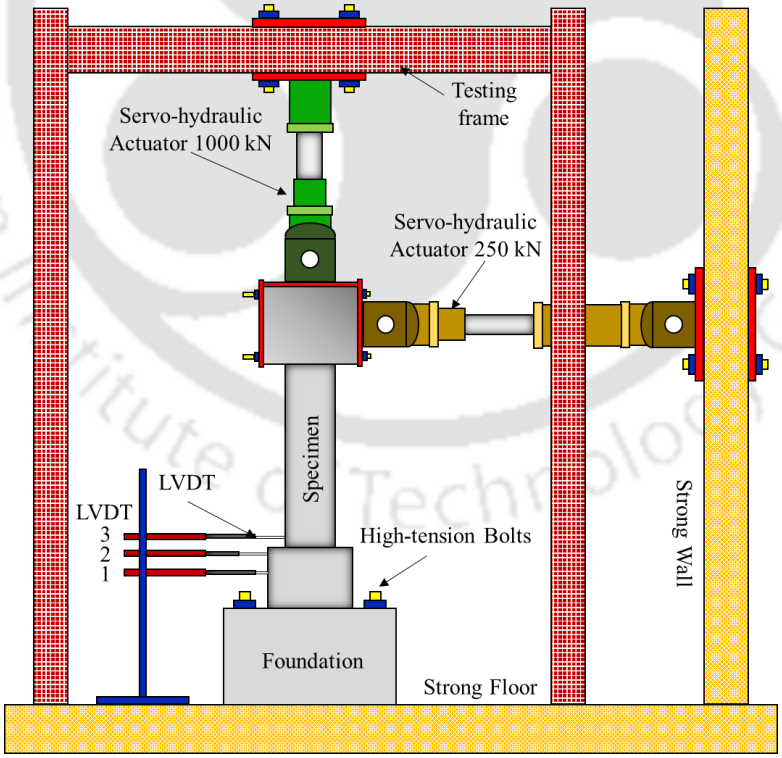

(b)

Fig. 5.6. Experimental set-up (a) overall view (b) schematic diagram

Lateral displacement was applied through a 250 kN servo-hydraulic actuator (Make: MTS, USA) with a stroke length of ± 250 mm. A FlexTest-GT controller (Make: MTS, USA) was used to control the servo-hydraulic actuator for application of load in displacement-control mode. A built-in data-acquisition system (DAQ) of the controller was used to obtain feedback signals. The lateral force and displacement of the test specimen was recorded by the built-in load cell and LVDT displacement sensor of the actuator, respectively.

The foundation of the test specimen was fixed to the strong floor with four high tension bolts. The vertical and horizontal actuators were supported against the test frame and the strong wall of the laboratory respectively as shown in Fig. 5.6. The vertical actuator was positioned on the pier head in such a way that the imposed load remained vertical, while allowing unrestricted lateral movement of the test specimen throughout the experiment. When the rehabilitated bridge pier is subjected to lateral loads, damage in the pier is most likely to be concentrated near the interface between the jacket and the original pier due to plastic hinge relocation. Hence, lateral deflections in the interface region of the test specimen were recorded using three linear variable differential transformers (LVDT) as shown in the figure.

5.4.2. Loading protocol

In the present study, a loading program with increasing multi-cycle displacement loading history was chosen. Lateral cyclic loading was applied at a low frequency of 0.025 Hz.

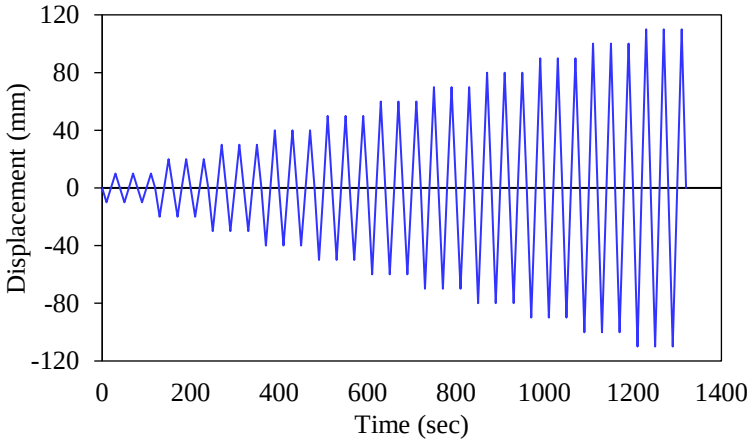

Fig. 5.7. Applied displacement history

The loading consisted of gradually increasing displacement amplitude, starting at ± 10 mm and progressing in 10 mm increments of displacement amplitudes till failure of the specimen. The applied incremental lateral displacement protocol is shown in Fig. 5.7. The test was discontinued when the load capacity of the test specimen reduced to around 70-80% of the peak load and/or upon fracture of the reinforcement bars.

5.4.3. Results and discussion

This sub-section summarises the results obtained from the experimental study of the rehabilitated bridge pier. Observed distribution of damage, force-displacement hysteretic behaviour, stiffness degradation, energy-dissipation capacity and equivalent viscous damping of the test specimen were investigated in this study.

5.4.3.1. Observed distribution of damage

The damage states of the test specimen at various displacement amplitudes are shown in Fig. 5.8.

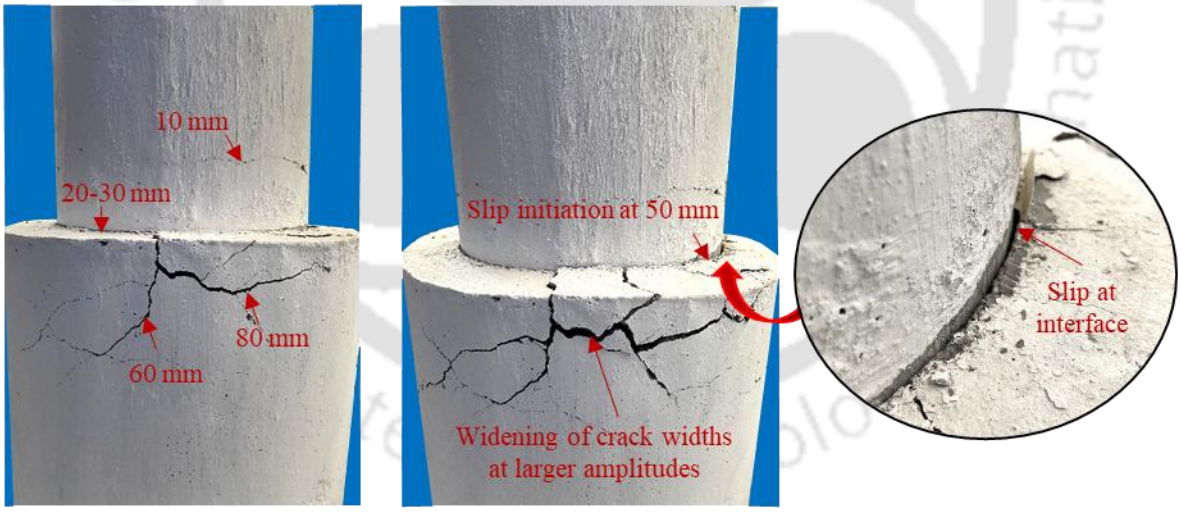

Fig. 5.8. Observed distribution of damage

At the end of the 10 mm displacement cycle, hairline cracks were observed at a distance of 110 mm from the top end of the jacket. New hairline cracks at the jacket pier interface were observed at the end of 20 and 30 mm displacement cycles. On further increase of the displacement amplitude, the crack location got shifted to the jacketed portion of the test specimen. A small slip in the interface was observed at the end of 50 mm

displacement amplitude. Hinge formation and spalling of concrete in the jacket was observed at the end of 70 mm displacement amplitude. Major cracking of concrete was observed at the top end of the jacket, at 80 mm displacement amplitude. The crack widths and spalling of concrete increased upon increase in the loading amplitude. Rupture of rebar was observed at the end of 110 mm. At this stage, the specimen exhibited got inclined permanently due to which vertical load could not be maintained. The test was stopped hereafter.

5.4.3.2. Force-displacement hysteretic behaviour and envelope curve

The force-displacement hysteretic behaviour of the test specimen is shown in Fig. 5.9(a). The envelope curve was plotted by connecting the points of peak lateral load corresponding to each displacement amplitude from the hysteresis curve [Fig. 5.9(b)]. The specimen reached its peak load of 113.6 kN at 2.22 % drift ratio. The fracture of a longitudinal reinforcement bar at a displacement amplitude of 110 mm, as shown in Fig. 5.9(a), is accompanied by a sudden drop in the load carrying capacity of the specimen.

Fig. 5.10(a) shows the force-displacement response of the original test specimen at the end of hybrid simulation, where the entire bridge, as shown in Fig. 1, was simulated numerically with the bridge pier being considered as experimental element (Kotoky *et al.* 2018). After the completion of the hybrid simulation, the test specimen was further subjected to cyclic loading tests to determine its ultimate load-carrying capacity. Fig. 5.10(b) shows the force-displacement response at the end of cyclic test.

On comparing the results of the original and rehabilitated bridge pier specimens, it may be observed that higher lateral load was resisted by the rehabilitated specimen while the maximum imposed displacement are more or less similar, when the experiments were terminated in both the cases due to the development of some instability in test specimen. It may be mentioned that moment capacities of both the original and rehabilitated test specimens are same and thus the latter resists more lateral load than the former due to reduction in the lever arm in the rehabilitated test specimen.

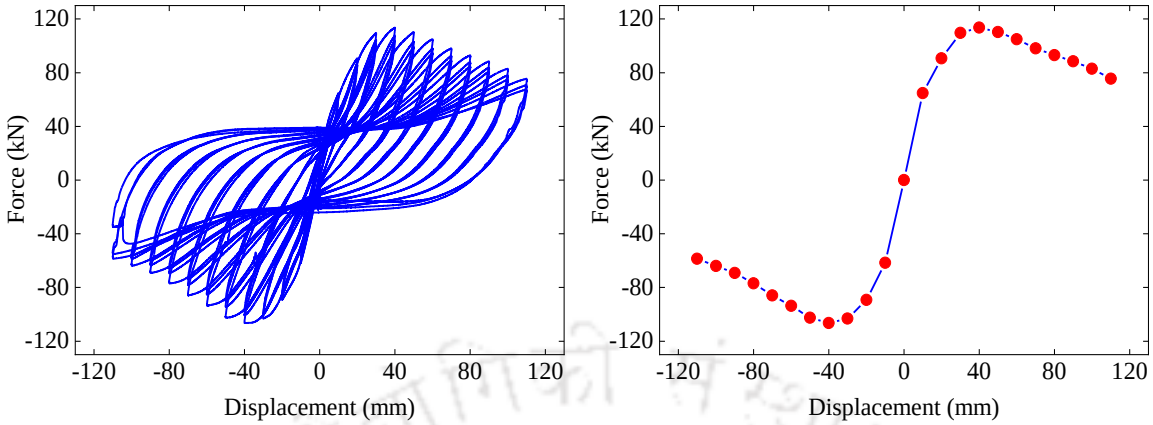

Fig. 5.9. (a) Hysteretic response of test specimen; (b) Envelope curve

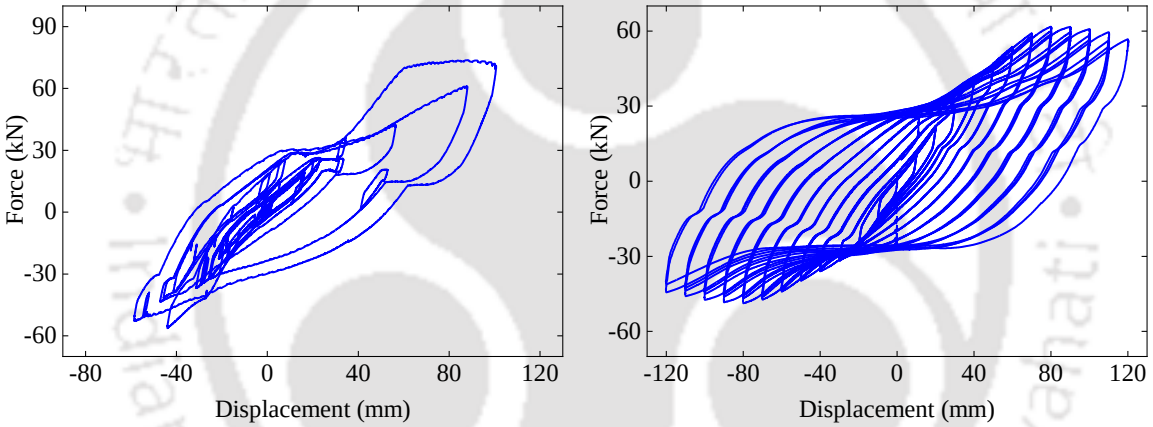

Fig. 5.10. Load-deformation response of original specimen at the end of (a) hybrid simulation (b) cyclic test (Kotoky *et al.* 2018)

5.4.3.3. Stiffness degradation

In the present study, secant stiffness of bridge pier was considered. It is calculated by:

$$K_{avg} = \frac{\left|P_{\max} - P_{\min}\right|}{\left|u_{\max} - u_{\min}\right|} \tag{5.4}$$

where, K_{avg} is the average secant stiffness of the specimen and P_{max} and P_{min} are the maximum and minimum loads at each displacement amplitude corresponding to its peak displacements u_{max} and u_{min}.

Fig. 5.11 shows the change in stiffness with drift ratio. The initial stiffness of the test specimen is 6.32 kN/mm. It may be observed that there is a sharp degradation in stiffness in the initial displacement amplitudes, after which it was gradual.

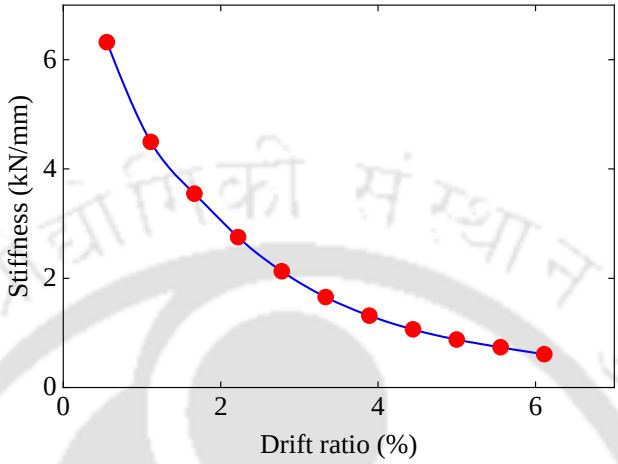

Fig. 5.11. Stiffness degradation of test specimen

5.4.3.4. Energy dissipation and damping

Energy dissipation capacity is one of the significant parameters that governs the seismic performance of a structure. It can be evaluated by computing the area enclosed by the hysteretic loops. Cumulative energy dissipated is calculated by summing up the energy dissipated in consecutive loops throughout the test till failure. Fig. 5.12(a) shows the energy dissipation of the specimen corresponding to each amplitude as well as the cumulative energy dissipation capacity of the test specimen. The total energy dissipated at the end of the test was 57.31 kNm.

Damping is another parameter that can be used to determine the energy dissipation capacity of a structure. The equivalent viscous damping ratio is defined as:

$$\xi = \frac{E_D}{4\pi E_{S0}} \tag{5.5}$$

where, E_D is the energy dissipated in a single hysteresis loop and E_{S0} is the maximum strain energy of an equivalent elastic system. The equivalent viscous damping ratio was calculated for the test specimen as shown in Fig. 5.12(b). The damping at failure of the specimen was 8.9%.

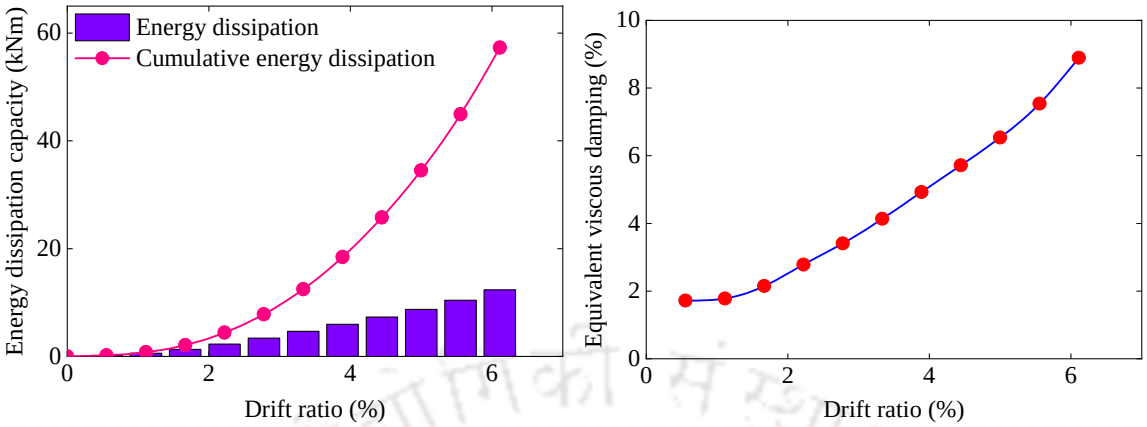

Fig. 5.12. (a) Energy dissipation capacity of test specimen; (b) Equivalent viscous damping

5.4.3.5. Displacement ductility

Displacement ductility refers to the capacity of a structure to withstand large deformations its inelastic range without substantial reduction in strength. Under the action of cyclic loads, ductile structures have the ability to dissipate a large amount of energy. The displacement ductility factor μ is defined as:

$$\mu = \frac{\Delta_u}{\Delta_y} \tag{5.6}$$

where, Δ_u and Δ_y are the maximum deformation and deformation at yield respectively.

Since the envelope curve may not have a well-defined yield point, it is difficult to predict the yield deformation of a structure. Researchers have proposed several alternate approaches for calculating yield displacement. For the present study, the yield displacement is calculated by the procedure proposed by Shannag *et al.* (2005) as the intersection point between the horizontal line through 0.8 times the ultimate load capacity and extension of the line through the origin and 0.5 times the ultimate load capacity, on either side of the envelope curve, as shown in Fig. 5.13. The yield displacement is obtained by averaging the values from both push and pull directions. Accordingly, the displacement ductility value of the test specimen was found to be 5.58. According to the Caltrans Seismic Design Criteria (2013), a minimum displacement ductility capacity of 3 has to be ensured regardless of the

displacement demand for desired plastic hinge rotational capacity. The rehabilitated specimen therefore satisfies this criterion.

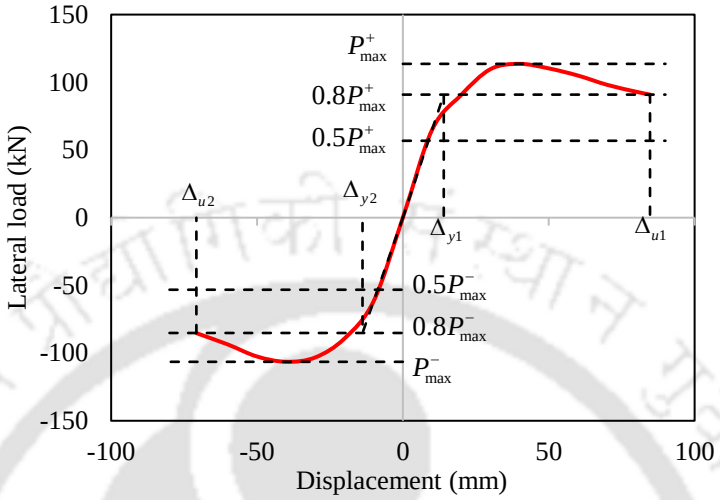

Fig. 5.13. Procedure for calculation of displacement ductility (Shannag *et al.*, 2005)

5.4.3.6. Deformation response

Fig. 5.14 shows the lateral deformation of the test specimen along the height of the test specimen, recorded by the LVDTs at all displacement amplitudes.

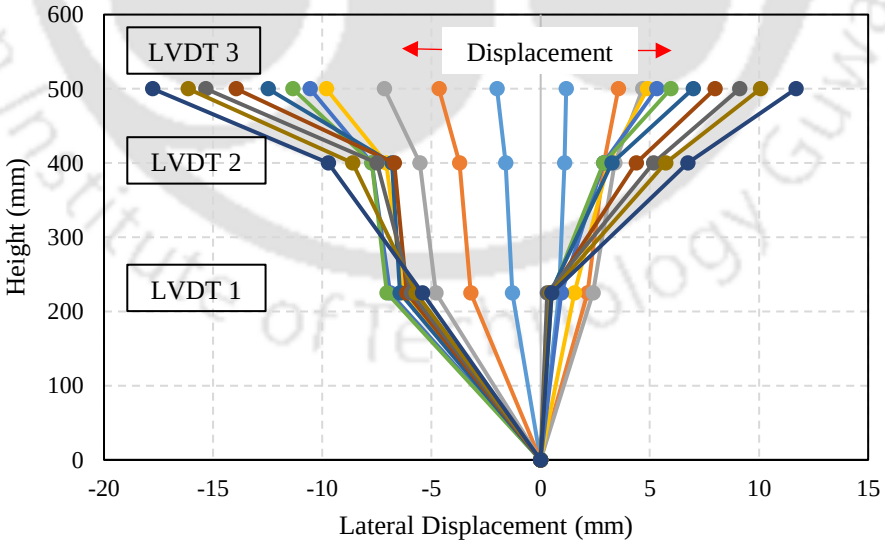

Fig. 5.14. Deformation profile of test specimen

The LVDTs were placed in the jacket-pier interface region which was expected to experience more damage as compared to rest of the pier. The lateral displacement profile

recorded by the LVDTs shows somewhat unsymmetrical load-deformation behaviour of the test specimen in push and pull directions when it was subjected to lateral cyclic loading as may be observed from Fig. 5.14. This is in expected line as the test specimen was obtained after retrofitting of a severely damaged specimen. Since LVDT 1 was located well below the jacket pier interface, it shows the least lateral deformation along the height at all drift levels.

5.5. Finite element modelling

Finite element analysis (FEA) proves to be one of the powerful tools for computing the response of structural components subjected to different loading schemes. However, in order to obtain accurate results from FEA, accurate modelling of materials, selection of elements and solution techniques are of utmost importance. In this study, 3D nonlinear finite element analysis was carried out using ABAQUS/CAE v.2021 to investigate the performance of the rehabilitated bridge pier under axial and lateral cyclic loading regimes. The key components determining the response of the test specimen are material nonlinearity, bond-slip behaviour of reinforcement bars and mechanical properties of the jacket-pier interface. These are discussed in the following subsections.

5.5.1. Material constitutive models

Constitutive models of the materials adopted in the finite element analysis of the test specimen are presented in the following sub-sections.

5.5.1.1. Concrete

In the present study, Concrete Damaged Plasticity (CDP) model available in ABAQUS was utilized to predict the inelastic behaviour of concrete using the concepts of isotropic damage elasticity as well as isotropic tensile and compressive plasticity. This model implements the yield function originally developed by Lubliner *et al.* (1989) and later modified by Lee and Fenves (1998) in order to account for concrete plasticity under tension and compression. The parameters of the CDP model are presented in Section 4.5.1. Both the cracking and crushing behaviour of concrete were defined using damage variables d_t and

d_c to model the degradation of strength and stiffness. Also, default tension and compression recovery factors as shown in Fig. 5.15 were adopted.

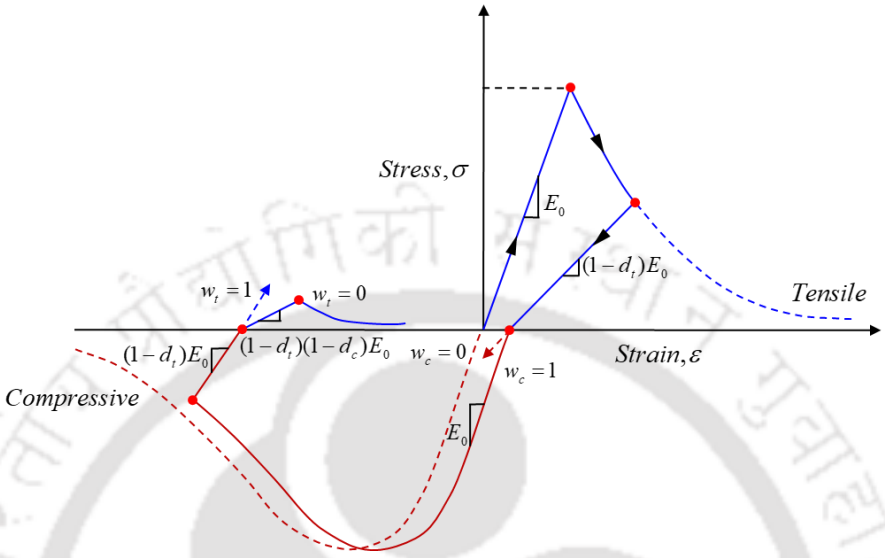

Fig. 5.15. ABAQUS CDP model under uniaxial load cycle (tension-compression-tension) assuming default values for the stiffness recovery factors: w_t = 0 and w_c = 1 in tension and compression respectively (ABAQUS Documentation 6.14)

To model the behaviour of concrete under compression, the axial stress-strain model of unconfined concrete as proposed by Mander *et al.* (1988) was used. Longitudinal and lateral steel reinforcements were modelled separately. The confinement effect of steel stirrups on the concrete in terms of increase in strength as well as ductility was automatically captured by the 3D FE model. In the elastic range, the stress-strain behaviour of concrete was defined using two parameters, i.e., Young's modulus (E_0) and Poisson's ratio (μ). Beyond this range, the stress-strain behaviour was defined in terms of yield stress (compressive stress) versus inelastic strains. Fig. 5.16(a) shows the compressive behaviour of concrete. To model the tensile behaviour of concrete, a linear elastic stress-strain relationship was considered in the pre-cracking stage. The tensile strength was defined as per IS 456 . A tension stiffening model, based on Wahalathantri *et al.* (2011), was adopted for defining a softening branch in the tensile stress-strain curve of concrete. Fig. 5.16(b) shows the tensile behaviour of concrete. To prevent kinematic instability, residual strengths of 10% of the peak stresses in both compression and tension were considered.

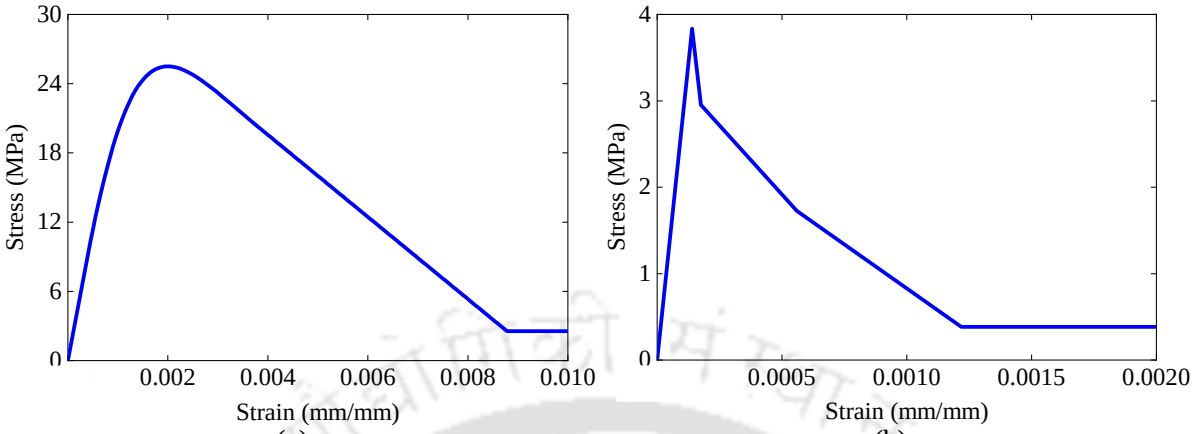

Fig. 5.16. Material models of concrete in (a) compression; (b) tension

5.5.1.2. Modified steel bar model

The experimental stress-strain curve of a typical bare steel rebar comprises of four zones: (a) linear elastic zone until yield stress f_y is attained; (b) yield plateau; (c) strain hardening zone in which the stress increases with strain till the ultimate tensile strength is reached; (d) strain softening zone in which the stress decreases until fracture occurs. Several researchers have pointed out that the stress-strain relationship of rebar is substantially different when it is embedded in concrete and hence proposed stress-strain models based on experimental as well as analytical studies. The most significant change in this model is the reduction in yield stress below f_y. Belarbi and Hsu (1994) carried out an experimental study and presented analytical expression for effective yield stress f_y^* of rebars embedded in concrete as:

$$\frac{f_y^*}{f_y} = 0.93 - 2B \tag{5.7}$$

$$B = \frac{1}{\rho}\left(\frac{f_{cr}}{f_y}\right)^{1.5} \tag{5.8}$$

where, ρ is the reinforcement ratio and f_{cr} is the tensile cracking stress of concrete corresponding to a cracking strain of around 8×10^{-5}.

A steel bar embedded in concrete and subjected to axial deformation is greatly influenced by the bond-slip behaviour at the interface. To simulate such concrete-rebar interaction, simplified approaches by modification of axial stress-strain of longitudinal bars embedded in concrete have been presented by few researchers (Dehestani & Mousavi, 2015; Wu & Pantelides, 2018). The present study incorporates the modified rebar model proposed by Dehestani and Mousavi (2015) to consider bond-slip effects of embedded reinforcement in the FE model. It is a bi-linear stress-strain relationship comprising of a linear elastic portion, with a modified elastic modulus E_s^* , till attaining f_y^* followed by a linear hardening portion. The total strain of a rebar of length *L*, is expressed as the sum of the strain equivalent to bond-slip and mechanical strain (*ΔL/L*) of the rebar, as shown in Fig 5.17. Accordingly, the modified elastic modulus of the rebar is given as:

$$E_s^* = \frac{f_y^*}{\varepsilon_s + (\delta / l)} \tag{5.9}$$

where, f_y^* is the effective yield stress of the rebar as calculated from Eq. (5.7), ε_s is the corresponding strain, δ is the maximum slip of the rebar and l is the bond strength transmission length between the rebar and the concrete around it.

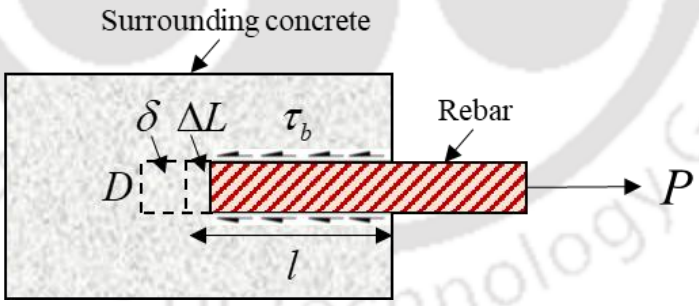

Fig. 5.17. Steel rebar in concrete

The maximum slip of the rebar δ, as proposed by Wu and Zhao (2013), is expressed as:

$$\delta = \frac{0.7315 + K}{5.176 + 0.3333K} \tag{5.10}$$

where, K is the combined confinement effect which is a function of the confinement effects of concrete K_{co} and steel stirrups K_{st} given by:

$$K = K_{co} + 33K_{st} \tag{5.11}$$

$$K_{co} = \frac{C}{d_b} \tag{5.12}$$

$$K_{st} = \frac{A_{st1}}{CS_{st}} \tag{5.13}$$

where, C is the cover of concrete, d_b is the diameter of rebar; A_{st1} and S_{st} are the area of a single leg of stirrup and its spacing respectively.

The bond strength transmission length, l is given by:

$$l = \frac{0.67}{2} S_{rm} \tag{5.14}$$

where S_{rm} is the average spacing of cracks which is obtained from Eq. (5.15) specified by CEB-FIP Model Code 1993 as:

$$S_{rm} = \frac{2}{3} \times \frac{d_b}{3.6\rho_{eff}} \tag{5.15}$$

where, ρ_{eff} is the effective reinforcement and is given by:

$$\rho_{eff} = \frac{A_s}{A_{c,eff}} \tag{5.16}$$

where, A_s is the total area of rebars at a section; $A_{c,eff}$ is the effective area of concrete in tension, as shown in Fig. 5.18, which was defined by Mousa *et al.* (2019) as:

$$A_{c,eff} = \frac{\pi(D^2 - (D - 5d_c)^2 / 4}{N} \tag{5.17}$$

where, d_c is the distance between the extreme tension fibre and centroid of the rebar; N is the number of longitudinal bars.

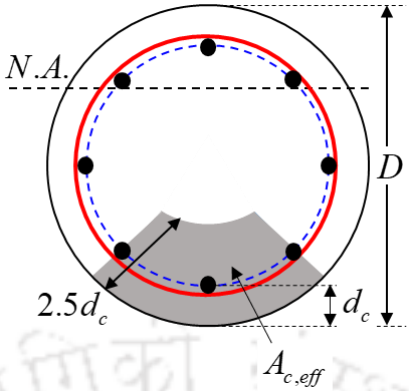

Fig. 5.18. Definition of $A_{c,eff}$ as per Mousa *et al.* (2019)

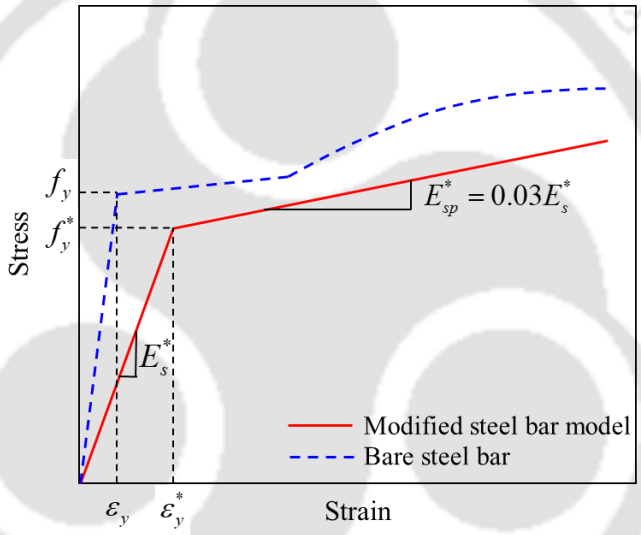

Fig. 5.19. Modified stress-strain model for rebar as per Dehestani and Mousavi (2015)

The hardening modulus of the modified rebar model is obtained from Eq. (5.18) as per recommendations of FEMA 356 and is given by:

$$E_{sp}^* = 0.03E_s^* \tag{5.18}$$

Substituting the values of all the parameters, the modified stress-strain curve of embedded rebar adopted in this study, which incorporates bond-slip effects, is shown in Fig. 5.19.

The uniaxial stress-strain relation in the elastic range is defined using Young's modulus and Poisson's ratio as 200 GPa and 0.3 respectively. The plastic behaviour is

defined by yield stress and corresponding plastic strain. For representing the material behaviour of steel reinforcement, a kinetic hardening plasticity model was adopted.

5.5.2. Jacket-pier interface modelling

The shear resistance at the interface of the original bridge pier and the newly cast reinforced concrete jacket is contributed by three mechanisms: cohesion, friction and action of shear connectors installed across the pier-jacket interface (Sakr *et al.*, 2020).

5.5.2.1. Traction-separation model for pier-jacket interface

The contact cohesive behaviour of the pier-jacket interface can be defined using a traction-separation model (ABAQUS Documentation 6.14). It is modelled as a surface interaction property assuming the default value of the thickness of the cohesive layer which is 1 mm. The traction separation law assumes a linear elastic behaviour initially until reaching the maximum traction followed by damage initiation, after which it decreases with damage evolution as shown in Fig. 5.20.

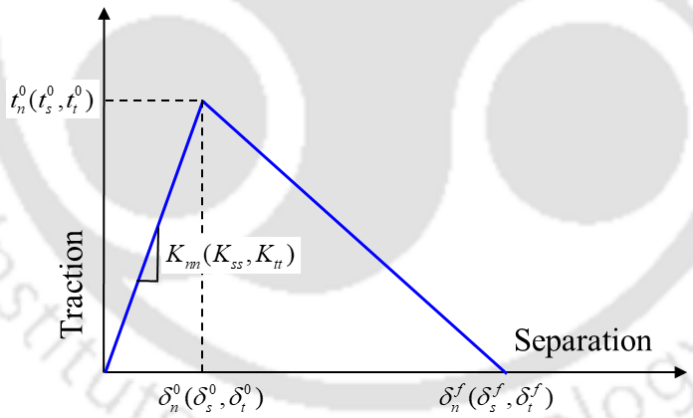

Fig. 5.20. Typical traction-separation response (ABAQUS Documentation 6.14)

The linear elastic stage is defined by initial stiffness components - K_{nn} in the normal direction and K_{ss} as well as K_{tt} in the tangential directions respectively. In the present study, K_{nn} is defined as the Young's modulus of concrete, K_{ss} and K_{tt} are assumed to be equal and are defined as the shear modulus of concrete. Damage initiation is assumed to occur when the nominal stresses at the interface corresponding to deformation purely normal to the interface or purely in the first and second shear direction reaches its peak values of t_n^0, t_s^0

and t_t^0 respectively (ABAQUS Documentation 6.14). These are set to the same value, which is the direct tensile strength of concrete (Zhu *et al.*, 2020), which is determined as per provisions of IS 456:2000. The evolution of damage is determined by specifying either the effective displacement at failure, δ_n^f or the total fracture energy, G^C. In this study, damage evolution is defined by the fracture energy approach proposed by Dudziak *et al.* (2021). The parameters of the traction-separation law are listed in Table 5.2.

Table 5.2. Parameters of traction-separation law

Parameters	**Values**
K_{nn} (N/mm^3)	27386
K_{ss}, K_{tt} (N/mm^3)	11410
t_n^0 , t_s^0 , t_t^0 (MPa)	3.84
G^C (N/mm)	49.47

5.5.2.2. Hard contact and friction co-efficient

The pressure-overclosure relationship in the pier-jacket interface was set as hard contact in the normal direction in ABAQUS. Hard contact is utilized as there is no penetration between the external surface of the original pier and the internal surface of the RC jacket.

A friction model with penalty formulation was implemented in the tangential direction. The friction coefficient for the interaction model were adopted from Eurocode 2 (EN1992-1-1:2004) for prediction of interface strength between concretes cast at different times. Table 5.3 enlists the values of friction coefficients for different types of interfaces. A parametric study would be conducted to determine the best possible interfacial configuration.

Table 5.3. Coefficient of friction (Eurocode 2)

	Type of interface			
	Very smooth	Smooth	Rough	Very rough
Co-efficient of friction (μ)	0.5	0.6	0.7	0.9

Shear connectors are of great importance in ensuring composite action between concrete surfaces cast at different times. U-shaped shear connectors were modelled as per details mentioned in Section 3.2 and a simple bilinear elasto-plastic stress-strain curve with Young's modulus of 200 GPa and a poisson's ratio of 0.3 was adopted for its material model as shown in Fig. 5.21.

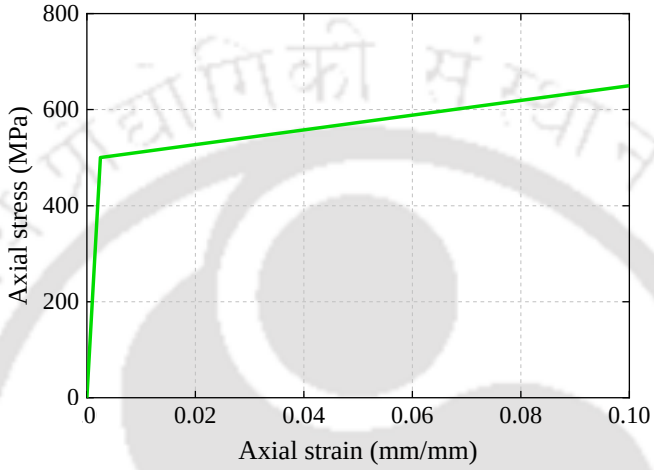

Fig. 5.21. Material model for shear connector

5.5.3. Details of FE model

Two element types, namely, C3D8R and T3D2 were utilized for development of the FE model. Concrete was modelled using continuum eight-node linear brick elements with reduced integration and hourglass control (C3D8R). The internal longitudinal and transverse reinforcements were modelled using two-nodded linear truss elements (T3D2). A set of mesh sensitivity analyses were carried out to arrive at the optimum mesh size for both accuracy as well as computational efficiency.

The base of the test specimen was fixed using the "encastre" boundary condition as shown in Fig 5.22. Fixity was assumed at the pier base because no signs of damage were observed in the pier-footing interface region due to relocation of plastic hinge. The lateral reinforcement, longitudinal reinforcement and shear connectors was embedded in the concrete column by applying the "embedded region" constraint.

Weight of the superstructure on the test specimen was applied as equivalent pressure at the top and lateral cyclic loading in the form of displacement boundary

condition was applied. The dynamic response was obtained using an explicit central-difference time integration scheme. An automatic time-incrementation scheme was selected to improve the rate of convergence of the solution.

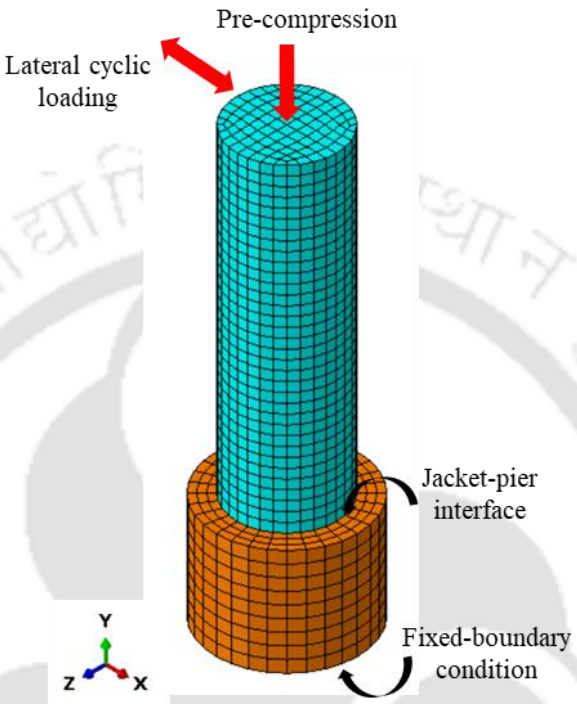

Fig. 5.22. Schematic diagram of a FE model of the test specimen

5.5.4. Results and discussion

Fig. 5.23(a) compares the numerical results obtained from ABAQUS with that obtained from the experiment. Effect of cohesion through traction-separation law and hard contact with friction coefficient were modelled at the jacket-pier interface. Further, a parametric study was conducted to determine the best possible interfacial configuration. In interaction model 1 (IM 1), tie-constraint was used to model the jacket-pier interface, which allowed complete transfer of loads between the two components. In interaction models 2, 3 and 4 (IM 2-4), traction-separation law along with hard contact in the normal direction and friction coefficients of 0.7, 0.8 and 0.9 respectively, were adopted in the tangential direction.

Comparison of the results shows that the FE model with IM 1 incorporating a tie constraint was unable to simulate the experimental load-deformation behaviour as it does

not allow for relative motion between the two surfaces at the jacket-pier interface. FE model with IM-4 was able to accurately capture both the strength and stiffness degradation of the rehabilitated RC bridge pier. Hence, this FE model was adopted in this study for further comparison with the experimentally obtained results. The peak load obtained numerically is in good agreement with that obtained from the experiment with a maximum error of 2.6% and 2.8% in the directions of push and pull respectively. Comparison of the envelope curves shows that the FE model was fairly successful in capturing the pre- as well as post-peak experimental response of the test specimen.

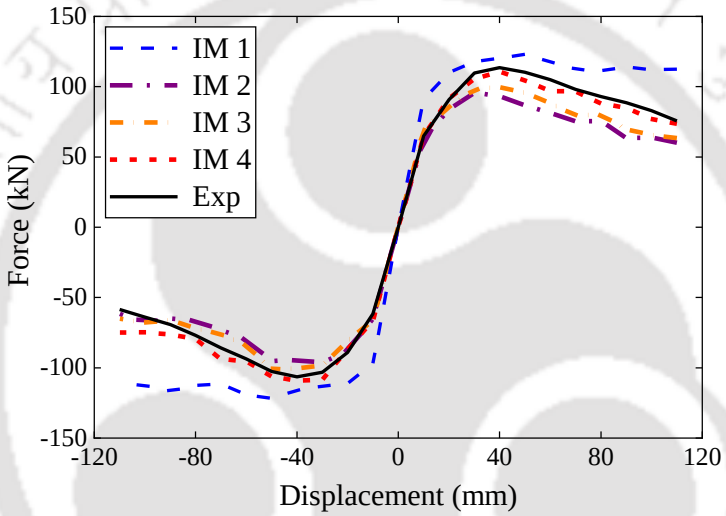

Fig. 5.23. Comparison of envelope curves obtained from FE analyses incorporating (a) various interaction models with experimental data (b) final adopted integration model, IM4 with experimental data.

The contour plot of DAMAGET parameter, which corresponds to the damage parameter of concrete in tension, was used for representation of the damage experienced by the test specimen during the experiment. Fig. 5.24 compares the experimental damage patterns in this region with those obtained from FE analysis. From figure, it may be observed that higher DAMAGET values were typically found near the top end of the jacket. At a distance of roughly 120 mm from the top end of the jacket, no damage was observed in the numerical model. This observation is consistent with the experimental damage pattern shown in Fig. 5.24. Additionally, excessive damage in the RC jacket in the form of spalling of concrete and diagonal cracks during the experiment could be captured well by

the numerical model, which illustrates the damage patterns in red correlating to the maximum DAMETET value of 0.9.

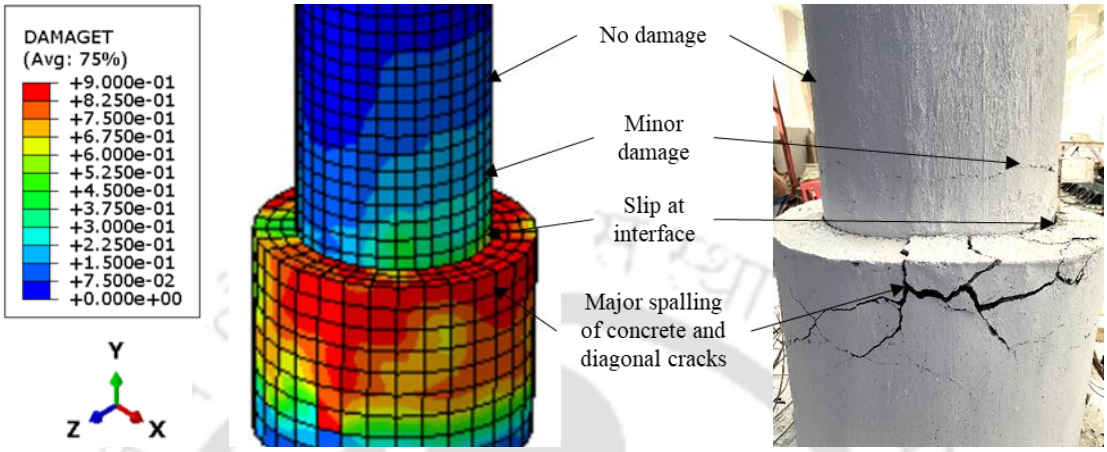

Fig. 5.24. Comparison of damage parameter in tension (DAMAGET) obtained from FE analyses with experimentally obtained damage patterns

As may be observed in Fig. 5.24(b), the interfacial model was also successful in modelling the slip at the jacket-pier interface. Thus, it may be concluded that the FE model adopted in this study is able to reasonably capture the damage patterns observed during experiment as well as the load-deformation behaviour of the test specimen.

5.6. Concluding remarks

Rehabilitation of severely damaged bridge pier models was done using RC jacketing method. The rehabilitation strategy was aimed to retrieve back at least the lost strength of the damaged bridge pier specimens as compared to its original strength. A plastic hinge relocation technique using RC jacketing was adopted. A loading protocol with increasing multi-cycle displacement history was chosen for the experimental investigation. The damage was observed to shift from the pier-foundation interface to the top end of the jacket. It was observed that the rehabilitated test specimen developed enhanced strength as compared to that of the original test specimen. 3D finite element analyses were also carried out to simulate the lateral cyclic response of the rehabilitated test specimens. The generated numerical model considered material nonlinearities, bond-slip behaviour of the longitudinal reinforcement bars as well as interaction between the jacket and core concrete. A parametric study was carried out to determine the best possible interfacial model to

accurately capture the experimental behaviour of the test specimen. The peak load obtained numerically is in good agreement with that obtained from the experiment with a maximum error in the order of 2.6% and 2.8% in the directions of push and pull respectively. A comparison between the damage patterns obtained during experiment and FE simulation confirmed the accuracy and validity of the FE model.

Chapter 6

Hybrid simulation of retrofitted RC bridge with Fe-SMA

6.1. General

The primary objective of this research is to investigate the seismic performance of rehabilitated RC bridge piers, which were further retrofitted for additional strength and ductility by active confinement using Fe-SMA strips. In this chapter, the framework of hybrid simulation, its numerical and experimental modules are explained in details. Hybrid simulation of an existing bridge is carried out with the retrofitted piers as the physical test specimens. To determine the ultimate capacity of the test specimens, cyclic tests were carried out after completion of hybrid simulation. Comparison of effectiveness of the various Fe-SMA retrofitting schemes was made based on the results of the hybrid and cyclic tests.

6.2. Hybrid simulation

Hybrid Simulation comprises of two key components, which interact with each other as shown in Fig. 6.1. The first component is a discrete model of the structure to be computationally analysed under dynamic loading conditions. The spatial discretization of the problem is done using the finite element method, and the temporal discretization is done using a time-stepping integration algorithm. The second component is the physical specimen that is to be tested in the laboratory along with sensing of response and acquisition of response data. Built-in LVDTs and load cells in the actuators, which facilitates the application of incremental displacements (+/-) calculated by the time-stepping integration algorithm, to the physical substructures through the middleware platform of a controller. The middleware platform provides the means of communication between the numerical module and experimental module in hybrid simulation. Command signal from the controller, in the form of displacement, is imposed on the physical substructure. Corresponding feedback signal, in the form of spring force generated in the test specimen,

is passed on to the time-stepping integration algorithm for advancement of the solution to the next time step of analysis.

In the hybrid simulation test, the 1/5th scaled models of the piers were treated as the physical components of the hybrid simulation of a bridge, while the prototype bridge was simulated numerically. The pier was modelled physically because it undergoes the most extensive damage under earthquake load. The key components of hybrid simulation are shown in Fig. 6.1.

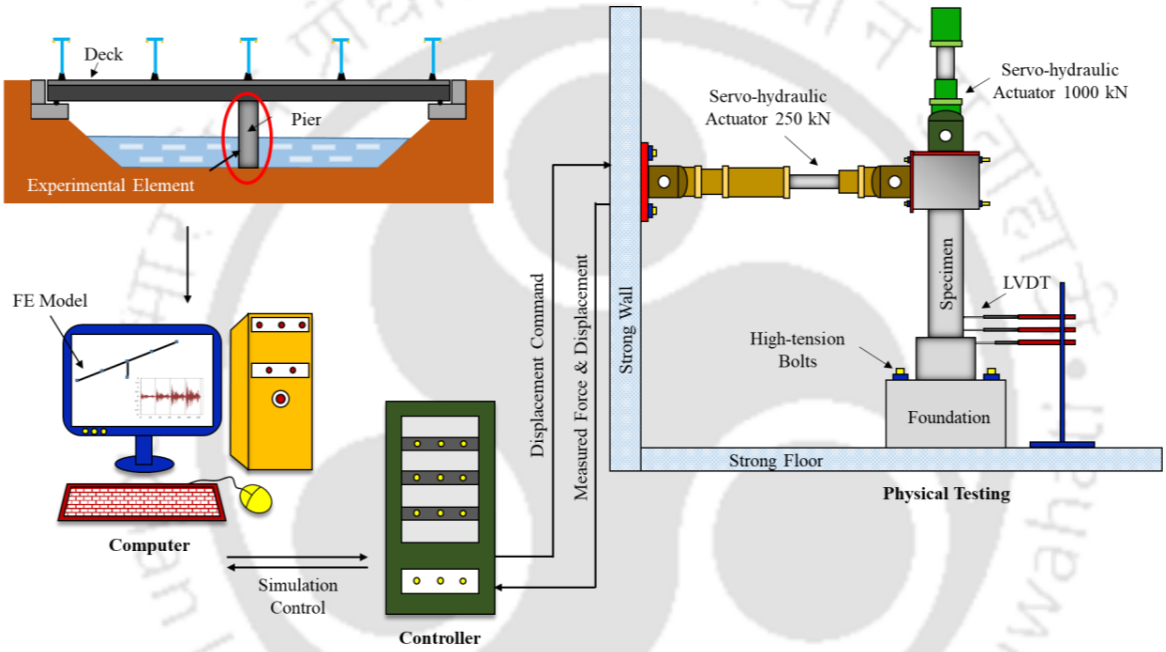

Fig. 6.1. Key components of hybrid simulation

6.2.1. Hybrid simulation framework

In hybrid simulation, dynamic behaviour of the structure can be evaluated by simulating the structural system by a discrete-parameter model that has only a finite number of degrees of freedom (d.o.f.). The resulting equations of motion for such an idealised multi d.o.f. model can be expressed in terms of a system of second-order ordinary differential equations as:

$$\mathbf{M}\mathbf{a}(t)+\mathbf{C}\mathbf{v}(t)+\mathbf{r}(t)=\mathbf{f}(t) \tag{6.1}$$

where **M** and **C** are the assembled mass and damping matrices respectively, **a***(t)* and **v***(t)* the acceleration and the velocity vectors respectively, **r***(t)* the structural restoring force vector and **f***(t)* the external force vector applied to the system.

To perform the hybrid simulation, *OpenSees* (Open System for Earthquake Engineering Simulation) was used to model and analyse the bridge structure. *OpenFresco* (Open-source Framework for Experimental Setup and Control) was used as a middleware to connect the finite element analysis software with an MTS Flex-Test GT controller (4 channels) through MTS Computer Simulation Interface and data acquisition software (Schellenberg, 2008). The generalized α-operator splitting (α-OS) scheme (Chung & Hulbert, 1993), with $\alpha = 0.5$ was used for hybrid simulation as it is a non-iterative implicit time integration method.

For each integration time step, the displacements that were to be applied at the top of the specimen were computed from the discrete model of the bridge structure. These displacements obtained from the numerical model were scaled using *Experimental Control* of OpenFresco platform as per similitude relationship prescribed by Harris and Sabnis (1999). The details of the similitude scaling relationship has been as per scaling factors is presented in Table 6.1. The MTS Flex-Test GT controller facilitated the application of these scaled displacements to physical substructure i.e. the model bridge pier. The built-in DAQ of the controller was used to acquire the feedback signal (resisting forces and displacement) which were again scaled and communicated to the time-stepping integration algorithm of the numerical module for advancement of the solution to the next step of analysis.

Table 6.1 Similitude scaling relationship

Parameter	**Scale factor**	**Prototype (1/5th scaled model)**
Displacement	S	5
Force	S^2	25
Time	$S^{1/2}$	2.24
Acceleration	1	1

Since quasi-static hybrid simulation was adopted for the present study, each load step also included a ramp time which extended the duration of the test as compared to that

of the ground motion considered. Additional compensation for time-delay was not required, since the actuators had sufficient time to attain its target motion.

6.2.2. Integration scheme

Time-stepping integration methods are categorized into two types – implicit and explicit methods. The explicit methods calculate the state of a system at the next time step from the currently known system status. On the other hand, implicit methods calculate the state of a system from the system states at current and next time steps. It can be mathematically depicted as:

Explicit method: $u(t+\Delta t) = f[u(t)]$

Implicit method: $u(t+\Delta t) = f[u(t), u(t+\Delta t)]$

In general, implicit methods used for solution of nonlinear problems need iterations and hence are challenging to execute in hybrid simulation. In addition, there are three requirements for the time-stepping integration methods: convergence, stability and accuracy (Chopra, 2007). Hence, for the present study, the Generalized-Alpha-OS direct integration method is implemented. The algorithm is a combination of the Operator-Splitting technique proposed by Hughes *et al.* (1979) and the Generalized-Alpha method developed by Chung and Hulbert (1993). The resulting integration scheme is a predictor-one-corrector method that does not require iterative equilibrium solution algorithms. The generalized-alpha-OS approach is unconditionally stable as long as the predictor stiffness is greater than the tangent stiffness at any given moment (Combescure & Pegon, 1997). By ensuring this requirement, unconditional stability can be achieved without employing computationally expensive, iterative methods.

The α-OS method developed by Combescure and Pegon (1997) for pseudo-dynamic hybrid simulation is depicted in a flowchart in Fig. 6.2. In this method, the state of a system at the $(n+1)^{th}$ consists of known terms from the previous n^{th} step as well as unknown terms that must be evaluated for arriving at the solution. In hybrid simulation method, displacement is the known term that is applied to the physical component and the measured feedback from it i.e. the displacement and the restoring forces are used for

evaluation of the unknown terms for advancement of the solution to the next time step of analysis.

The mass and damping matrices are represented by **M** and **C** respectively, *a* and *v* are the acceleration and velocity vectors, *r* is the structural restoring force vector and *f* the external force vector applied to the system. u_n, v_n and a_n are the known displacement, velocity and acceleration vectors at time *t*. The initial stiffness matrix of the physical component determined prior to analysis, $\mathbf{K}^{\mathbf{I}}$ is used for correcting the predicted restoring force which is further used for calculation of acceleration at time t_{n+1}.

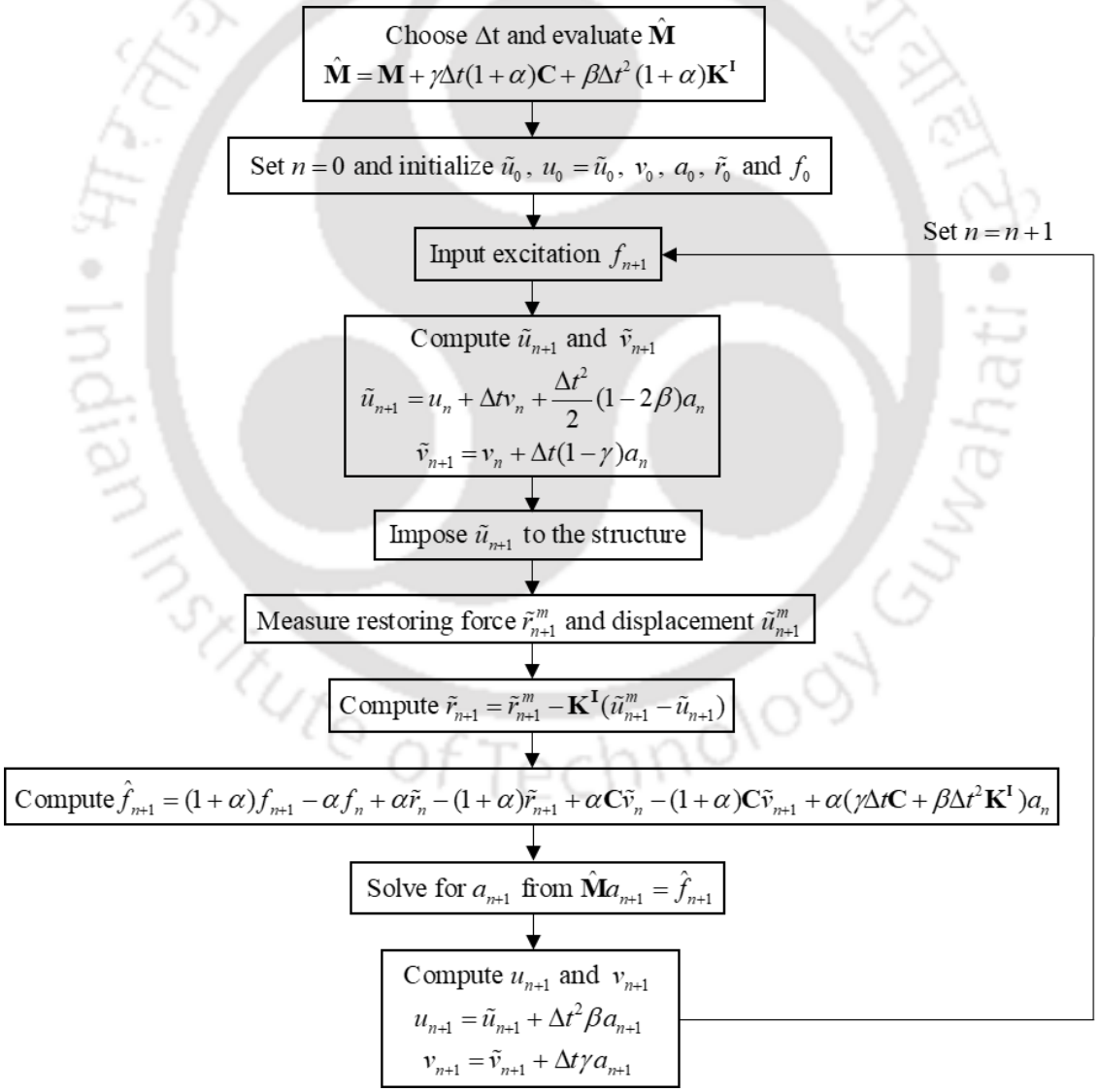

Fig. 6.2. Flowchart for hybrid simulation procedure using α -OS integration scheme (Combescure & Pegon, 1997)

6.3. Numerical model of bridge structure

A prototype bridge in Tripura, as shown in Fig. 6.3 was considered in the present study. The bridge was of the semi-integral type, where the superstructure was integrally connected to the pier. Appropriate boundary conditions were defined at both the ends to allow for any horizontal displacement induced by thermal contraction and expansion, vehicular traffic, or seismic events. The 3D finite element modelling of the prototype bridge was carried out in *OpenSees*, which is an open-source object-oriented software framework developed by McKenna (1997). Details of the various modelling aspects are discussed in the following subsections.

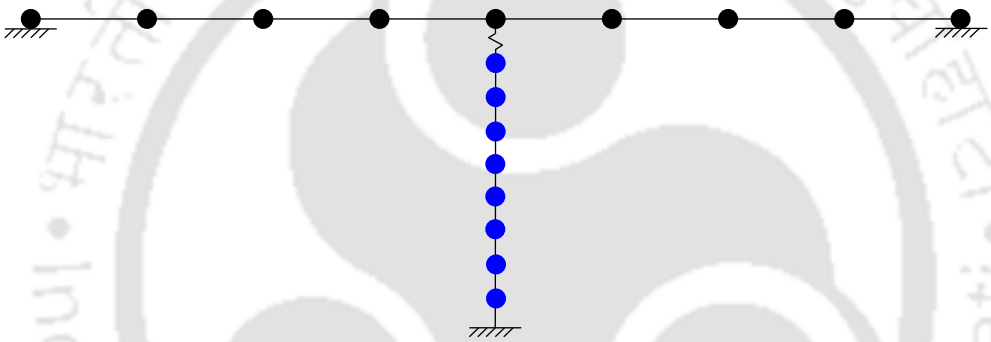

Fig. 6.3. Finite element model of the bridge

6.3.1. Modelling of superstructure

The superstructure of the considered bridge is represented by its deck. Bridge deck is assumed to remain elastic during seismic events and hence was modelled using the *ElasticBeamColumn* element available in the *Opensees* library. The deck ends were provided with rollers. The deck was discretised using 8 numbers of elements of equal length. Masses were lumped at each node based on the tributary length. The sectional properties of the deck of the bridge under study are given in Table 6.1.

Table 6.2. Properties of deck

E (kN/mm^2)	I_z (mm^4)	I_y (mm^4)	A (mm^2)	Weight (kN/m)
2.97 ×10^7	1.25	1.57	3.91	125.43

6.3.2. Modelling of pier

The pier is considered as the most crucial component for resisting lateral seismic loads, and hence was modelled using fibre-based *NonlinearBeamColumn* elements. These are based on displacement-based formulation, where sectional deformations are interpolated from an approximate displacement field and the principle of virtual work is used to form element equilibrium relationship. For approximation of non-linear element response, constant axial deformation and linear curvature are enforced along the length of the element. Additionally, mesh refinement of the element is needed to represent higher order distributions of deformations. Hence, the pier was discretized into eight elements; two in the RC jacket and six in the original pier. The cross-section of the elements was defined using the *FibreSection* approach which comprises of concrete patches and reinforcement layers. The discretization of the fibre section of the pier is illustrated in Fig. 6.4. The base of the pier was considered as fixed.

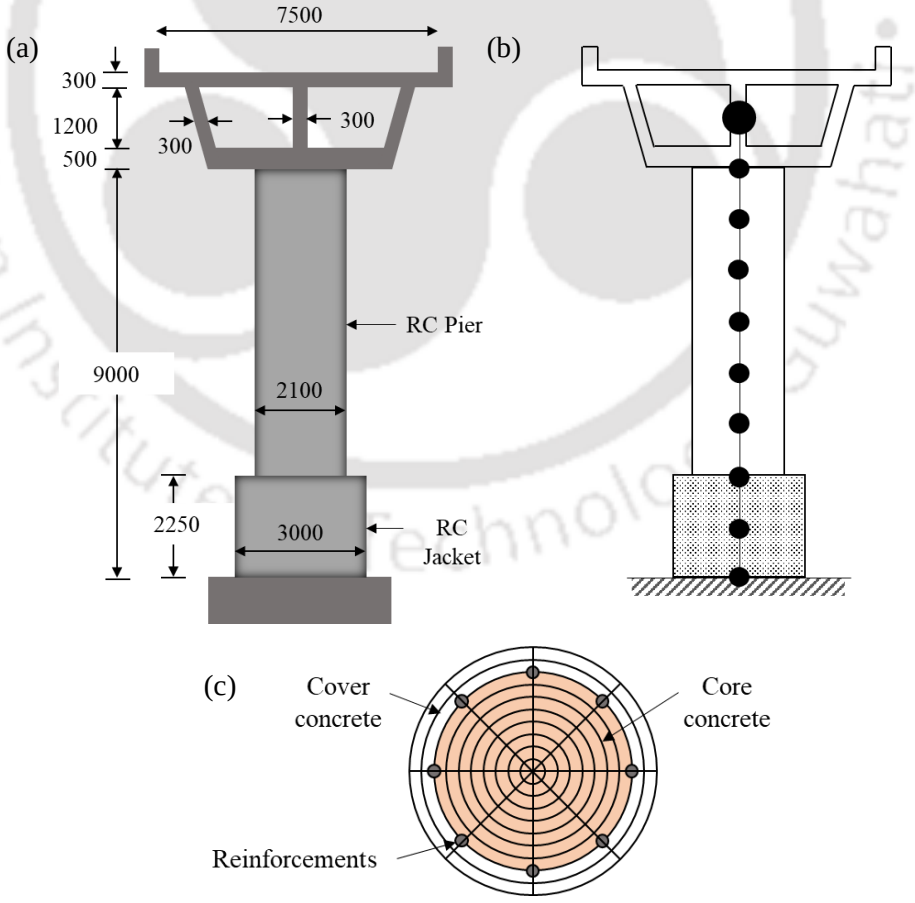

Fig. 6.4. (a) Prototype bridge pier (b) FE Model (c) Pier fibre section

6.3.2.1. Material modelling

Concrete was modelled using the Kent-Scott-Park model in combination with linear tension softening, designated in *OpenSees* as *Concrete02* [Fig. 6.5(a)]. The parameters of *Concrete02* for unconfined concrete were obtained from the results of compressive test of concrete cube and split cylinder test of concrete. Reinforcing steel was modelled as a bilinear material with kinematic hardening material designated in *OpenSees* as *Steel01* [Fig. 6.5(b)]. Based on laboratory test, yield strength of steel was taken as 500 MPa and elastic modulus of steel was considered as 200 GPa. A strain hardening value of 0.018 was used for this material.

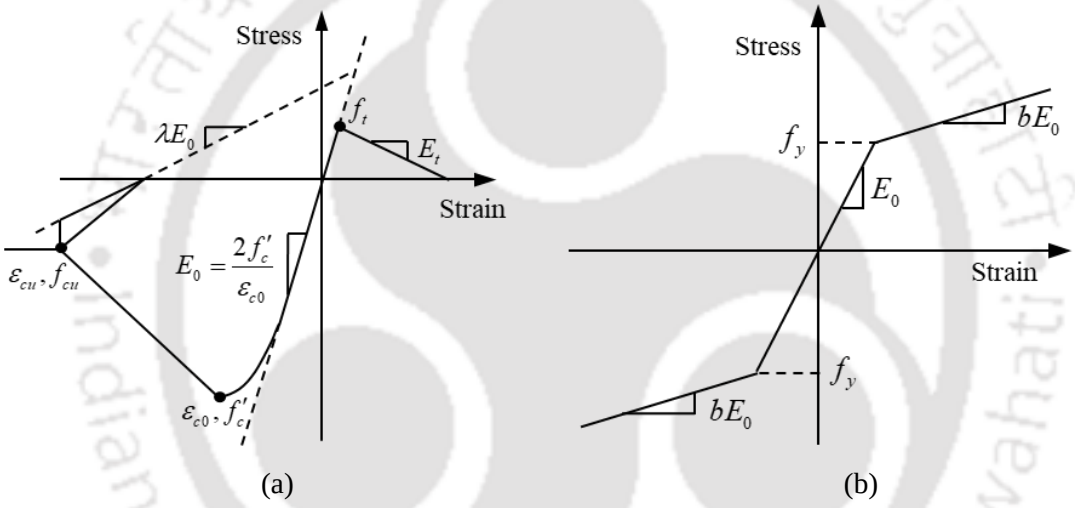

Fig. 6.5. Material modes of (a) concrete (b) steel

6.3.2.2. Modelling of mass

It is essential that the mass of bridge components be precisely estimated since the seismic response of a bridge is sensitive to mass (Nielson, 2005). According to the recommendations made by Aviram *et al.* (2008), the deck should be appropriately discretized, and translational masses should be lumped at each node based on its tributary length. The translational mass of the deck was determined by multiplying the volume of the element by the density of the concrete. The rotational masses were however not considered as the bridge was straight and torsional behaviour was insignificant.

6.3.2.3. Modelling of damping

Damping of a bridge is determined by the condition of the bridge i.e. whether it is cracking or yielding. Newmark and Hall (1982) suggested a damping value of 3-5% of critical damping for reinforced concrete bridges with significant cracking that is subjected to low intensity ground motion. However, the damping value for a yielding bridge with structural damage in the ductile components as a result of severe seismic conditions is estimated at 7-10% of critical damping. Hence, for the initial numerical model, damping was defined as 5% of critical damping as per recommendations of design codes for RC structures. In the present study, the Rayleigh damping model was used for construction of damping matrix by considering a constant damping ratio. The damping matrix is formed by a linear combination of the mass and stiffness matrices multiplied by Rayleigh coefficients which were calculated using the first two modal periods of the structure.

6.4. Details of test specimen

The test specimens consisted of four 1/5th-scaled severely damaged pier models of a prototype bridge in Tripura, India, which were rehabilitated by RC jacketing method designed and implemented as per detailed procedure presented in Chapter 5. The rehabilitation strategy was further aimed at relocation of the plastic hinge away from the pier-foundation interface using RC jacketing, allowing for easier repair and retrofitting in the event of any future occurrences of seismic damages. Further, different strategies were used for fixing Fe-SMA strips in the bridge piers at the relocated plastic hinge zone for enhancement of seismic performance. The details of the retrofitting schemes and its step-by-step implementation procedure is presented in the following sub-sections.

6.4.1. Fe-SMA strengthening schemes

Three retrofitting schemes, as shown in Fig. 6.6(b-d), were adopted in the present study in which Fe-SMA strips were used in the form of (a) hoop reinforcement (H) (b) end anchored (EA) reinforcement and (c) combination of hoop and EA (EAH).

Specimen C is the control specimen. In Specimen H, Fe-SMA hoops were spaced equally in the plastic hinge zone of the bridge pier. It aims at utilizing the recovery stress

of the pre-strained Fe-SMA strips for application of active confinement pressure on the pier as shown in Fig. 6.6(b). In Specimen EA, pre-strained Fe-SMA strips were end-anchored on the surface of the bridge pier as shown in Fig. 6.6(c). Activation of restrained strips resulted in the development of pre-stress (pre-compression) in the concrete at the plastic hinge zone. It is a simple, fast and efficient strengthening method of bridge pier which makes it suitable for easy in-situ implementation. In Specimen EAH, a combination of EA and hoop reinforcement, as shown in Fig. 6.6(d), was studied.

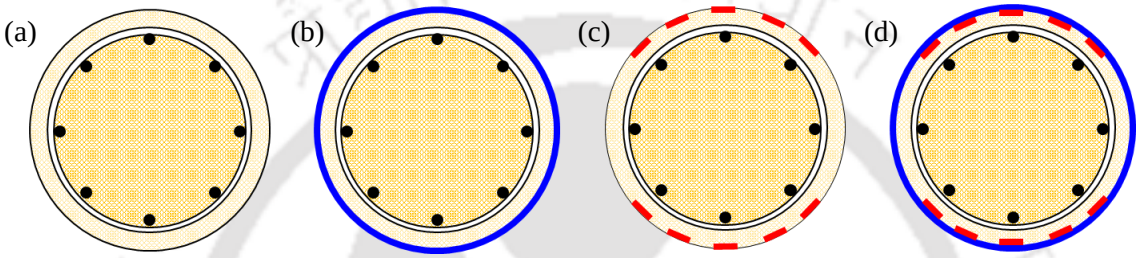

Fig. 6.6. Cross-sectional view of test specimens (a) C (b) H (c) EA (d) EAH

6.4.2. Retrofitting procedure of jacketed bridge piers using Fe-SMA strips

SMA strips of length 9 m, width 120 mm and thickness 1.5 mm were procured from reFer AG (Switzerland). These strips were thermally activated at 160-180°C by resistive heating using a step-down transformer. The desired current density for activation was 6-9 A/mm^2. A high current density is favourable so as to reduce the exposure of concrete to a high temperature for longer duration. Since there was a high current requirement in the laboratory for resistive heating, the width of the strips used in this study was limited to 24 mm. These strips were cut into required lengths in a hydraulic shearing machine and were used for retrofitting. High strength bolts of diameter 8 mm, FBN II 8/10 (Make: Fisher) were used for anchorage of the strips into the concrete. Accordingly, holes were drilled into the Fe-SMA strips in a drilling machine using an 8.5 mm carbide drill-bit as shown in Fig. 6.7(a). For the hoop retrofitting scheme, the strips were bent into the required diameter in a plate rolling machine. The edges of these strips were also bent up to about 30 mm so as to facilitate proper grip by the holders used for resistive heating as shown in Fig. 6.7(b).

For EA and H retrofitting schemes, Fe-SMA strips were directly fixed on the concrete surface as prior cutting of grooves was not required. However, in the EAH scheme,

grooves were first cut on the concrete surface to facilitate proper confinement of concrete in the EAH scheme as shown in Fig. 6.7(c). To protect the surface of the concrete during thermal activation of Fe-SMA strips, a heat-resistant protective coating was applied. Holes were drilled at predetermined locations to facilitate push-through installation of the high-strength anchors as shown in Fig. 6.7(d). After cleaning the drilled holes, Fe-SMA strips were fixed at their locations. The two ends of the Fe-SMA strips were held tightly by the two holders of the step-down transformer and power was turned on. The temperature was continuously checked by an infrared temperature gun as shown in Fig. 6.7(e). Resistive heating of the strips took less than a minute for attaining a temperature of 160°C. Power supply was cut once the desired temperature was attained. Shortening of the strips was visible to the naked eye.

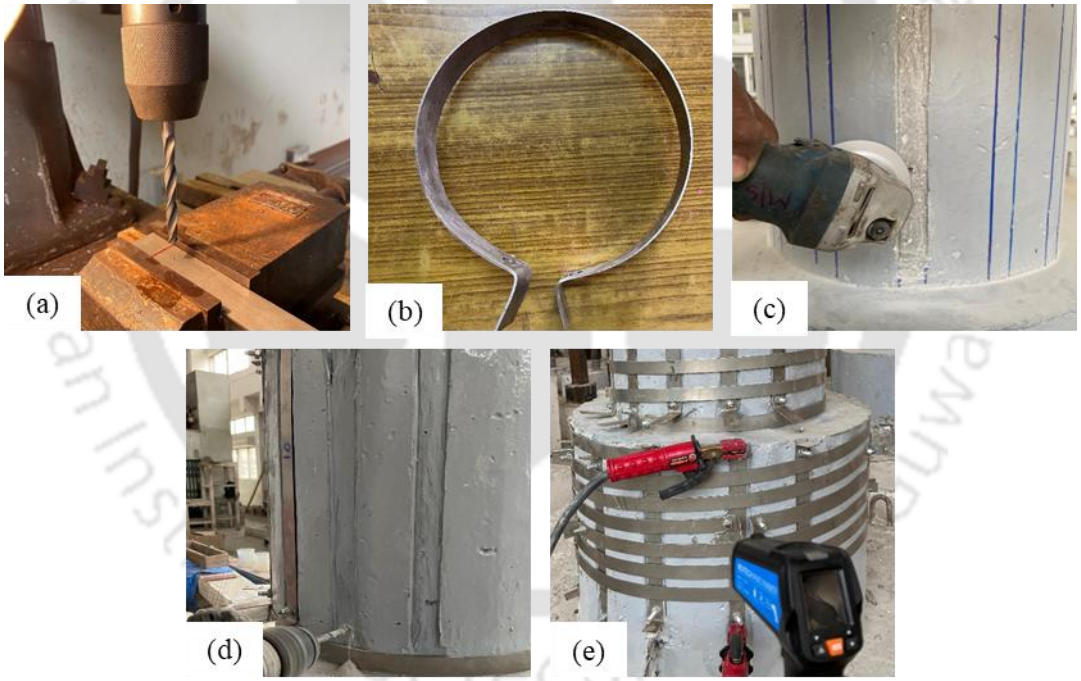

Fig. 6.7. Fe-SMA strengthening scheme (a) drilling of holes in the cut Fe-SMA strips; (b) representative bent strips; (c) cutting of grooves for EAH specimen; (d) drilling of holes and fixing of strips; (e) thermal activation of Fe-SMA strips.

For the EA retrofitting scheme, out of 20 nos. of Fe-SMA strips, 10 nos. in the original pier of length 400 mm and 10 nos. in the jacket of length 300 mm were fixed on the surface of the specimen as shown in Fig. 6.8(a). For the hoop retrofitting scheme, a target confinement pressure of 1.09 MPa was achieved by fixing 10 nos. of Fe-SMA strips

in the original pier at a spacing of 51.5 mm c/c and 9 nos. of Fe-SMA strips in the RC jacket at a spacing of 37.5 mm c/c as shown in Fig. 6.8(b). The EAH retrofitting scheme was a combination of EA and hoop retrofitting scheme as shown in Fig. 6.8(c).

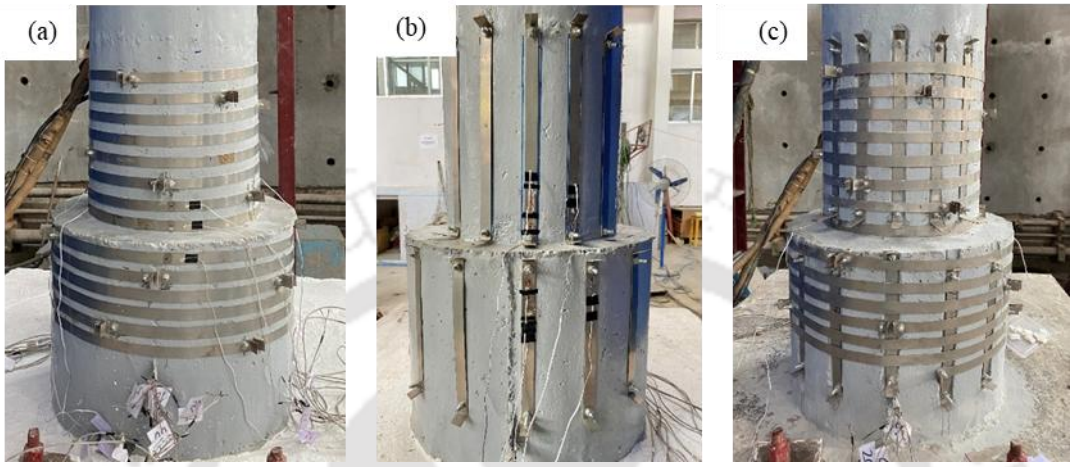

Fig. 6.8. Fe-SMA strengthening schemes (a) H (b) EA (c) EAH

6.5. Experimental programme

6.5.1. Test set-up and instrumentation

The weight of the superstructure on the prototype bridge pier was evaluated using the detailed drawings of the bridge. For the test specimen, scaling factor was decided considering artificial mass simulation, based on the similitude laws proposed by Harris and Sabnis (1999). Accordingly, a servo-hydraulic actuator of 1000 kN capacity (Make: MTS Inc., USA) was used to apply a load of 140 kN to simulate self-weight of the bridge deck, through a loading arrangement as shown in Fig. 6.9. Lateral displacement was applied through a 250 kN servo-hydraulic actuator (Make: MTS, USA) with a stroke length of ± 250 mm. A FlexTest-GT controller (Make: MTS, USA) was used to control the servo-hydraulic actuator. Loads were applied through it and a built-in data-acquisition system (DAQ) of the controller was used to obtain feedback signals. The lateral force and displacement of the test specimen were recorded by the built-in load cell and LVDT of the MTS actuator respectively.

The foundation of the test specimen was fixed to the strong floor with four high tension bolts. The vertical and horizontal actuators were supported against the test frame

and the strong wall of the laboratory respectively as shown in Fig. 6.9. The positioning arrangement of the vertical actuator on the pier head ensured that the imposed load remained vertical, while allowing unrestricted lateral movement of the test specimen throughout the experiment.

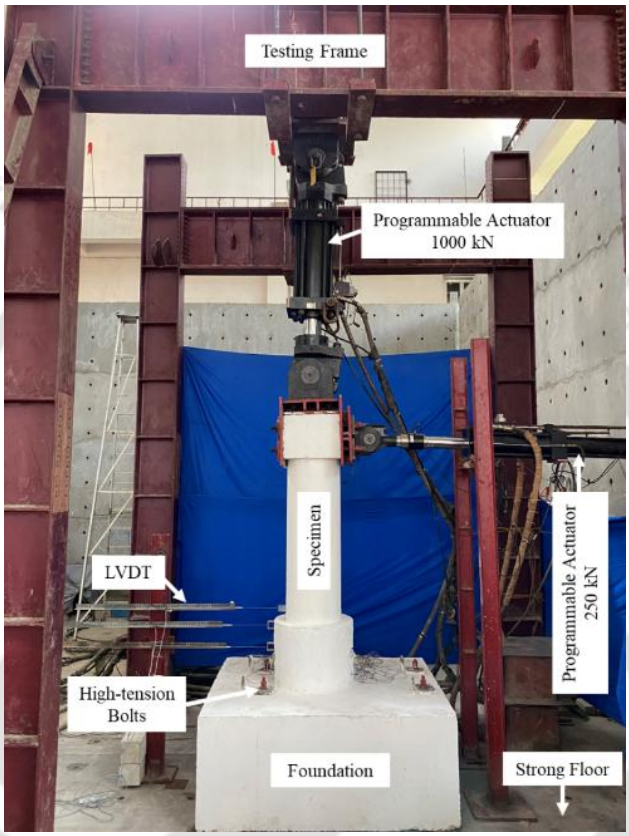

Fig. 6.9. Overall view of test set-up

When the rehabilitated bridge pier was subjected to lateral loads, damage in the pier was most likely to be concentrated near the top end of the jacket, where plastic hinge is likely to be relocated. Hence, lateral deflections in this region of the test specimen were recorded using three LVDTs as shown in the Fig. 6.9. Variation of strain in the Fe-SMA strips in this region was monitored using electrical resistance strain gauges of 350-ohm resistance having a gauge length of 3 mm. Fig. 6.10 shows the position of the strain gauges fixed on the Fe-SMA strips in the test specimens. Data from these strain gauges were used to identify and compare the differences in strain variation in the test specimens.

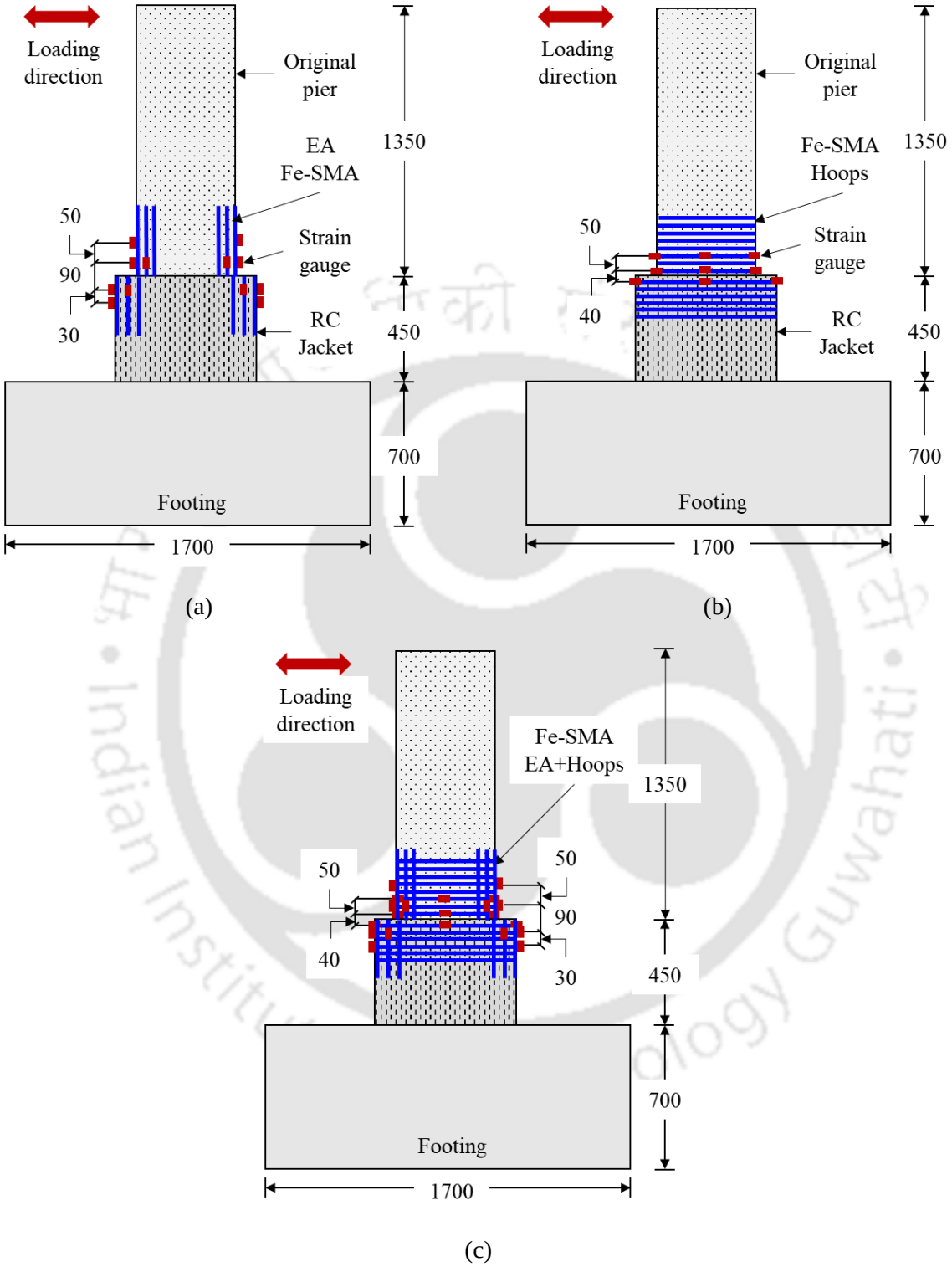

Fig. 6.10. Position of strain gauges in test specimens (a) EA; (b) H and (c) EAH

6.5.2. Selection of Earthquake Time History

In the present study, the time histories of North-South component of El Centro, 1940 Imperial Valley earthquake, which is widely used for seismic response analyses of structures was adopted to excite the test model. The ground-acceleration history was made spectrum compatible with the maximum credible earthquake (MCE) response spectrum for Zone V in India as per IS 1893 Part I (2002). The peak ground acceleration (PGA) and duration of the record was 0.319 g and 32 s, respectively.

One of the important factors that determine the severity of damage sustained by a structure during an earthquake is its intensity. To analyse the behaviour of the structure over a damage spectrum ranging from minor cracking to major damage, the ground motion record was scaled to four seismic intensity levels: 0.5, 1, 2 and 3 times MCE levels. Hence, the earthquake record used in the hybrid simulation comprised of the four scaled segments of the intensity levels, 0.5, 1, 2 and 3MCE of 32 seconds each, that were applied in a sequential order as shown in Fig. 6.11. The ramp time was set to 0.1 s in the *OpenFresco* platform. The actual test duration for hybrid simulation was 520 seconds (Kotoky *et al.* 2018).

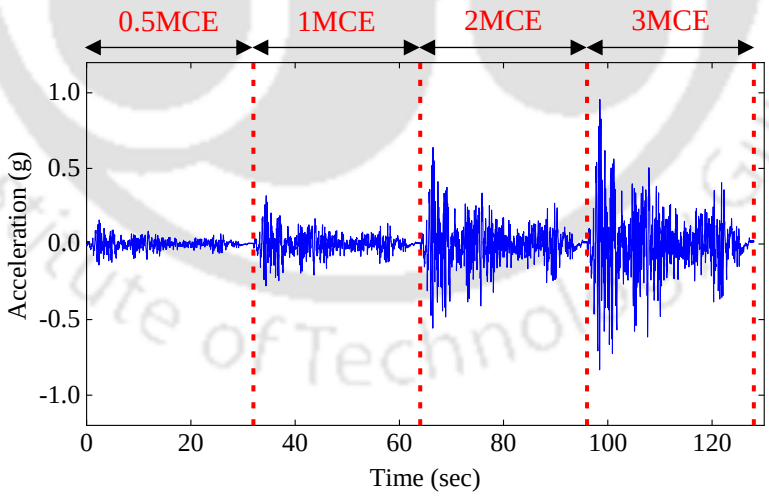

Fig. 6.11. Scaled acceleration time histories of El Centro (N-S), 1940 ground motion of four different intensity levels

6.5.3. Loading protocol for cyclic test

Following the completion of the hybrid simulation, cyclic loading tests were performed to determine the ultimate load-carrying capacity of the bridge piers with various Fe-SMA strengthening schemes. A loading program with increasing multi-cycle displacement loading history was chosen. Lateral cyclic loading was applied at a low frequency of 0.025 Hz. The loading consisted of three cycles of gradually increasing displacement amplitude, starting at ± 10 mm and progressing in 10 mm increments of displacement amplitudes till failure of the specimen. The applied incremental lateral displacement protocol is shown in Fig. 6.12. The test was discontinued when the load capacity of the test specimen reduced to around 70-80% of the peak load and/or upon rupture of the reinforcement bars. Additionally, the damage in jacket-pier interface region was monitored, and the testing was terminated when the damage level was deemed to be significant enough to compromise the overall safety of the test-setup.

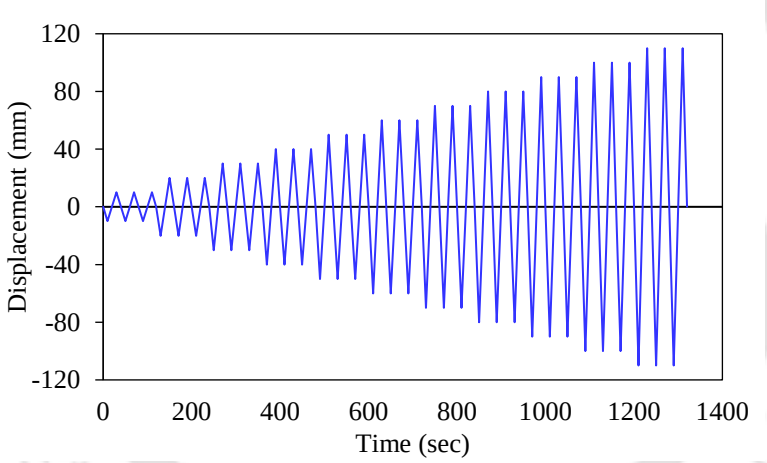

Fig. 6.12. Cyclic loading history

6.6. Test results

This section summarises the results obtained from the experimental study of the test specimens. The key parameters in this experimental investigation are - observed distribution of damage, force-displacement hysteretic behaviour, stiffness degradation, energy-dissipation capacity and ductility. Additionally, the measured strain responses of the different types of test specimens are presented.

6.6.1. Observed distribution of damage

The damage states of all the four specimens, C, EA, H and EAH, at the end of hybrid simulation are shown in Fig. 6.13. In Specimen C, at the end of test under seismic excitation of intensity 2 MCE, the first crack was observed along the circumference of the original pier at a distance of 70-100 mm from the interface of the jacket and original pier as shown in Fig. 6.13(a). During the test under seismic excitation of intensity 3 MCE, slip at the interface of jacket and the original pier was observed. Crack at the top end of the jacket was observed to propagate to the jacket at this stage.

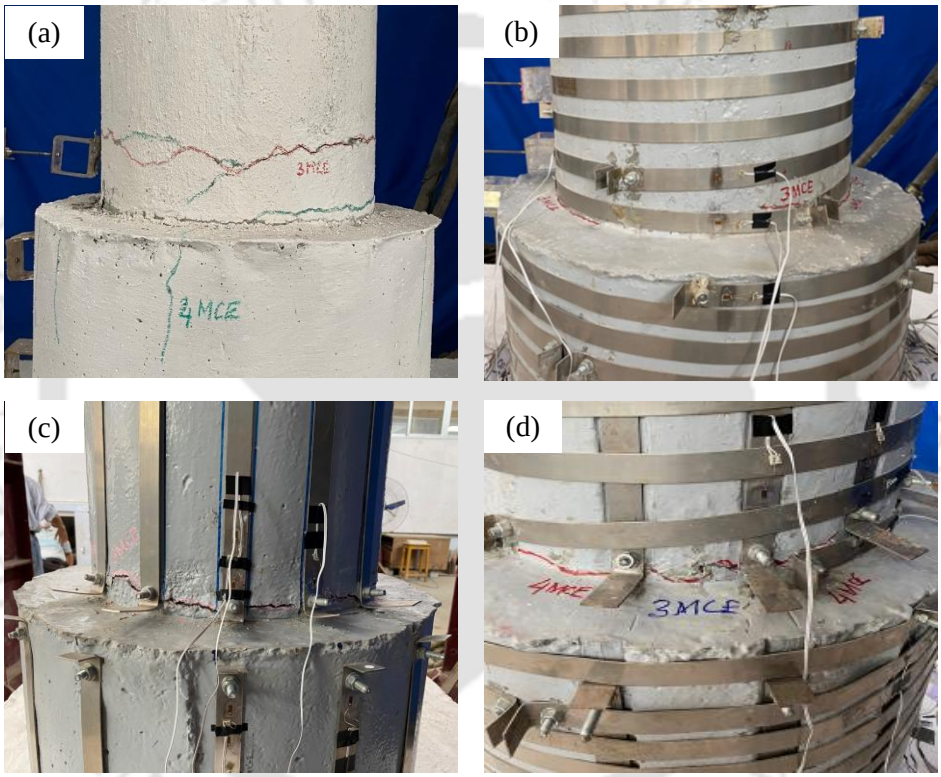

Fig. 6.13. Damage states of test specimens at the end of hybrid simulation (a) C; (b) H; (c) EA; (d) EAH.

The position of first crack for Specimen EA, was at about 10 mm from the jacket-pier interface as shown in Fig. 6.13(b), occurred during the test under seismic excitation of intensity 2 MCE. On further increase in the excitation intensity from 2 MCE to 3 MCE, the crack width increased. Movement between the jacket and the original pier was also observed. Minor cracks were also observed in the jacketed portion of the specimen.

In case Specimen H, cracks at only one level i.e. the jacket-pier interface was observed at the end of 3 MCE test as shown in Fig. 6.13(c). At this stage, slip at the interface

of jacket and the original pier was observed. Similar observations were also recorded for Specimen EAH as shown in Fig. 6.13(d).

The damage states of all the four specimens at the end of cyclic test are shown in Fig. 6.14. In the control specimen, no new cracks were observed till a displacement amplitude of 60 mm. However, cracks formed in the test specimen, during hybrid simulation, were observed to increase in width. At 70 mm displacement, major spalling of concrete occurred at the jacket-pier interface because of lateral thrust of the original pier on the jacket. Spalling of concrete was observed at the top end of the jacket. Rupture of longitudinal reinforcement and increase in width of the cracks were observed at 80 mm displacement. At the end of 90 mm displacement, diagonal crack was observed in the jacketed portion as shown in Fig. 6.14(a). At this stage, the specimen inclined permanently, due to which vertical load could not be maintained. The test was stopped thereafter.

In the Specimen EA, it was observed that the relative movement between the jacket and the original specimen in the vertical direction was less as compared to that of the control specimen. New cracks during cyclic loading were not observed till a displacement amplitude of 60 mm. Minor hairline cracks were observed in the jacket at a displacement amplitude of 70 mm. At a displacement amplitude of 90 mm, an Fe-SMA strip got separated from the specimen as shown in Fig. 6.14(b). The crack width at this stage increased to 5 mm. Spalling of concrete was also observed at the top end of the jacket. At 100 mm displacement, rupture of two longitudinal reinforcement bars was observed. This caused the load-carrying capacity to drop to around 75% of the peak load, leading to termination of the test.

In Specimen H, new cracks during cyclic loading were not observed till a displacement level of 60 mm. Due to slight slippage at the jacket-pier interface, the pier exerted pressure on the jacket during cyclic loading, which lead to formation of cracks on the upper surface of the jacket. At 80 mm displacement, the original pier was observed to undergo rotation about the top end of the jacket, as shown in Fig. 6.14(c). Two longitudinal bars ruptured at 120 mm displacement. There was however, no propagation of cracks to the jacket. This was due to efficient confinement of the concrete in the jacket by the Fe-SMA hoops.

In the EAH specimen, new cracks during cyclic loading were not observed till a displacement level of 50 mm. Increase in widths of existing cracks during hybrid simulation were observed. At 60 mm displacement, small cracks were observed in the lateral loading direction in regions where Fe-SMA hoops were absent. However, no cracks were observed in the perpendicular direction because of the presence of the Fe-SMA hoops. The crack widths increased as the displacement amplitudes increased. At 80 mm displacement, a longitudinal bar ruptured followed by another at 100 mm and the third at 110 mm. The test was terminated thereafter.

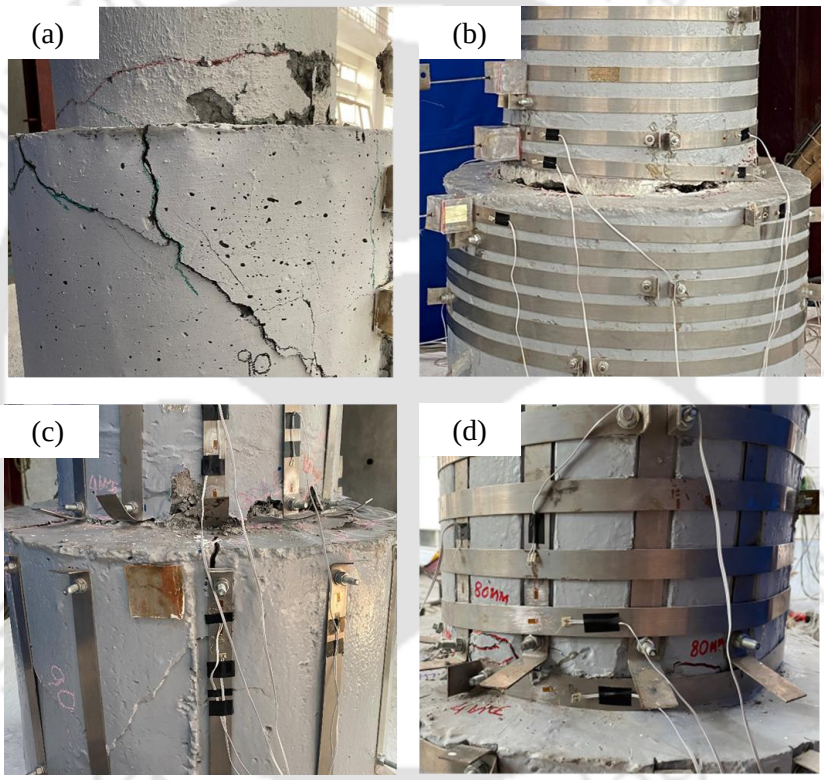

Fig. 6.14. Damage states of test specimens at the end of cyclic test (a) C; (b) H; (c) EA; (d) EAH.

6.6.2. Force-displacement hysteretic behaviour and envelope curve

The lateral force-displacement hysteretic responses of the test specimens under seismic excitation of intensity levels 0.5 MCE, 1 MCE, 2 MCE and 3 MCE are presented in Figs. 6.15-6.18 respectively. At an intensity level of 0.5 MCE, it can be observed that Specimens EA and EAH showed an increase of 13.07% and 17% in peak loads in the push (+) direction and 21.83% and 24.65% in the pull (-) direction respectively as compared to the control specimen C. However, the increase in peak loads for Specimen H was 1.98% and 4.38% in

the push and pull directions respectively. Additionally, Specimens: H, EA and EAH exhibited a decrease by 2.9%, 16.04% and 19.92% respectively in the drift at the top of the pier corresponding to the peak lateral load. This can be attributed to the enhancement of stiffness by the addition of Fe-SMA strips in the test specimens. Similar increase in peak load was observed for the intensity levels 1-3 MCE. The maximum increase in peak load for Specimens H, EA and EAH specimens were 9.16%, 21.83% and 30.03% respectively.

Even though all possible measures were undertaken during rehabilitation of the damaged specimens by RC jacketing including hacking of surface of the old concrete and application of bonding agent before casting of new concrete, some slip was still observed at the jacket-pier interface during hybrid simulation under seismic excitation of 3 MCE intensity level. Hence, owing to poor composite action of the jacket and the original pier and cracking of concrete in the jacketed portion of the specimen, the drift at the top of Specimen C was the highest. Addition of Fe-SMA strips in the form of hoops increased the confinement of the Specimen H in the relocated plastic hinge zone leading to a maximum of 4.48% decrease in the drift at the top of the pier. On the other hand, end-anchored strips increased the stiffness of the relocated plastic hinge zone, thereby decreasing its drift. It may however be observed that this effectiveness reduces with an increase in intensity of seismic excitation, due to slip at the jacket-pier interface. Specimen EAH exhibits superior performance in reducing the drift at the top of the pier specimen as it not only increases the stiffness of the relocated plastic hinge zone but also facilitates proper composite action between the jacket and the original pier by increasing the confinement of the zone and preventing damage in that zone.

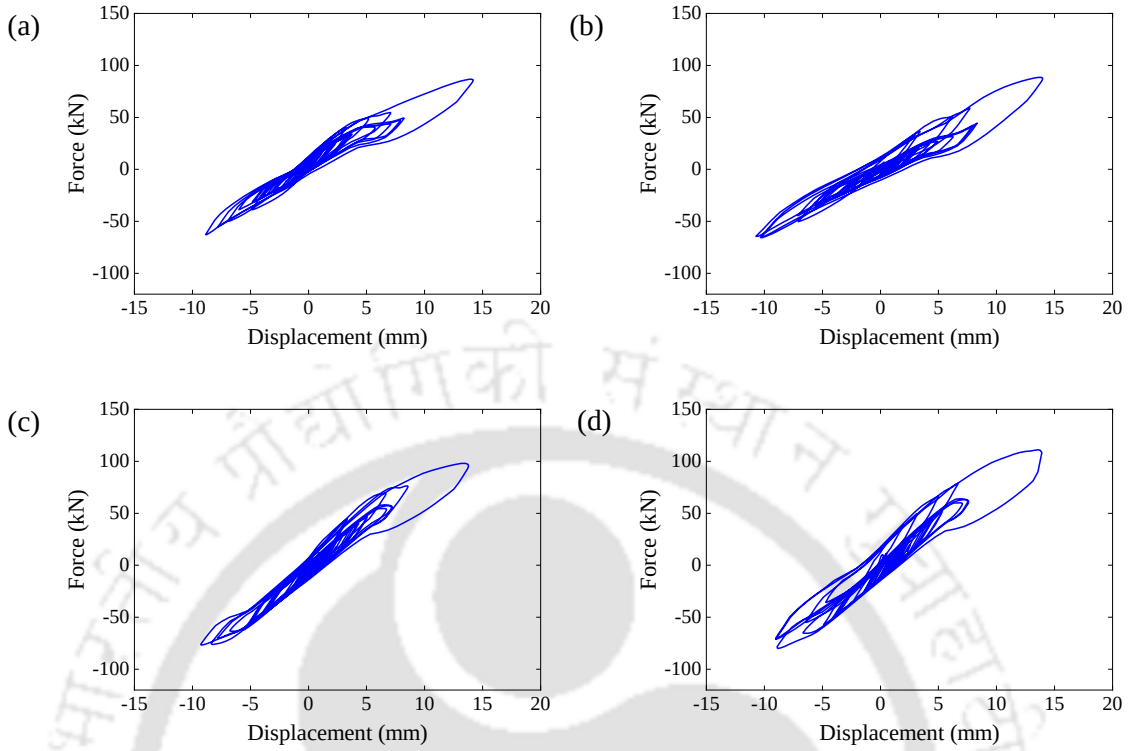

Fig. 6.15. Force-displacement hysteresis at an intensity level of 0.5 MCE of specimens (a) C; (b) H; (c) EA and (d) EAH

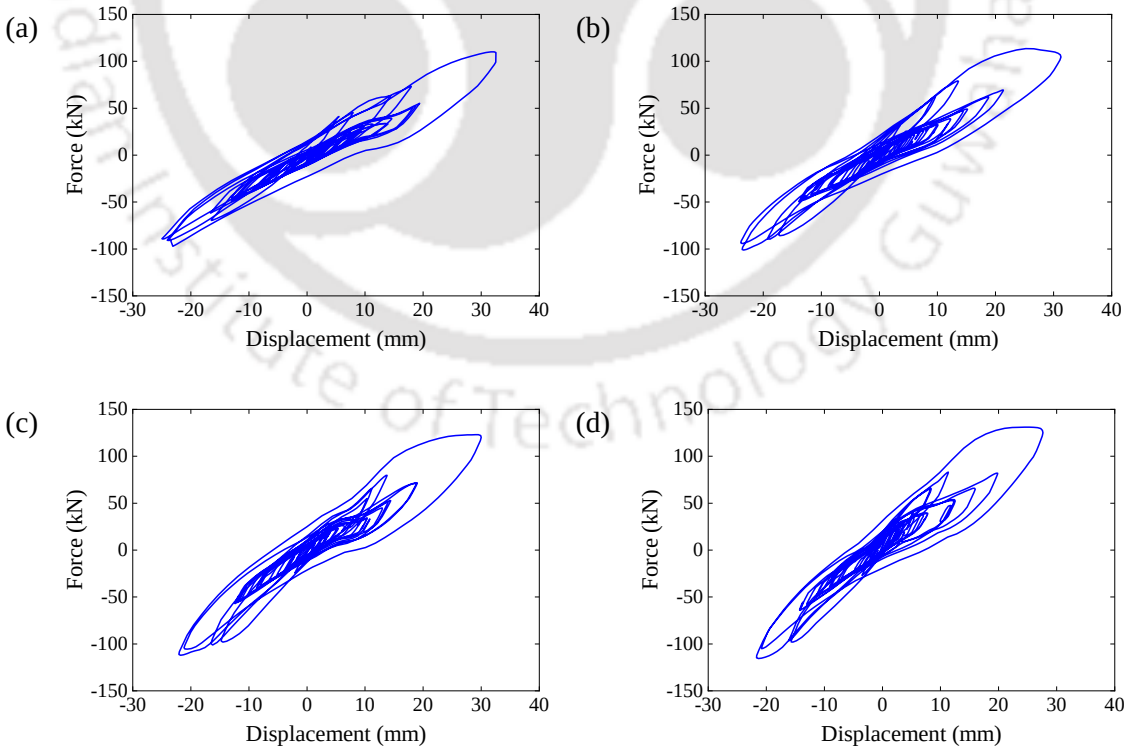

Fig. 6.16. Force-displacement hysteresis at an intensity level of 1 MCE of specimens (a) C; (b) H; (c) EA and (d) EAH

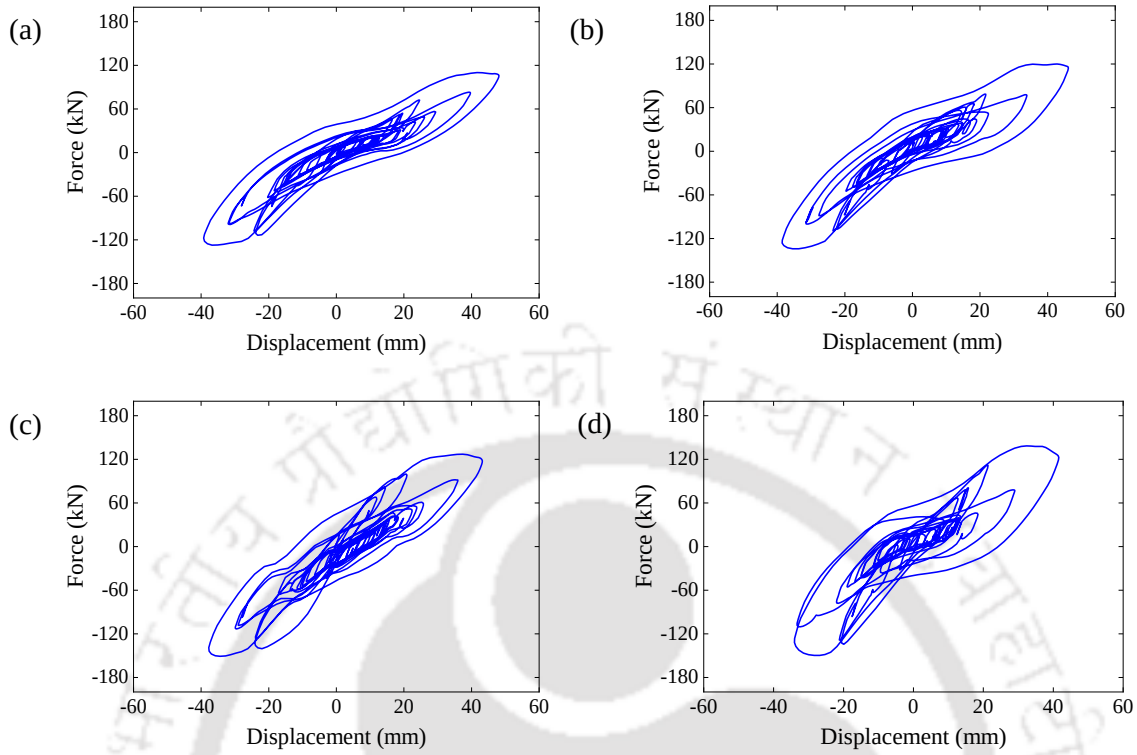

Fig. 6.17. Force-displacement hysteresis at an intensity level of 2 MCE of specimens (a) C; (b) H; (c) EA and (d) EAH

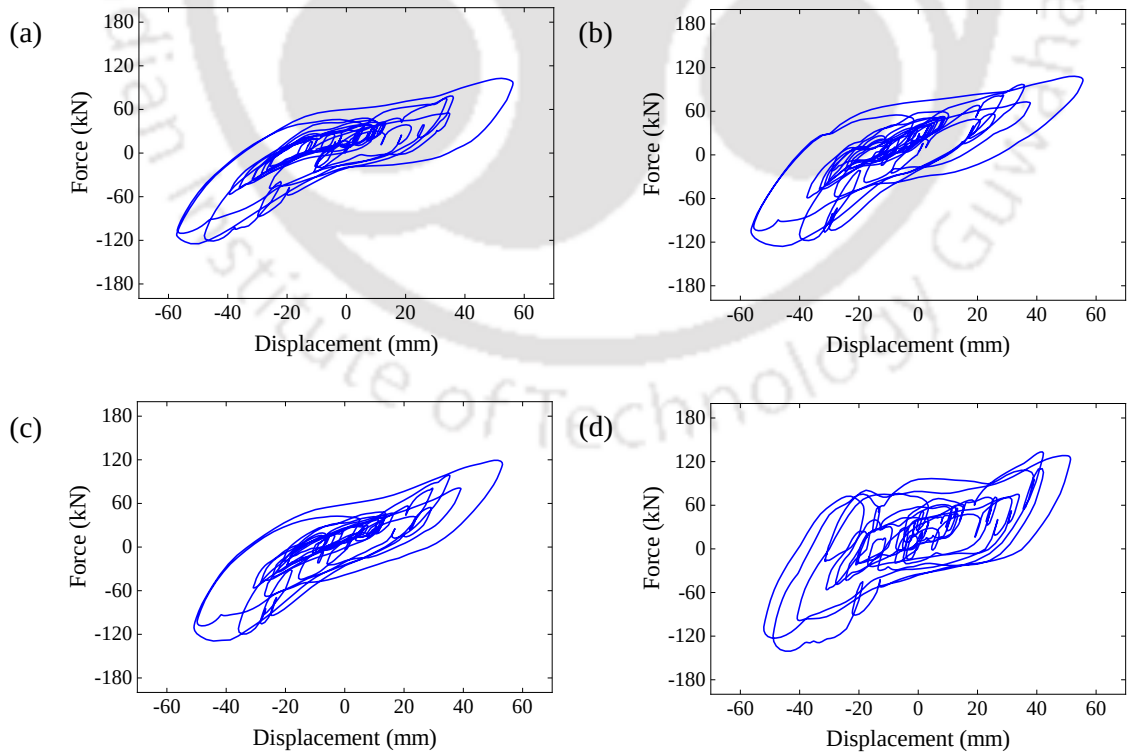

Fig. 6.18. Force-displacement hysteresis at an intensity level of 3 MCE of specimens (a) C; (b) H; (c) EA and (d) EAH

Force-displacement behaviour and backbone curves of all the test specimens at the end of the cyclic loading test are shown in Fig. 6.19 and Fig. 6.20 respectively. It may be observed that Specimen C attained its peak loads at a drift ratio of 3.33% in both push (+) and pull (-) directions. Specimen EA attained its peak loads at 3.33% and 3.89% drift ratios in push and pull directions respectively. In Specimens H and EAH peak load was attained at 3.89% drift ratio in both the directions. The peak lateral load carrying capacity of Specimen H showed an increase of 6.8% as compared to that of the control Specimen C, indicating that Fe-SMA in the form of hoop reinforcement didn't contribute much in increasing the peak lateral load. However, Specimen EA and EAH showed an 18.4% and 35.6% increase in the load carrying capacity as compared to that of the Specimen C. Since concrete is weak in tension, the vertical prestressing effect of end-anchored Fe-SMA strips reduces the tensile stress in concrete, while marginally increasing the overall compressive stress in the compression zone. This establishes that the pre-compression induced by the end-anchored Fe-SMA strips provided enhanced resistance to the applied lateral displacement. The combination of Fe-SMA hoops and end-anchored reinforcement improved the lateral load carrying capacity as well as maximum drift at failure because vertical prestressing with active hoop confinement showed better synergy.

The ultimate lateral displacement of specimens C, EA, H and EAH are 90 mm, 100 mm, 120 mm and 120 mm respectively. The percentage improvement in failure displacement of EA specimen as compared to the control specimen was 11.1% and for H and EAH the increase was 33.3%. This indicated that bridge pier specimens with Fe-SMA in the form of end-anchored reinforcement exhibited marginal improvement in failure displacement whereas specimens with hoop reinforcement showed a very good improvement. Additionally, it is evident that a combination of hoops and end-anchored Fe-SMA was successful in improving both the strength as well as well as ultimate lateral displacement of the un-strengthened control specimen.

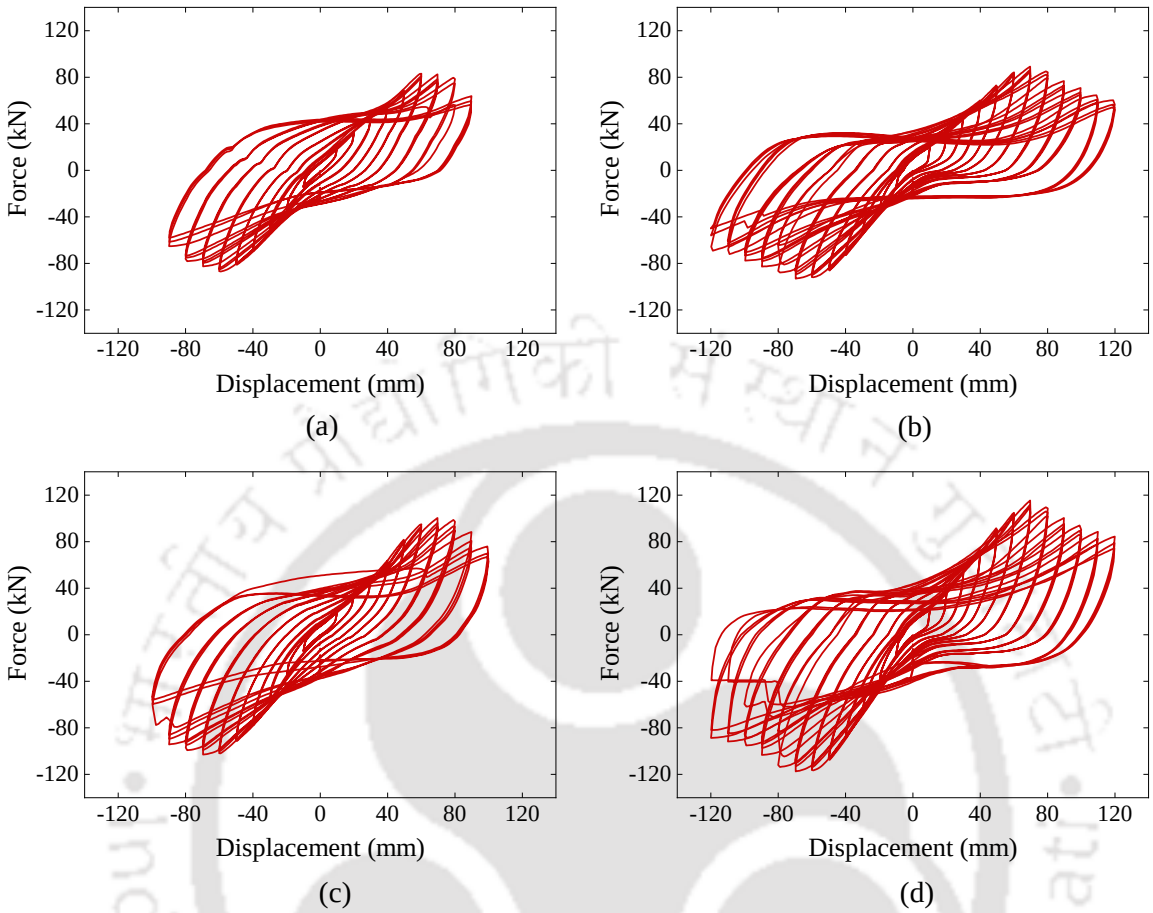

Fig. 6.19. Force-displacement hysteresis of specimens (a) C; (b) H; (c) EA and (d) EAH at the end of cyclic test

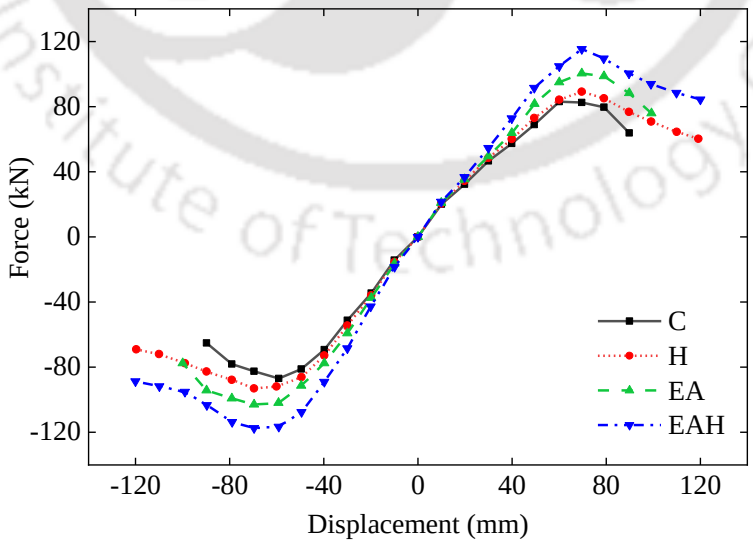

Fig. 6.20. Backbone curve for all specimens at the end of cyclic test

6.6.3. Cumulative Energy Dissipation

Fig. 6.21 shows the cumulative energy dissipation capacities of the test specimens during cyclic test performed after hybrid simulation. In the initial applied displacement amplitudes, the energy dissipation was lower because the damage was limited to the cover concrete only. However, energy dissipation increased with increase in damage accumulation caused by repeated loading-unloading cycles and slip in the jacket-pier interface region. Energy dissipation capacities of Specimens H and EAH were higher because the rate of degradation of strength as observed from the backbone curve (Fig. 6.20) was gradual as compared to Specimens C and EA. Further, Specimens H and EAH could sustain till 6.67% drift. Hence the cumulative energy dissipation capacities of Specimens H and EAH exhibited an increase of 116% and 134% respectively as compared to an increase of 37.81% in Specimen EA.

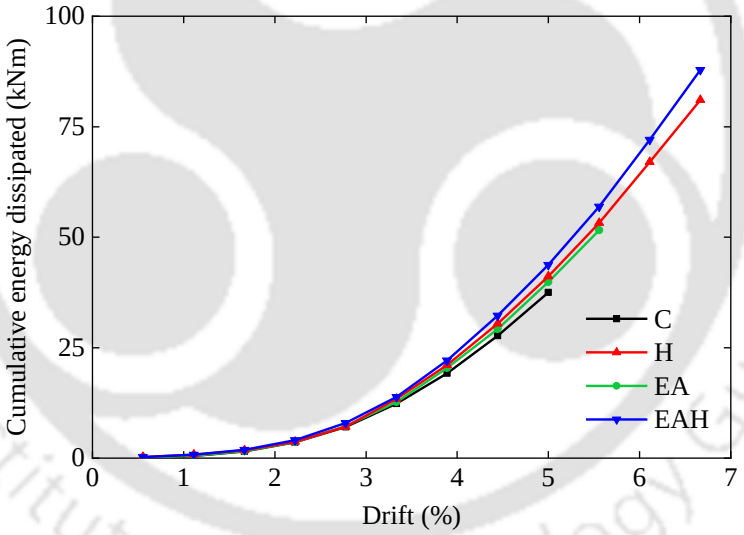

Fig. 6.21. Energy dissipation at different drift ratios in cyclic test

6.6.4. Stiffness Degradation during Cyclic Test

Fig. 6.22 shows the change in stiffness with increase in imposed displacement. The initial stiffness of Specimen EAH was the highest among all the specimens. Addition of Fe-SMA strips in the form of hoops and end-anchored strips in the loading direction resulted in a substantial increase in the stiffness of the bridge pier as shown in Fig. 6.22.

It can be observed that although the Specimens C and H had almost similar initial stiffness, the rate of degradation of Specimen H was however much lower as compared to the control specimen. Further, Specimens H and EAH could sustain a drift of 6.67% as compared to 5% and 5.56% of Specimens C and EA respectively. This behaviour may be attributed to the enhancement of ductility by incorporating Fe-SMA hoops. Specimen EA and control followed a similar degradation pattern while similar trend was observed in Specimens H and EAH.

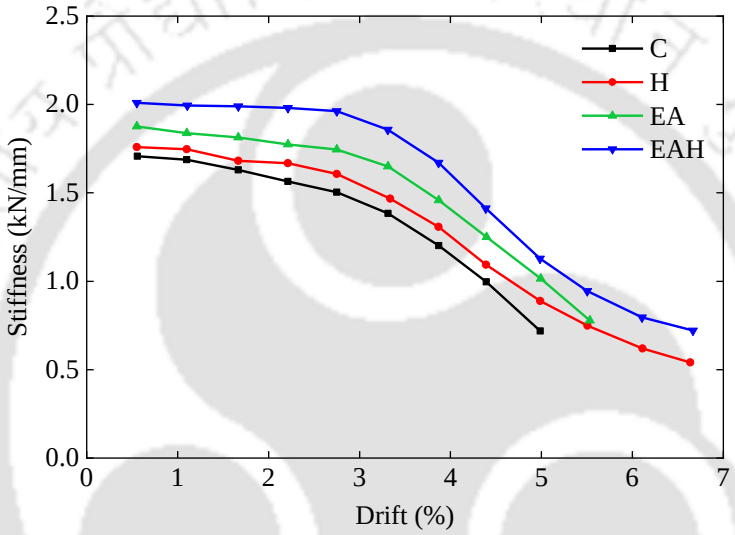

Fig. 6.22. Stiffness degradation during cyclic test

6.6.5. Displacement ductility

Fig. 6.23 shows the displacement ductility of all the specimens during cyclic tests. For the present study, the yield displacement was calculated by the procedure proposed by Shannag *et al.* (2005) details of which are provided in Chapter 5. Accordingly, the displacement ductility value of the test specimens C, EA, H and EAH were found to be 2.09, 2.11, 2.33 and 2.43 respectively. Specimens H and EAH outperformed Specimen EA by exhibiting an increase of 11% and 16.3% as compared to Specimen C, while the increase was only 0.95% for Specimen EA.

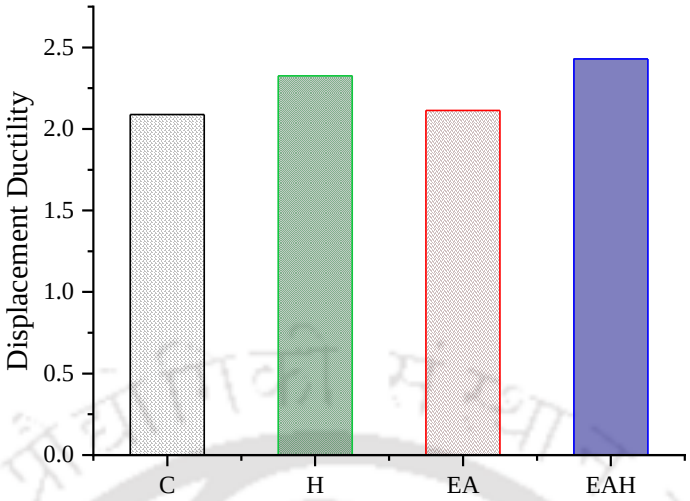

Fig. 6.23. Displacement ductility of all the specimens during cyclic test

6.6.6. Strain distribution in Fe-SMA strips

Strain profiles of end-anchored Fe-SMA strips in the loading direction of Specimens EA and EAH are plotted in Fig. 6.24. In both the specimens, the strain gauges positioned at 485 mm above the pier-foundation interface i.e. 35 mm from the top end of the jacket was observed to display the highest strain as compared to that of the other three strain gauges along the same line in the vertical direction. This was anticipated as the strain gauge in the Fe-SMA strips end-anchored to the original pier would encounter the highest flexural strain due to relocation of the plastic hinge away from the pier-foundation interface. Comparison of strain profiles in Figs. 6.24 (a) and (b) shows that the end-anchored strips in Specimen EAH experienced lower growth of strain at all stages of loading as compared to that of Specimen EA. This was also expected as the additional confinement provided by a combination of hoops to the end-anchored reinforcement resulted in less damage in Specimen EAH.

Similar to axial strain of end anchored strips in Specimens EA and EAH, strain gauges in Fe-SMA hoops of Specimens H and EAH also displayed the highest circumferential strain at 465 mm above the pier-foundation interface i.e. 15 mm from the top end of the jacket as compared to the other two strain gauges shown in Fig. 6.10 (b). Hence, strain data recorded at this position was utilized for comparison of strain developed in the hoops of Specimens H and EAH. Fig. 6.25 compares the circumferential strain histories of the two specimens at an intensity level of 3 MCE.

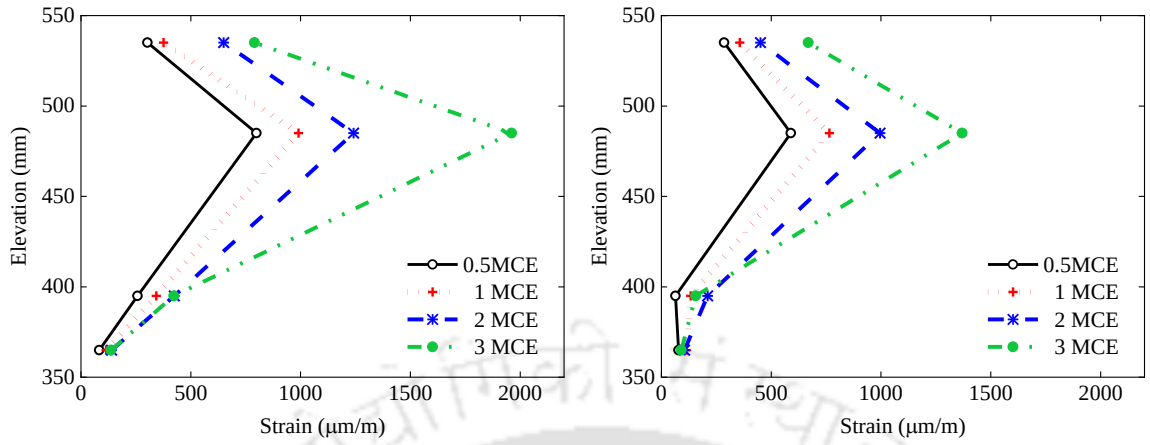

Fig. 6.24. Strain profile of end-anchored Fe-SMA strip in the loading direction of Specimen (a) EA; (b) EAH

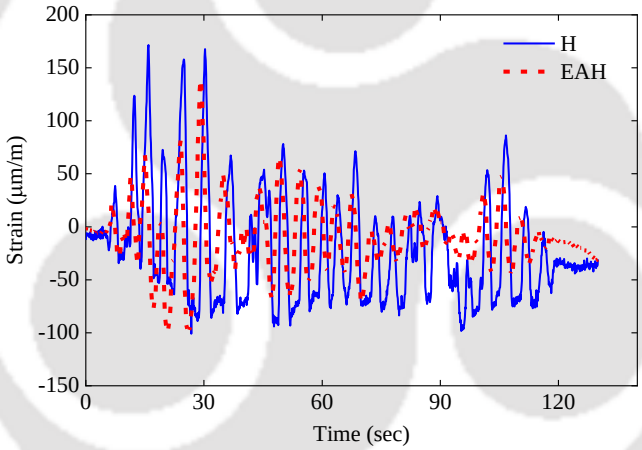

Fig. 6.25. Comparison of strain history of Fe-SMA hoop at a height of 465 mm from the footing in Specimen H and EAH

It is evident from the figure that the Fe-SMA hoops in Specimen EAH showed lower strain as compared to that of Specimen H. This delayed growth of strain observed in Specimen EAH resulted in improved seismic performance as compared to that of Specimens EA and H.

6.7. Concluding remarks

Hybrid simulation of an existing bridge was carried out with retrofitted piers strengthened using different configurations of Fe-SMA strips to explore the effectiveness of the

retrofitting schemes under seismic loading. Three retrofitting schemes were adopted in the present study in which Fe-SMA strips were used in the form of hoop reinforcement (H), end anchored (EA) reinforcement and a combination of hoop and EA (EAH). Cyclic testing was carried out after completion of hybrid simulation to determine the ultimate capacities of the test specimens. Test results demonstrated that bridge pier specimens with Fe-SMA in the form of end-anchored reinforcement exhibited enhanced load carrying capacity and marginal improvement in ultimate displacement, whereas specimens with hoop reinforcement showed improved ductility. Combination of hoops and end-anchored Fe-SMA was successful in improving both the strength as well as ultimate lateral displacement of the control specimen. Strains in end-anchored strips in Specimen EAH experienced lower growth at all stages of loading as compared to that of Specimen EA. Additionally, Fe-SMA hoops in Specimen EAH showed lower circumferential strain as compared to that of Specimen H. This delayed growth of strain observed in Specimen EAH resulted in improved seismic performance as compared to that of Specimens EA and H.

Chapter 7

Calibration of finite element model

7.1. General

This chapter scrutinizes the assumptions made in the numerical modelling of the bridge system in the previous chapter. Evaluation of the assumptions is done based on the observations and results obtained from the hybrid simulation. Comparison of the load-displacement behaviour of the test specimens obtained from the numerical model with that obtained from hybrid simulation reveal certain inconsistencies in the modelling assumptions. Hence, calibration of the FE model is carried out to reduce these inconsistencies. Additionally, details of 3D FE analyses carried out using the calibrated model of the RC jacketed pier presented in Chapter 5 with different Fe-SMA strip configurations, considered during experimental investigation, are presented in this chapter.

7.2. Modelling assumptions

The accuracy with which the response of a bridge structure subjected to seismic loads is predicted, depends to a large extent on the reliability of the numerical model. The preliminary numerical model adopted for simulating the bridge structure is presented in Chapter 6. This initial model was developed with a few assumptions which are commonly used for modelling of bridge structure using finite element method (Frankie, 2013). These are listed below:

- *Deck remains elastic*

  Numerical analyses carried out by several researchers have demonstrated that the deck of a bridge structure remains elastic during the seismic events. In addition to this, seismic design codes all throughout the world, including the Indian codes, recommend that the deck be designed elastically. As a result, the assumption that the deck remains within elastic range under seismic loads is widely accepted.

Hence, changes in the modelling of bridge superstructure were not required for model updation.

- *Fixity at the pier base*

  In the present study, it was assumed that the base of the pier was fixed i.e. with no translational and rotational movement. From hybrid simulation, it was observed that the damage in the bridge pier corresponding to all the four level of seismic excitations was located at the top end of the RC jacket. No rotational movement was observed at the base of the pier due to relocation of the plastic hinge away from the pier-footing interface. Hence, the assumption of fixity at the pier base is acceptable and no modification to the boundary condition at the pier base was necessary for model updation.

- *Rayleigh damping of 5% to account for non-hysteretic damping effects*

  In the preliminary model, damping was modelled using the Rayleigh damping. A damping ratio of 0.05 was assumed and the damping coefficients were determined using the time periods corresponding to the first two modes. The assumed damping ratio is supposed to capture the response in line with the results of hybrid simulations.

- *Monolithic behaviour at the jacket-pier interface*

  Several researchers have carried out numerical analyses of RC columns strengthened by RC jackets and have concluded that interface modelling is essential for representation of true behaviour of the interface. In the initial FE model, a monolithic behaviour was assumed at the jacket-pier interface. During the hybrid simulation tests, it was observed that the RC jacket and the original pier acted/responded monolithically under lower intensity levels of the input excitation. However, at higher intensity levels, slip in the jacket-pier interface was observed. When interfacial slip occurred, the composite action of the jacket and the original pier was affected, leading to reduction in stiffness at the relocated plastic hinge region. Hence, to account for the slip at the jacket-pier interface, calibration of the numerical model was carried out.

- *No bond-slip between concrete and embedded steel bar*

  Not considering bond-slip in a RC fiber-section, results in an overestimation of the stiffness of the FE model. Repeated loading-unloading cycles causes bond slippage between steel and concrete, leading to a decreased energy dissipation, referred to as pinching. This pinching in hysteretic behaviour can affect the overall structural response, hence it needs to be accounted for in the numerical model. In the preliminary model, bond-slip behaviour of the longitudinal rebars were not considered. However, in order to further improve the accuracy of the response as obtained from the numerical model, updation in the modelling of embedded rebars was carried out.

7.3. Comparison of hybrid simulation results with preliminary numerical model

The force-displacement hysteretic responses of the control specimen C obtained from the preliminary numerical model for all the intensity levels are compared to those obtained from hybrid simulation, as shown in Fig. 7.1(a-d). At a lower intensity of seismic excitation i.e. 0.5 MCE, it can be observed that the peak force and its corresponding displacement closely matches with the experimental results. This can be attributed to the fact that the specimen did not experience damage, implying that it was still in the elastic range. At this stage, the original pier and the RC jacket acted monolithically. However, with increase in the intensity level of seismic excitation, some slip was observed at the jacket-pier interface which led to increase in the drift at the top of Specimen C. Further, at higher intensity levels, there is a considerable likelihood of bond-slip at the rebar-concrete interface.

However, results from the preliminary numerical model demonstrated higher values of peak-load and lower values of corresponding displacement because of the assumption of monolithic behaviour between the original pier and the jacket. Hence, the preliminary numerical model for Specimen C was updated using experimental results to account for its post elastic behaviour as observed from experiments. This updated model was further utilized in the modelling of Specimens H, EA and EAH.

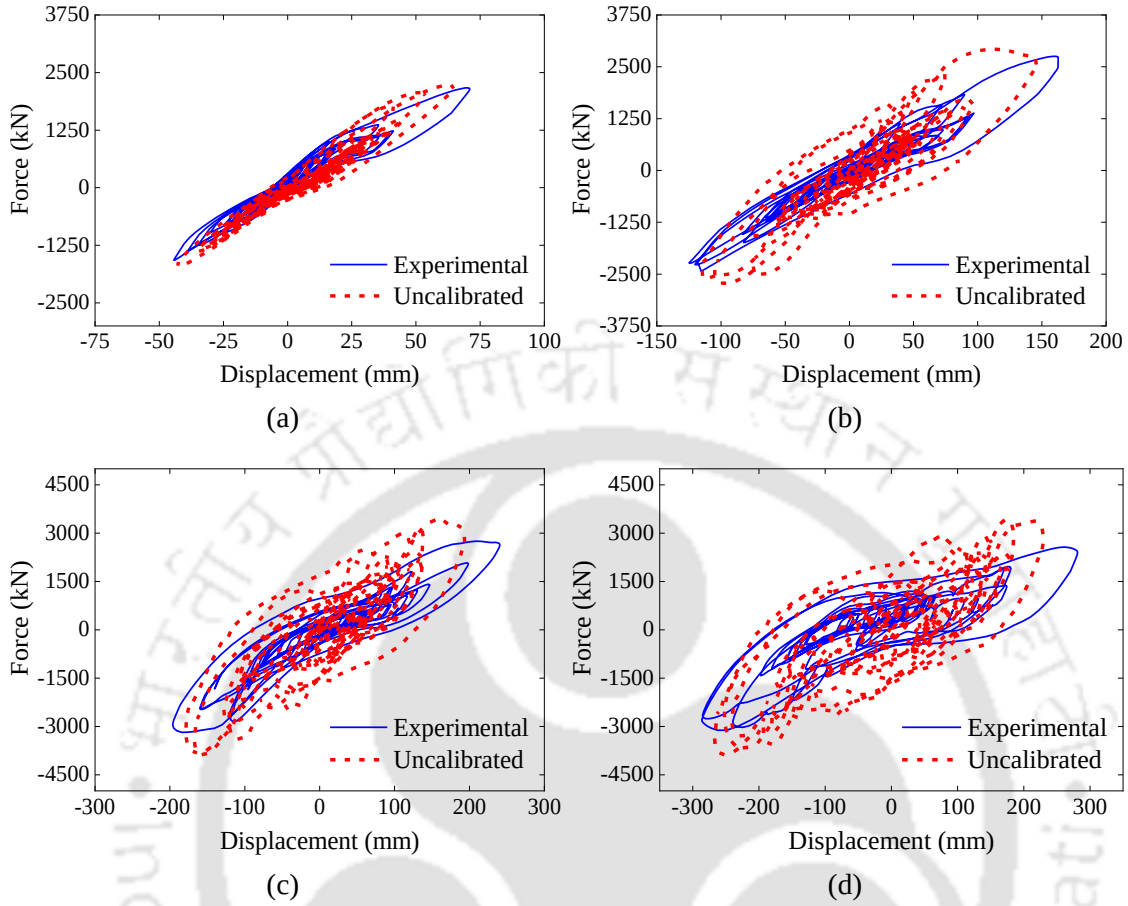

Fig. 7.1. Comparison of experimental results with results from uncalibrated numerical model of Specimen C for (a) 0.5 MCE; (b) 1 MCE; (c) 2 MCE and (d) 3 MCE intensity levels.

7.4. Model calibration procedure and results

The model calibration procedure and the results obtained from the updated models are presented in the following sub-sections:

7.4.1. Specimen C

To account for the bond-slip at the concrete-rebar interface, the present study incorporates the modified rebar model proposed by Dehestani and Mousavi (2015) to consider bond-slip effects of embedded reinforcement in the FE model. It is a bi-linear stress-strain relationship comprising of a linear elastic portion, with a modified elastic modulus E_s^*, till attaining f_y^* followed by a linear hardening portion. Details of the model are furnished in Chapter 5.

To predict the behaviour of the RC jacketed bridge pier model by taking into consideration the effect of slip between the jacket and the pier, a slip co-efficient η was used. A slip coefficient of 1 implies there is no loss of slip at the interface due to friction and the section behaves monolithically. The concrete strength as well as the yield strength of the steel bars in the jacket was reduced with η. For calibrating the numerical model of the Specimen C, a parametric study was conducted to arrive at the value of η. It was found that for a value of η = 0.9, the numerical model was able to closely simulate the experimental behaviour during hybrid simulation. Hence, the strength of concrete in the RC jacket and the yield strength of the steel bars in the jacket were reduced to 0.9 times its original value to account for the interfacial slip. Fig. 7.2 shows the comparison of results obtained from the FE analysis incorporating the updated model with those obtained from hybrid simulation.

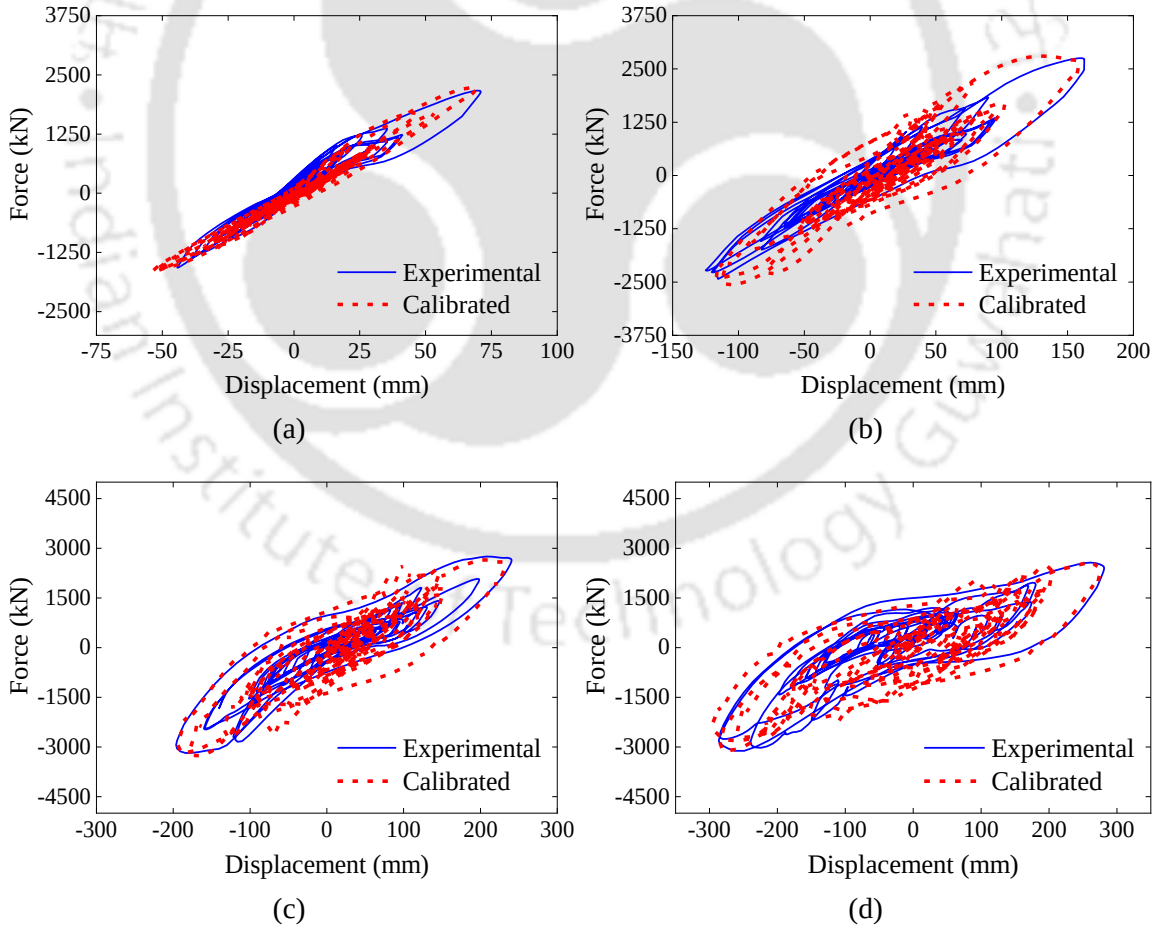

Fig. 7.2. Comparison of experimental results with results from calibrated numerical model of Specimen C for (a) 0.5 MCE; (b) 1 MCE; (c) 2 MCE and (d) 3 MCE intensity levels.

7.4.2. Specimen H

The prototype Specimen H and its retrofitting scheme are shown in Figs. 7.3(a) and (b) respectively. The FE model of the specimen is divided into four zones: Zone 1-RC jacketed region; Zone 2-Fe-SMA hoop confined RC jacketed region; Zone 3-Fe-SMA hoop confined original RC pier and Zone 1- original RC pier as shown in Fig. 7.3(c). Modelling of Zones 1 and 4 have already been discussed in Chapter 6.

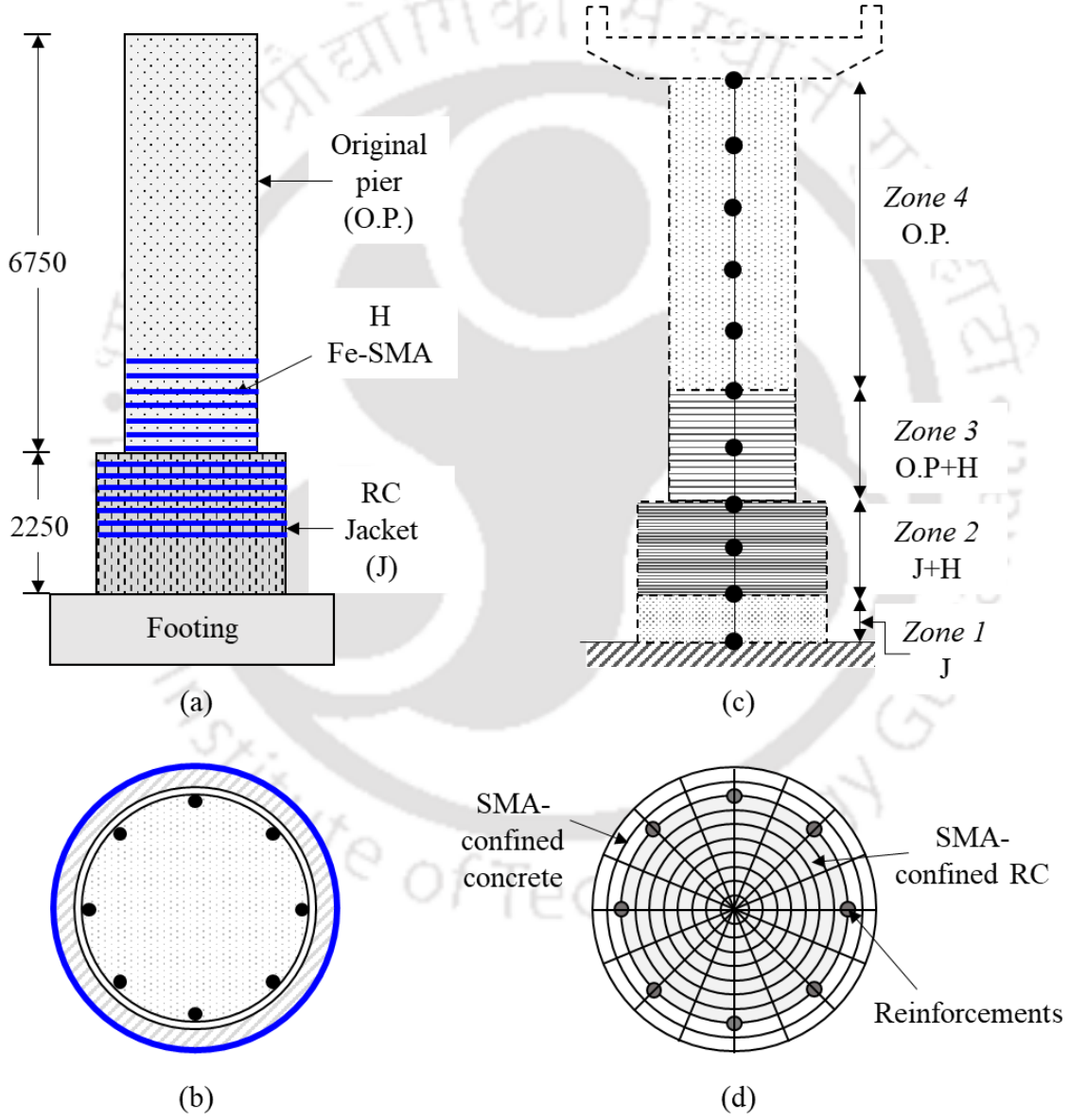

Fig. 7.3. (a) Prototype Specimen H; (b) cross-section; (c) FE model and (d) fibre section of the model

The fibre section of the retrofitted zones of Specimen H is shown in Fig. 7.3(d). To incorporate the effects of active confinement induced by the external Fe-SMA strips and internal steel stirrups, the parameters of core concrete were determined using the expressions proposed for Fe-SMA confined reinforced concrete, as presented in Section 4.8. Since the cover concrete was confined with the SMA hoops only, expressions proposed for Fe-SMA confined concrete (Section 4.4) were utilized for determination of parameters of the stress-strain model. The strengths of the core and cover concrete in Zone 2 was reduced to 0.9 times its original value to account for loss of slip at the interface. Fig. 7.4 shows the comparison of results obtained from the FE analysis with those obtained from hybrid simulation. Results show that the FE model could quite reasonably simulate the experimental behaviour of Specimen H.

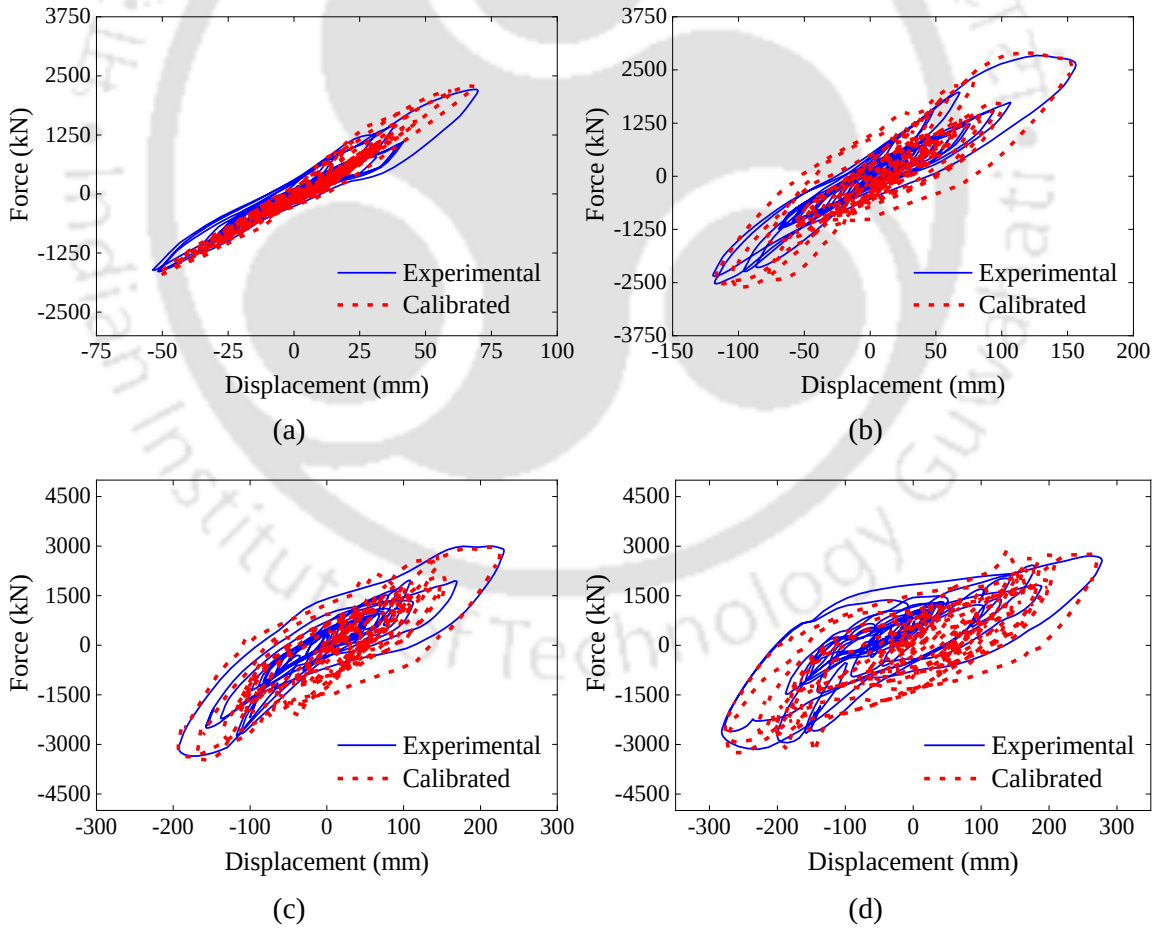

Fig. 7.4. Comparison of experimental results with results from calibrated numerical model of Specimen H for (a) 0.5 MCE; (b) 1 MCE; (c) 2 MCE and (d) 3 MCE intensity levels.

7.4.3. Specimen EA

The prototype Specimen EA and its retrofitting scheme are shown in Figs. 7.5(a) and (b) respectively. The FE model of the specimen is divided into four zones: Zone 1-RC jacketed region; Zone 2- RC jacketed region with end-anchored Fe-SMA reinforcement; Zone 2- original pier with end-anchored Fe-SMA reinforcement and Zone 1- original RC pier, as shown in Fig. 7.5(c).

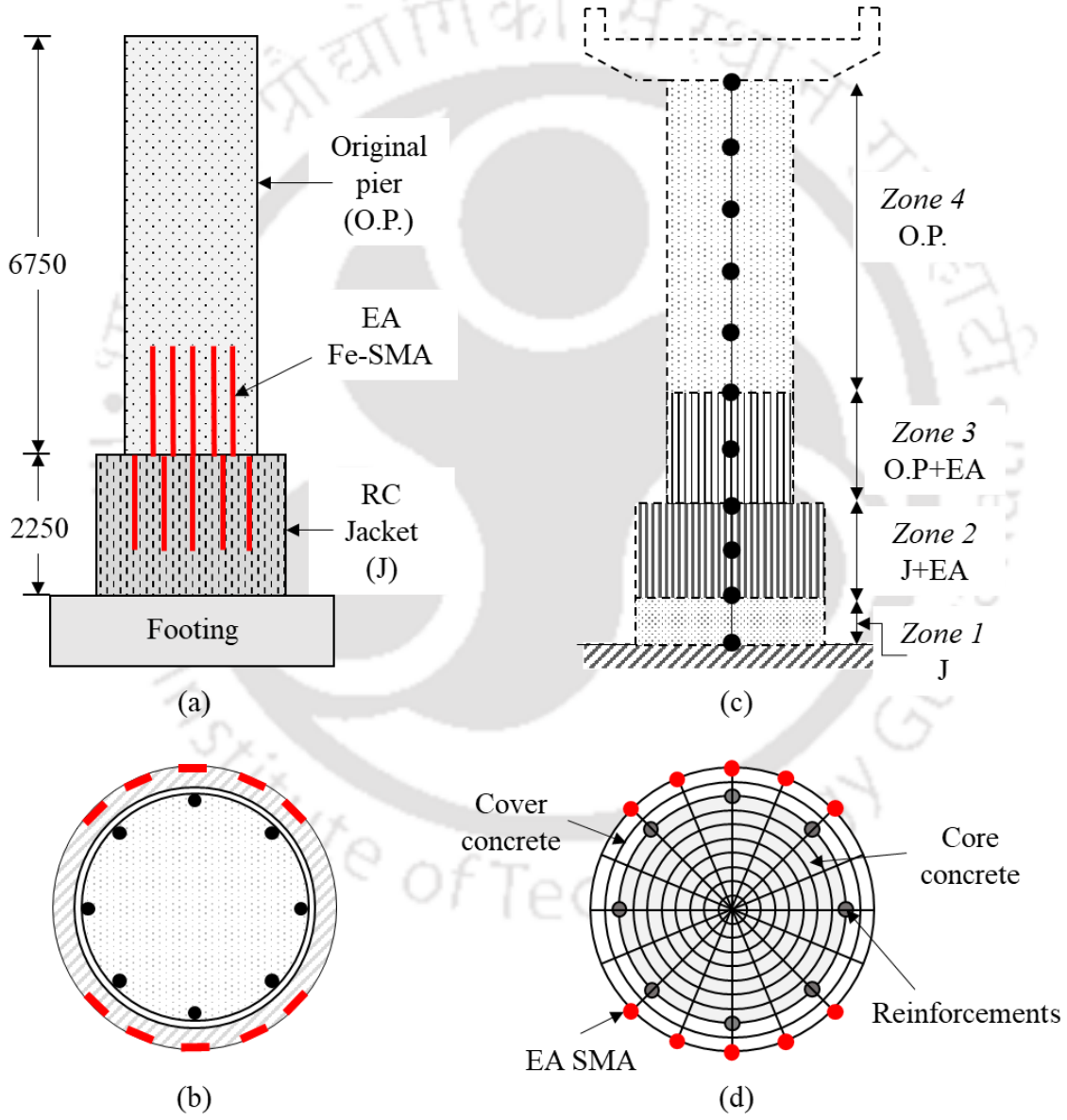

Fig. 7.5. (a) Prototype Specimen EA; (b) cross-section; (c) FE model and (d) fibre section of the model

The fibre section of the retrofitted zones of Specimen EA is shown in Fig. 7.5(d). The end-anchored Fe-SMA strips in Zones 2 and 3 were modelled using reinforcement layers, similar to that used for modelling of longitudinal steel bars. The Fe-SMA strips were modeled by a Giuffre-Menegotto-Pinto uniaxial strain-hardening material model available in OpenSees as *Steel02* with a hardening ratio of 1, as the material behaves linearly in the strain range it experienced during experiments. An initial stress of 350 MPa corresponding to the recovery stress of the Fe-SMA strips was assigned to its material model. Fig. 7.6 shows the comparison of results obtained from the FE analysis with those obtained from hybrid simulation. The FE model of Specimen EA was able to closely represent its experimental behaviour.

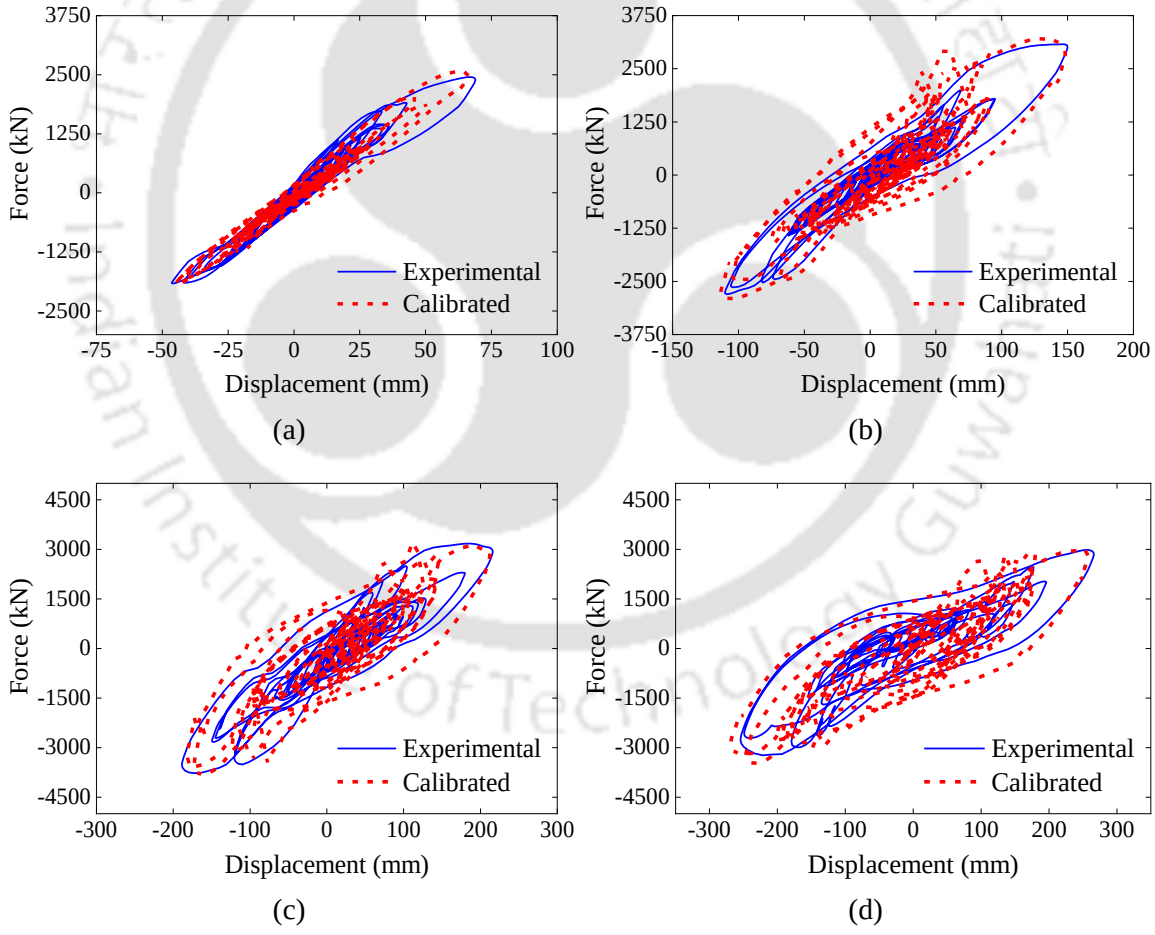

Fig. 7.6. Comparison of experimental results with results from calibrated numerical model of Specimen EA for (a) 0.5 MCE; (b) 1 MCE; (c) 2 MCE and (d) 3 MCE intensity levels.

7.4.4. Specimen EAH

The prototype Specimen EAH and its retrofitting scheme are shown in Figs. 7.7(a) and (b) respectively. The FE model of the specimen is divided into four zones: Zone 1-RC jacketed region; Zone 2- RC jacketed region with hoops and end-anchored Fe-SMA reinforcement; Zone 2- original pier with hoops and end-anchored Fe-SMA reinforcement and Zone 1- original RC pier, as shown in Fig. 7.7(c).

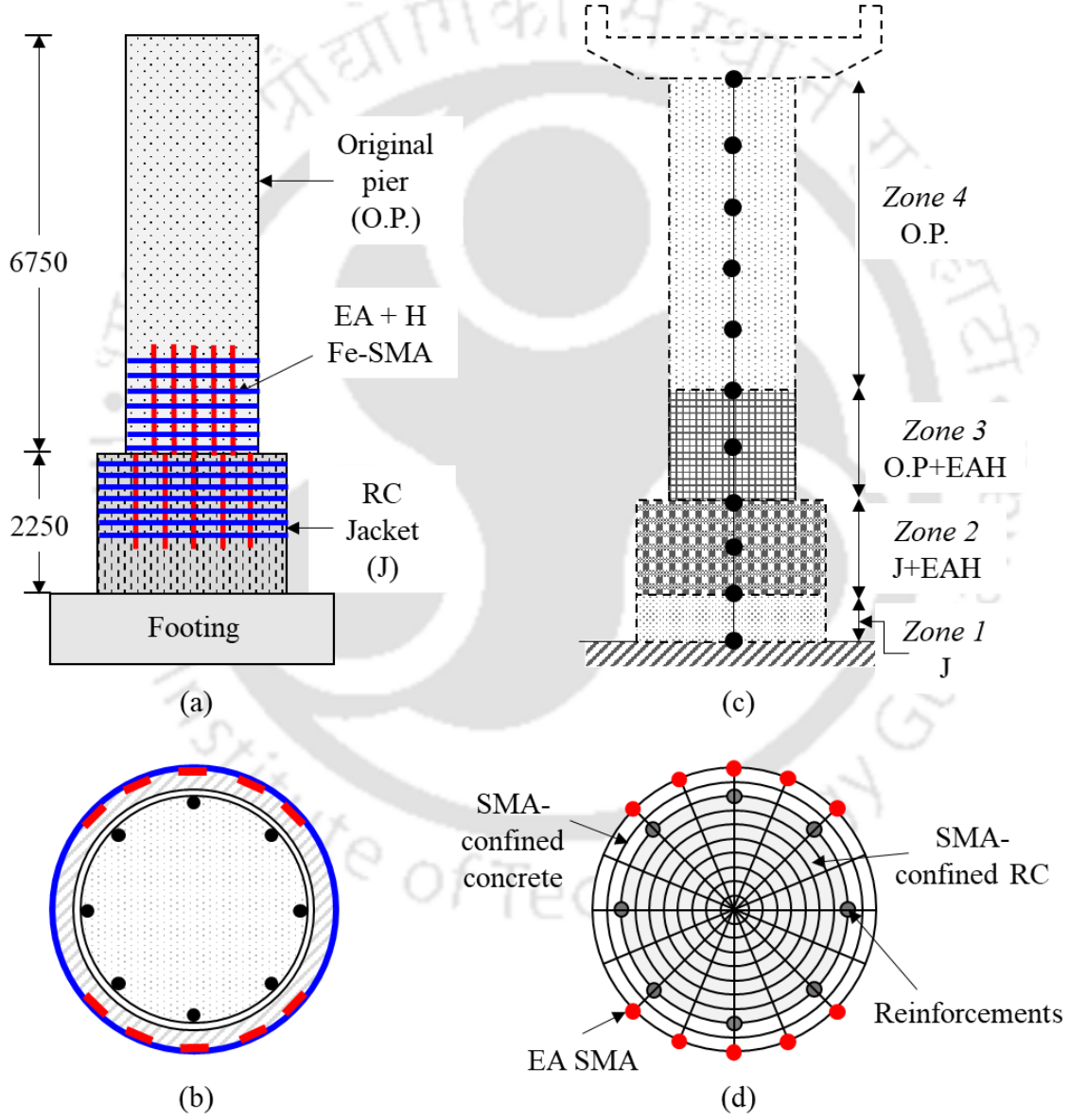

Fig. 7.7. (a) Prototype Specimen EAH; (b) cross-section; (c) FE model and (d) fibre section of the model

The fibre section of the retrofitted zones of Specimen EA is shown in Fig. 7.7(d). Material modelling of Specimen EAH was a combination of Specimens H and EA. Fig. 7.8 shows the comparison of results obtained from the FE analysis with those obtained from hybrid simulation. Results show that the response from FE model agrees quite well, with those from experimental investigation of Specimen EAH.

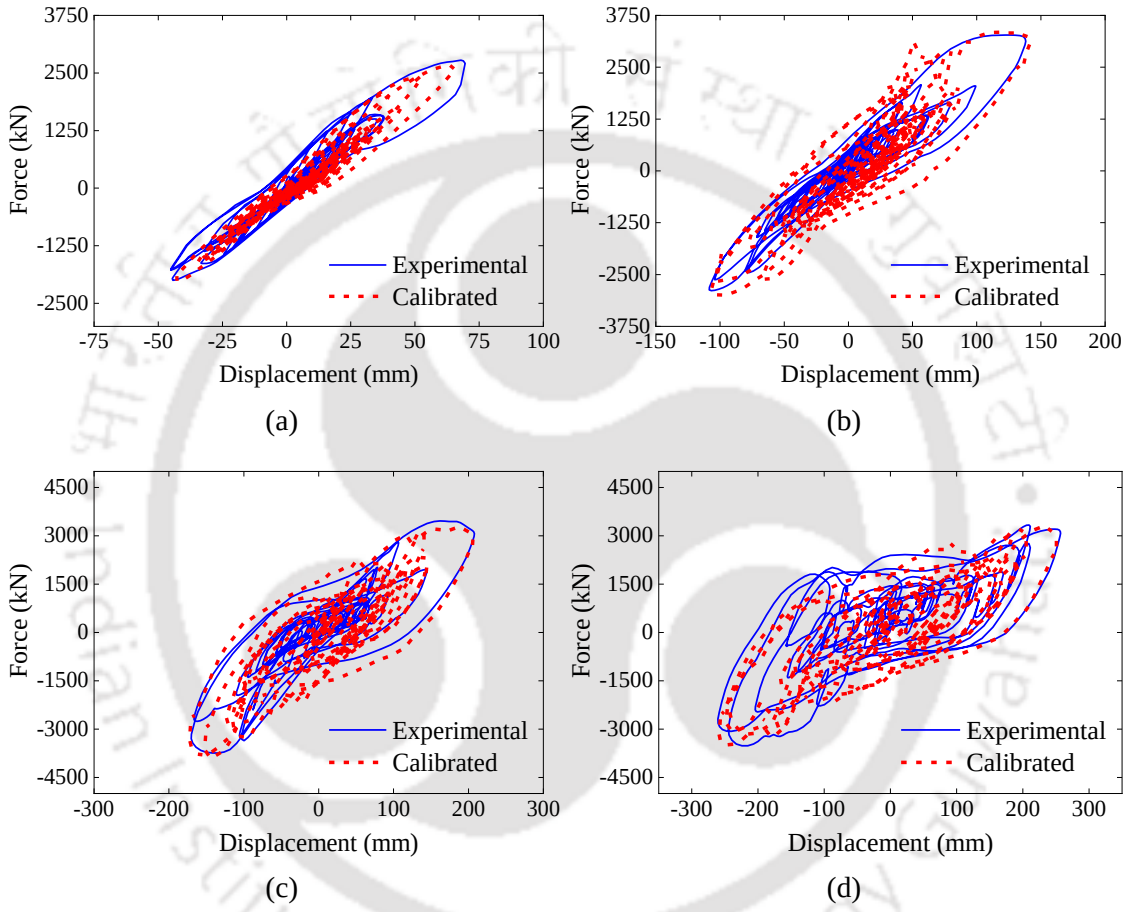

Fig. 7.8. Comparison of experimental results with results from calibrated numerical model of Specimen EAH for (a) 0.5 MCE; (b) 1 MCE; (c) 2 MCE and (d) 3 MCE intensity levels.

7.5. Validation of FE models of Fe-SMA retrofitted bridge pier specimens

The bridge pier specimens with different Fe-SMA strip configurations along with the control specimen were simulated using ABAQUS v.2021. Loading conditions on the bridge pier models were kept similar to those experienced by the prototype bridge pier during hybrid simulation. For this purpose, the both the displacement as well as time of the

experimental displacement-time history as recorded at the pier top were scaled as per similitude scaling relationship presented in Table 6.1 and was given as input to the FE model. Hence, the loading scheme of the FE model comprised of four scaled segments of the displacement-time histories recorded at the top of the prototype pier during hybrid simulation corresponding to the intensity levels, 0.5, 1, 2 and 3MCE of 32 seconds each, that were applied in a sequential order. This was followed by application of lateral cyclic loading in the form of displacement boundary condition to simulate the cyclic tests carried out after hybrid simulation. A schematic diagram representing the loading scheme in the FE model is shown in Fig. 7.9.

For this purpose, the validated 3D FE model of the RC jacketed pier presented in Chapter 5 was used in this study. Details of various modelling aspects related to material nonlinearity, bond-slip behaviour of reinforcement bars and mechanical properties of the jacket-pier interface are furnished in Section 5.5. The Fe-SMA strips, used as prestressing elements in the bridge pier specimens experienced load reversals during experimental investigation. Hence, the cyclic stress-strain behaviour of thermally activated Fe-SMA strips were evaluated at a loading-unloading strain range of $\Delta\varepsilon_0$=0.2%, based on the maximum strain recorded by the strain gauges fixed on the Fe-SMA strips during hybrid simulation, as presented in Section 3.4.1.6. After the initial loading cycle, it was observed that the Fe-SMA strips exhibited an almost linear behaviour in the subsequent loading and unloading cycles, with a Young's modulus of 175 GPa. Hence, in the present study, the linear portion of the cyclic stress-strain response of the Fe-SMA strips was adopted in its material modelling. The modelling of Fe-SMA strips and its prestressing effect in Fe-SMA strips is presented in Section 4.5.5. Details of FE model are presented in Section 5.5.3.

The resulting base shear-time histories and force-displacement envelope curves generated at the base of the pier in the FE model during hybrid simulation and cyclic test respectively, were compared with those obtained from the experimental investigation for validation of the 3D FE model. The damage patterns obtained during FE analyses were also compared with the experimentally observed damage patterns.

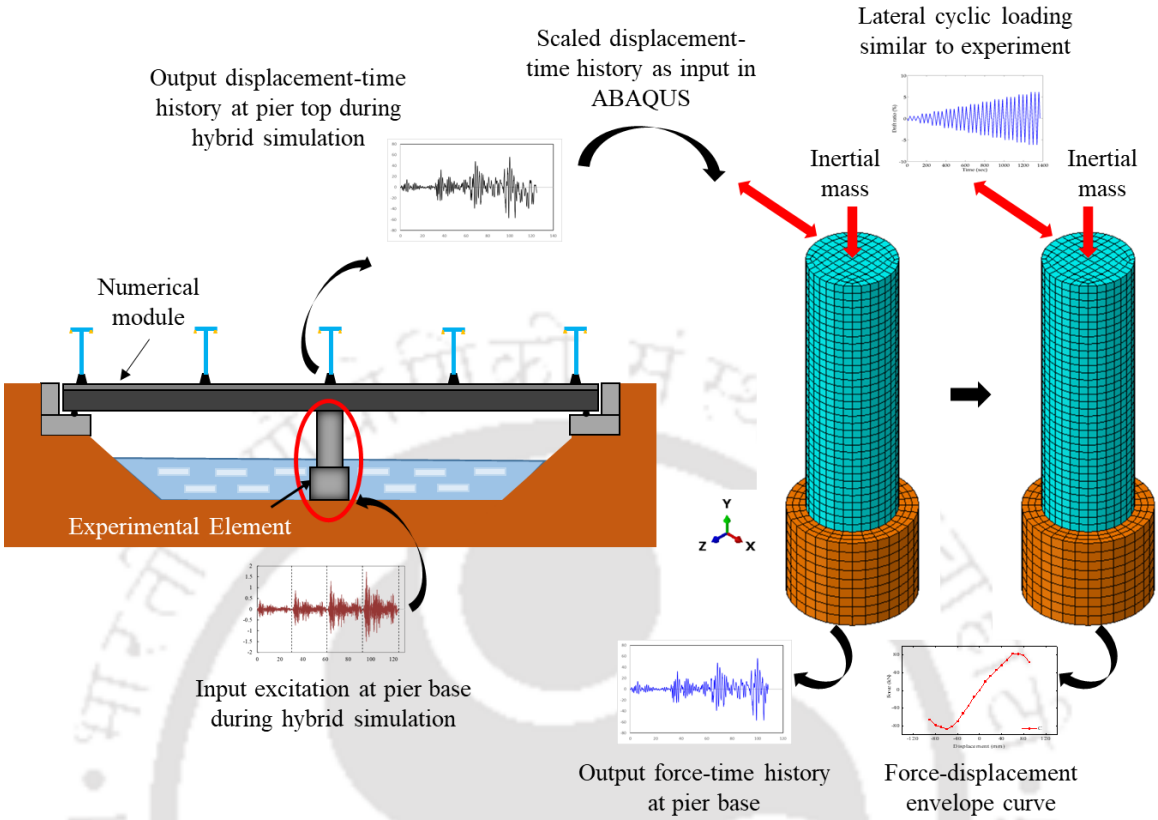

Fig. 7.9. Schematic diagram representing the loading scheme in the FE analysis

7.5.1. Results of hybrid simulation

The contour plot of DAMAGET parameter was used for representation of the damage experienced by the FE models during hybrid simulation as shown in Fig. 7.10. These were used for comparison with the damage patterns observed during experimental investigation.

From Fig. 7.10(a), it may be observed that higher DAMAGET values were typically found at a distance of roughly 80 mm from the top end of the RC jacket in Specimen C. Slip at the interface as well as propagation of cracks to the RC jacket could also be captured by the FE model. As observed in Fig. 7.10(b), the FE model of Specimen H displayed damage only at the original pier section above the top end of the RC jacket at a height of 30-40 mm. The FE model of Specimen EA showed maximum damage at the top end of the RC jacket, in the direction of loading, as shown in Fig. 7.10(c). This observation is consistent with the experimental damage pattern. The FE model of Specimen EAH shows

damage only at the top end of the RC jacket as shown in Fig. 7.10(d). These observations match reasonably well with the experimentally observed damage patterns.

Figs. 7.11-7.14 presents the displacement-time histories of Specimens C, H, EA and EAH recorded at the pier top during hybrid simulation respectively, corresponding to four intensity levels 0.5 MCE, 1 MCE, 2 MCE and 3 MCE. Comparison of corresponding experimental base shear-time histories with those obtained from FE analyses are also presented. Results show that the FE models of all the test specimens could quite reasonably simulate its respective experimental behaviour.

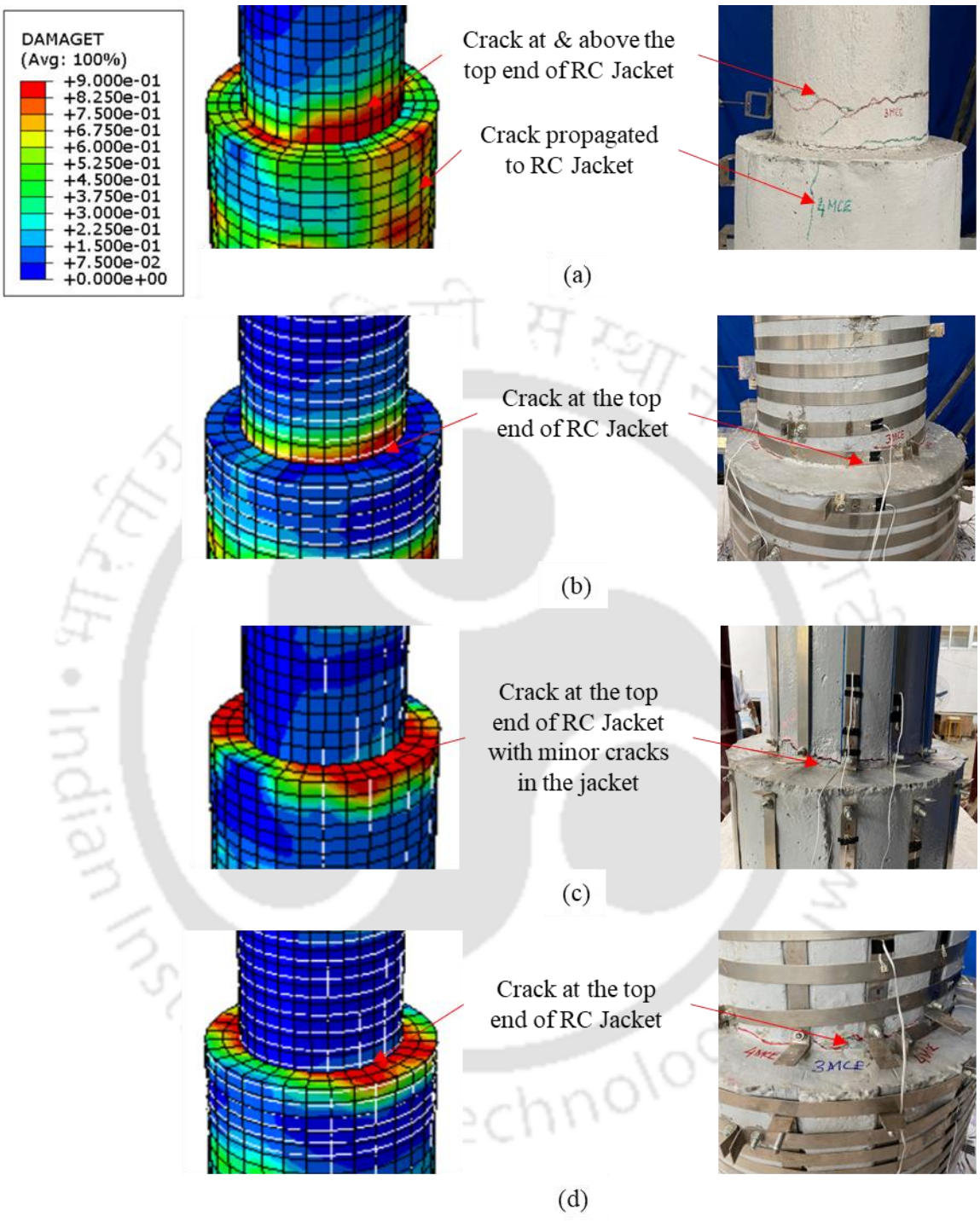

Fig. 7.10. Comparison of experimental damage patterns at the end of hybrid simulation with that obtained from FE analyses of Specimens (a) C; (b) H; (c) EA and (d) EAH

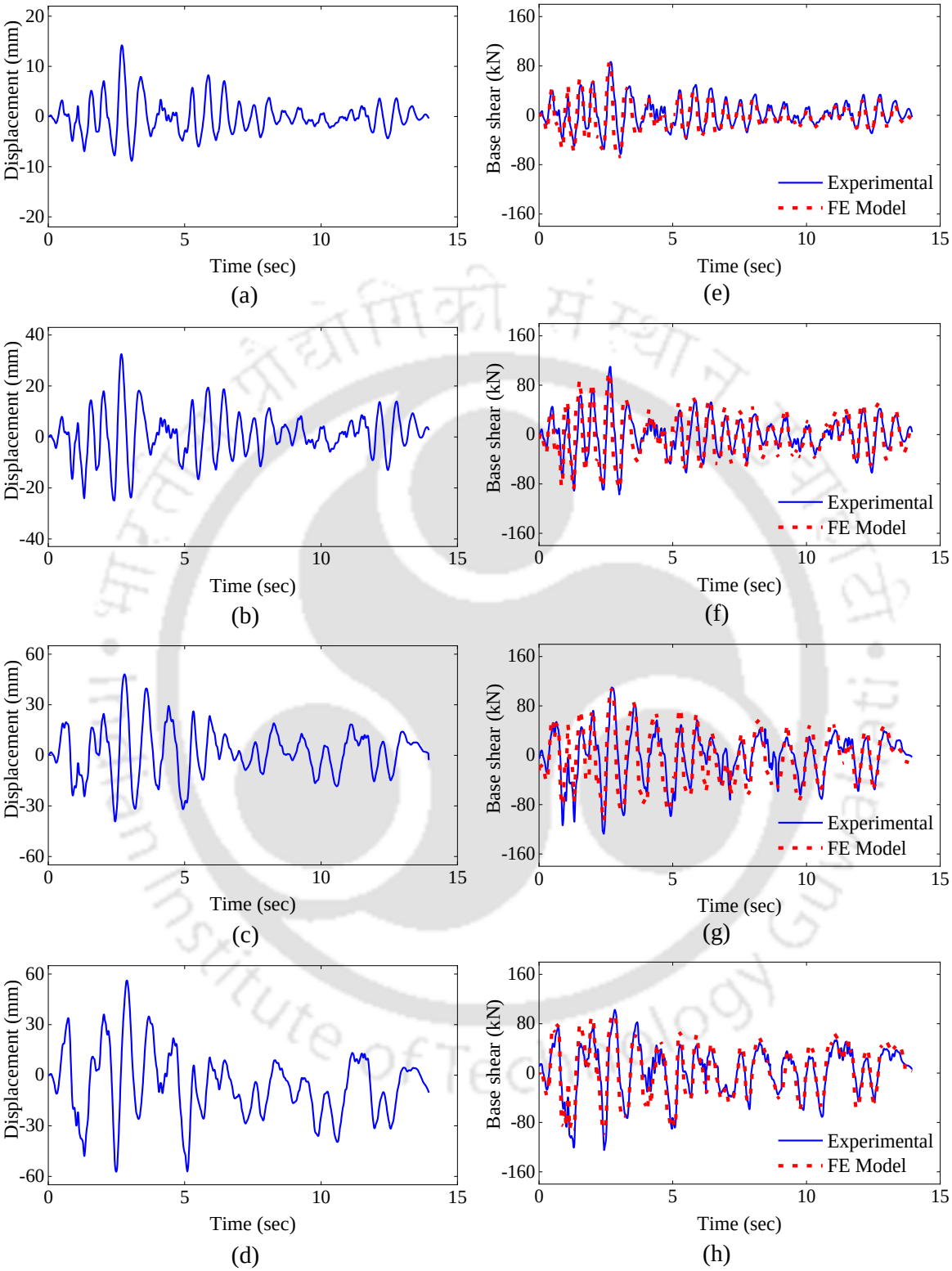

Fig. 7.11. (a-d) Displacement-time histories of Specimen C corresponding to intensities 0.5 MCE, 1 MCE, 2 MCE and 3 MCE; (e-h) Comparison of corresponding experimental base shear-time histories with the results obtained from FE analyses.

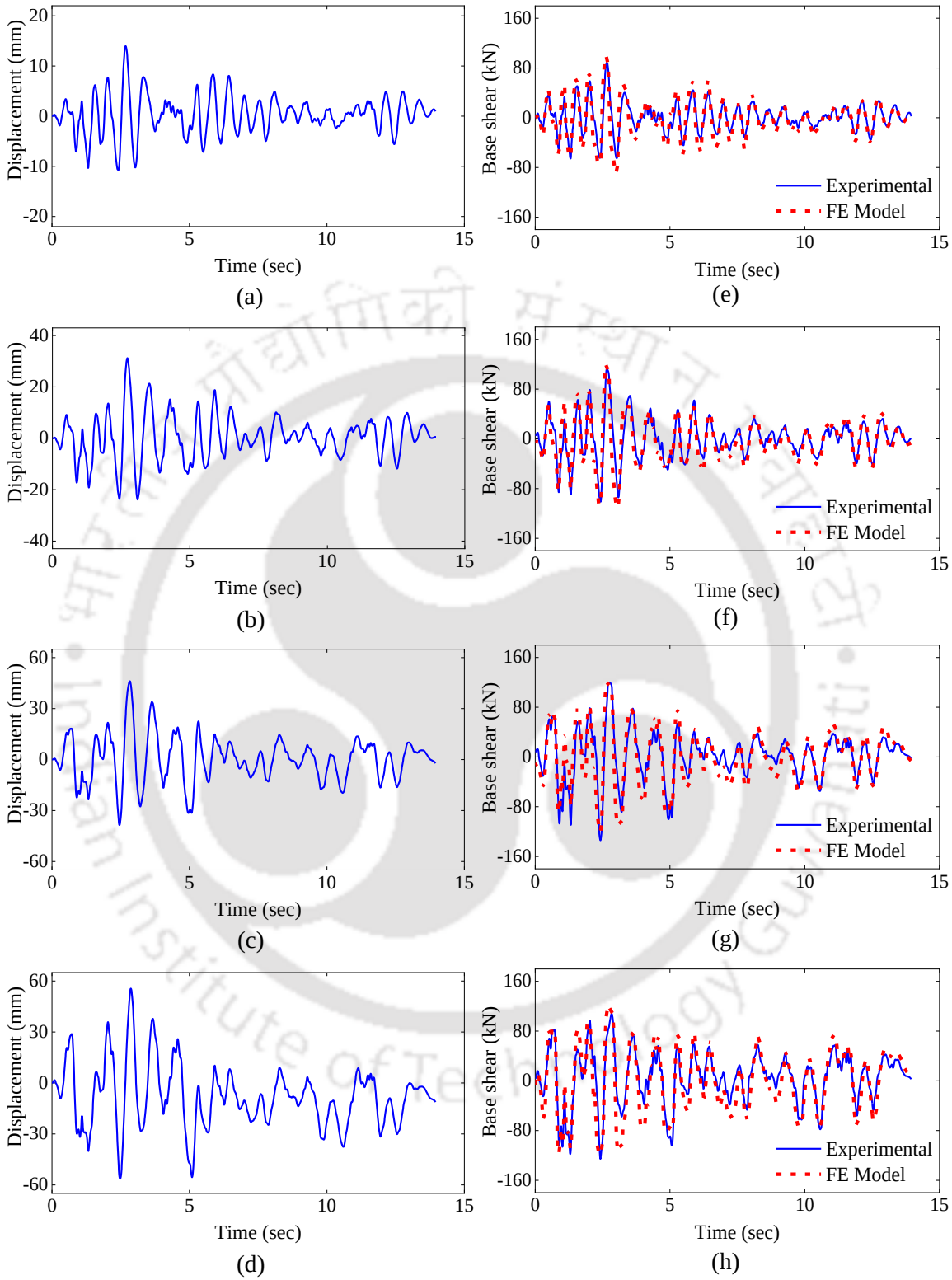

Fig. 7.12. (a-d) Displacement-time histories of Specimen H corresponding to intensities 0.5 MCE, 1 MCE, 2 MCE and 3 MCE; (e-h) Comparison of corresponding experimental base shear-time histories with the results obtained from FE analyses.

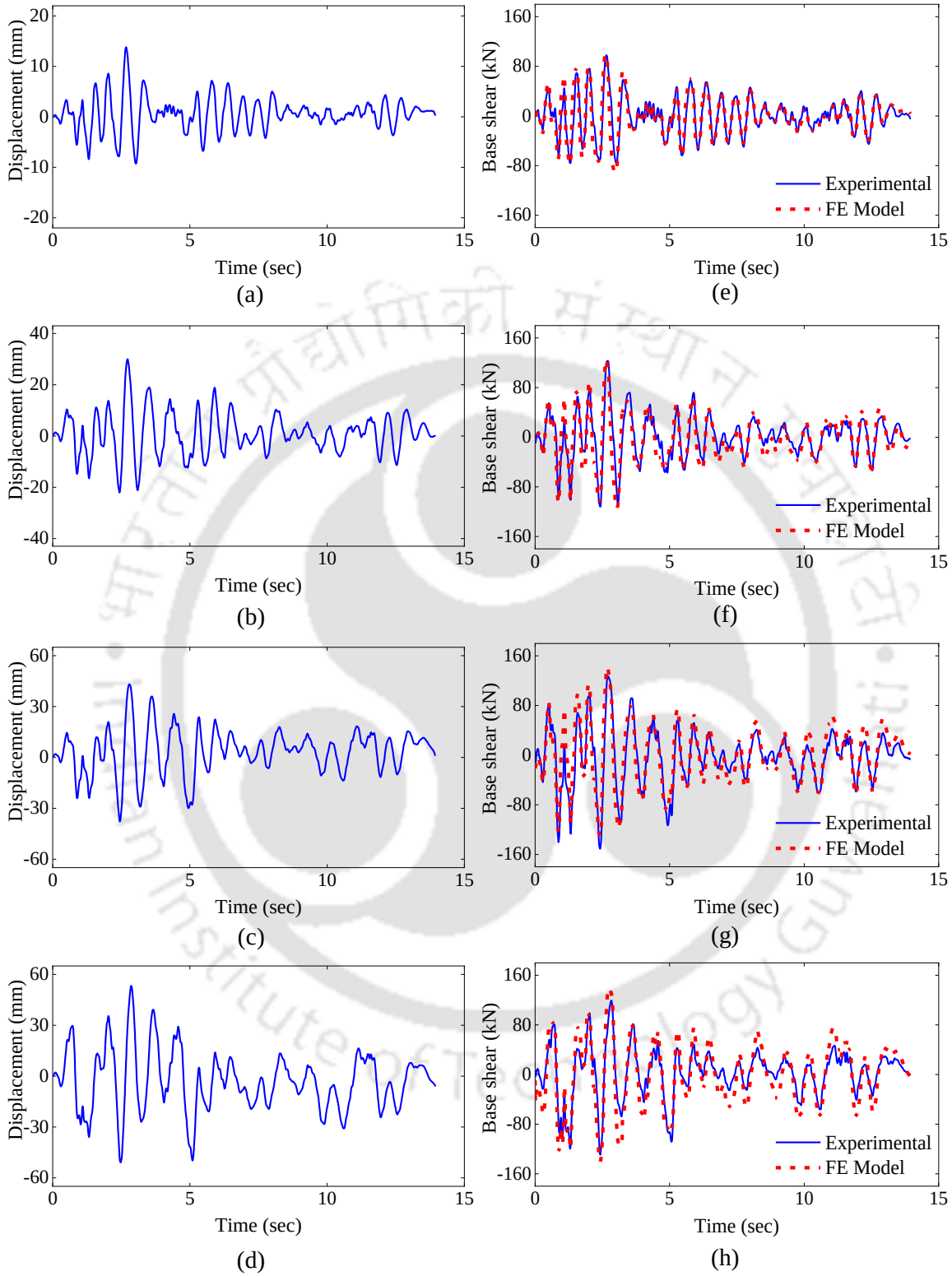

Fig. 7.13. (a-d) Displacement-time histories of Specimen EA corresponding to intensities 0.5 MCE, 1 MCE, 2 MCE and 3 MCE; (e-h) Comparison of corresponding experimental base shear-time histories with the results obtained from FE analyses.

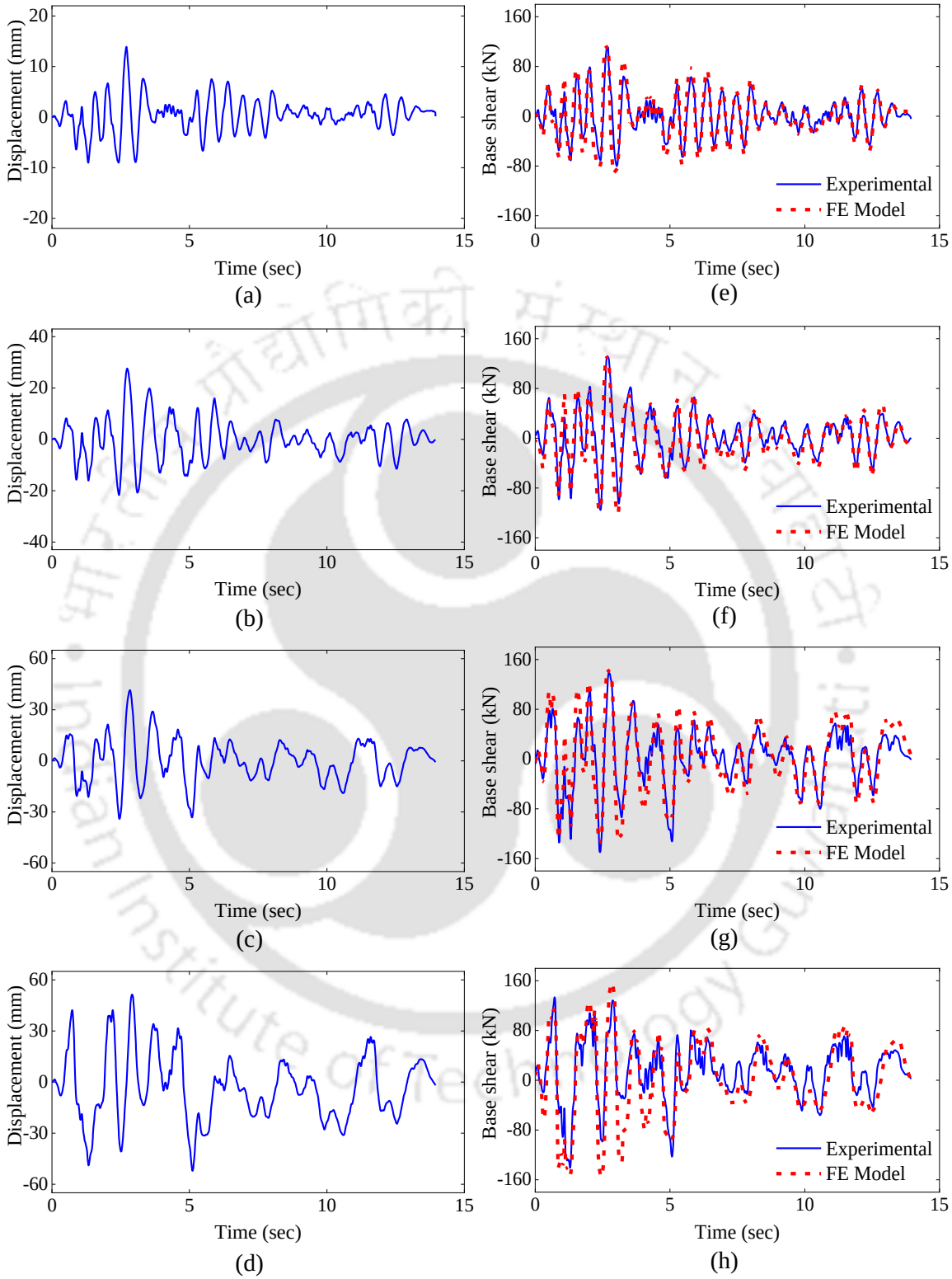

Fig. 7.14. (a-d) Displacement-time histories of Specimen EAH corresponding to intensities 0.5 MCE, 1 MCE, 2 MCE and 3 MCE; (e-h) Comparison of corresponding experimental base shear-time histories with the results obtained from FE analyses.

7.5.2. Results of cyclic test

After the end of the hybrid simulation, cyclic tests were carried out. The contour plot of DAMAGET parameter at the end of cyclic tests are shown in Fig. 7.15. These were used for comparison with the experimental damage patterns.

From Fig. 7.15(a), it may be observed that higher DAMAGET values were typically found till a distance of roughly 160 mm from the top end of the RC jacket in Specimen C. Cracks in the RC jacket could also be captured by the FE model. As observed in Fig. 7.15(b), the FE model of Specimen H displayed damage only at the relocated plastic hinge region. Rotation of the pier, leading to major damage, was also observed at this region, during experimental investigation. Due to effectiveness of hoop confinement, cracks were not propagated to the jacket. The FE model of Specimen EA showed maximum damage at the top end of the RC jacket, in the direction of loading. Propagation of cracks to the jacket was observed after an end-anchored strip got separated from the specimen, as shown in Fig. 7.15(c). This observation is consistent with the experimental damage pattern. The FE model of Specimen EAH shows damage only at the top end of the RC jacket as shown in Fig. 7.15(d). These observations match reasonably well with the experimental damage patterns.

Figs. 7.16(a-d) compares the envelope curves of Specimens C, H, EA and EAH as obtained from FE analyses with those obtained from experimental studies. Comparison of the envelope curves shows that the FE model, which considered material nonlinearities, bond-slip behaviour of the longitudinal reinforcement bars as well as interaction between the jacket and core concrete, was fairly successful in capturing the experimental response of the test specimen. The peak load of all the test specimens obtained numerically is in good agreement with that obtained from the experiment, with a maximum error of 17% and 19% in the directions of push and pull respectively. Additionally, comparison between the damage patterns obtained during experiment and FE simulation confirmed the accuracy and validity of the FE model.

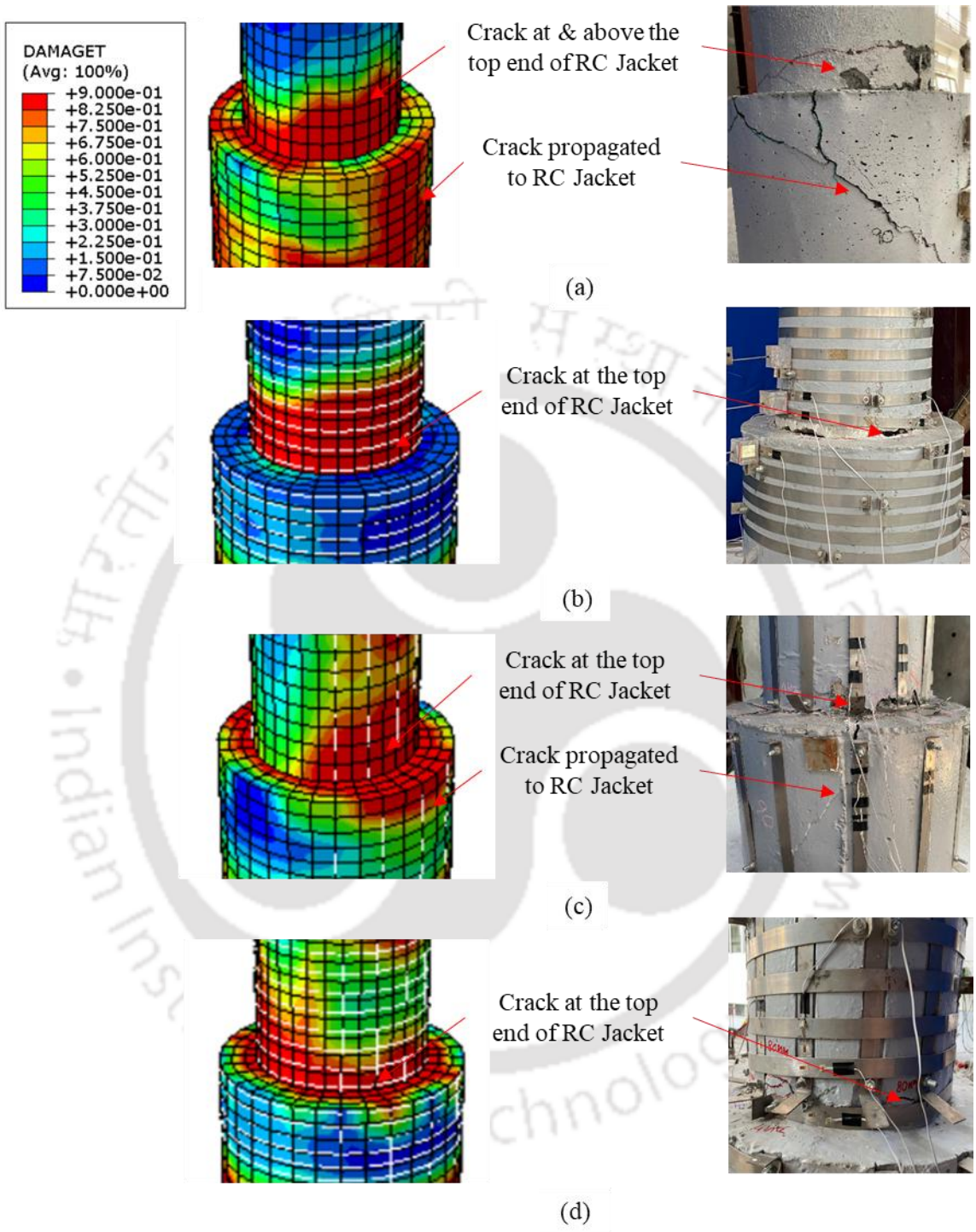

Fig. 7.15. Comparison of experimental damage patterns at the end of cyclic tests with that obtained from FE analyses of Specimens (a) C; (b) H; (c) EA and (d) EAH

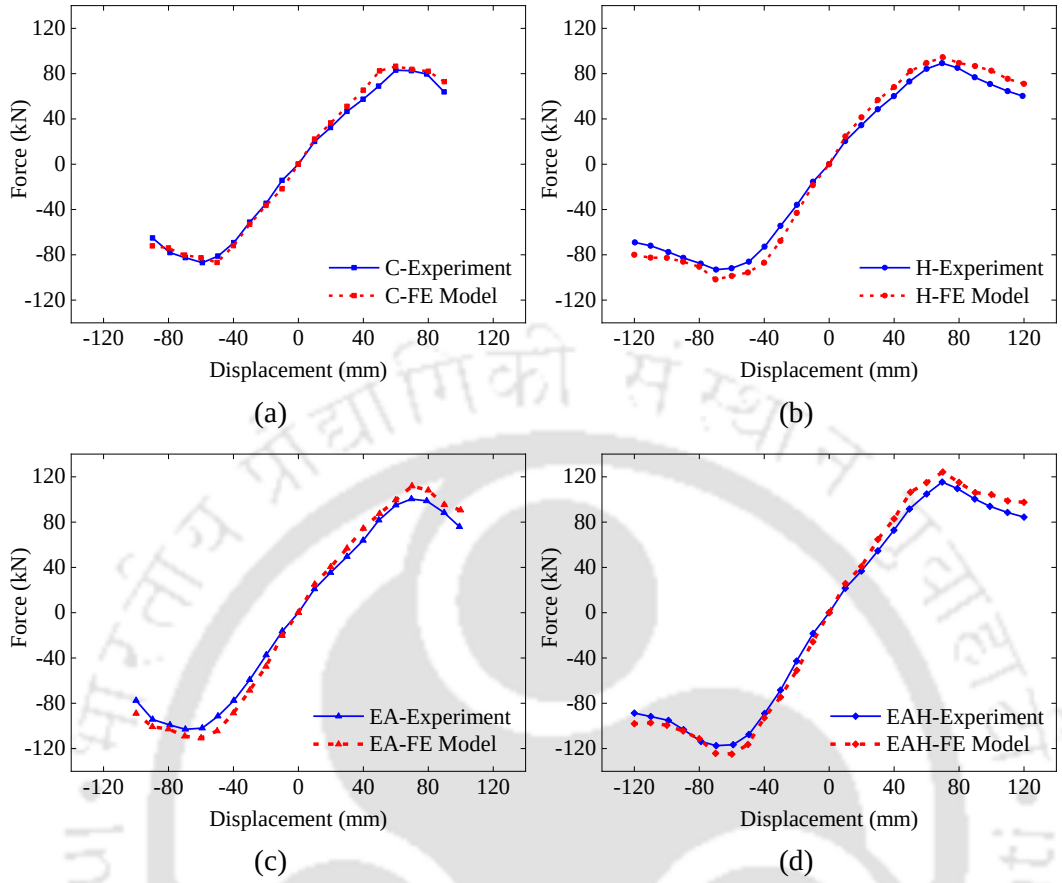

Fig. 7.16. Comparison of envelope curves of FE analyses with experimental data of Specimens: (a) C; (b) H; (c) EA and (d) EAH.

7.6. Concluding remarks

In this chapter, the numerical model of the bridge, as discussed in Chapter 6, was updated on the basis of results from hybrid simulations. Calibration was done by incorporation of bond-slip effects and slip at the jacket-pier interface. Additionally, the bridge pier specimens with different Fe-SMA strip configurations were simulated using ABAQUS. The resulting base shear-time histories generated at the base of the pier in the FE model and damage patterns were compared with the experimental results. It may be mentioned that, while the experiments were conducted on rehabilitated specimens which had undergone severe damage, the FE models however did not have any such uncertainties. Taking this into consideration, both the updated model of the bridge simulated in *Opensees* and the 3D FE model of the test specimens simulated using ABAQUS could quite reasonably simulate its experimental behaviour.

Chapter 8

Summary and conclusions

8.1 Summary

Bridges are designated as lifeline structures of the transportation infrastructure network. The implementation of capacity design philosophy for seismic design of bridge systems ensures that plastic hinges are located in columns while safeguarding other components against damage. Replacement of RC bridge columns, damaged during seismic events, is time-consuming, laborious, and expensive. Hence, numerous studies have been undertaken by researchers to develop new techniques for retrofitting and rehabilitation of RC bridge piers.

Addition of lateral confinement to concrete, whether internal or external, has long been proven to significantly improve strength and ductility of concrete. Several studies have shown that active confinement outperforms passive confinement in terms of enhancing the strength and ultimate strain of concrete due to prior application of confining pressure, which delays the initiation of damage in concrete. This study explored a new scheme for active confinement of RC bridge piers using cost-effective Fe-SMA strips as an alternative to the expensive NiTi-based SMAs. Prior to its usage in bridge piers, the recovery stress, monotonic tensile stress-strain behaviour and cyclic stress-strain behaviour of the Fe-SMA strips were evaluated for material characterization. Reduced recovery stress after stress relaxation was obtained in the range of 352-356 MPa. The ultimate tensile strength and strain at rupture was found to be in the range of 937- 942 MPa and 33-37% respectively. Phase characterization of Fe-SMA samples were done by XRD and the development of its microstructure was investigated using FESEM.

Further, an experimental investigation was conducted to evaluate the behaviour of plain concrete cylinders partially confined with Fe-SMA strips under uniaxial compressive loading. The increase in strength and ductility due to Fe-SMA confinement with respect to the unconfined concrete strength and Fe-SMA strip spacing were evaluated. Three different grades of concrete (21.7 MPa, 26.3 MPa and 30.3 MPa) and three different active confining

pressures (1.09 MPa, 1.76 MPa and 2.44 MPa) were adopted to study its influence on the stress-strain response of Fe-SMA-confined concrete specimens. On increasing the active confining pressure from 1.09 MPa to 2.44 MPa, corresponding increase in the peak stress in the range of 24.9%-68.5% was observed as compared to that of the unconfined concrete specimens. Similarly, it can be observed that there is substantial improvement in ultimate strength as well as ductility due to Fe-SMA confinement. Thereafter, regression analyses on test data were carried out to propose an empirical stress-strain equation of partially confined Fe-SMA concrete.

To understand the overall confinement effect of external Fe-SMA and internal longitudinal and transverse reinforcement on concrete, the proposed empirical model for Fe-SMA confined plain concrete was combined with Mander's model for steel rebar confined concrete to propose an empirical model for Fe-SMA confined RC specimens. Following that, 3D-FE models of concrete columns were developed in ABAQUS with varying unconfined concrete strengths, internal lateral steel reinforcements and external Fe-SMA confinement and were analysed under monotonic compressive loading. The results obtained from FE analyses were compared with the empirical stress-strain model for Fe-SMA-confined RC. Additionally, to obtain better accuracy in predicting the values of the parameters of the stress-strain relationship of Fe-SMA confined reinforced concrete, regression analyses were carried out on the results of FEA and an empirical model was proposed based on it. It was observed that the maximum AAE in predicting the parameters, f'_{cc}, ε'_{cc}, f_{res}, f_{ult} and $\varepsilon_{ult,}$ was less than 3.4%. The AR corresponding to all the parameters was 0.99.

In the present study, 1/5th scaled damaged pier models of a prototype bridge located in severest seismic zone in India were considered. These specimens were previously tested by Kotoky *et al.* (2018) at IIT Guwahati, which resulted in severe damage in the form of crushing of core concrete and yielding as well as rupture of reinforcement at the interface zone of the pier and foundation. Rehabilitation of severely damaged bridge pier models were done using RC jacketing method. The rehabilitation strategy was aimed to retrieve back at least the lost strength of the damaged bridge pier specimens as compared to its original strength. A plastic hinge relocation technique using RC jacketing was adopted. The

specimens were subjected to lateral cyclic loading to evaluate its performance with respect to that of the original specimen. 3D finite element analyses were also carried out to simulate the lateral load response of the rehabilitated test specimens. The generated numerical model considered material nonlinearities, bond-slip behaviour of the longitudinal reinforcement bars as well as interaction between the jacket and core concrete. A parametric study was carried out to determine the best possible interfacial model to accurately capture the experimental behaviour of the test specimen.

The rehabilitated bridge piers were further retrofitted using three configurations of Fe-SMA strips namely hoop (H), end-anchored (EA) and a combination of the previous two approaches (EAH). In the H retrofitting scheme, Fe-SMA hoops were spaced equally in the plastic hinge zone of the bridge pier for application of active confinement pressure on the pier. In the EA retrofitting scheme, pre-strained Fe-SMA strips were end-anchored on the surface of the bridge pier for development of pre-compression in the concrete at the plastic hinge zone. In the EAH retrofitting scheme, a combination of EA and hoop reinforcement was studied for both pre-compression and active confinement.

To investigate the seismic performance of the retrofitted RC bridge piers, hybrid simulation was considered for the detailed study. Hybrid simulation has two modules: numerical module comprising of the numerical model of the prototype bridge and experimental module comprising of the scaled models of the piers. Four input excitations corresponding to different intensity levels were used in hybrid simulation, followed by quasi-static cyclic tests to determine the ultimate capacity of these test specimens. Comparison of effectiveness of the various Fe-SMA retrofitting schemes was made based on the results of the hybrid and cyclic tests.

The comparison of experimental results with those from the numerical model highlighted the need for model calibration to improve the response. Bond-slip effects and slip at the jacket-pier interface was approximately accounted for in the updated model. The parameters of Fe-SMA confined plain as well as reinforced concrete were obtained from the empirical stress-strain models developed earlier. The force-displacement hysteretic behaviour of the test specimens obtained from the updated model agreed well with those obtained from experiments. Additionally, the bridge pier specimens with different Fe-SMA

strip configurations were simulated using ABAQUS. For simulating similar loading conditions on the test specimens during FEA, as experienced during hybrid simulation of the prototype bridge, the experimental displacement-time history recorded at the pier top was given as input in the FE model. The resulting base shear-time histories generated at the base of the pier in the FE model were compared with the experimental results for validation of the 3D FE model.

8.2 Conclusions

Major conclusions from the present study may be summarized as follows:

- During the first load cycle of cyclic test, Fe-SMA exhibited nonlinear behaviour. However, for subsequent cycles an almost linear behaviour was observed for the strain range considered in this study.
- The proposed scheme of using Fe-SMA strips for partial wrapping of concrete is very effective in enhancing strength and ductility of an axially loaded concrete specimens. Effectiveness of Fe-SMA confinement increases with an increase in the active confining pressure.
- The residual stress of Fe-SMA confined concrete is independent of concrete strength and only depends on the active confining pressure on concrete.
- The proposed empirical model for Fe-SMA confined RC specimens, obtained by regression analyses, based on data from 3D FE analyses of concrete specimens with varying concrete strength, internal reinforcement and external Fe-SMA confinements, can be easily incorporated in any standard FE software for analysis of such Fe-SMA confined RC specimens using an idealized stick model.
- A systematically adopted step-by-step procedure for rehabilitation of severely damaged pier specimen in the form of concrete jacket, is capable of retrieving the seismic performance of the original pier specimen and relocating the plastic hinge away from the pier-footing interface.
- Calibration of numerical model of RC jacketed pier incorporating concrete-rebar interaction and jacket-pier interface shear, by comparing with experimentally

observed responses is an effective means of performance enhancement of FE model.

- Bridge pier specimens with Fe-SMA in the form of end-anchored reinforcement exhibited enhanced load carrying capacity and marginal improvement in failure displacement, whereas specimens with hoop reinforcement showed improved ductility.
- Combination of hoops and end-anchored Fe-SMA was successful in improving both the strength as well as ultimate lateral displacement of RC bridge pier specimens.
- Strains in end-anchored strips in Specimen EAH experiences lower growth at all stages of loading as compared to that of Specimen EA. Additionally, Fe-SMA hoops in Specimen EAH show lower circumferential strain as compared to that of Specimen H. This delayed growth of strain in Specimen EAH results in improved seismic performance as compared to that of Specimens EA and H.
- The calibrated FE model of the bridge using experimental results is capable of closely simulating its experimental behaviour. This model can be used for seismic vulnerability assessment of the bridge.
- Validated 3D FE models of the Fe-SMA retrofitted specimens can be used as a practical and cost-effective tool for identification of effects of various design parameters on the seismic behaviour of RC bridge piers retrofitted using Fe-SMA strips.

8.3 Recommendations for future research

Additional work may be undertaken in the following areas:

- Real time hybrid simulation can be performed to bring forth inertial effect and actual damping effect under the action of earthquake excitation on the structure.
- Seismic fragility analysis using experimentally observed damage state and calibrated numerical model of the bridge.
- Parametric study to examine the performance of the bridge piers with respect to a number of important parameters including level of confinement pressure, volumetric ratio of longitudinal reinforcement, slenderness ratio and axial load.

- Comparative performance assessment of bridge piers with Fe-SMA strips in the form of end-anchored and near-surface mounted reinforcements.

References

ABAQUS Documentation, Version 6.14-2 (2014). Dassault Systémes Simulia Corp., Providence.

Abbiati, G., Bursi, O. S., Caperan, P., Di Sarno, L., Molina, F. J., Paolacci, F., & Pegon, P. (2015). Hybrid simulation of a multi- span RC viaduct with plain bars and sliding bearings. *Earthquake Engineering & Structural Dynamics, 44*(13), 2221-2240.

Abouali, S., Shahverdi, M., Ghassemieh, M., & Motavalli, M. (2019). Nonlinear simulation of reinforced concrete beams retrofitted by near-surface mounted iron-based shape memory alloys. *Engineering Structures, 187*, 133-148.

Andrawes, B., & Shin, M. (2008). *Seismic retrofitting of bridge columns using shape memory alloys.* Paper presented at the Active and Passive Smart Structures and Integrated Systems 2008.

ASTM. E8/E8M-15a:2016. *Standard Test Methods for Tension Testing of Metallic Materials*, ASTM International, West Conshohocken, PA.

Aviram, A., Mackie, K. R., & Stojadinović, B. (2008). *Guidelines for nonlinear analysis of bridge structures in California*: Pacific earthquake engineering research center.

Bassani, P., & Besseghini, S. (2001). NiTiCu shape memory alloy: Superplastic elongation during thermal cycling. *Le Journal de Physique IV, 11*(PR8), Pr8-381-Pr388-386.

Belarbi, A., & Hsu, T. T. (1994). Constitutive laws of concrete in tension and reinforcing bars stiffened by concrete. *Structural Journal, 91*(4), 465-474.

Bett, B. J., Klingner, R. E., & Jirsa, J. O. (1988). Lateral load response of strengthened and repaired reinforced concrete columns. *Structural Journal, 85*(5), 499-508.

Caltrans. Caltrans Seismic Design Criteria:2013. Sacramento, CA: California Department of Transportation.

Carrion, J. E., Spencer, B., & Phillips, B. M. (2009). Real-time hybrid simulation for structural control performance assessment. *Earthquake Engineering and Engineering Vibration, 8*(4), 481-492.

CEB-FIP Model Code:1993. Thomas Telford Ltd., London.

ChaiI, Y. H., Priestley, M. N., & Seible, F. (1991). Seismic retrofit of circular bridge columns for enhanced flexural performance. *Structural Journal, 88*(5), 572-584.

Chang, L., & Read, T. (1951). Behavior of the elastic properties of AuCd. *Trans Met Soc AIME, 191*, 47.

Chen, Q., & Andrawes, B. (2017). Cyclic stress–strain behavior of concrete confined with NiTiNb-shape memory alloy spirals. *Journal of Structural Engineering, 143*(5), 04017008.

Cheng, C.-T., Yang, J.-C., Yeh, Y.-K., & Chen, S.-E. (2003). Seismic performance of repaired hollow-bridge piers. *Construction and Building Materials, 17*(5), 339-351.

Cho, C.-G., Kim, Y.-Y., Feo, L., & Hui, D. (2012). Cyclic responses of reinforced concrete composite columns strengthened in the plastic hinge region by HPFRC mortar. *Composite Structures, 94*(7), 2246-2253.

Choi, E., Chung, Y.-S., Choi, D.-H., & DesRoches, R. (2012). Seismic protection of lap-spliced RC columns using SMA wire jackets. *Magazine of Concrete Research, 64*(3), 239-252.

Choi, E., Chung, Y.-S., Park, J., & Cho, B.-S. (2010). Behavior of reinforced concrete columns confined by new steel-jacketing method. *ACI Structural Journal, 107*(6).

Chopra, A. K. (2007). *Dynamics of structures*: Pearson Education India.

Chung, J., & Hulbert, G. (1993). A time integration algorithm for structural dynamics with improved numerical dissipation: the generalized-α method.

Cladera, A., Montoya-Coronado, L. A., Ruiz-Pinilla, J. G., & Ribas, C. (2020). Shear strengthening of slender reinforced concrete T-shaped beams using iron-based shape memory alloy strips. *Engineering Structures, 221*, 111018.

Cladera, A., Weber, B., Leinenbach, C., Czaderski, C., Shahverdi, M., & Motavalli, M. (2014). Iron-based shape memory alloys for civil engineering structures: An overview. *Construction and Building Materials, 63*, 281-293.

Combescure, D., & Pegon, P. (1997). α-Operator splitting time integration technique for pseudodynamic testing error propagation analysis. *Soil Dynamics and Earthquake Engineering, 16*(7-8), 427-443.

Czaderski, C., Shahverdi, M., Brönnimann, R., Leinenbach, C., & Motavalli, M. (2014). Feasibility of iron-based shape memory alloy strips for prestressed strengthening of concrete structures. *Construction and Building Materials, 56*, 94-105.

Czaderski, C., Shahverdi, M., & Michels, J. (2021). Iron based shape memory alloys as shear reinforcement for bridge girders. *Construction and Building Materials, 274*, 121793.

Dang, J., & Aoki, T. (2013). Bidirectional loading hybrid tests of square cross- sections of steel bridge piers. *Earthquake Engineering & Structural Dynamics, 42*(8), 1111-1130.

Darwin, D., Lutz, L. A., & Zuo, J. (2005). *Recommended provisions and commentary on development and lap splice lengths for deformed reinforcing bars in tension*.

Dasgupta, R. (2014). A look into Cu-based shape memory alloys: Present scenario and future prospects. *Journal of Materials Research, 29*(16), 1681-1698.

Dehestani, M., & Mousavi, S. (2015). Modified steel bar model incorporating bond-slip effects for embedded element method. *Construction and Building Materials, 81*, 284-290.

Dong, Z., Klotz, U. E., Leinenbach, C., Bergamini, A., Czaderski, C., & Motavalli, M. (2009). A novel Fe- Mn- Si shape memory alloy with improved shape recovery properties by VC precipitation. *Advanced engineering materials, 11*(1- 2), 40-44.

Dudziak, S., Jackiewicz-Rek, W., & Kozyra, Z. (2021). On the Calibration of a Numerical Model for Concrete-to-Concrete Interface. *Materials, 14*(23), 7204.

Eid, R., & Paultre, P. (2007). Plasticity-based model for circular concrete columns confined with fibre-composite sheets. *Engineering Structures, 29*(12), 3301-3311.

Eid, R., & Paultre, P. (2008). Analytical model for FRP-confined circular reinforced concrete columns. *Journal of Composites for Construction, 12*(5), 541-552.

El-Hacha, R., & Rojob, H. (2018). Flexural strengthening of large-scale reinforced concrete beams using near-surface-mounted self-prestressed iron-based shape-memory alloy strips. *PCI J, 63*(6), 51-62.

ElSouri, A. M., & Harajli, M. H. (2011). Seismic repair and strengthening of lap splices in RC columns: carbon fiber–reinforced polymer versus steel confinement. *Journal of Composites for Construction, 15*(5), 721-731.

Elwi, A. A., & Murray, D. W. (1979). A 3D hypoelastic concrete constitutive relationship. *Journal of the Engineering Mechanics Division, 105*(4), 623-641.

Eurocode 2:2004. *Design of concrete structures - Part 1-1: General rules and rules for buildings*, ASTM International, West Conshohocken, PA.

FEMA. 356:2000. *Prestandard and commentary for the seismic rehabilitation of buildings*, Federal Emergency Management Agency: Washington, DC, USA.

Frankie, T. M. (2013). *Impact of complex system behavior on seismic assessment of RC bridges*: University of Illinois at Urbana-Champaign.

Fukuyama, K., Higashibata, Y., & Miyauchi, Y. (2000). Studies on repair and strengthening methods of damaged reinforced concrete columns. *Cement and Concrete Composites, 22*(1), 81-88.

Ghafoori, E., Hosseini, E., Leinenbach, C., Michels, J., & Motavalli, M. (2017). Fatigue behavior of a Fe-Mn-Si shape memory alloy used for prestressed strengthening. *Materials & Design, 133*, 349-362.

Ghafoori, E., Neuenschwander, M., Shahverdi, M., Czaderski, C., & Fontana, M. (2019). Elevated temperature behavior of an iron-based shape memory alloy used for prestressed strengthening of civil structures. *Construction and Building Materials, 211*, 437-452.

Guo, W., Zeng, C., Gou, H., Gu, Q., Wang, T., Zhou, H., Wu, J. (2021). Real-time hybrid simulation of high-speed train-track-bridge interactions using the moving load convolution integral method. *Engineering Structures, 228*, 111537.

Hakuno, M., Shidawara, M., & Hara, T. (1969). *Dynamic destructive test of a cantilever beam, controlled by an analog-computer.* Paper presented at the Proceedings of the Japan society of civil engineers.

Harris, H. G., & Sabnis, G. (1999). *Structural modeling and experimental techniques*: CRC press.

He, R., Grelle, S., Sneed, L. H., & Belarbi, A. (2013). Rapid repair of a severely damaged RC column having fractured bars using externally bonded CFRP. *Composite Structures, 101*, 225-242.

He, R., Yang, Y., & Sneed, L. H. (2015). Seismic repair of reinforced concrete bridge columns: Review of research findings. *Journal of Bridge Engineering, 20*(12), 04015015.

Hilber, H. M., Hughes, T. J., & Taylor, R. L. (1977). Improved numerical dissipation for time integration algorithms in structural dynamics. *Earthquake Engineering & Structural Dynamics, 5*(3), 283-292.

Hose, Y. D., Priestley, M., & Seible, F. (1997). *Strategic relocation of plastic hinges in bridge columns*. Retrieved from

Hosseini, E., Ghafoori, E., Leinenbach, C., Motavalli, M., & Holdsworth, S. R. (2018). Stress recovery and cyclic behaviour of an Fe–Mn–Si shape memory alloy after multiple thermal activation. *Smart Materials and Structures, 27*(2), 025009.

Hughes, T. J., Pister, K. S., & Taylor, R. L. (1979). Implicit-explicit finite elements in nonlinear transient analysis. *Computer Methods in Applied Mechanics and Engineering, 17*, 159-182.

Ilki, A., Peker, O., Karamuk, E., Demir, C., & Kumbasar, N. (2008). FRP retrofit of low and medium strength circular and rectangular reinforced concrete columns. *Journal of Materials in Civil Engineering, 20*(2), 169-188.

IS. 383:2016 *Coarse and Fine Aggregate for Concrete - Specification*, Bureau of Indian Standards, New Delhi.

IS. 456:2000. *Plain and Reinforced Concrete-Code of Practice*, Bureau of Indian Standards, New Delhi.

IS. 1489 (Part 2):1991. *Specification for Portland-pozzolana cement: Part 2 Calcined clay based*, Bureau of Indian Standards, New Delhi.

IS. 1893(1):2002 *Criteria for Earthquake Resistant Design of Structures, Part 1: General provisions and Buildings*, Bureau of Indian Standards, New Delhi.

IS. 2386(1):1963. *Methods of Test for Aggregates for Concrete, Part I: Particle Size and Shape*, Bureau of Indian Standards, New Delhi.

IS. 2386(3):1963. *Methods of test for aggregates for concrete, Part 3: Specific gravity, density, voids, absorption and bulking*, Bureau of Indian Standards, New Delhi.

IS. 4031(4):1988. *Methods of physical tests for hydraulic cement, Part 4: Determination of consistency of standard cement paste*, Bureau of Indian Standards, New Delhi.

IS. 4031(5):1988. *Methods of physical tests for hydraulicccement, Part 5: Determination of initial and final settingtimes*, Bureau of Indian Standards, New Delhi.

IS. 4031(11):1988. *Methods of physical tests for hydraulic cement, Part 11: Determination of density*, Bureau of Indian Standards, New Delhi.

IS. 13920:2016. *Ductile Detailing of RCC Structures Subjected to Seismic Forces Code of Practice*, Bureau of Indian Standards, New Delhi.

Jung, D., Wilcoski, J., & Andrawes, B. (2018). Bidirectional shake table testing of RC columns retrofitted and repaired with shape memory alloy spirals. *Engineering Structures*, *160*, 171-185.

Kajiwara, S., Liu, D., Kikuchi, T., & Shinya, N. (2001). Remarkable improvement of shape memory effect in Fe-Mn-Si based shape memory alloys by producing NbC precipitates. *Scripta materialia*, *44*(12), 2809-2814.

Koster, M., Lee, W., Schwarzenberger, M., & Leinenbach, C. (2015). Cyclic deformation and structural fatigue behavior of an FE–Mn–Si shape memory alloy. *Materials Science and Engineering: A*, *637*, 29-39.

Kotoky, N., Deb, S. K., & Dutta, A. (2018). HyFRC Bridge Piers with Different Detailing at Pier–Foundation Interface. *Journal of Bridge Engineering*, *23*(6), 04018035.

Krish, Z. F., Kowalsky, M. J., & Nau, J. M. (2021). Seismic repair of circular reinforced concrete bridge columns by plastic hinge relocation with grouted annular ring. *Journal of Earthquake Engineering*, *25*(12), 2371-2405.

Krstulovic-Opara, N., & Thiedeman, P. D. (2000). Active confinement of concrete members with self-stressing composites. *Materials Journal, 97*(3), 297-308.

Kupfer, H., Hilsdorf, H. K., & Rusch, H. (1969). *Behavior of concrete under biaxial stresses.* Paper presented at the Journal proceedings.

Lee, J., & Fenves, G. L. (1998). Plastic-damage model for cyclic loading of concrete structures. *Journal of engineering mechanics, 124*(8), 892-900.

Lee, W., Partovi- Nia, R., Suter, T., & Leinenbach, C. (2016). Electrochemical characterization and corrosion behavior of an Fe- Mn- Si shape memory alloy in simulated concrete pore solutions. *Materials and Corrosion, 67*(8), 839-846.

Lee, W., Weber, B., Feltrin, G., Czaderski, C., Motavalli, M., & Leinenbach, C. (2013). Stress recovery behaviour of an Fe–Mn–Si–Cr–Ni–VC shape memory alloy used for prestressing. *Smart Materials and Structures, 22*(12), 125037.

Leinenbach, C., Lee, W., Lis, A., Arabi-Hashemi, A., Cayron, C., & Weber, B. (2016). Creep and stress relaxation of a FeMnSi-based shape memory alloy at low temperatures. *Materials Science and Engineering: A, 677*, 106-115.

Liang, X., & Sritharan, S. (2018). Effects of confinement in circular hollow concrete columns. *Journal of Structural Engineering, 144*(9), 04018159.

Lim, J. C., & Ozbakkaloglu, T. (2015). Unified stress-strain model for FRP and actively confined normal-strength and high-strength concrete. *Journal of Composites for Construction, 19*(4), 04014072.

Lubliner, J., Oliver, J., Oller, S., & Oñate, E. (1989). A plastic-damage model for concrete. *International Journal of solids and structures, 25*(3), 299-326.

Mahin, S. A., Shing, P.-S. B., Thewalt, C. R., & Hanson, R. D. (1989). Pseudodynamic test method—Current status and future directions. *Journal of Structural Engineering, 115*(8), 2113-2128.

Mander, J. B., Priestley, M. J., & Park, R. (1988). Theoretical stress-strain model for confined concrete. *Journal of Structural Engineering, 114*(8), 1804-1826. doi:Doi 10.1061/(Asce)0733-9445(1988)114:8(1804)

Maruyama, T., & Kubo, H. (2011). Shape Memory and Superelastic Alloys, Technologies and Applications. *Woodhead Publishing limited*.

McKenna, F. T. (1997). *Object-oriented finite element programming: frameworks for analysis, algorithms and parallel computing*: University of California, Berkeley.

Melton, K., Simpson, J., & Duerig, T. (1986). *A new wide hysteresis NiTi based shape memory alloy and its applications.* Paper presented at the Proceedings of the International Conference on Martensitic Transformations. ICOMAT-86.

Michels, J., Shahverdi, M., & Czaderski, C. (2018). Flexural strengthening of structural concrete with iron- based shape memory alloy strips. *Structural Concrete, 19*(3), 876-891.

Mirmiran, A., & Shahawy, M. (1997). Dilation characteristics of confined concrete. *Mechanics of Cohesive‐frictional Materials: An International Journal on Experiments, Modelling and Computation of Materials and Structures, 2*(3), 237-249.

Miyagi, T., Yamakawa, T., Li, W., & Rahman, M. (2004). *A study of emergency retrofit using prestressing bars and steel plates for damaged columns.* Paper presented at the Proceedings of Thirteenth World Conference on Earthquake Engineering.

Moghaddam, H., Samadi, M., Pilakoutas, K., & Mohebbi, S. (2010). Axial compressive behavior of concrete actively confined by metal strips; part A: experimental study. *Materials and Structures, 43*(10), 1369-1381.

Montoya-Coronado, L. A., Ruiz-Pinilla, J. G., Ribas, C., & Cladera, A. (2019). Experimental study on shear strengthening of shear critical RC beams using iron-based shape memory alloy strips. *Engineering Structures, 200*, 109680.

Mousa, S., Mohamed, H. M., & Benmokrane, B. (2019). Cracking and crack control in circular concrete bridge members reinforced with fiber-reinforced polymer bars. *Journal of Bridge Engineering, 24*(1), 04018108.

Nakashima, M. (1990). *Integration techniques for substructure pseudo-dynamic test.* Paper presented at the 4th US National Conference on Earthquake Engineering, 1990. 5.

Nakashima, M., Ishii, K., Kamagata, S., Tsutsumi, H., & Ando, K. (1988). *Feasibility of pseudo dynamic test using substructuring techniques.* Paper presented at the Proceeding of 9th World Conference on Earthquake Engineering. Tokyo, Japan.

Nesheli, K. N., & Meguro, K. (2006). *Seismic retrofitting of earthquake-damaged concrete columns by lateral pre-tensioning of FRP belts.* Paper presented at the Proc., 8th US National Conf. on Earthquake Engineering.

Newmark, N. M., & Hall, W. J. (1982). Earthquake spectra and design. *Engineering monographs on earthquake criteria*.

Nielson, B. G. (2005). *Analytical fragility curves for highway bridges in moderate seismic zones*: Georgia Institute of Technology.

Obata, M., & Goto, Y. (2002). Multi-directional pseudo dynamic experiment of steel bridge piers. In *Advances in Steel Structures (ICASS'02)* (pp. 171-178): Elsevier.

Omori, T., Ando, K., Okano, M., Xu, X., Tanaka, Y., Ohnuma, I., Ishida, K. (2011). Superelastic effect in polycrystalline ferrous alloys. *Science, 333*(6038), 68-71.

Otsuka, H. (1991). Fe-Mn-Si based shape memory alloys. *MRS Online Proceedings Library (OPL), 246*.

Parks, J. E., Brown, D. N., Ameli, M., & Pantelides, C. P. (2016). Seismic Repair of Severely Damaged Precast Reinforced Concrete Bridge Columns Connected with Grouted Splice Sleeves. *ACI Structural Journal, 113*(3).

Paulay, T., & Priestley, M. N. (1992). *Seismic design of reinforced concrete and masonry buildings* (Vol. 768): Wiley New York.

Pegon, P., & Pinto, A. (2000). Pseudo- dynamic testing with substructuring at the ELSA Laboratory. *Earthquake Engineering & Structural Dynamics, 29*(7), 905-925.

Pinto, A., Pegon, P., Magonette, G., & Tsionis, G. (2004). Pseudo- dynamic testing of bridges using non- linear substructuring. *Earthquake Engineering & Structural Dynamics, 33*(11), 1125-1146.

Popovics, S. (1973). A numerical approach to the complete stress-strain curve of concrete. *Cement and concrete research, 3*(5), 583-599.

Priestley, M. N., Seible, F., & Calvi, G. M. (1996). *Seismic design and retrofit of bridges*: John Wiley & Sons.

Priestly, M., Seible, F., & Fyfe, E. (1993). Repair of shear column using fiberglass/epoxy jacket and epoxy injection. *Rep. No. 93-04, Job No. 90, 8*.

Richart, F. E., Brandtzæg, A., & Brown, R. L. (1928). *A study of the failure of concrete under combined compressive stresses*. Retrieved from University of Illinois at Urbana Champaign:

Rodrigues, H., Furtado, A., Arêde, A., Vila-Pouca, N., & Varum, H. (2018). Experimental study of repaired RC columns subjected to uniaxial and biaxial horizontal loading and variable axial load with longitudinal reinforcement welded steel bars solutions. *Engineering Structures, 155*, 371-386.

Rojob, H., & El-Hacha, R. (2017). Self-prestressing using iron-based shape memory alloy for flexural strengthening of reinforced concrete beams. *ACI Structural Journal, 114*(2), 523.

Rojob, H., & El-Hacha, R. (2018). Fatigue performance of RC beams strengthened with self-prestressed iron-based shape memory alloys. *Engineering Structures, 168*, 35-43.

Rousakis, T. C., & Tourtouras, I. S. (2014). RC columns of square section–passive and active confinement with composite ropes. *Composites Part B: Engineering, 58*, 573-581.

Rutledge, S. T., Kowalsky, M. J., Seracino, R., & Nau, J. M. (2014). Repair of reinforced concrete bridge columns containing buckled and fractured reinforcement by plastic hinge relocation. *Journal of Bridge Engineering, 19*(8), A4013001.

Saadatmanesh, H., Ehsani, M. R., & Jin, L. (1997). Repair of earthquake-damaged RC columns with FRP wraps. *ACI Structural Journal, 94*, 206-215.

Saatcioglu, M., & Yalcin, C. (2003). External prestressing concrete columns for improved seismic shear resistance. *Journal of Structural Engineering, 129*(8), 1057-1070.

Sakr, M. A., El Korany, T. M., & Osama, B. (2020). Analysis of RC columns strengthened with ultra-high performance fiber reinforced concrete jackets under eccentric loading. *Engineering Structures, 220*, 111016.

Sato, A., Chishima, E., Soma, K., & Mori, T. (1982). Shape memory effect in $\gamma \rightleftarrows \epsilon$ transformation in Fe-30Mn-1Si alloy single crystals. *Acta Metallurgica, 30*(6), 1177-1183.

Sawaguchi, T., Kikuchi, T., Ogawa, K., Yin, F. X., Kajiwara, S., Kushibe, A., & Ogawa, T. (2006). *Internal friction of Fe-Mn-Si-based shape memory alloys containing Nb and C and their application as a seismic damping material.* Paper presented at the Key Engineering Materials.

Schellenberg, A., & Mahin, S. (2006). *Integration of hybrid simulation within the general-purpose computational framework OpenSees.* Paper presented at the Eighth US National Conference on Earthquake Engineering.

Schellenberg, A. H. (2008). *Advanced implementation of hybrid simulation*: University of California, Berkeley.

Shahverdi, M., Czaderski, C., Annen, P., & Motavalli, M. (2016). Strengthening of RC beams by iron-based shape memory alloy bars embedded in a shotcrete layer. *Engineering Structures, 117*, 263-273.

Shahverdi, M., Czaderski, C., & Motavalli, M. (2016). Iron-based shape memory alloys for prestressed near-surface mounted strengthening of reinforced concrete beams. *Construction and Building Materials, 112*, 28-38.

Shahverdi, M., Michels, J., Czaderski, C., & Motavalli, M. (2018). Iron-based shape memory alloy strips for strengthening RC members: Material behavior and characterization. *Construction and Building Materials, 173*, 586-599.

Shannag, M. J., Abu-Dyya, N., & Abu-Farsakh, G. (2005). Lateral load response of high performance fiber reinforced concrete beam–column joints. *Construction and Building Materials, 19*(7), 500-508.

Shin, M., & Andrawes, B. (2010). Experimental investigation of actively confined concrete using shape memory alloys. *Engineering Structures, 32*(3), 656-664.

Shin, M., & Andrawes, B. (2011a). Emergency repair of severely damaged reinforced concrete columns using active confinement with shape memory alloys. *Smart Materials and Structures, 20*(6), 065018.

Shin, M., & Andrawes, B. (2011b). Lateral cyclic behavior of reinforced concrete columns retrofitted with shape memory spirals and FRP wraps. *Journal of Structural Engineering, 137*(11), 1282-1290.

Soroushian, P., Ostowari, K., Nossoni, A., & Chowdhury, H. (2001). Repair and strengthening of concrete structures through application of corrective posttensioning forces with shape memory alloys. *Transportation Research Record, 1770*(1), 20-26.

Takahashi, K., Udagawa, K., & Seki, M. (1975). Nonlinear earthquake response analysis of structures by a computer actuator on-line system: Part I, details of the system. *Transactions of the Architectural Institute of Japan, 229*, 77-83.

Takanashi, K., & Nakashima, M. (1987). Japanese activities on on-line testing. *Journal of engineering mechanics, 113*(7), 1014-1032.

Tanaka, Y., Himuro, Y., Kainuma, R., Sutou, Y., Omori, T., & Ishida, K. (2010). Ferrous polycrystalline shape-memory alloy showing huge superelasticity. *Science, 327*(5972), 1488-1490.

Teng, J., Huang, Y., Lam, L., & Ye, L. (2007). Theoretical model for fiber-reinforced polymer-confined concrete. *Journal of Composites for Construction, 11*(2), 201-210.

Terzic, V., & Stojadinovic, B. (2014). Hybrid simulation of bridge response to three-dimensional earthquake excitation followed by truck load. *Journal of Structural Engineering, 140*(8), A4014010.

Thewalt, C., & Mahin, S. (1987). Hybrid solution techniques for generalized pseudodynamic testing (UCB/EERC-87/09). *University of California, Berkeley, Berkeley*.

Tsai, W. T. (1988). Uniaxial compressional stress-strain relation of concrete. *Journal of Structural Engineering, 114*(9), 2133-2136.

Vandoros, K. G., & Dritsos, S. E. (2008). Concrete jacket construction detail effectiveness when strengthening RC columns. *Construction and Building Materials, 22*(3), 264-276.

Vosooghi, A., Saiidi, M. S., & Gutierrez, J. (2008). Rapid repair of RC bridge columns subjected to earthquakes. In *Concrete Repair, Rehabilitation and Retrofitting II* (pp. 415-416): CRC Press.

Wahalathantri, B., Thambiratnam, D., Chan, T., & Fawzia, S. (2011). *A material model for flexural crack simulation in reinforced concrete elements using ABAQUS.* Paper presented at the Proceedings of the first international conference on engineering, designing and developing the built environment for sustainable wellbeing.

Watanabe, Y., Miyazaki, E., & Okada, H. (2002). Enhanced mechanical properties of Fe-Mn-Si-Cr shape memory fiber/plaster smart composite. *Materials Transactions, 43*(5), 974-983.

Wu, R.-Y., & Pantelides, C. P. (2018). Concentrated and distributed plasticity models for seismic repair of damaged RC bridge columns. *Journal of Composites for Construction, 22*(5), 04018044.

Wu, Y.-F., & Zhao, X.-M. (2013). Unified bond stress–slip model for reinforced concrete. *Journal of Structural Engineering, 139*(11), 1951-1962.

Yamazaki, Y., Nakashima, M., & Kaminosono, T. (1989). Reliability of pseudodynamic test in earthquake response simulation. *Journal of Structural Engineering, 115*(8), 2098-2112.

Yang, J., & Wang, J. (2018). Seismic performance of shear-controlled CFRP-strengthened high-strength concrete square columns under simulated seismic load. *J. Compos. Constr, 22*(6), 04018061.

Yu, T., Teng, J., Wong, Y., & Dong, S. (2010). Finite element modeling of confined concrete-II: Plastic-damage model. *Engineering Structures, 32*(3), 680-691.

Zerbe, L., Vieira, D., Belarbi, A., & Senouci, A. (2022). Uniaxial compressive behavior of circular concrete columns actively confined with Fe-SMA strips. *Engineering Structures, 255*, 113878.

Zhu, Y., Zhang, Y., Hussein, H. H., & Chen, G. (2020). Numerical modeling for damaged reinforced concrete slab strengthened by ultra-high performance concrete (UHPC) layer. *Engineering Structures, 209*, 110031.

List of publications

Journals:

1. M. Sarmah, A. Dutta, and A. Dutta, "Axial Stress-Strain Model for Concrete Actively Confined with Fe-SMA Strips," Engineering Structures. *(Under review)*

2. M. Sarmah, S. K. Deb, and A. Dutta, "Rehabilitation of Severely Damaged RC Bridge Piers: Experimental and Numerical Investigation," Journal of Earthquake Engineering. *(Under review)*

3. M. Sarmah, S. K. Deb, and A. Dutta, "Hybrid simulation for evaluation of seismic performance of highway bridge with pier retrofitted using Fe-SMA strips" ASCE Structures. *(Communicated)*

4. M. Sarmah, A. Dutta, and S. K. Deb, "3D finite element modelling of RC bridge piers retrofitted using Fe-SMA strips" Engineering Structures. *(Communicated)*

5. M. Sarmah, A. Dutta, and S. K. Deb, "Calibration of 3D finite element model of highway bridge with pier retrofitted using Fe-SMA strips" Bulletin of Earthquake Engineering. *(Communicated)*

Book Chapter:

1. M. Sarmah, S.K. Deb and A. Dutta (2022), "Rapid Retrofitting of RC Columns Using Fe-SMA for Enhanced Seismic Performance," In: T.G. Sitharam, S. Kolathayar, R.S. Jakka, V. Matsagar (eds) Theory and Practice in Earthquake Engineering and Technology. Springer Tracts in Civil Engineering. Springer, Singapore. https://doi.org/10.1007/978-981-19-2324-1_8

Conferences:

1. M. Sarmah, S.K. Deb and A. Dutta (2018), "Seismic Rehabilitation of Bridge Pier using Fe-SMA – A Review" Proceedings of the 2nd International Conference on Civil Engineering for Sustainable Development – Opportunities and Challenges, Assam Engineering College.

2. M. Sarmah, S.K. Deb and A. Dutta (2020), "Active Confinement for Strength and Ductility Enhancement of Concrete Using Fe-SMA Strips" Proceedings of the 17th World Conference on Earthquake Engineering, Sendai, Japan.